Conference Proceedings of the Society for Experimental Mechanics Series

Zhu Mao *Editor*

Model Validation and Uncertainty Quantification, Volume 3

Proceedings of the 40th IMAC, A Conference and Exposition on Structural Dynamics 2022

Springer

Conference Proceedings of the Society for Experimental Mechanics Series

Series Editor
Kristin B. Zimmerman
Society for Experimental Mechanics, Inc.,
Bethel, CT, USA

The Conference Proceedings of the Society for Experimental Mechanics Series presents early findings and case studies from a wide range of fundamental and applied work across the broad range of fields that comprise Experimental Mechanics. Series volumes follow the principle tracks or focus topics featured in each of the Society's two annual conferences: IMAC, A Conference and Exposition on Structural Dynamics, and the Society's Annual Conference & Exposition and will address critical areas of interest to researchers and design engineers working in all areas of Structural Dynamics, Solid Mechanics and Materials Research.

Zhu Mao
Editor

Model Validation and Uncertainty Quantification, Volume 3

Proceedings of the 40th IMAC, A Conference and Exposition on Structural Dynamics 2022

Springer

Editor
Zhu Mao
Department of Mechanical and Materials Engineering
Worcester Polytechnic Institute
Worcester, MA, USA

ISSN 2191-5644 ISSN 2191-5652 (electronic)
Conference Proceedings of the Society for Experimental Mechanics Series
ISBN 978-3-031-04089-4 ISBN 978-3-031-04090-0 (eBook)
https://doi.org/10.1007/978-3-031-04090-0

This Springer imprint is published by the registered company Springer Nature Switzerland AG
The registered company address is: Gewerbestrasse 11, 6330 Cham, Switzerland

Preface

Model Validation and Uncertainty Quantification represents one of nine volumes of technical papers presented at the 40th IMAC, A Conference and Exposition on Structural Dynamics, organized by the Society for Experimental Mechanics, and held February 7–10, 2022. The full proceedings also include volumes titled *Nonlinear Structures & Systems*; *Dynamics of Civil Structures*; *Dynamic Substructures*; *Special Topics in Structural Dynamics & Experimental Techniques*; *Rotating Machinery, Optical Methods & Scanning LDV Methods*; *Sensors and Instrumentation, Aircraft/Aerospace and Dynamic Environments Testing*; *Topics in Modal Analysis & Parameter Identification*; and *Data Science in Engineering*.

Each collection presents early findings from experimental and computational investigations on an important area within structural dynamics. Model validation and uncertainty quantification (MVUQ) is one of these areas.

Modeling and simulation are routinely implemented to predict the behavior of complex dynamical systems. These tools powerfully unite theoretical foundations, numerical models, and experimental data which include associated uncertainties and errors. The field of MVUQ research entails the development of methods and metrics to test model prediction accuracy and robustness while considering all relevant sources of uncertainties and errors through systematic comparisons against experimental observations.

The MVUQ Technical Division at the Society for Experimental Mechanics would like to thank the authors, presenters, session organizers, and session chairs for their participation and effort in this track.

Worcester, MA, USA — Zhu Mao

Contents

Chapter 1
On Model Validation and Bifurcating Systems: An Experimental Case Study

Keith Worden, David J. Wagg, and Malcolm Scott

Abstract This chapter demonstrates some of the problems that can arise when validating models of nonlinear bifurcating systems and the approaches that can avoid them. Validation is the process of determining the extent to which a model accurately represents the structure or system of interest. Additional care needs to be taken when attempting to validate models of nonlinear systems because of bifurcations that may occur. These phenomena present a difficulty for validation because if a model does not precisely capture the bifurcation points, then the model's predictions could be very inaccurate, even if the model is (parametrically) very close to the real system. This situation could lead to a good model being dismissed if data generated close to a bifurcation point were used to validate it. In this chapter, experimental data were gathered from a three-storey shear building structure with a harsh nonlinearity between the top two floors, and bifurcations were observed in the structural response. Two models are constructed here, with parameters estimated using Bayesian system identification: a linear model and a nonlinear model. Selected features and metrics were then used to compare the model predictions to the test data. The results show that an appropriate model could be rejected if an inappropriate validation strategy is employed, purely as a result of slightly misplaced bifurcations. It is demonstrated that discrimination can be improved by taking modelling uncertainties into account as part of the validation process.

Keywords Validation and verification · Nonlinear systems · Bifurcations · Bayesian system identification

1.1 Introduction

The purpose of this chapter is to discuss some issues associated with the validation of computational models of nonlinear systems: in particular, systems that *bifurcate*. It is a very late follow-up to the paper [1], which discussed some of the issues in the context of a single-degree-of-freedom (SDOF) system. In this chapter, results will be presented for more realistic (MDOF) nonlinear systems and will address some of the issues involved in identifying and validating such systems. In this chapter, the definition of *model validation* is taken from [2]: "Validation is the process of determining the degree to which a model is an accurate representation of the real world from the perspective of the intended uses of the model." The process of validation—as a baseline—typically involves comparing model simulations to experimental data; this can be done directly, or features can be extracted from the data and compared. Model uncertainties must also be taken into account during validation. A key point in the definition above is that relating to "intended use" of the model. While complete validation might be theoretically desirable, i.e., one establishes that the model provides a perfect description of physical reality, this is likely to be impossible. In practice, one would typically be satisfied by showing that the model is effective over a given set of circumstances and in making a restricted set of possible predictions over that set.

The framework for model validation for linear systems is arguably in a fairly healthy state; this is partly because of the "smoothness" of linear systems; if the parameters of a linear system model are perturbed slightly, the perturbed model predictions will only depart slightly from the predictions of the original model; there is *continuity* in the response, as a function of parameters. This state of affairs will also hold for *weakly nonlinear* systems; however, it will fail for nonlinear systems that *bifurcate* [3]. Such systems may change their output responses drastically, given even small changes in their parameters. Bifurcations can occur in many different forms, but one of the most important types in structural dynamics are the *jump phenomena* observed during experimental tests when a sine-wave excitation is varied in its frequency. The situation

K. Worden (✉) · D. J. Wagg · M. Scott
Dynamics Research Group, Department of Mechanical Engineering, University of Sheffield, Sheffield, UK
e-mail: k.worden@sheffield.ac.uk; d.j.wagg@sheffield.ac.uk; m.s.scott@sheffield.ac.uk

Z. Mao (eds.), *Model Validation and Uncertainty Quantification, Volume 3*, Conference Proceedings of the Society for Experimental Mechanics Series, https://doi.org/10.1007/978-3-031-04090-0_1

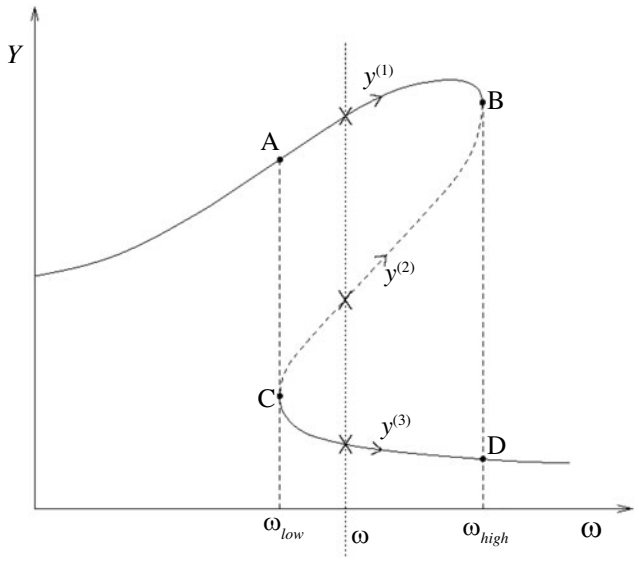

Fig. 1.1 Frequency response of the harmonically forced Duffing oscillator

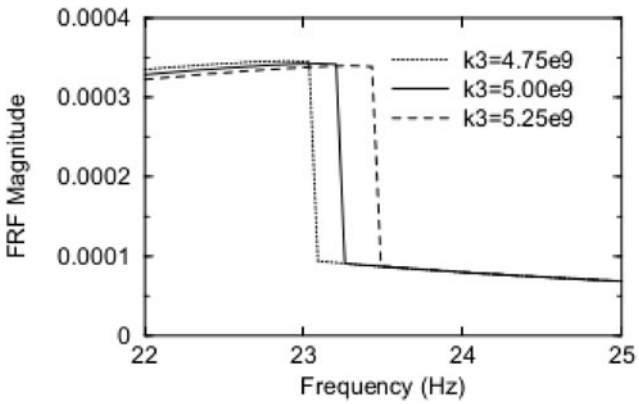

Fig. 1.2 FRFs for Duffing systems with slightly different k_3 parameters

is summed up quite nicely in Fig. 1.1, which expresses the amplitude response of an SDOF Duffing oscillator system [3],

$$m\ddot{y} + c\dot{y} + ky + k_3 y^3 = x(t). \tag{1.1}$$

As the excitation $x(t) = X\cos(\omega t)$ experiences a smooth change in the frequency ω, there is a smooth increase in the response amplitude. If X is small, such that the system has a nominally linear behaviour, the response will reach a peak (resonance) and then decline smoothly with further frequency increase. If, however, X is large, at some frequency ω_{high}, the amplitude will drop sharply from its high value to a low value (point B in the figure drops to point D). If the frequency is swept down from high values, a jump *up* will occur at some frequency ω_{low}.

A common approach to model validation is to give a quantified measure of how accurate the predictions made by the model will be, taking into account all possible sources of uncertainty [4]. Such sources include uncertainties in the excitation parameters or in the parameters of the model, if it has been identified from data. Bifurcations are clearly an issue here. Consider Fig. 1.2; this shows the range of jump frequencies obtained if the nonlinear stiffness, k_3 in Duffing's equation, is varied from 4.75×10^9 to 5.25×10^9. Clearly, a small error in this parameter, if identified from data, could make the difference between a small amplitude prediction and a large one.

The issue for validation is this: suppose that one has identified a very good model from data. Furthermore, suppose that one is attempting to validate the model by comparing its predictions from measured data, using an error metric like the normalised mean-square error (NMSE), defined by

$$J(\underline{\theta}) = \frac{100}{N\sigma_y^2}\sum_{i=1}^{N}(\ddot{y}_i - \hat{\ddot{y}}_i(\underline{\theta}))^2, \tag{1.2}$$

where the $\ddot{y}_i$ are measured samples from an acceleration time series, and $\hat{\ddot{y}}_i(\underline{\theta})$ are the corresponding predictions from the model; $\underline{\theta}$ are the model parameters and N response points are sampled and have variance σ_y^2. (With the normalisation here, an NMSE value of 5% can be considered to indicate a good model, while a value of 1% indicates excellence [3]). If the model parameters are an arbitrarily small value below the "true" parameters, a sine excitation at the "wrong" frequency will elicit a very large difference in the responses, and one might be inclined to reject a good model.

The original paper [1] made a number of observations on the effects of bifurcation on model validation and suggested a number of comparison features that might be less sensitive to small errors in model parameters. However, the discussion was limited to SDOF systems and did not make contact with reality in a number of respects. The objective of the current paper is to take the discussion a little further by considering MDOF systems and actually comparing identified model predictions with reality, using a real experimental structure.

1.2 Experimental Case Study

In order to discuss some of the issues referred to earlier, data were acquired from a laboratory structure; this was a model of a three-storey shear building, with substantial masses representing the floors. The mass of the columns could be neglected in comparison to the floors, so the structure had effectively three DOFs. In fact, the structure was heavily influenced by the structure discussed in [5], which was developed at Los Alamos National Laboratories. That structure was affectionately known as the "bookshelf" structure and will be referred to as such here. The main difference between the structure here and the LANL original is that the original was mounted on linear bearings and excited at the base, whereas here the base of the structure is fixed to a testing table and forcing is applied at the first storey using an electrodynamic shaker. A schematic of the new bookshelf is given in Fig. 1.3.

Each "shelf" of the bookshelf rig is made from a solid rectilinear aluminium block of dimensions 350 × 255 × 25 mm and has a mass of approximately 6.4 kg. At each corner, the shelves are connected to the upright beams using a block and four bolts. A column is bolted to the underside of the top floor, and a motion-limiting constraint, referred to here as the

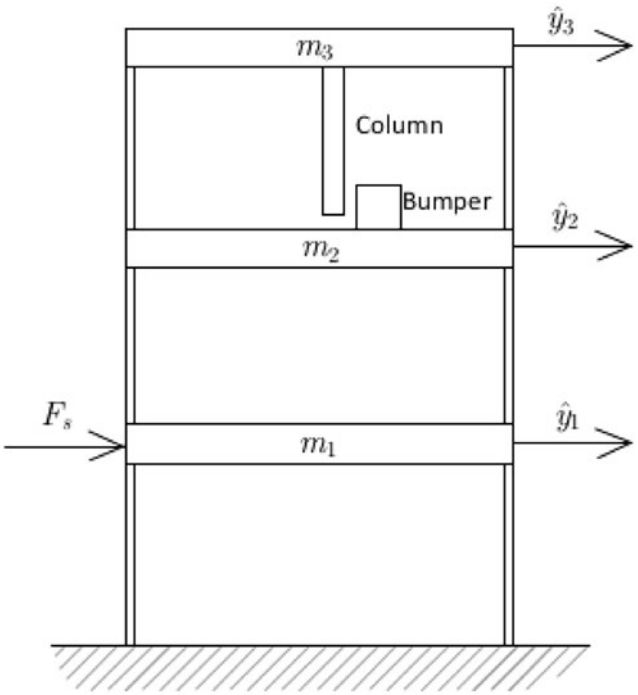

Fig. 1.3 Schematic of "bookshelf" rig

Table 1.1 Excitation frequencies and amplitudes of data

Excitation frequency (Hz)	Amplitude (N)	Excitation frequency (Hz)	Amplitude (N)	Excitation frequency (Hz)	Amplitude (N)
17	156	28	229	53	94
17.5	154	32	311	55	128
18	138	36	203	57	195
18.5	120	40	208	60	155
19	82	44	151	66	257
19.5	54	46	126	67	258
19.7	96	47	102	70	249
20	150	47.5	82	72	203
20.5	168	48	80	73	221
21	170	48.5	77	74	189
21.5	172	51.5	82	75	168
24	269	52	89		

"bumper," is bolted to the top of the second floor. The position of the bumper can be moved in order to adjust the gap d between the column and the bumper. The system responses were measured using accelerometers attached to each floor/shelf. Both data acquisition and shaker control were accomplished using an LMS SCADAS-3 interface connected to a PC running LMS Test.Lab software.

1.2.1 Test Sequence

Two groups of data were gathered, each consisting of 35 data sets generated using periodic forcing between 17 and 75 Hz; this frequency range contains the first two natural frequencies of the structure. Higher frequencies were not considered because the bumper–column impacts caused the results to become very noisy. The test frequencies were concentrated more in regions where preliminary tests showed more nonlinear phenomena. Some additional measurements were made to give a more accurate picture of the frequency response and to locate bifurcation (jump) frequencies. The first group of data was taken with the gap between the bumper and column too far apart for them to engage and is referred to here as the *linear data*. Linearity of the system in this case was confirmed using reciprocity checks and noting the absence of any response harmonics. The second group of data was gathered with the gap d set to approximately 0.5 mm and is referred to here as the *nonlinear data*. The excitation amplitudes were adjusted so that the response amplitudes for each data set were at a similar level; this was done for three reasons: (1) to ensure that the bumper engaged for the nonlinear data; (2) to ensure that the measurement noise was small compared to the measured response; and (3) to ensure that the response amplitudes were not big enough to compromise the linearity of system when the bumper did not engage. The forcing amplitudes for the nonlinear data are shown in Table 1.1; similar amplitudes were used for the linear data.

Sinusoidal excitation was chosen here as it is known to generally produce the strongest manifestation of nonlinear phenomena. A good approximation to sinusoidal forcing was fairly simple to achieve for the structure in its linear state. However, when the bumper engaged, the harsh nonlinearity made controlling the input force rather difficult. The nonlinear experimental results presented below resulted from periodic forcing of a similar nature to that shown in Fig. 1.4. The force signal contains harmonics at multiples of the forcing frequency and the natural frequencies of the system. This pollution does not pose a problem from a model validation point of view because the measured forcing from the test data could be used as an input to a model when generating features. Furthermore, despite the non-sinusoidal forcing, multiple bifurcations were still observed in the test data.

1.2.2 Response Data

For many of the excitation frequencies, the time histories of the linear and nonlinear data look very different; an example of this can be seen in the plot in Fig. 1.5 that shows the second floor response when excited at 44 Hz. The linear system

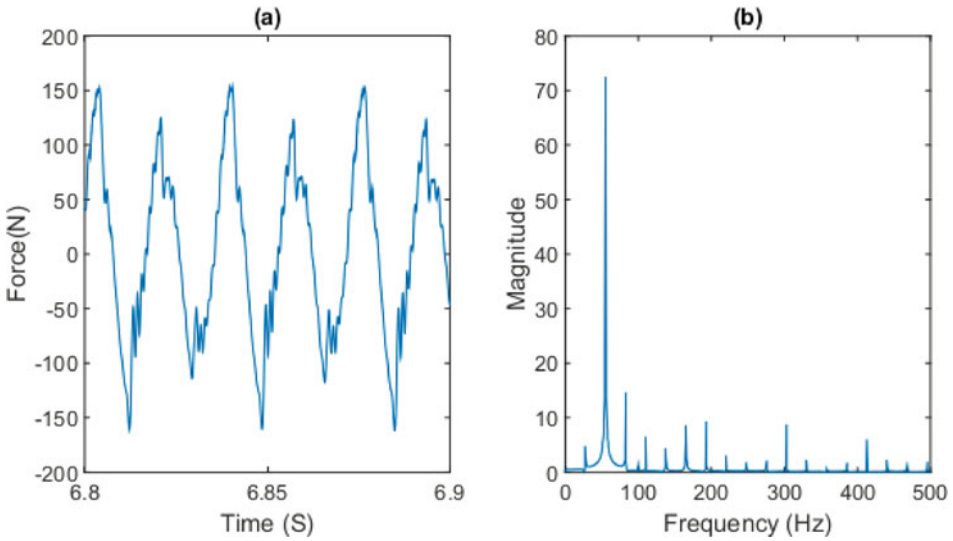

Fig. 1.4 Example of force signal applied to the bookshelf structure rig: (**a**) time history; (**b**) spectral density

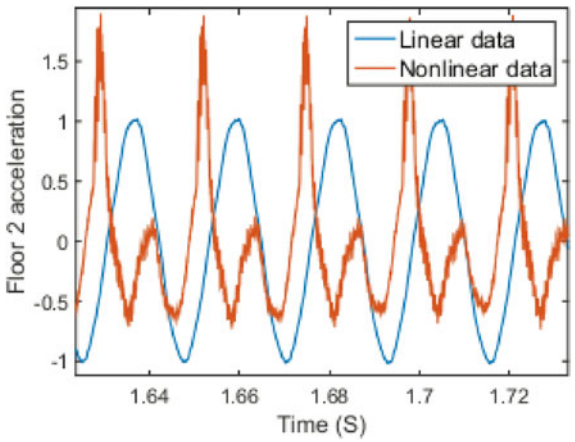

Fig. 1.5 Acceleration time histories at 44 Hz, linear and nonlinear data

response is close to sinusoidal, whereas the nonlinear response is very asymmetric, showing a strong second harmonic. Plots of frequency response values (acceleration amplitude divided by forcing amplitude) for the linear and nonlinear data are shown in Fig. 1.6. For non-harmonic responses, the amplitude here is taken as half of the peak to peak distance. When in its linear state, the structure has its first two natural frequencies at around 19.3 and 49.5 Hz; in its nonlinear state, the maximum response values were seen at 19.5 and 51.5 Hz. At the second resonance, the nonlinear data shows a "bending" of the peak that is typical of dynamic systems with a hardening stiffness [3]. Figure 1.6 also shows a sharp drop after the second peak of the nonlinear response; this is a result of a saddle-node "jump" bifurcation as discussed in the introduction here. Further tests were made to pinpoint bifurcation frequencies; as expected, these were sensitive to forcing amplitude. At forcing levels of 115, 130, and 150 N, the response amplitude jumps took place at 53.558, 54.557, and 55.065 Hz, respectively. A nice example of a jump can be seen in Fig. 1.7, which shows the acceleration time histories at 55.065 and 55.066 Hz at 150 N forcing. If the rig is excited very close to one of these bifurcation frequencies, its response has two possible stable amplitudes. By perturbing the system, it was possible to switch the response between them. Briefly resting a hand on the top floor caused it to move from the high-to-low-amplitude response; it could be returned to the high-amplitude response by giving the top floor a sharp tap.

At periodic excitations between 65 and 75 Hz, the nonlinear data shows subharmonic oscillations, as in Fig. 1.8, which shows the acceleration time history when excited at 68 Hz. It is likely that these are as a result of period-doubling bifurcations, but constructing bifurcation diagrams for the test data is problematic because of the measurement noise and stiffness coupling effects.

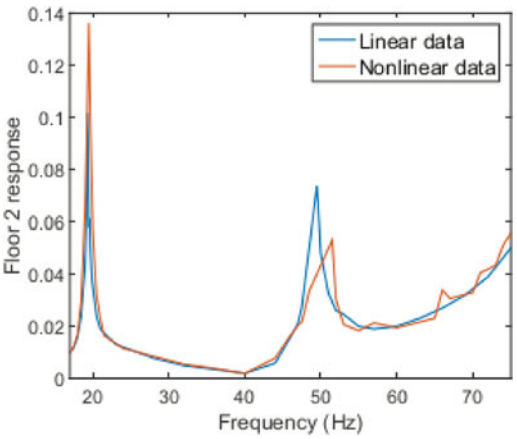

Fig. 1.6 Plot showing response of the second floor to periodic forcing, linear and nonlinear data

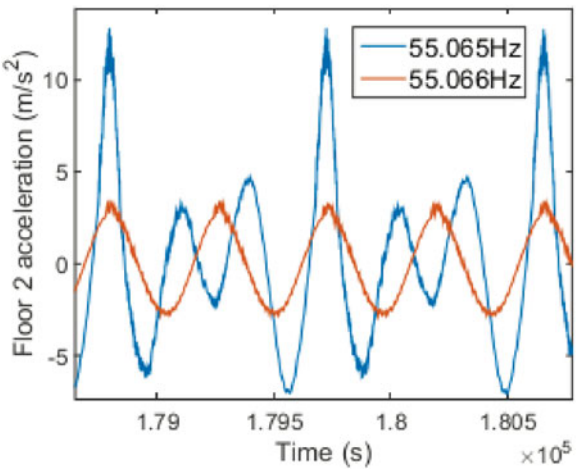

Fig. 1.7 Second floor acceleration time histories, when excited at 55.065 and 55.066 Hz

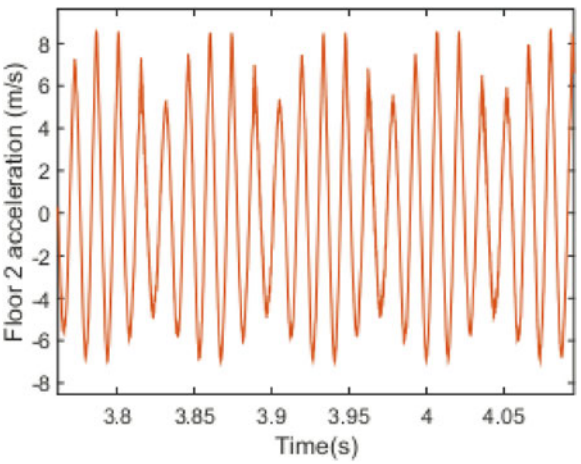

Fig. 1.8 Second floor acceleration when excited at 68 Hz

1.3 Model Development and Parameter Estimation

1.3.1 Equations of Motion

For the purposes of illustrating validation strategies, two models of the bookshelf rig have been created here: a linear model and a nonlinear model. These differ only in that the nonlinear model accounts for the bumper mechanism. In each case, the rig is modelled as a lumped-mass, three-degree-of-freedom system. For the linear model, it is assumed that there is a linear stiffness and damping between each floor, giving equations of motion,

$$\begin{aligned}\ddot{y}_1 &= (F_s - k_1 y_1 - k_2(y_1 - y_2) - c_1\dot{y}_1 - c_2(\dot{y}_1 - \dot{y}_2))/m_1\\ \ddot{y}_2 &= (-k_2(y_2 - y_3) - k_3(y_2 - y_3) - c_2(\dot{y}_1 - \dot{y}_2) - c_3(\dot{y}_2 - \dot{y}_3))/m_2\\ \ddot{y}_3 &= (-k_3(y_3 - y_2) - c_3(\dot{y}_2 - \dot{y}_3))/m_3,\end{aligned} \tag{1.3}$$

where y_i, k_i, c_i, and m_i are, respectively, the floor displacements, stiffness coefficients, damping coefficients, and floor masses for $i = \{1, 2, 3\}$ (Fig. 1.3); overdots denote differentiation with respect to time. For the nonlinear model, it is assumed that there is an additional linear stiffness between the top two floors, when the bumper is in contact; the equations of motion become

$$\begin{aligned}\ddot{y}_1 &= (F_s - k_1 y_1 - k_2(y_1 - y_2) - c_1\dot{y}_1 - c_2(\dot{y}_1 - \dot{y}_2))/m_1\\ \ddot{y}_2 &= (-k_2(y_2 - y_3) - k_3(y_2 - y_3) - F_c - c_2(\dot{y}_1 - \dot{y}_2) - c_3(\dot{y}_2 - \dot{y}_3))/m_2\\ \ddot{y}_3 &= (-k_3(y_3 - y_2) - c_3(\dot{y}_2 - \dot{y}_3))/m_3,\end{aligned} \tag{1.4}$$

where

$$F_c = \begin{cases} 0 & \text{if } (y_3 - y_2) < d \\ k_c(y_2 - y_3 + d) & \text{if } (y_3 - y_2) \geq d \end{cases} \tag{1.5}$$

with k_c the additional linear stiffness from the bumper and d the clearance between the bumper and column when the structure is at rest. Clearly, the effects of the bumper–column interaction are considerably more complicated than a simple bilinear stiffness; however, these are difficult to model with a simple lumped-mass system. The bilinear model was chosen as a baseline, as such systems are still capable of producing the significant nonlinear phenomena observed in the test data: amplitude jumps, superharmonics, and subharmonics [3].

The responses here were simulated using a fourth-order Runge–Kutta scheme with a timestep of 4×10^{-5}. The short sampling interval was necessary because of the discontinuous nature of the nonlinearity. The simulation allowed the forcing to be taken from actual measurements on the rig, as well as using sine-wave and random excitation. Typically, the initial 150 forcing cycles were discarded to remove transient effects.

Some preliminary results on model validation for this structure were presented in [6].

1.3.2 Parameter Estimation

The parameter estimation problem here is quite demanding; there are 11 parameters involved, and one—the clearance d—enters the equations in a nonlinear fashion. Two algorithms were applied here in order to produce the final estimates. In the first step, the *self-adaptive differential evolution* (SADE) algorithm was used [7]. SADE has proved to be a powerful choice in previous work for models that are nonlinear in the parameters and can operate directly on the measured accelerations without the need to integrate to velocity and displacement [8]. Although SADE can estimate confidence intervals for parameters [9], it assumes they have Gaussian distributions, which may be misleading for nonlinear systems. To better characterise the uncertainty in the parameters, a second identification step was applied—a Bayesian approach [10], with the SADE algorithm providing the initial parameter estimates. In this case, a vanilla Metropolis–Hastings (MH) algorithm was used. The Bayesian approach allows sampling from the actual parameter distributions, so that histograms or density estimates can be computed and displayed. Both of these algorithms, SADE and Bayesian ID, have been applied effectively on variants of the bookshelf structure in the past [11, 12].

In the first exercise here, a linear baseline model was identified using data acquired with the structure in its *nonlinear* state. As both SADE and the MH algorithm are stochastic algorithms, ten runs were carried out for each algorithm, and the results with lowest cost were selected. The training data were composed of ten sets of response data generated by excitation frequencies between 18 and 60 Hz with 150 cycles per frequency; in each case, the NMSE and parameters were averaged to give the final result. In the best run, SADE gave an acceptable NMSE of 5.4%. The MH algorithm was then run using the SADE parameter estimates as initial values; a Gaussian proposal distribution was used with variances set at 2% of the initial estimates. The priors on the parameters were taken as uniform, with bounds one order of magnitude below and above the SADE estimates. A burn-in period of 5000 iterations was used, after which 30,000 iterations were required for the algorithm to converge on a stationary distribution. With the MH step, the average NMSE between the linear model and nonlinear training data improved slightly to 5.2%. The results of the parameter estimation, of both the SADE and MH steps, are reported in Table 1.2.

Table 1.2 Linear model parameter values found using SADE and the MH algorithm

Parameter	SADE estimate	MH—mean	MH—standard deviation
m_1	6.4 kg	6.89 kg	0.402 kg
m_2	6.64 kg	6.67 kg	0.39 kg
m_3	6.26 kg	6.08 kg	0.355 kg
k_1	4.32×10^5 N/m	4.29×10^5 N/m	0.229×10^5 N/m
k_2	6.39×10^5 N/m	6.28×10^5 N/m	0.357×10^5 N/m
k_3	3.99×10^5 N/m	3.57×10^5 N/m	0.145×10^5 N/m
c_1	53.0 Ns/m	76.8 Ns/m	8.30 Ns/m
c_2	99.2 Ns/m	118 Ns/m	8.76 Ns/m
c_3	6.2 Ns/m	5.19 Ns/m	0.429 Ns/m

Table 1.3 Nonlinear model parameter values found using SADE and the MH algorithm

Parameter	SADE estimate	MH—mean	MH—standard deviation
m_1	6.69 kg	6.76 kg	0.412 kg
m_2	6.65 kg	6.63 kg	0.401 kg
m_3	6.26 kg	6.17 kg	0.395 kg
k_1	4.36×10^5 N/m	4.28×10^5 N/m	0.260×10^5 N/m
k_2	6.34×10^5 N/m	6.38×10^5 N/m	0.346×10^5 N/m
k_3	3.56×10^5 N/m	3.58×10^5 N/m	0.157×10^5 N/m
c_1	78.0 Ns/m	79.0 Ns/m	7.37 Ns/m
c_2	110.2 Ns/m	119.1 Ns/m	8.62 Ns/m
c_3	6.9 Ns/m	5.12 Ns/m	0.463 Ns/m
k_c	5.06×10^5 N/m	4.83×10^5 N/m	0.384×10^5 N/m
d (mm)	0.480	0.491	0.0358

The second exercise here was to estimate parameters for the nonlinear model from the *nonlinear structure*. In this case, a three-stage process was used because the MH algorithm failed to work without good initial estimates, but SADE struggled to produce good estimates when all 11 parameters were included. In the first stage, parameters were estimated for the linear model with the structure in its *linear state*. In the second stage, the nonlinear model was estimated with the *nonlinear* data, with the mass and stiffness estimates held at the values from the previous stage; this produced estimates of k_c and d and refined the damping estimates. With this procedure, the first stage gave an NMSE of 3.0% for the linear model and 4.3%, which were considered acceptable. Using the SADE estimates as initial estimates, as before, the MH algorithm was then run, with the same settings as used previously. The MH run reduced the NMSE to 3.7%, averaged over the three floors. The parameters from these algorithms are given in Table 1.3. Apart from the low NMSE values, it is reassuring that the mass estimates are all close to the calculated mass of the floor blocks (6.4 kg), with m_3 slightly lower as it has less column mass entrained. The parameter histograms from MH are presented in Fig. 1.9; note that some of these appear quite non-Gaussian.

1.4 Validation Features and Metrics for Nonlinear Systems

In structural dynamics applications, a *feature* is a subset of data extracted from the raw data of a dynamic response, which can be used to compare experimental data to a model output. A *metric* represents a quantitative evaluation of the similarity between recorded and predicted features. Described below are a selection of features and the metrics used in the following sections. The features are time histories, FRFs, and bifurcation points, and the metrics are NMSEs and t-statistics. Only features appropriate to periodically excited systems are considered here. A good discussion of features for validating models of randomly excited systems is given in [5].

The first feature considered is the system response time history itself, typically either displacement, velocity, or acceleration. Acceleration is the most commonly used as it is arguably the easiest to measure. A common metric used for comparing time histories is the NMSE defined in Eq. (1.2). The advantages of comparing time series for model validation are that they are information rich; disadvantages are that they are unlikely to be the "quantity of interest" for the intended use of the model, the model might do a good job of predicting important aspects of system behaviour but still have a poor NMSE

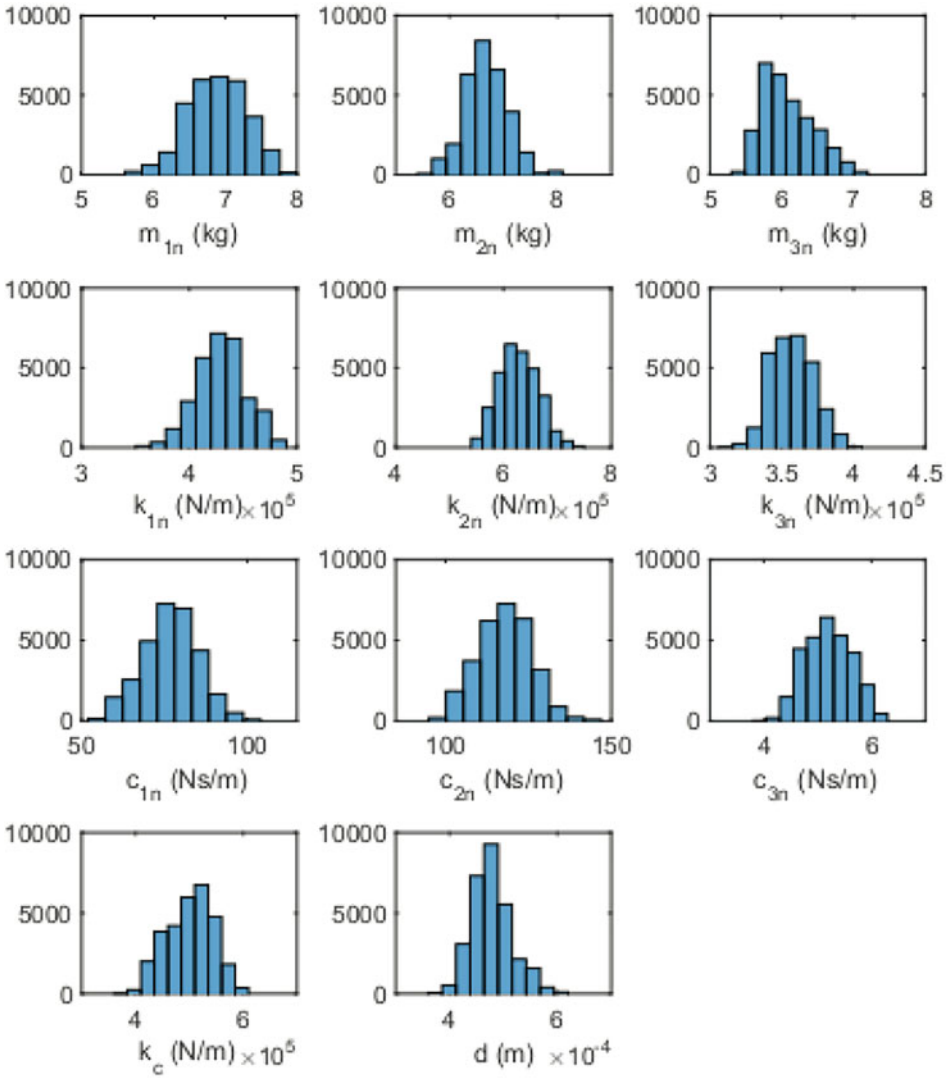

Fig. 1.9 Histograms of the nonlinear parameter values generated by the MH algorithm

between time histories, and it is difficult to take uncertainties into account. Furthermore, as discussed in [1], the NMSE has problems with systems that are sensitive to initial conditions.

Frequency response functions (FRFs) are options for validation features; these are straightforwardly estimated for random excitation or swept-sines. However, care is needed for nonlinear systems, as different excitations produce different FRF estimates, and an FRF estimated by random excitation may not represent well the behaviour of the system with harmonic forcing [3]. FRFs for swept-sine excitation of nonlinear structures can be challenging to obtain because precise control of the input waveform is needed. FRFs can be compared in the same way as time histories, using an NMSE as the metric.

While features and metrics can be used in a deterministic fashion for validation, it is much better to account for uncertainties. If parameter uncertainties can be propagated to give response value probability *distributions*, appropriate metrics exist for comparing these [5]. (As discussed in [1], FRFs and probability densities can be features that are insensitive to initial conditions.) A good discussion on statistical tests for validation metrics is given in [13]. Hypothesis tests for validation usually require an assumption about the distribution of interest; often they are taken to be Gaussian. In the Gaussian case, a simple measure of discrepancy is the t-statistic,

$$t = \frac{|r - \overline{r}|}{s}, \tag{1.6}$$

where r is the measured feature and $\bar{r}$ and s are the sample mean and standard deviation of the predicted feature distribution. If the response distribution is not Gaussian, it may be possible to make a transformation to bring it closer before computing the t-statistic. The Box–Cox transformation is a simple transformation used to remove skewness from distributions [14], as follows:

$$r_\lambda = \frac{\lambda r - 1}{\lambda}, \tag{1.7}$$

where λ is a constant that is chosen to minimise the skewness of the transformed distribution.

For nonlinear systems, a good approach is to select features that directly address that nonlinearity; in the current context, a good feature would be the jump or frequency bifurcation. It is clearly important to know whether the structure and model will jump at different frequencies.

The following section will describe the application of these features and metrics in validating the models identified for the experimental bookshelf structure.

1.5 Validation

This section presents the results of validating the linear and nonlinear models of the bookshelf structure using three different features: time histories, FRFs, and bifurcation frequencies. For each feature, deterministic and non-deterministic metrics were considered, the latter taking uncertainty into account. Twenty-five data sets, gathered using periodic forcing between 17 and 75 Hz, were used for model validation. These were separate from the training data used to estimate the parameters. In the analysis, the uncertainty in the parameter estimates from the MH algorithm was propagated into the model outputs.

The Markov chains from the algorithm generated 30,000 samples of each parameter. First of all, a Maximin Latin Hypercube design was used to select 1000 subsamples that covered the parameter space. For each parameter, the model was run for 300 forcing periods with the measured shaker forces as excitation, and the first 150 cycles were discarded to eliminate transients. For each simulation, the NMSE was calculated, giving a distribution over the runs; the frequency response amplitude was also calculated for each set of response data. These distributions were used to calculate the non-deterministic validation metrics in the following two sections.

1.5.1 Time Histories

The deterministic validation metric used here was the NMSE between modelled and measured acceleration time histories. In each model run, the measured force from the shaker was used as input. Model parameter values were taken as the mean of the distributions estimated in Sect. 1.3.2. The average NMSEs for the linear and nonlinear model were 17% and 35%, respectively. These might be considered high, but it should be noted that this is the first time the models have encountered validation data. At first sight, it appears that the linear model is performing better; however, a closer look is needed. In fact, the high average for the nonlinear models is because of three data sets generating very high errors; at 52 and 53 Hz, the nonlinear model gives errors of 200% and 500%, respectively. These high values are a result of the model misplacing the bifurcation frequency and predicting high response amplitudes when the true values are low (and *vice versa*). This highlights a disadvantage of using time-series features for models of bifurcating systems; the model is penalised for replicating the bifurcation behaviour of the system unless it does so near-perfectly. After removing the three "outliers," the NMSEs are plotted as shown in Fig. 1.10, from which it is clear that the nonlinear model generally produces better predictions.

Figure 1.11 shows the modelled and measured time histories of the second floor acceleration when the structure is excited at 21 Hz. While the nonlinear model reproduces the harmonic content seen in the real system, it actually generates an error of 6% compared to the 3% of the linear model. This effect is because of the incorrect phase of the harmonics; this is another example of the model being penalised for replicating the nonlinear behaviour of the system unless it does so extremely closely.

When the parameter uncertainty is propagated, distributions of the NMSEs result, as shown in Fig. 1.12. The plot shows the maximum and minimum values for each frequency. As before, the errors are dominated by some very high values; however, in the mean (with outliers removed), the nonlinear model performs better than the linear one. At some frequencies close to the bifurcation point, the NMSE distributions were bimodal depending on whether they correctly predicted the upper or lower branch for the amplitude.

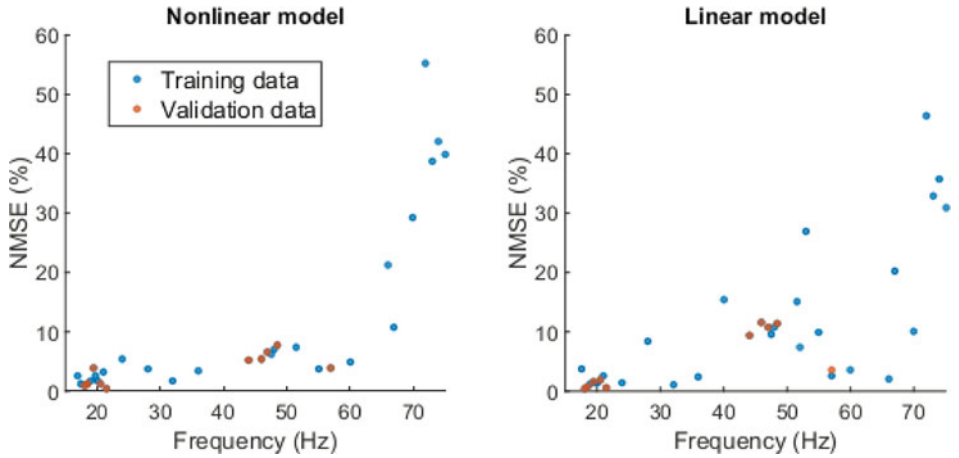

Fig. 1.10 NMSE values below 30% for nonlinear training and validation data, linear and nonlinear models

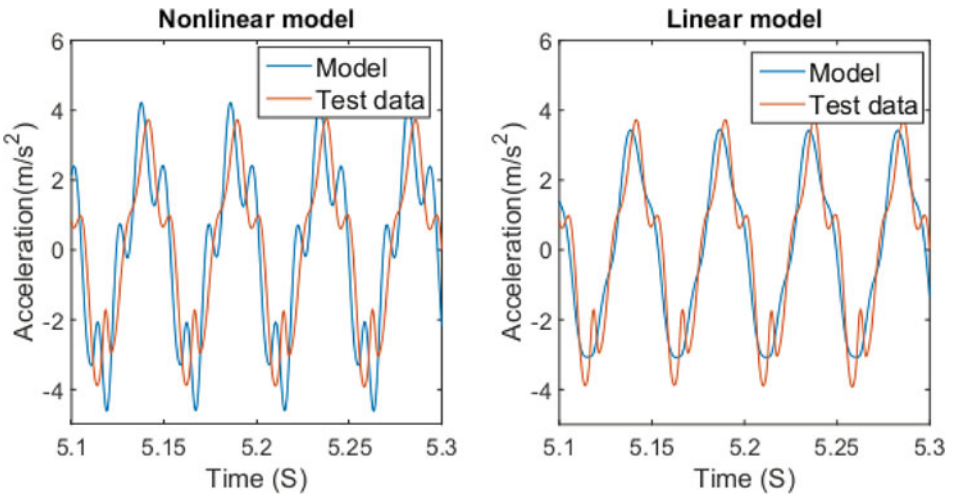

Fig. 1.11 Modelled and measured acceleration when excited at 21 Hz, linear and nonlinear models

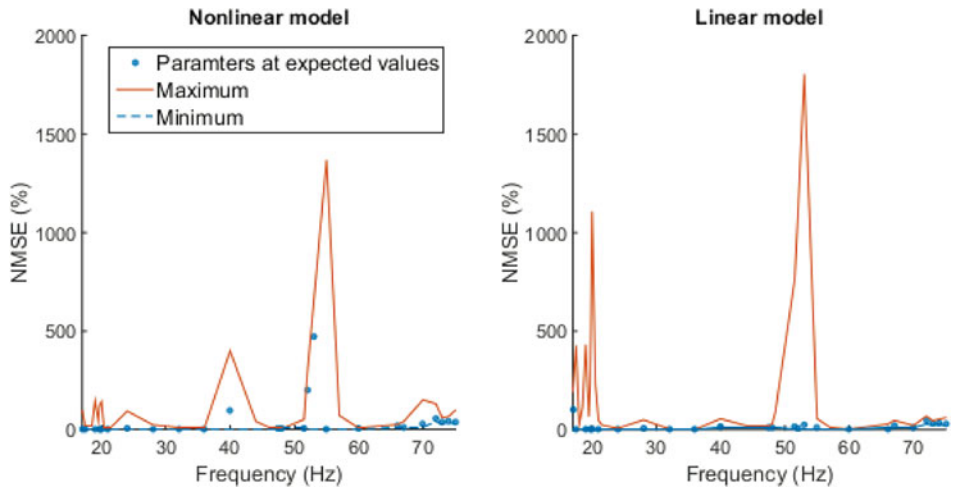

Fig. 1.12 Plot showing maximum and minimum NMSE values for each forcing frequency

1.5.2 Frequency Response

Plots of the modelled and measured frequency responses (acceleration amplitude divided by forcing amplitude) for the second floor are shown in Fig. 1.13. The model frequency responses were generated using time histories simulated with the model parameters at their expected values. In this case, the linear model appears to outperform the nonlinear one; the respective errors are 30% are 60%. The discrepancy is the result of the nonlinear model incorrectly predicting the lower amplitude beyond 52 Hz.

The model parameter uncertainty was propagated once more, to give distributions for the frequency response values. Many of these distributions looked Gaussian "by eye," generally those away from the second natural frequency. Some of the distributions showed marked skewness; an example for the 18 Hz frequency is given in Fig. 1.14. This figure also shows that the mode of the nonlinear model distribution is at the measured value from the structure, while the linear model is clearly biased. At frequencies close to the second natural frequency, the response distributions for the nonlinear model became bimodal again because the model incorrectly predicted the amplitude branch.

A plot showing the uncertainty in the modelled frequency responses of the second floor, alongside the test data, is given in Fig. 1.15. The shaded area is bounded by the maximum and minimum values of the predicted response distributions. The bimodal nature of the distributions for the nonlinear model can be seen in the figure between 51.5 and 55 Hz. For both models, the majority of the measured response values is within the bounds of the model distributions; however, the nonlinear model has a single exception at 52 Hz, while the linear model has four exceptions at 53, 55, 57, and 72 Hz.

In order to quantify the distance between the measured values and the model distributions, the response value distributions were transformed using Box–Cox transformations and the t-statistics were computed in each case (see Sect. 1.4). In almost every case, the t-statistic was lower for the nonlinear model than for the linear, with the main exceptions occurring around

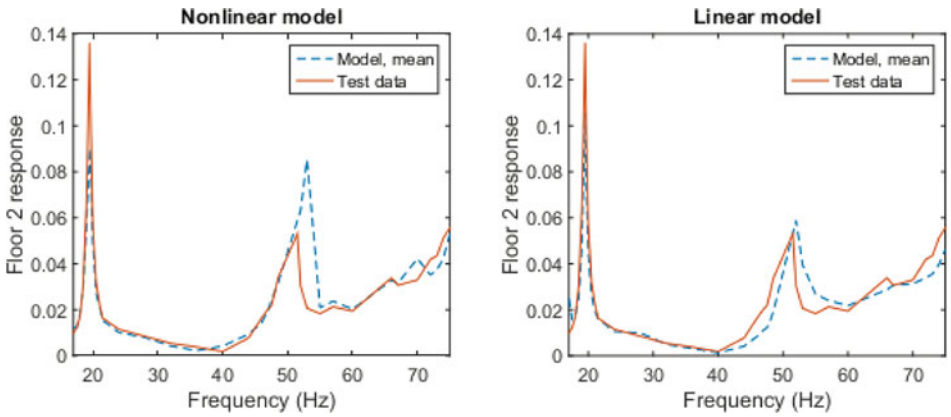

Fig. 1.13 Modelled and measured responses of Floor 2 to periodic forcing at different frequencies, nonlinear and linear models

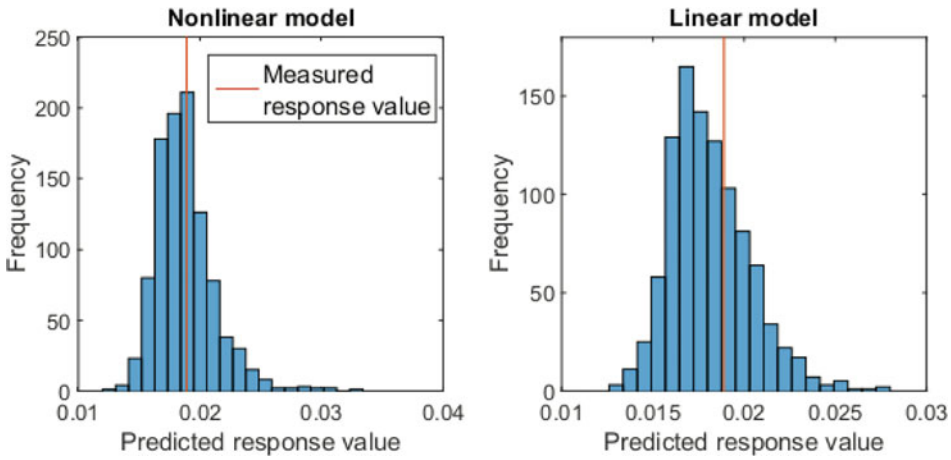

Fig. 1.14 Histogram showing predicted response value of second floor at 18 Hz, nonlinear and linear models. Predicted response value

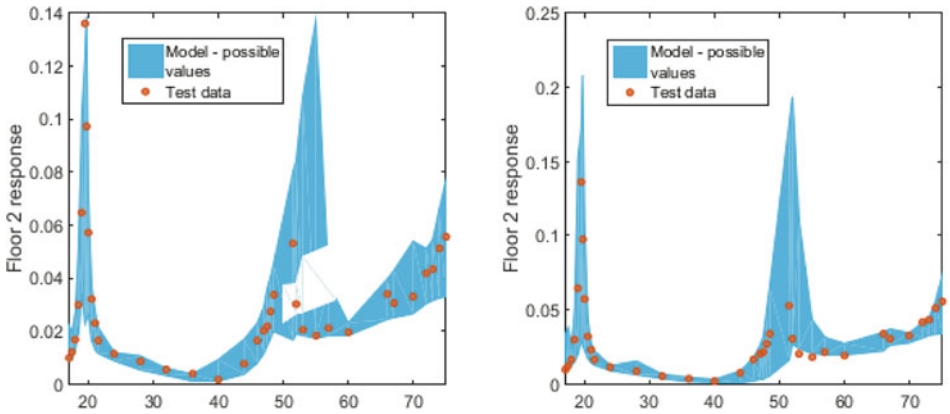

Fig. 1.15 Uncertainty of the modelled response of second floor to periodic forcing at different frequencies. Excitation frequency (Hz) t-statistic, nonlinear model t-statistic, linear model

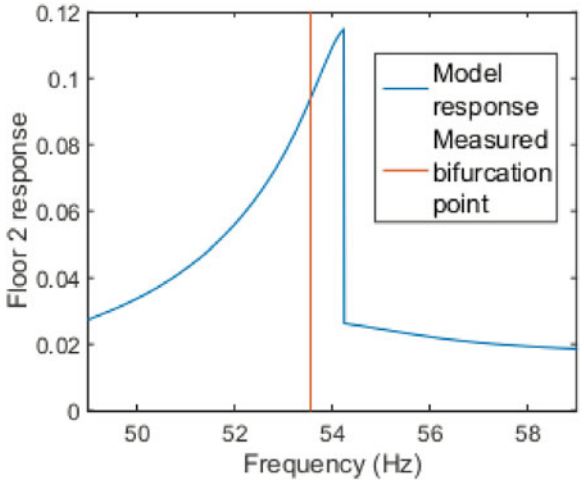

Fig. 1.16 Modelled response close to bifurcation point: excitation amplitude 115 N

the bifurcation frequency where the response distributions for the nonlinear model were bimodal. The mean values of the t-scores over all the frequencies tested were 1.30 for the nonlinear model and 1.66 for the linear model. Care must be taken with the t-statistic, as it can favour models with higher uncertainty (because of the variance in its denominator), and this is not necessarily what is needed. In this case, the parameter distributions had comparable variances, but this uncertainty propagated through to *narrower* response distributions for the nonlinear model, so the t-statistics are actually underestimating the nonlinear model performance.

1.5.3 Bifurcation Behaviour

In the tests, the bookshelf rig showed two types of bifurcations: a saddle-node bifurcation leading to a jump in amplitude just above the second natural frequency and period-doubling bifurcations leading to subharmonics between 65 and 75 Hz. Linear systems do not bifurcate, so the linear model cannot replicate this behaviour. A comparison between the bifurcation behaviours of the bookshelf rig and the nonlinear model is given below.

Data were gathered to show the frequencies at which amplitude jumps occurred at two different forcing amplitudes: 115 and 150 N. For each amplitude, a time history was recorded just above and below the bifurcation point. These time histories are referred to here as the *bifurcation data*. At 115 and 130 N, with parameters set at their expected values, the model shows amplitude jumps at similar points to those seen in the test data, as seen in Fig. 1.16. This plot replicates a stepped-sine test but uses measured forces from the rig at the bifurcation point, rather than sine waves. The frequency is varied by changing the timestep between points. At 150 N, the model did not jump but did show a discontinuity in its transition to the low-amplitude response, shown in Fig. 1.17. One should recall that this is a bilinear system rather than one of Duffing type [3].

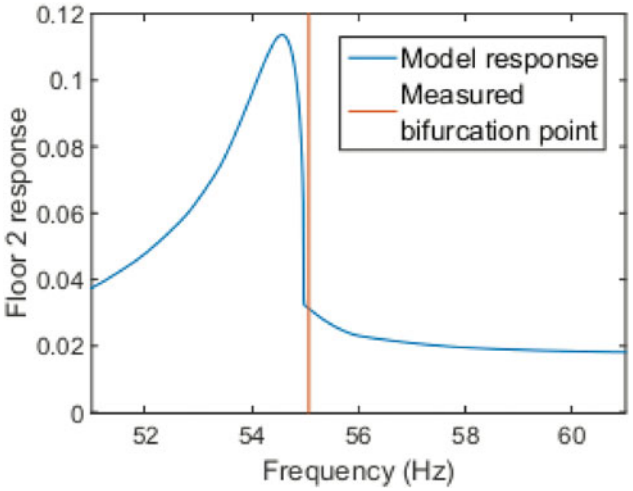

Fig. 1.17 Modelled response close to bifurcation point: excitation amplitude 150 N

Fig. 1.18 Histogram showing model uncertainty in the predicted bifurcation frequency: forcing amplitude 115 N

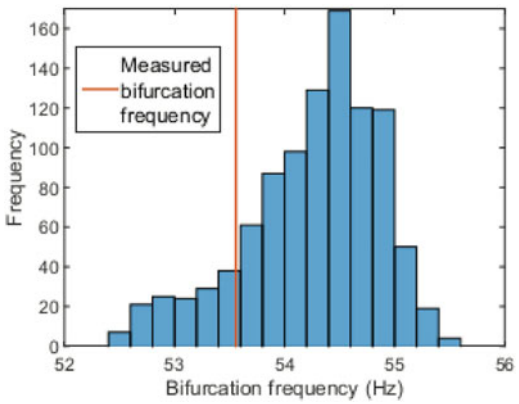

Fig. 1.19 Histogram showing model uncertainty in the predicted bifurcation frequency: forcing amplitude 150 N

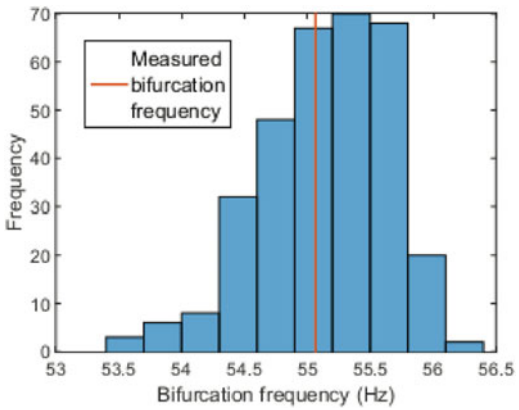

As before, the uncertainty in the predicted bifurcation frequency was characterised by propagating the parameter uncertainty through the model. The same MLH design of 1000 parameter values was used as in the previous section, and the bifurcation point was found by bracketing it between converging pairs of upper/lower frequencies. The resulting distributions for amplitudes of 115 and 150 N are shown in Figs. 1.18 and 1.19.

While the model did not jump with an excitation amplitude of 150 N and the parameters at their expected values, it did jump at this forcing amplitude for around 30% of the parameter vectors in the MLH design. At 115 N, the model bifurcated for all 1000 vectors in the MLH design. An intermediate study at 130 N showed jumps at 80% of the sampled parameters. These results suggest that nonlinear model is doing quite a good job of replicating the saddle-node bifurcation behaviour of the system.

1.6 Discussion and Conclusions

In this chapter, experimental data was gathered from a three-storey experimental structure with a harsh nonlinearity. Two models were then created of the structure, one linear and one nonlinear. A selection of validation features and metrics were then applied to the models. The different approaches to validation gave quite different outcomes. In terms of the NMSEs for the time histories and frequency responses, the raw statistics made the linear model look much better than the nonlinear model; however, a closer look and proper consideration of uncertainties showed the opposite conclusion. Furthermore, the nonlinear model successfully captured the bifurcation behaviour of the bookshelf rig in qualitative terms. The results show that a model that accurately represents the physics of the true nonlinear structure can appear much worse than one that does not and could be rejected as a result of slightly misplaced bifurcation points, unless the correct validation strategy is employed. This issue still occurs if only a small proportion of the validation data is close to the bifurcation point. The results suggest that the NMSE is a poor validation metric unless an extremely accurate model is required because the model can be penalised for replicating the nonlinear behaviour of a system unless it does so nearly perfectly.

While it is known that it is important to take uncertainties into account when validating a model, the results here show that this is particularly true for bifurcating systems. The problems illustrated here for validating models of nonlinear bifurcating systems can be mitigated by ensuring that model uncertainties are appropriately accounted for. This can be done by propagating model uncertainties to give probability distributions for the model outputs and using statistical tests to compare them to the test data. Only parameter uncertainty was considered here, but ideally, when validating a model, all forms of modelling and experimental uncertainty should be taken into account. It is possible that nonlinearity may introduce difficulties in incorporating other forms of uncertainty, but this was considered to be outside the scope of this study.

It is worth reiterating two of the purposes of model validation: first, choosing whether to accept a model or to reject it and perform further model development; second to quantify the accuracy with which the model can make predictions. These two steps are often done as part of the same process, i.e., the model will be accepted when it reaches an acceptable level of predictive accuracy. However, for nonlinear systems, it may be desirable to introduce some extra criteria that must be met before the model is accepted because of the wide range of behaviours they can exhibit; bifurcations being a perfect example. Taking the above case study as an example, suppose that the quantity that the model is required to predict is the response to periodic forcing, then this would dictate the feature that is used to assess the model accuracy. If one wanted to provide further confirmation that the model had captured the system characteristics fully, then further features could be investigated. The above results suggest that comparing the bifurcation characteristics would be a more suitable way of doing this than comparing the time histories.

It should be noted that nonlinearity causes a diverse range of phenomena, only a small number of which were observed here. Care should therefore be taken in generalising these conclusions to different nonlinear systems.

Acknowledgments The authors would like to thank the UK EPSRC for funding via the Established Career Fellowship EP/R003645/1 and the Programme Grants EP/R006768/1 and EP/K003836/1. The authors would also like to thank Drs Rob Barthorpe and Daniela Tiboaca of the University of Sheffield for help in commissioning the experimental rig and for useful discussions on Bayesian inference and validation.

References

1. Worden, K.: Some thoughts on model validation for nonlinear systems. In: Proceedings of IMAC XVII – 17^{th} International Modal Analysis Conference, Orlando, FL (2001)
2. Guide for the verification and validation of computational fluid dynamics simulations. Technical Report KAIAA-G-077-1998, American Institute of Aeronautics and Astronautics, 1998
3. Worden, K., Tomlinson, G.R.: Nonlinearity in Structural Dynamics: Detection, Identification and Modelling. Institute of Physics Press (2001)
4. Thacker, B.H., Doebling, S.W., Hemez, F.M., Anderson, M.C., Pepin, J.E., Rodriguez, E.A.: Concepts of model verification and validation. Technical report, Los Alamos National Laboratory, 2004
5. Nishio, M., Hemez, F.M., Worden, K., Park, G., Takeda, N., Farrar, C.R.: Feature extraction for structural dynamics model validation. In: Conference Proceedings of the Society for Experimental Mechanics, pp. 153–163 (2011)
6. Scott, M., Tiboaca, O.D., Barthorpe, R.J., Wagg, D.J., Worden, K.: On the validation of nonlinear MDOF system models. In: Proceedings of 27^{th} International Conference on Noise & Vibration Engineering, Leuven (2016)
7. Qin, A.K., Suganthan, P.N.: Self-adaptive differential evolution algorithm for numerical optimization. In: Proceedings of 2005 IEEE Congress on Evolutionary Computation, vol. 2, pp. 1785–1791 (2005)
8. Worden, K., Manson, G.: On the identification of hysteretic systems, Part I: fitness landscapes and evolutionary identification. Mech. Syst. Signal Process. **29**, 201–212 (2012)
9. Worden, K., Becker, W.E.: On the identification of hysteretic systems, Part II: Bayesian sensitivity analysis and parameter confidence. Mech. Syst. Signal Process. **29**, 213–227 (2012)

10. Worden, K., Hensman, J.J.: Parameter estimation and model selection for a class of hysteretic systems using Bayesian inference. Mech. Syst. Signal Process. **32**, 153–169 (2012)
11. Worden, K., Tiboaca, O.D., Antoniadou, I., Barthorpe, R.J.: System identification of an MDOF experimental structure with a view towards validation and verification. In: Proceedings of the 33^{rd} International Modal Analysis Conference, Orlando, FL (2015)
12. Tiboaca, O.D., Green, P.L., Barthorpe, R.J., Antoniadou, I., Worden, K.: Bayesian inference and RJMCMC in structural dynamics – on experimental data. In: Proceedings of the 34^{th} International Modal Analysis Conference, Orlando, FL (2016)
13. Liu, Y., Chen, W., Arendt, P., Huang, H.Z.: Towards a better understanding of validation metrics. J. Mech. Des. **133**, 071005 (2011)
14. Box, G.E.P., Cox, D.R.: An analysis of transformations. J. R. Stat. Soc. B **26**, 211–252 (1964)

Chapter 2
A Comparative Assessment of Online and Offline Bayesian Estimation of Deterioration Model Parameters

Antonios Kamariotis, Luca Sardi, Iason Papaioannou, Eleni N. Chatzi, and Daniel Straub

Abstract Many preventive maintenance schemes for managing structural deterioration rely on stochastic deterioration models. In this context, continuous structural health information can be employed within a Bayesian framework to update the distributions of the time-invariant deterioration model parameters. Bayesian parameter estimation can be performed either in an online or an offline fashion. In this contribution, we investigate different online and offline algorithms implemented for learning the model parameters, and their uncertainty, considering a probabilistic model of fatigue crack growth that is updated with continuous crack monitoring measurements. The numerical investigations provide insights on the performance of the different algorithms in terms of accuracy of the posterior estimates and computational cost.

Keywords Bayesian inference · Particle filter · Markov chain Monte Carlo · Uncertainty quantification · Structural deterioration

2.1 Introduction

The tracking and tackling of deterioration is a major challenge throughout the structural life cycle. To address this challenge, stochastic models describing the various deterioration processes can be employed, which typically contain time-invariant parameters with prior uncertainty. The deployment of sensors on structures allows for a continuous monitoring of such deterioration processes. Efficient use of continuous monitoring data within a Bayesian framework can lead to posterior estimates of the time-invariant deterioration model parameters, which is indispensable for the task of performing informed predictions on the deterioration process evolution. An important distinction can be made between online and offline Bayesian parameter estimation [1], which is the main focus of this contribution. Although the typical use of online methods, such as the particle filter [2], targets the tracking of the system's response (dynamical state) by means of a state-space formulation, these can also be used in pure recursive estimation of time-invariant parameters, such as the system properties. The task of estimating time-invariant parameters is most commonly performed with the use of offline Markov chain Monte Carlo (MCMC) methods. However, use of offline methods in setups where the measurements are obtained sequentially at different points in time can become computationally unaffordable.

2.2 Offline and Online Bayesian Parameter Estimation

This work is based on the premise that a stochastic deterioration model is available, with $\boldsymbol{\theta} \in \mathbb{R}^d$ a vector containing the d unknown time-invariant parameters. In a Bayesian framework, $\boldsymbol{\theta}$ is modeled as a vector of random variables (RVs), with their prior uncertainty described by a prior distribution $\pi_{pr}(\boldsymbol{\theta})$. Monitoring of the deterioration process leads to a set of noisy measurements $\{y_1, y_2, \dots\}$ obtained in a sequential manner at different points in time $\{t_1, t_2, \dots\}$. The measurements can be

A. Kamariotis (✉) · L. Sardi · I. Papaioannou · D. Straub
Engineering Risk Analysis Group, Technical University of Munich, Munich, Germany
e-mail: antonis.kamariotis@tum.de; luca.sardi@tum.de; iason.papaioannou@tum.de; straub@tum.de

E. N. Chatzi
Institute of Structural Engineering, ETH Zurich, Zurich, Switzerland
e-mail: chatzi@ibk.baug.ethz.ch

Z. Mao (eds.), *Model Validation and Uncertainty Quantification, Volume 3*, Conference Proceedings of the Society for Experimental Mechanics Series, https://doi.org/10.1007/978-3-031-04090-0_2

used to learn the posterior distribution of $\boldsymbol{\theta}$ through application of Bayes' rule. Different posterior distributions might be of interest; for instance, one might be interested in updating the distribution of $\boldsymbol{\theta}$ in a sequential manner, i.e., at every time step t_n when a new measurement y_n is obtained (given all the set of measurements $\{y_1, y_2, \ldots, y_n\}$ available up to t_n, denoted as $y_{1:n}$). In such settings, the use of offline MCMC algorithms is not practical, as a different chain needs to be generated for each posterior $\pi_{pos}(\boldsymbol{\theta}|\, y_{1:n})$, and the previously obtained posterior $\pi_{pos}(\boldsymbol{\theta}|\, y_{1:n-1})$ is not accounted for. In a static scenario, one might seek estimation of a single posterior density $\pi_{pos}(\boldsymbol{\theta}|\, y_{1:N})$. Using Bayes' rule, this posterior distribution of interest can be estimated

$$\pi_{pos}\left(\boldsymbol{\theta}|y_{1:N}\right) \propto \pi\left(y_{1:N}|\boldsymbol{\theta}\right)\ \pi_{pr}\left(\boldsymbol{\theta}\right) \tag{2.1}$$

where $\pi(y_{1:N}|\,\boldsymbol{\theta})$ is the likelihood function. For the latter task, typically offline MCMC methods can be employed to obtain the posterior distribution. In structural deterioration setups, where each measurement is obtained at a different point in time, each evaluation of the likelihood function within the MCMC process requires the whole set of measurements to be processed, which induces a significant computational cost.

Online particle filter methods operate in a sequential fashion, i.e., they use $\pi_{pos}(\boldsymbol{\theta}|\, y_{1:n-1})$ to obtain $\pi_{pos}(\boldsymbol{\theta}|\, y_{1:n})$ via importance resampling [2], having to account only for the new measurement y_n. They can be used in exactly the same way both for updating the distribution of $\boldsymbol{\theta}$ in an online sequential manner and for static scenarios, where only a single posterior density $\pi_{pos}(\boldsymbol{\theta}|\, y_{1:N})$ is of interest. In the latter case, they use the sequence of measurements to sequentially arrive to the final posterior density of interest via estimating all the intermediate distributions. Online particle filtering methods suffer from two distinct issues. In most cases, after a certain number of update steps, almost all the particles comprise zero (or close to zero) weights, the so-called degeneracy problem [2]. This problem is alleviated by the use of adaptive resampling procedures based on the effective sample size. When using online particle filters to estimate a posterior distribution of interest for time-invariant parameters, for which the process noise is formally zero, one runs into the issue of sample impoverishment [2]. This means that after the resampling step, most (or in extreme cases all) of the particles in the sample set end up having the exact same value, i.e., the particle set consists of only few (or one) distinct particles. The degeneracy and sample impoverishment issues render estimation of static parameters with online particle filters a challenging task.

Herein, we implement an offline MCMC-based particle filter (SMC); an online particle filter (PF), which performs Gaussian mixture (GM)-based resampling to counteract the degeneracy and sample impoverishment; and the online iterated batch importance sampling algorithm (IBIS) [3], which employs offline MCMC steps after resampling for counteracting the abovementioned issues. We apply these three algorithms on the numerical example that is described below.

2.3 Numerical Investigation

A fracture mechanics-based model serves as a use case. This describes the crack growth evolution under increasing stress cycles [4]. The crack growth follows an ordinary differential equation, known as the Paris-Erdogan law, with solution

$$a(n) = \left[\left(1 - \frac{m}{2}\right)\exp\left(C_{ln}\right)\Delta S^m \pi^{m/2} n + {a_0}^{(1-m/2)}\right]^{(1-m/2)^{-1}} \tag{2.2}$$

a [mm] is the crack length, n [−] is the number of stress cycles, ΔS [Nmm^{-2}] is the stress range per cycle when assuming constant stress amplitudes, and C_{ln} and m represent empirically determined model parameters. To express the crack size as a function of the number of stress cycles n, the boundary condition $a(n=0) = a_0$ is imposed. We assume that noisy measurements of the crack y_n are obtained sequentially at different values of n. A multiplicative error is assumed for the measurement equation, i.e., $y_n = a_n \exp\left(\varepsilon_n\right)$. Under this assumption, the likelihood function for a measurement at a given n is shown in Eq. (2.3). Table 2.1 shows the prior probability distribution model for each of the random variables $\boldsymbol{\theta}$ of the deterioration model of Eq. (2.2), as well as the assumed probabilistic model of the measurement error.

$$L\left(y_n; a_n\right) = \frac{1}{\sigma_{\varepsilon_n}\sqrt{2\pi}} \exp\left[-\frac{1}{2}\left(\frac{\ln\left(y_n\right) - \mu_{\varepsilon_n} - \ln\left(a_n\right)}{\sigma_{\varepsilon_n}}\right)^2\right] \tag{2.3}$$

Table 2.1 Prior model for the deterioration model parameters and the measurement error

Parameter	Distribution	Mean	Standard deviation	Correlation
a_0	Exponential	1	1	–
ΔS	Normal	60	10	–
C_{ln}, m	Bi-normal	$(-33; 3.5)$	$(-0.47; 0.3)$	$\rho_{C_{ln},m} = -0.9$
$\exp(\varepsilon_n)$	Lognormal	1.0	0.1508	–

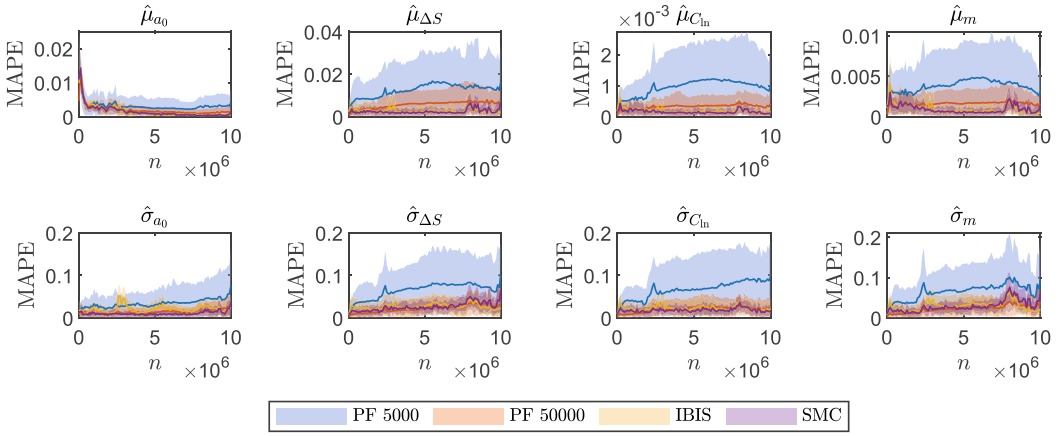

Fig. 2.1 Comparison of the MAPE evaluated for the three different applied filters. The full lines show the mean and the shaded areas the 90% credible intervals from 50 different runs of the different algorithms

An underlying "true" deterioration process $a^*(n)$ for $n = k\Delta n$, with $k = 1, \ldots, 100$ and $\Delta n = 10^5$ is generated for $a_0^* = 2.0$, $\Delta S^* = 50.0$, $C_{ln}^* = -33.5$, and $m^* = 3.7$, and a synthetic noisy crack measurement y_n is generated at each $\Delta n = 10^5$. We are interested in estimating the complete set of 100 posterior densities $\pi_{pos}(\boldsymbol{\theta} \,|\, y_{1:n})$. A reference posterior solution for each of the $\pi_{pos}(\boldsymbol{\theta} \,|\, y_{1:n})$ is generated using acceptance-rejection sampling [5].

We apply the offline MCMC-based SMC filter with 5000 particles, the online GM-based PF filter with 5000 and 50,000 particles, and the online IBIS filter, which performs resampling using offline MCMC steps with 5000 particles to estimate all the 100 $\pi_{pos}(\boldsymbol{\theta} \,|\, y_{1:n})$ posterior densities. We evaluate the performance of each filter by taking the mean absolute percentage error (MAPE) with respect to the reference posterior solution. Figure 2.1 reveals that SMC and IBIS yield superior performance, with similar results, as expected, since they both use MCMC steps in their solution. However, the IBIS is an intrinsically online algorithm, which performs offline MCMC steps only when the effective sample size drops below a threshold; hence it has a much lower computational cost. The online PF with 5000 particles performs worst, however at the lowest computational cost. Using 50,000 particles, the online PF performance increases significantly, and it provides results of a quality comparable with the SMC and IBIS results. The IBIS with 5000 particles and the PF with 50,000 particles have comparable computational costs.

2.4 Conclusion

For the specific low-dimensional numerical investigation presented herein, it is demonstrated that online particle filters lead to time-invariant deterioration model parameters posterior results of comparable quality to the results obtained with an offline MCMC-based filter, but at a significantly lower computational cost. In problems with higher dimensionality, it should be expected that the use of purely online filters will lead to posterior estimates of reduced quality.

Acknowledgments The authors would like to gratefully acknowledge the support of the TUM Institute for Advanced Study.

References

1. Kantas, N., Doucet, A., Singh, S.S., Maciejowski, J., Chopin, N.: On particle methods for parameter estimation in state-space models. *Statistical Science*. **30**(3), 328–351 (2015)
2. Särkkä, S.: Bayesian filtering and smoothing. Cambridge University Press, Cambridge (2013)
3. Chopin, N.: A sequential particle filter method for static models. *Biometrika*. **89**(3), 539–551 (2002)
4. Ditlevsen, O., Madsen, M.: Structural reliability methods. Wiley, Chichester (1996)
5. Rubinstein, R.Y., Kroese, D.P.: Simulation and the Monte Carlo method, 3rd edn. Wiley, Hoboken (2016)

Chapter 3
Finite Element Model Updating Using a Shuffled Complex Evolution Markov Chain Algorithm

Marwan Sherri, Ilyes Boulkaibet, Tshilidzi Marwala, and Michael I. Friswell

Abstract In this paper, a probabilistic-based evolution Markov chain algorithm is used for updating finite element models. The Bayesian approaches are well-known algorithms used for quantifying uncertainties associated with structural systems and several other engineering domains. In this approach, the unknown parameters and their associated uncertainties are obtained by solving the posterior distribution function, which is difficult to attain analytically due to the complexity of the structural system as well as the size of the updating parameters. Alternatively, Markov chain Monte Carlo (MCMC) algorithms are very popular numerical algorithms used to solve the Bayesian updating problem. These algorithms can approximate the posterior distribution function and obtain the unknown parameters vector and its associated uncertainty. The Metropolis-Hastings (M-H) algorithm, which is the most common MCMC algorithms, is used to obtain a sequence of random samples from a posterior probability distribution. Different approaches are proposed to enhance the performance of the Metropolis-Hastings where M-H depends on a single-chain and random-walk step to propose new samples. The evolutionary-based algorithms are extensively used for complex optimization problems where these algorithms can evolve a population of solutions and keep the fittest solution to the last. In this paper, a population-based Markov chain algorithm is used to approximate the posterior distribution function by drawing new samples using a multi-chain procedure for the Bayesian finite element model updating (FEMU) problem. In this algorithm, the M-H method is combined with the Scuffled Complex Evolution (SCE) strategy to propose new samples where a proposed sample is established through a stochastic move, survival for the fittest procedure, and the complex shuffling process. The proposed SCE-MC algorithm is used for FEMU problems where a real structural system is investigated and the obtained results are compared with other MCMC samplers.

Keywords Bayesian model updating · Markov chain Monte Carlo · Scuffled complex evolution · Finite element model · Evolutionary algorithm

3.1 Introduction

Finite element methods (FEMs) are the common tools for engineering analysis [1–3]. These approaches are adopted for different physical disciplines, including structural dynamics, heat transfer, fluid flow, and electromagnetic potential. In structural engineering, FEMs are sufficient to predict the response of simple structural system. In contrast, the reliability of the FEM results might be decreased when dealing with complex structural systems. Therefore, the finite element model updating (FEMU) techniques are employed to minimize the dissimilarities between the FEM solutions and the real structural

M. Sherri (✉)
Department of Mechanical Engineering Science, University of Johannesburg, PO, Auckland Park, South Africa

I. Boulkaibet
College of Engineering and Technology, American University of the Middle East, Kuwait City, Kuwait
e-mail: ilyes.boulkaibet@aum.edu.kw

T. Marwala
Institute of Intelligent Systems, University of Johannesburg, PO, Auckland Park, South Africa
e-mail: tmarwala@uj.ac.za

M. I. Friswell
College of Engineering, Swansea University, Bay Campus, Swansea, UK
e-mail: m.i.friswell@swansea.ac.uk

Z. Mao (eds.), *Model Validation and Uncertainty Quantification, Volume 3*, Conference Proceedings of the Society for Experimental Mechanics Series, https://doi.org/10.1007/978-3-031-04090-0_3

data [4–7]. The FEMU methods are classified in two main classes: (i) direct updating approaches and (ii) indirect updating approaches. Direct updating methods are computationally efficient since they only use one updating step to achieve the structural updating goal. In these methods, the system properties (i.e., mass and stiffness matrices) are directly equated to the structural measured mode shapes. However, the dimensionality of the acquired solutions by the FE analysis is normally larger than the measured data. Thus, direct updating methods may produce unrealistic physical components. On the other hand, the indirect updating methods, also refer to iterative techniques, are guaranteed to produce physically realistic updating results and to increase the correlations between FE solutions and the actual experimental data.

The Bayesian framework is well-known for quantifying the uncertainties that are associated with the system parameters. In Bayesian theory, the uncertainties of the modeled parameters are defined through the posterior probability density function (PDF). The function defines the updating parameters as random variables. Unfortunately, the analytical solutions for this function cannot be attained. That is due to the complexity and the high-dimensionally of this function. Alternatively, sampling methods are used to approximate solutions for complex distribution. Among these methods, the Markov chain Monte Carlo (MCMC) [8, 9], represented by the Metropolis-Hastings (M-H) algorithm [10, 11], is the most known approach to draw samples from complex probability distributions. The generated samples (proposals or solutions) are then used to approximate solutions for the posterior PDF, thereby updating the required FEM. However, MCMC methods are limited when several updating parameters are involved, as well as when the structure under consideration is sufficiently complex. For that reason, further updating methods are advised to merge with the MCMC procedure to improve the ability of drawing new proposals.

The evolutionary algorithms (EAs) are well recognized natural-inspired methods used for optimization problems [12–14]. Generally, the evolution-based search algorithm utilizes the availability of the current generation, known as solution or population, to produce a potentially more accurate solution. The interacting population at each step (iteration) is modified through specific operators to produce the next generation. Each individual solution is evaluated by a fitness function. This function is defined as the objective function of the optimization problem. The estimation of the function reflects the solution which the individual provides. EAs are promising techniques for the optimization scope. The evolutionary paradigm is implemented through different classes and for wide range of application.

In this paper, a shuffled complex evolution Markov chain algorithm is used to update a 2-D frame structure with measured data. The algorithm uses a population of solution and evolves through shuffling and partitioning into complexes. Next, the algorithm applies the metropolis acceptance rule to accept or reject the proposed solutions. As a result, this combination of the two procedures generates more accurate updating parameters. The following section explains the Bayesian inference for FEMU problem. Section 3.3 details the implementation of shuffled complex evolution Markov chain. In addition, Sect. 3.3 shows the implementation of the algorithm to sample from the posterior PDF of a Bayesian approach. Section 3.4 shows the application of the algorithm to update a 2-D frame structure with real data. Finally, the paper is concluded in Sect. 3.5.

3.2 Bayesian Inference

The Bayesian approach defines the uncertain parameters as random vector. Each parameter is determined as a stochastic variable as given by Bays' rule [3, 15–17]:

$$P\left(\boldsymbol{\theta}|\,\mathcal{D},\mathcal{M}\right) \propto P\left(\mathcal{D}|\,\boldsymbol{\theta},\mathcal{M}\right)\;P\left(\boldsymbol{\theta}|\,\mathcal{M}\right) \tag{3.1}$$

$\boldsymbol{\theta}$ is the vector of updating parameters $\boldsymbol{\theta} \in \boldsymbol{\Theta} \subset \mathcal{R}^d$. $\mathcal{D}$ is the experimental data of the structural system, represented by the natural frequencies f_i^m and mode shapes $\boldsymbol{\phi}_i^m$. $\mathcal{M}$ represents the model class of the system, where each model class is defined by a different set of updating parameters. $P\left(\boldsymbol{\theta}|\,\mathcal{M}\right)$ refers to the prior PDF that offers the previous knowledge of the uncertain parameters $\boldsymbol{\theta}$ given $\mathcal{M}$ and with the absence of $\mathcal{D}$. $P\left(\mathcal{D}|\,\boldsymbol{\theta},\mathcal{M}\right)$ is the likelihood function that describes the difference between the measured data and the analytical solutions. $P\left(\boldsymbol{\theta}|\,\mathcal{D},\mathcal{M}\right)$ is the posterior PDF of the updating parameters given a model class $\mathcal{M}$ and the measured data $\mathcal{D}$. Since only one model class is considered by this paper, $\mathcal{M}$ is removed for simplicity.

The likelihood function is given by:

$$P\left(\mathcal{D}|\,\boldsymbol{\theta}\right) = \frac{1}{\left(\frac{2\pi}{\beta_c}\right)^{N_m/2}\prod_{i=1}^{N_m} f_i^m}\exp\left(-\frac{\beta_c}{2}\sum\nolimits_i^{N_m}\left(\frac{f_i^m - f_i}{f_i^m}\right)^2\right) \tag{3.2}$$

N_m is the number of measured modes, and β_c is an arbitrary constant. f_i^m and f_i are the ith measured and analytical natural frequencies.

The prior $P(\boldsymbol{\theta})$, that provides the initial knowledge of the updating parameter $\boldsymbol{\theta}$, is defined by a Gaussian probability distribution:

$$P(\boldsymbol{\theta}) = \frac{1}{(2\pi)^{Q/2}\prod_{i=1}^{Q}\frac{1}{\sqrt{\alpha_i}}}\exp\left(-\sum_i^Q \frac{\alpha_i}{2}\left\|\theta^i - \theta_0^i\right\|^2\right) = \frac{1}{(2\pi)^{Q/2}\prod_{i=1}^{Q}\frac{1}{\sqrt{\alpha_i}}}\exp\left(-\frac{1}{2}(\boldsymbol{\theta}-\boldsymbol{\theta}_0)^T\,\Sigma^{-1}\,(\boldsymbol{\theta}-\boldsymbol{\theta}_0)\right) \tag{3.3}$$

where Q is the number of the uncertain parameters, $\boldsymbol{\theta}_0$ represents the mean value of the uncertain parameters, α_i is the coefficient of uncertain parameters, $i = 1, \ldots, Q$, and the Euclidean norm of $*$ is noted by $\|*\|$.

The posterior PDF $P(\boldsymbol{\theta}|\mathcal{D})$ of the updating parameters $\boldsymbol{\theta}$ given the measured data $\mathcal{D}$ can be now described by substituting Eqs. (3.2) and (3.3) into Eq. (3.1):

$$P(\boldsymbol{\theta}|\mathcal{D}) \propto \frac{1}{Z_s(\alpha,\beta_c)}\exp\left(-\frac{\beta_c}{2}\sum_i^{N_m}\left(\frac{f_i^m - f_i}{f_i^m}\right)^2 - \sum_i^Q \frac{\alpha_i}{2}\left\|\theta^i - \theta_0^i\right\|^2\right) \tag{3.4}$$

where,

$$Z_s(\alpha,\beta_c) = \left(\frac{2\pi}{\beta_c}\right)^{N_m/2}\prod_{i=1}^{N_m} f_i^m (2\pi)^{Q/2}\prod_{i=1}^{Q}\frac{1}{\sqrt{\alpha_i}} \tag{3.5}$$

Equation (3.4) represents the final form of the posterior PDF. The same function is employed as the objective function for evolutionary procedure. The dimensionality of the unknown parameters along with the complexity of the uncertain search bounds may affect the accuracy of the solutions. However, in the next section, the shuffled complex evolution Markov chain method is explained and detailed to solve the Bayesian FEMU problem.

3.3 Shuffled Complex Evolution Markov Chain Algorithm

The shuffled complex evolution Markov chain (SCE-MC) [18, 19] is a population-based algorithm for global optimization problems. It aims to infer the target function by combining the advantages of the Metropolis-Hastings sampler with the shuffled complex evolution (SCE) approach [20, 21]. The algorithm applies the controlled random search with competitive evolution and complex shuffling to continuously update the proposal distribution. In addition, the SCE-MC's evolution procedure evolves the proposed samples to the posterior PDF through sequence of iterations. As a result, the SCE-MC method has the ability to improve the best parameter set found in the search space every iteration. Thus, the population (Markov chains) is continuously evolved toward the optimal region in the search. The main advantage of this algorithm, in comparison to the standard SCE method, is to avoid trapping into a region with lower posterior density, which prevents most of the population to converge toward a single mode or to collapse into relatively small region of a single best parameter set (local minimum) (Fig. 3.1).

In addition, the SCE-MC algorithm uses a large number of population, N, which offers the ability for wide exploration of the parameters space, thereby raising the chance to find the global optimum of the parameter set in few iterations. Usually, a population size $N = 10d$ is sufficient to approximate a complex target distribution. The parallel sequence provides a

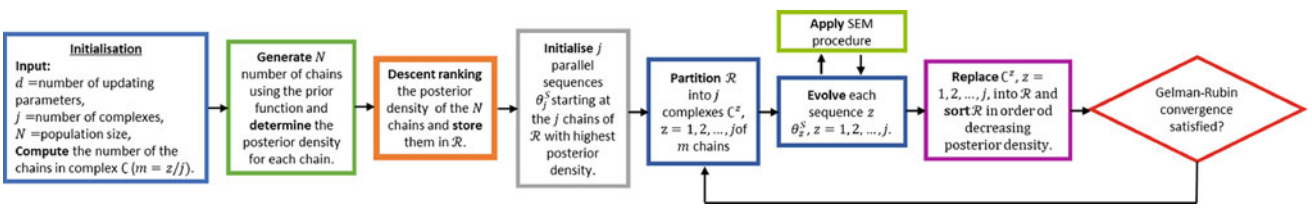

Fig. 3.1 Flow chart of the SCE-MC algorithm

mechanism for a simultaneous different region exploration. Thus, the number of j (number of parallel sequencing) enables the algorithm to seek several regions of attraction and allows to apply the heuristic test to check the convergences. A default set $j = d$ is enough for wide exploration. The user can define a greater number of sequences as the complexity of the posterior function increased. Partition into complexes brings the possibility for each individual (Markov chain) sequence to collect more knowledge about the search space during the evolution step. The shuffling process for these complexes assists the surviving for the sequence through a global sharing of the information which is already collected by each parallel sequence. The implementation of this process produces a robust sampling procedure that uses the MCMC principles for global optimum solutions.

The SCE-MC algorithm uses the Sequence Evolution Metropolis (SEM) procedure to produce new candidates (samples) in each parallel sequence θ_z^S. This can be done by creating draws from an adaptive proposal distribution through the use of the information induced in m chains of $\mathbb{C}^z$. This paper applies the default SEM procedure as explained in [18]. Another important feature of the SCE-MC algorithm is the convergence to the stationery posterior distribution. The algorithm applies the Gelman-Rubin rule [18] to estimate the convergence status. This rule is to determine the scale reduction $\sqrt{SR}$ between the chains (sequences) and the variances as given by:

$$\sqrt{SR} = \sqrt{\frac{t-1}{t} + \frac{j+1}{j.t}\frac{V}{U}} \tag{3.6}$$

where t is the number within each sequence, V is the variance between the j sequence means, and U is the average of the j within sequence variance for the parameters under consideration, respectively. Note that the product of j and t is identical to the total number of derived samples (number of algorithmic iterations T). The convergence of each parameter occurs when $\sqrt{SR}$ is close to 1. However, since this score is difficult to achieve, Gelman-Rubin suggested using value less than 1.2 to declare convergence to a stationary distribution. On the other hand, the algorithm can work through pre-defined number of iterations, which can be used to compare two updating procedures at the same number of iterations.

The SCE-MC algorithm for Bayesian FEMU is summarized as follows:

1. **Create population**: generate N number of chains $\{\boldsymbol{\theta}_1, \boldsymbol{\theta}_2, \ldots, \boldsymbol{\theta}_N\}$ randomly from the prior distribution $P(\boldsymbol{\theta}_i)$.
2. **Compute posterior**: calculate the posterior density for each generated chain $\{P(\boldsymbol{\theta}_1|D), P(\boldsymbol{\theta}_2|D), \ldots, P(\boldsymbol{\theta}_N|D)\}$.
3. **Descent ranking**: sort N chains in order of decreasing the posterior density and store them in matrix $\mathcal{R}$ $[1:N, 1:d+1]$, where d is the number of the updating parameters and the first row of $\mathcal{R}$ represents the chain with highest posterior density.
4. **Initialize parallel sequence**: start the parallel sequencing of the chains, $\boldsymbol{\theta}_1^S, \boldsymbol{\theta}_2^S, \ldots, \boldsymbol{\theta}_j^S$, such that $\boldsymbol{\theta}_z^S$ is $\mathcal{R}$ $[z, 1:d+1]$, where $z = 1, 2, \ldots, j$.
5. **Complex partitioning**: partition the N chains of the matrix $\mathcal{R}$ into $z_{\mathbb{C}}$ complexes $\mathbb{C}^1, \mathbb{C}^2, \ldots, \mathbb{C}^z$, where each complex $\mathbb{C}$ contains k chains, such that the first complex includes $j(i-1)+1$ ranked chains, the second complex includes every $j(i-1)+2$ ranked chains of the matrix $\mathcal{R}$, and so on, where $i = 1, 2, \ldots, k$.
6. **Sequence evolving**: evolve each of the parallel sequences according to the Sequence Evolution Metropolis procedure.
7. **Shuffle complexes**: unpack all complexes $\mathbb{C}$ back into $\mathcal{R}$, then rank the chains in order of decreasing posterior density and reshuffle the N chains into j complexes according to the procedure specified in step 5.
8. **Termination**: check the Gelman-Rubin convergence criteria or use maximum number of iterations. If any of these conditions is satisfied, stop. Otherwise return to step 6.

3.4 Application: Updating the Young's Modulus

A 2-D steel frame structure, as shown by Fig. 3.2, is used to demonstrate the performance of the SCE-MC algorithm for Bayesian FE model updating. The structure is fixed to the ground from its bottom side [22]. The overall height of the frame is 1.5 m and the span of the beam is 0.5 m. Each story of the structure has the same height of 0.5 m. The structure is assembled with five beams; two vertical beams, making up the right and the left side of the structure, are noted as Beam-1and Beam-2, respectively. The other three are horizontal beams noted as Beam-3 at the bottom side, Beam-4 in the middle, and Beam-5 at the top. All the beams have the same cross-sectional dimensions: their width is 75 mm, and their thickness is 5 mm. The material density of the frame is 7850 kg/m^3, and the elastic modulus is 2.0×10^{11}N/m^2.

An instrumental hammer with a rubber tip was used to excite the frame, where the frequency range of interest is about 0–100 Hz. Aaccelerometers with magnet bases are mounted on the vertical and horizontal beams to measure the response. The

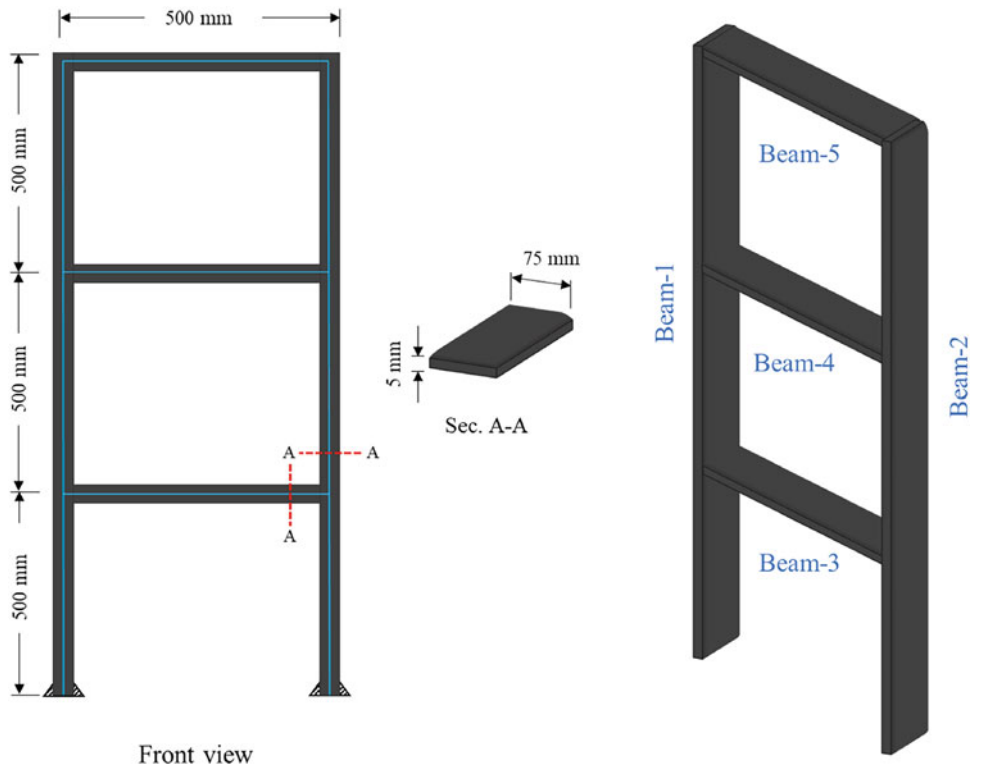

Fig. 3.2 the 2-D frame structure

first five natural frequencies and mode shapes in the range of 0 – 100 Hz were extracted. The measured natural frequencies are $\omega_m = \{4.23, 14.03, 25.45, 44.81, 58.12\}$ Hz. the FEMU application was implemented through the MATLAB environment [23], and the FE model was developed using the structural dynamic toolbox [24]. A 2-D geometrical beam element is used to simulate the frame model. The obtained analytical frequencies with the mode shapes are illustrated in Fig. 3.3.

In this application, the modulus of elasticity of the five structural beams (Beam-1 to Beam-5) is selected as the updating parameters. The updating vector is $\boldsymbol{\theta} = \{E_{m1}, E_{m2}, E_{m3}, E_{m4}, E_{m5}\}$, where E_{m1} represents the elastic modulus of Beam-1 and so on. Then, $\boldsymbol{\theta} = \{2 \times 10^{11}, 2 \times 10^{11}, 2 \times 10^{11}, 2 \times 10^{11}, 2 \times 10^{11}\}$. The updating parameters are bounded by $\boldsymbol{\theta}_{\max}$ and $\boldsymbol{\theta}_{\min}$ to keep the updated values realistic, where $\boldsymbol{\theta}_{\max} = \{2.4 \times 10^{11}, 2.4 \times 10^{11}, 2.4 \times 10^{11}, 2.4 \times 10^{11}, 2.4 \times 10^{11}\}$ and $\boldsymbol{\theta}_{\min} = \{1.6 \times 10^{11}, 1.6 \times 10^{11}, 1.6 \times 10^{11}, 1.6 \times 10^{11}, 1.6 \times 10^{11}\}$. The variance vector is $\sigma^2 = \{5 \times 10^{11}, 5 \times 10^{11}, 5 \times 10^{11}, 5 \times 10^{11}, 5 \times 10^{11}\}$, and the total number of iterations is $t_s = 500$. Meanwhile, the number of complexes $z_{\complement}$ in the SCE-MC algorithm is set to 5 and the population size $N = 50$. On the other hand, the M-H method is set as its default settings with increasing the size of its move.

In this application, the SCE-MC algorithm and the canonical M-H method are applied to update the same structure, this aims to compare the two algorithms and to highlight the improvements gained when combining the M-H criterion with the evolutionary mechanism. Both algorithms were tested to update the frame structure for several independent runs. Each updating trial was set to the same algorithmic settings and parameters. Table 3.1 presents the updated parameters by the SCE-MC algorithm and the M-H method. The initial values of the elastic modulus are given in the table for the five updating elements. The final updated values as shown in the table are different to the initial states. This shows that both algorithms produced realistic updated parameters that keep physical meaning for the updating feature. The table also includes the coefficient of variation (cov) of the updated parameters from each algorithm. This coefficient measures the level of precision within the samples produced by the updating methods. The cov is defined as the ratio of the standard deviation A to the mean value θi (the value of the final updated parameter), i.e., cov$= \frac{\sigma_i}{\theta_i}$.

Generally, the cov values obtained by the SCE-Mc algorithms are better than the M-H method. The sampling precision that happens in the SCE-MC procedure is due to the use of large number of population. Thus, the selected solutions reflect the best results among the other solutions. Contrary, the M-H applies a single move only to propose the new solutions state. However, the cov of the still reflect a quiet acceptable range.

Figure 3.4 illustrates the boxplots of the generated samples by SCE-MC algorithm. On each box, the central dark blue line represents the median, and the light blue box spans indicate the 25th and 75th percentile (the range that bounds 25%

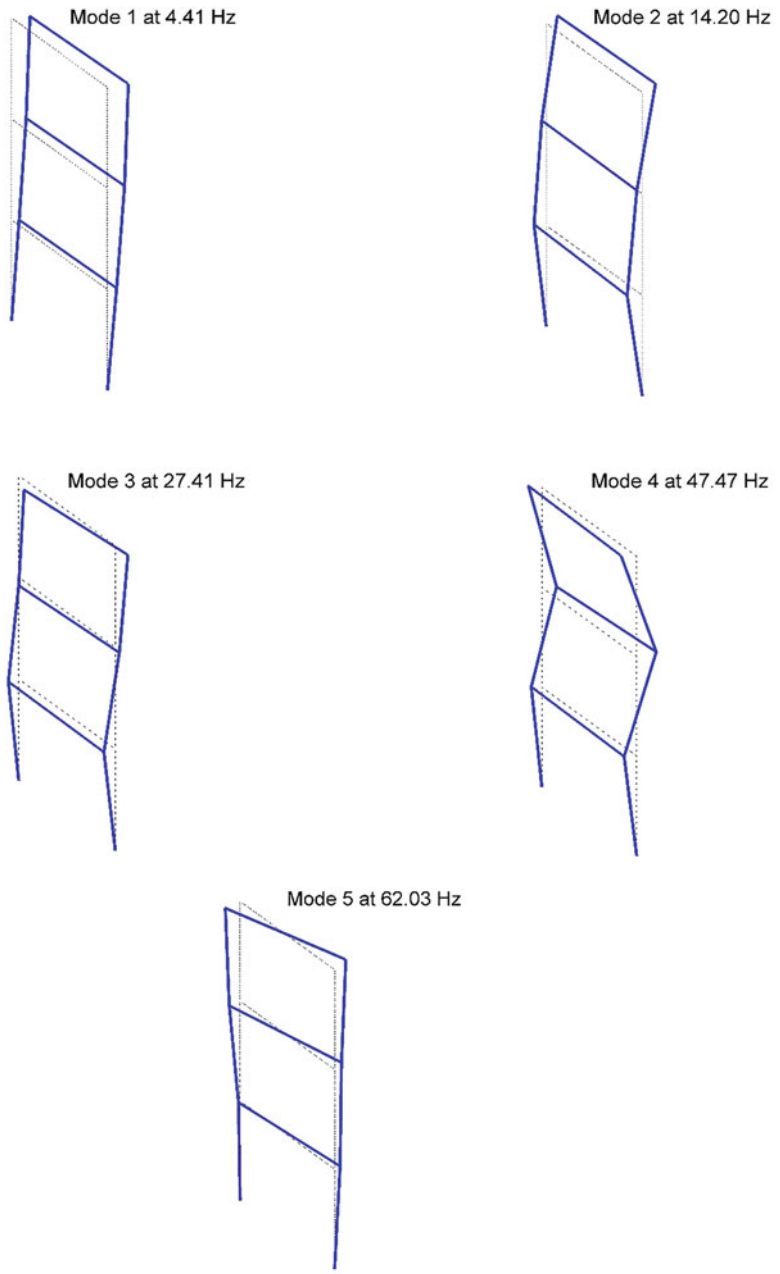

Fig. 3.3 The analytical frequencies and the mode shapes of the 2-D frame structure

Table 3.1 The updated elastic modulus of the 2-D frame structure using the M-H and the SCE-MC

Updating the elastic modules E_m (N/m^2)					
	Initial FEM	M-H method	cov (%) $\frac{\sigma_i}{\theta_i}$	SCE-MC method	cov (%) $\frac{\sigma_i}{\theta_i}$
E_{m1}	2.0×10^{11}	1.929×10^{11}	3.15	1.987×10^{11}	2.02
E_{m2}	2.0×10^{11}	2.050×10^{11}	3.77	1.945×10^{11}	2.63
E_{m3}	2.0×10^{11}	2.196×10^{11}	4.31	2.287×10^{11}	3.54
E_{m4}	2.0×10^{11}	2.087×10^{11}	2.31	2.107×10^{11}	2.18
E_{m5}	2.0×10^{11}	2.127×10^{11}	3.44	2.163×10^{11}	3.07

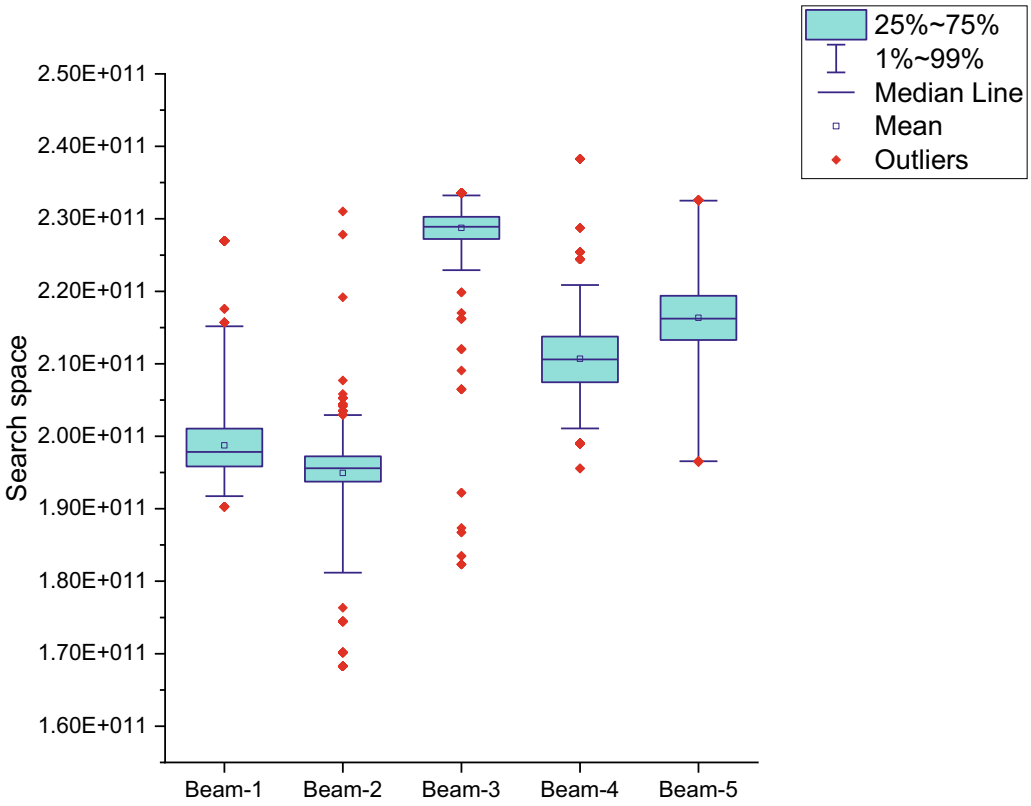

Fig. 3.4 Boxplot of the random samples by the SCE-MC algorithm

to 75% of samples). The whiskers (dark blue horizontal lines) extend to the most extreme samples position (from 1% to 99% of samples are placed within this range), and *red dot* symbol denotes the outliers. This figure indicates the sampling performance of the SCE-MC algorithm. The convergence toward the high region of solutions can be seen from the figure as 25~75% of the samples are concentrated around the mean (a small dark blue square at the central). The outliers are expected to appear, since the algorithm uses a population size of 50 Markov chains, which creates a challenge to converge all set of chains simultaneously.

The correlations between the updated parameters are shown in Fig. 3.5. A small rate correlation demonstrates that both updating parameters are weakly correlated (<0.3), while a larger rate means a highly correlation (>0.7). The positive or negative correlation indicates that the variables relatively affect each other. The SCE-MC algorithm has successfully sampled from the posterior PDF since no highly absolute correlation is observed.

The updated natural frequencies are given in Table 3.2. The results indicate that the SCE-MC updating method has updated the natural frequencies for the five modes with outcomes that are better than the initial FE model. The percentage absolute mode error $\frac{|f_i^m - f_i|}{f_i^m}$ is included in the table to compare the differences between the measured and the updated frequencies. The table also presents the total average error (*TAE*), which gives a general overview of the updated modes, and is determined due $TAE = \frac{1}{N_\omega}\sum_{i=1}^{N_\omega}\frac{|f_i^m - f_i|}{f_i^m}$, where N_ω is the number of the updated frequencies. The SCE-MC has successfully minimized the *TAE* from its initial state to 2.67%. On the other hand, the M-H algorithms has completed the updating process with 3.8% for the *TAE*. It can be shown here the SCE-MC has the advanced ability to update the frame structure and to produce efficient updating solutions.

Figure 3.6 shows the convergence of the *TAE* for the SCE-MC and the M-H algorithms when updating the natural frequencies of the 2-D frame structure. The SCE-MC algorithm utilizes 50 Markov chains and 5 evolutionary complexes to implement the updating process. Thereby, the algorithm tests and shuffles a number of 50 solutions at each iteration. This mechanism provides the algorithm with the ability to reach a quick convergence. It shows in the plot that the algorithm started with *TAE* which is higher than the *TAE* of initial FE model. This indicates the effectiveness of the evolving process which is implemented by the algorithm to explore a wider region of the search space and iteratively select the best set of solutions. The convergence of the SCE-MC method, as seen in the figure, is achieved before the first 100 iterations.

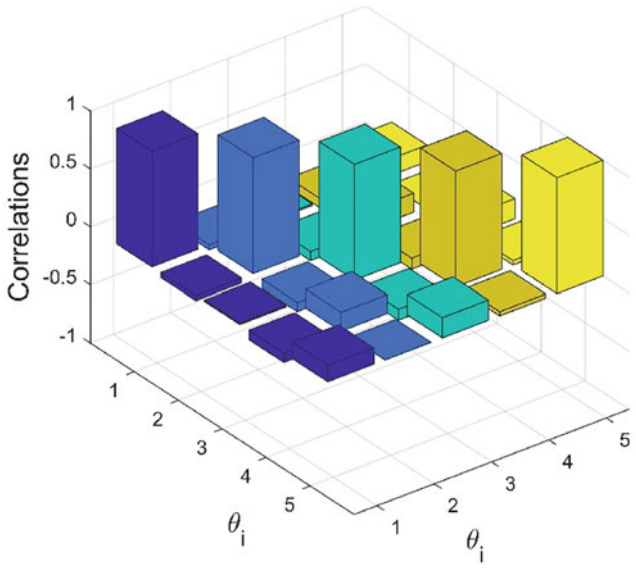

Fig. 3.5 The correlation between the updating parameters obtained by SCE-MC algorithm

Table 3.2 The updated natural frequencies using M-H and the SCE-MC algorithms

Modes	Measured frequency (Hz)	Initial frequency (Hz)	Error (%)	M-H Method frequency (Hz)	Error (%)	SCE-MC Method frequency (Hz)	Error (%)
1	4.23	4.41	4.36	4.29	1.42	4.326	2.26
2	14.03	14.2	1.2	14.46	3.09	14.209	1.27
3	25.45	27.40	7.69	27.31	7.33	26.58	4.46
4	44.81	47.47	5.94	45.81	2.23	43.98	1.83
5	58.12	62.03	6.73	61.0	4.95	60.17	3.53
TAE	–		**5.18**	**–**	**3.80**	**–**	**2.67**

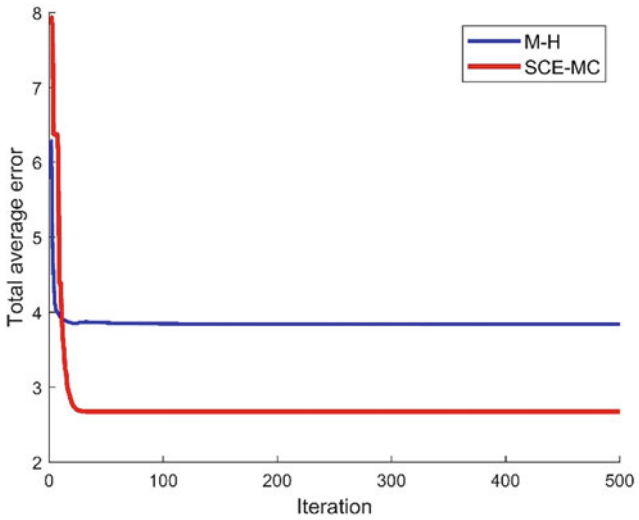

Fig. 3.6 Convergence of the total average error of the 2-D frame structure using the SCE-MC algorithms

For the purpose of comparing the results of both updating methods, the M-H and the SEC-MC methods, the M-H algorithm is set to have a relatively large jump at iteration, which facilitates the M-H procedure to have its maximum performance and quickest convergence within 500 iterations only for the FEMU application. This is used to highlight the limitations for each updating method when used to solve the same updating conditions.

3.5 Conclusion

This paper has introduced the shuffled complex evolution Markov chain algorithm for Bayesian updating problem. The presented algorithm merges the advantages of the Metropolis-Hastings method, controlled stochastic search, competitive evolution, and complex shuffling to evolve population of samples to approximate the posterior PDF of the Bayesian model. The algorithm has been tested to update a FE model of a 2-D frame structure. The Young's modulus is chosen to be updated. Five updating elements are considered for the updating problem. In addition, the posterior function includes five natural frequencies which are collected from modal experiment. It is found that the SCE-MC algorithm requires large number of population to propose desired samples and that is correlated with the complexity of the posterior function. The algorithm is also affected by the number of the complexes used to partition and sequencing the population. Increasing the number of the complexes offers more opportunities to rank and sequence the solutions, therefore giving the chance to converge to a higher region of solutions. However, this may raise the computational demand of the problem.

The updated parameters have reflected realistic updating values. The obtained set of solutions has minimized the total average error of the updated natural frequencies. The obtained results were compared with the outcomes of the M-H algorithm and found that the performance of the SCE-MC method is more efficient. It's advised for future work to investigate the SCE-MC algorithm with another evolutionary Markov chain method.

References

1. Hughes, T.J.: The finite element method: linear static and dynamic finite element analysis. Courier Corporation, Mineola (2012)
2. Rao, S.S.: The finite element method in engineering. Butterworth-heinemann, Oxford (2017)
3. Marwala, T., Boulkaibet, I., Adhikari, S.: Probabilistic finite element model updating using Bayesian statistics: applications to aeronautical and mechanical engineering. Wiley, Chichester (2016)
4. Marwala, T.: Finite element model updating using computational intelligence techniques: applications to structural dynamics. Springer, London (2010)
5. Friswell, M., Mottershead, J.E.: Finite element model updating in structural dynamics. Springer, Dordrecht (2013)
6. Zárate, B.A., Caicedo, J.M.J.E.S.: Finite element model updating: multiple alternatives. Eng. Struct. **30**(12), 3724–3730 (2008)
7. Jaishi, B., Ren, W.-X.: Structural finite element model updating using ambient vibration test results. J. Struct. Eng. **131**(4), 617–628 (2005)
8. Boulkaibet, I., Mthembu, L., Marwala, T., Friswell, M., Adhikari, S.: Finite element model updating using Hamiltonian Monte Carlo techniques. Inverse Probl. Sci. Eng. **25**(7), 1042–1070 (2017)
9. Carlin, B.P., Chib, S.: Bayesian model choice via Markov chain Monte Carlo methods. J. R. Stat. Soc. Ser. B. **57**(3), 473–484 (1995)
10. Hastings, W.K.: Monte Carlo sampling methods using Markov chains and their applications. Biometrika. **57**(1), 97–109 (1970)
11. Geyer, C.J.: Practical Markov chain Monte Carlo. Stat. Sci. **5**, 473–483 (1992)
12. Sherri, M., Boulkaibet, I., Marwala, T., Friswell, M.: A differential evolution Markov chain Monte Carlo algorithm for Bayesian model updating. In: Special topics in structural dynamics, volume 5, pp. 115–125. Springer (2019)
13. Sherri, M., Boulkaibet, I., Marwala, T., Friswell, M.: Bayesian finite element model updating using a population Markov Chain Monte Carlo algorithm. In: Special topics in structural dynamics & experimental techniques, volume 5, pp. 259–269. Springer (2021)
14. Boulkaibet, I., Mthembu, L., Marwala, T., Friswell, M., Adhikari, S.: Finite element model updating using an evolutionary Markov Chain Monte Carlo algorithm. In: Dynamics of civil structures, volume 2, pp. 245–253. Springer (2015)
15. Boulkaibet, I., Marwala, T., Mthembu, L., Friswell, M., Adhikari, S.: Sampling techniques in Bayesian finite element model updating. In: Topics in model validation and uncertainty quantification, volume 4, pp. 75–83. Springer (2012)
16. Boulkaibet, I.: Finite element model updating using Markov Chain Monte Carlo techniques. University of Johannesburg (2014)
17. Dearden, R., Friedman, N., Andre, D.: Model-based Bayesian exploration. preprint arXiv:1301.6690 (2013)
18. Vrugt, J.A., Gupta, H.V., Bouten, W., Sorooshian, S.: A shuffled complex evolution metropolis algorithm for optimization and uncertainty assessment of hydrologic model parameters. Water Resour. Res. **39**(8) (2003)
19. Vrugt, J.A., Gupta, H.V.: A shuffled complex evolution metropolis algorithm for estimating. Calibration Watershed Model. **6**, 105 (2003)
20. Duan, Q., Sorooshian, S., Gupta, V.: Effective and efficient global optimization for conceptual rainfall-runoff models. Water Resour. Res. **28**(4), 1015–1031 (1992)
21. Duan, Q., Gupta, V.K., Sorooshian, S.: Shuffled complex evolution approach for effective and efficient global minimization. J. Optim. Theory Appl. **76**(3), 501–521 (1993)
22. Hou, R., Xia, Y., Zhou, X.: Structural damage detection based on l1 regularization using natural frequencies and mode shapes. Struct. Control Health Monit. **25**(3), e2107 (2018)
23. "MathWorks .Inc," https://www.mathworks.com/products/matlab.html
24. "Structural Dynamics Toolbox & FEMLink," https://www.sdtools.com/

Chapter 4
On the Dynamic Virtualization of a 3D-Printed Scaled Wind Turbine Blade

Heorhi Brzhezinski, Silvia Vettori, Emilio Di Lorenzo, Bart Peeters, Eleni Chatzi, and Francesco Cosco

Abstract Innovative production techniques, such as 3D printing of metals, require attention both in the production and in the post-production phase. In fact, such manufacturing processes introduce higher margins of uncertainty compared to more canonical processes. As a consequence, they require an increased effort to succeed in delivering representations for the so-called dynamic virtualization process. Virtualization encompasses the ensemble of activities that are aimed at formulating the virtual model of a given structure and subsequently validating and updating this model in order to guarantee a realistic and accurate response prediction in a broad range of operating conditions. This chapter explores the main challenges related to the mentioned limitations, in the context of a down-scaled industrially relevant case study: a 3D-printed scaled titanium Wind Turbine (WT) blade. The scaled blade has been the object of a complete virtualization process: from the design by means of conventional WT blade tests, up to its "Digital-Twin" establishment, where we exploit state-of-the-art Virtual Sensing (VS) techniques, due to their intrinsic capability of "enriching" the high-fidelity model's predictions with information extracted from test data.

Keywords Wind turbine blades · 3D printing · Dynamic tests · Digital Twin · Virtual Sensing

4.1 Introduction

The 3D printing process of metals introduces technological challenges, e.g., limitations to 3D-printed specimens dimensions. For this reason, it is common practice to print the several sub-parts of the final product individually and then weld them together. Weld beads create areas of structural properties discontinuity that are difficult to be modeled. Moreover, intrinsic manufacturing process defects and thickness variations due to surface post-processing often arise. Canonical virtualization techniques produce realistic estimates under static conditions. Within the dynamic domain, the punctual stiffness variation caused by the mentioned limitations leads to large discrepancies between the "Digital Twin" and the physical structure. A model updating process based on experimental data can be installed to fill this gap. However, data acquired during dynamic tests derives from a few instrumented locations along the entire structure. The full-field response of the system can be obtained through the use of Virtual Sensing (VS) techniques [1–6], i.e., methods that allow to estimate quantities of interest by combining a limited set of measurements and a validated finite element (FE) model. Kalman-type filters are commonly adopted for the purpose of VS. When joint input-state-response estimation is addressed, extensions of the standard Kalman

H. Brzhezinski · F. Cosco
Department of Mechanical Engineering, Energy Engineering and Management, DIMEG, University of Calabria, Rende, Italy
e-mail: francesco.cosco@unical.it

S. Vettori (✉)
Siemens Digital Industries Software, Leuven, Belgium

Institute of Structural Engineering, ETH Zürich, Zürich, Switzerland
e-mail: silvia.vettori@siemens.com

E. Di Lorenzo · B. Peeters
Siemens Digital Industries Software, Leuven, Belgium
e-mail: emilio.dilorenzo@siemens.com; bart.peeters@siemens.com

E. Chatzi
Institute of Structural Engineering, ETH Zürich, Zürich, Switzerland
e-mail: chatzi@ibk.baug.ethz.ch

Z. Mao (eds.), *Model Validation and Uncertainty Quantification, Volume 3*, Conference Proceedings of the Society for Experimental Mechanics Series, https://doi.org/10.1007/978-3-031-04090-0_4

filter (KF) such as the Augmented Kalman filter (AKF) [7] and the Dual Kalman filter (DKF) [8] can be exploited. Within this work, the AKF [9] is tested on a 3D-printed scaled titanium Wind Turbine (WT) blade with the purpose of enriching its "Digital Twin" response predictions and performing load identification. The paper starts from Sect. 4.2, which describes the 3D-printed WT blade and the test campaign object of this work. The next section introduces the WT blade FE model and overviews the carried out model updating activities. Section 4.4 describes the results of the input-response estimation obtained via the AKF during the tests presented in Sect. 4.2.

4.2 3D-Printed Scaled Titanium WT Blade: Test Campaign

The case study analyzed in this chapter concerns a 3D-printed scaled titanium WT blade. The CAD model used to print the titanium blade has been retrieved scaling down an existing larger CAD model shared by DTU Wind Energy in the framework of the ReliaBlade research project. This CAD model is related to a 12.6m blade entirely designed and manufactured at DTU Wind Energy. The entire 3D-printed specimen, manufactured by 3D Systems (Leuven, Belgium), comprises the scaled blade and a flange that was designed to allow the blade clamping to a concrete block. Figure 4.1 shows the manufacturing process, which consisted of the following steps:

- Four sub-parts of the entire structure have been 3D-printed.
- A stress relief heat treatment has been applied to the four sub-parts.
- The four sub-parts have been welded together.
- The plate has been removed using wire through Electrical Discharge Machining (EDM).
- A polishing process has been applied to the structure to obtain the final surface.

This section describes the setup adopted during the test campaign carried out at Siemens Digital Industries Software (Leuven, Belgium) on the scaled blade, along with the series of tests performed with different types of excitation. Figure 4.2 shows the setup adopted during the measurements on the scaled WT blade. During all the hereby described tests, the WT blade was clamped to a concrete block as depicted in detail in Fig. 4.5.

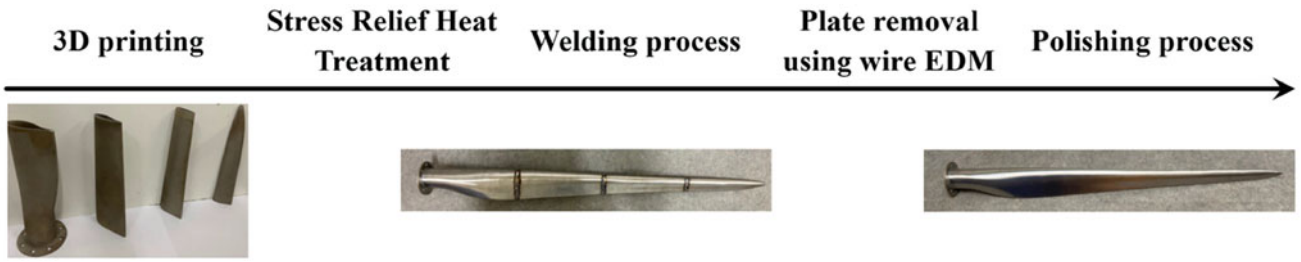

Fig. 4.1 3D-printed scaled titanium WT blade manufacturing process

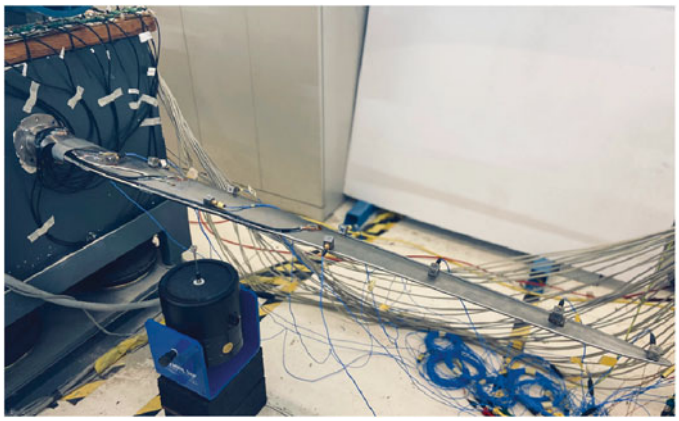

Fig. 4.2 Experimental setup

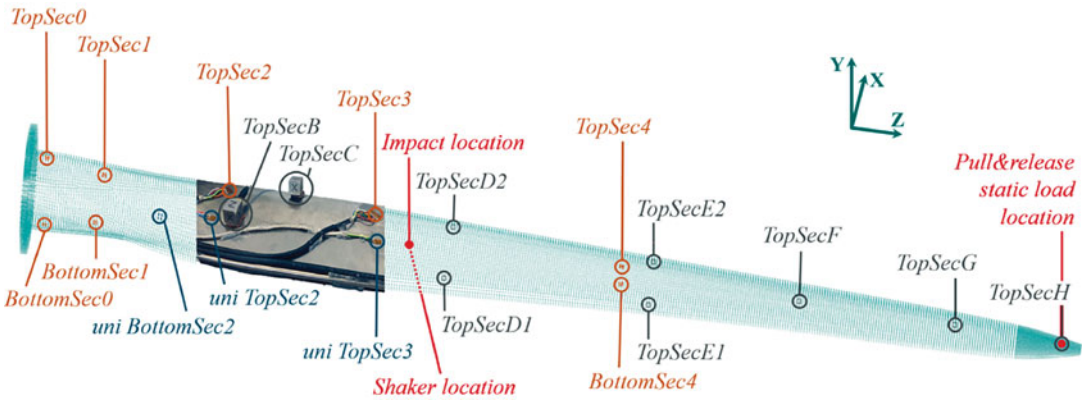

Fig. 4.3 Sensors' setup. USGs are reported in blue, rosettes in orange, accelerometers in black, and inputs locations in red

Table 4.1 Experimental modal frequencies and damping for the titanium WT blade in clamped-free conditions

Modes	Frequency (Hz)	Damping (%)
1	25.0	1.27
2	55.0	0.91
3	90.4	0.56
4	193.2	0.56
5	236.4	0.32
6	343.2	1.78

Fig. 4.4 Static load applied at the blade tip during pull and release tests

The entire setup includes 3 types of sensors: 4 uniaxial strain gauges (USGs), 10 rosettes, and 10 tri-axial accelerometers. During the test campaign, a Simcenter SCADAS system and Simcenter Testlab software have been used for data acquisition. The strain sensors are arranged in sections along the blade on both the top and bottom blade surfaces as shown in Fig. 4.3. On the other hand, the accelerometers have been positioned only on the top surface.

Three types of tests have been performed according to the adopted excitation: impact testing using a modal hammer, shaker testing, and the so-called pull and release tests. Figure 4.3 shows the locations of the impact and the shaker on the structure. Data acquired during the impact test has been used to determine the scaled WT blade modes, which have been extracted using Simcenter Polymax. Table 4.1 reports the resulting experimental frequencies and damping.

During shaker testing, constant frequency sine tests and continuous random tests up to 500 Hz were carried out. Finally, as common practice for WT blades, pull and release tests were carried out. During this type of tests, the blade in clamped-free boundary conditions (BCs) is pulled downward and then released for recording its free vibration response. As shown in Fig. 4.4, during the hereby described test campaign, the static load has been applied by hanging a mass (known weight equal to 1.5 kg) at the blade tip. The blade release has been reproduced by cutting the plastic tie used to hang the mass.

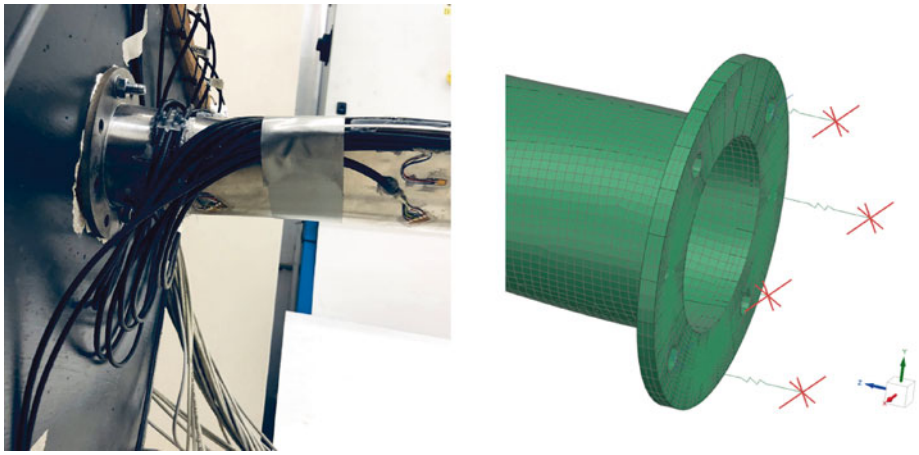

Fig. 4.5 Scaled WT blade clamping system (left). FE model BCs (right)

Table 4.2 FE model parameter values before and after optimization

	Spring's stiffness (N/mm)	Young's modulus (Gpa)	Poisson's ratio (/)	Density (kg/mm^3)
Initial values	30,000	121	0.34	4.430×10^{-6}
Final values	33,167.2	116.039	0.34208	4.873×10^{-6}

4.3 3D-Printed Scaled Titanium WT Blade: FE Model Validation

The scaled WT blade FE model has been developed in Simcenter 3D starting from the CAD model used for 3D printing. The mesh is made up of around 65,000 nodes and 33,804 six-sided solid elements. The initial isotropic material (Ti6Al4V) properties have been defined according to the data sheet provided by the manufacturer. Figure 4.5 (left) shows the physical BCs obtained by means of 2 bolts used to clamp the flange to the concrete block and a layer of glue. The described BCs have been recreated in the FE model through two RBE2 connections at the holes where the bolts were placed and four springs. In particular, the flange has been divided into four parts, each connected to a spring via a RBE2 connection. As shown in Fig. 4.5 (right), the free ends of the springs have been fixed. An initial stiffness value of 30,000 N/mm was used for each spring.

The numerical modes have been computed using NX Nastran SOL 103, and the frequency range 0–500 Hz has been chosen for validation. Experimental tests in this range have revealed the 6 natural frequencies reported in Table 4.1. In order to update the FE model, NX Nastran SOL 200 has been adopted in Simcenter 3D, and the experimental modes and frequencies reported in Sect. 4.2 have been used as reference. The following parameters have been set to be adjusted by the optimization: springs stiffness, isotropic material Young's modulus, Poisson's ratio, and density. Some of the ranges have been imposed from the processing data sheet provided by the manufacturer of the WT blade. The others were kept below a 10% deviation. Table 4.2 reports the parameters initial and optimized values.

Figure 4.6 shows the Modal Assurance Criterion (MAC) diagram between the reference experimental modes and the updated numerical modes. Table 4.3 reports the optimization results in terms of modal frequencies.

4.4 Joint Input-Response Estimation Through the AKF during Random and Pull and Release Tests on the 3D-Printed Scaled WT Blade

This work exploits the AKF for simultaneously estimating the 3D-printed WT blade response and the load it was subjected to during the shaker tests (continuous random excitation) and the pull and release tests described in Sect. 4.2. In order to reduce the computational effort derived by the high dimensionality of the FE model, a Reduced Order Model (ROM) has been built following the procedure described in [10–12]. The six normal modes reported in Fig. 4.6 have been used to build the ROM, along with one residual attachment mode related to the unknown (for the filter) force [11, 12]. The attachment mode has been computed as a static mode under a unitary input applied at the unknown excitation position. Therefore, two different attachment modes have been used for the pull and release and the continuous random tests.

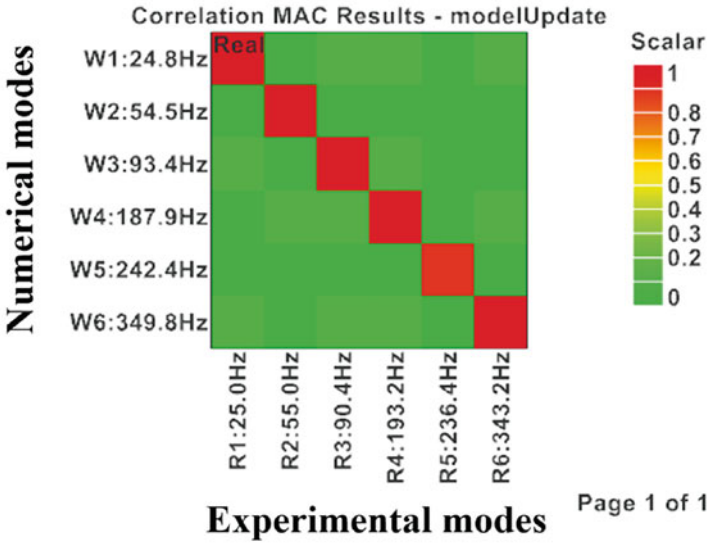

Fig. 4.6 MAC between numerical and experimental mode shapes from hammer test

Table 4.3 Experimental and updated numerical frequencies for the titanium WT blade in clamped-free conditions

Modes	Experimental frequency (Hz)	Numerical frequency (Hz)	Absolute error (Hz)	Percentage error (%)
1	25.020	24.758	−0.262	−1.047
2	55.004	54.512	−0.492	−0.894
3	90.426	93.405	2.979	3.294
4	193.201	187.902	−5.299	−2.743
5	236.416	242.358	5.942	2.513
6	343.176	349.807	6.631	1.932

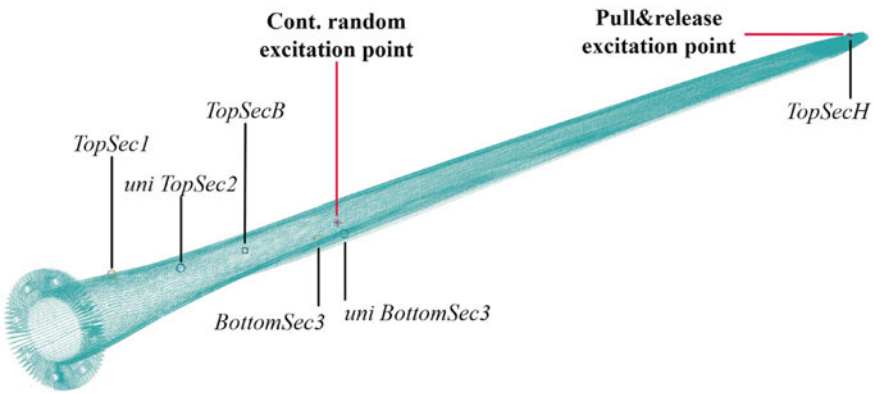

Fig. 4.7 Tests excitation points and "observed" locations for joint input-response estimation through the AKF

The AKF algorithm has been employed within this work to perform predictions basing on a set of measurements from different types of sensors, i.e., strain and acceleration. To check the effectiveness of the filter, only a few sensors over the entire set of responses acquired during tests were used as observations for the AKF. The remaining sensors data have been used as reference to check for the validity of the estimated responses. Figure 4.7 shows the observations set adopted for both the pull and release and the continuous random tests. In the framework of Kalman-type filters, model uncertainties and measurement errors are taken into account by including, respectively, the process and the measurement noise terms within the system representation. These are stationary mutually uncorrelated Gaussian noises with given associated covariance matrices. For the hereby presented case study, the measurement noise covariance has been retrieved from the background noise recorded by sensors during tests. The process noise covariance has been instead tuned by trial and error.

Figure 4.8 shows a comparison of the input time history estimated by the AKF (in magenta) and the actual input (in black) applied to the system for both the pull and release and the random tests. During the random tests, the force applied by the

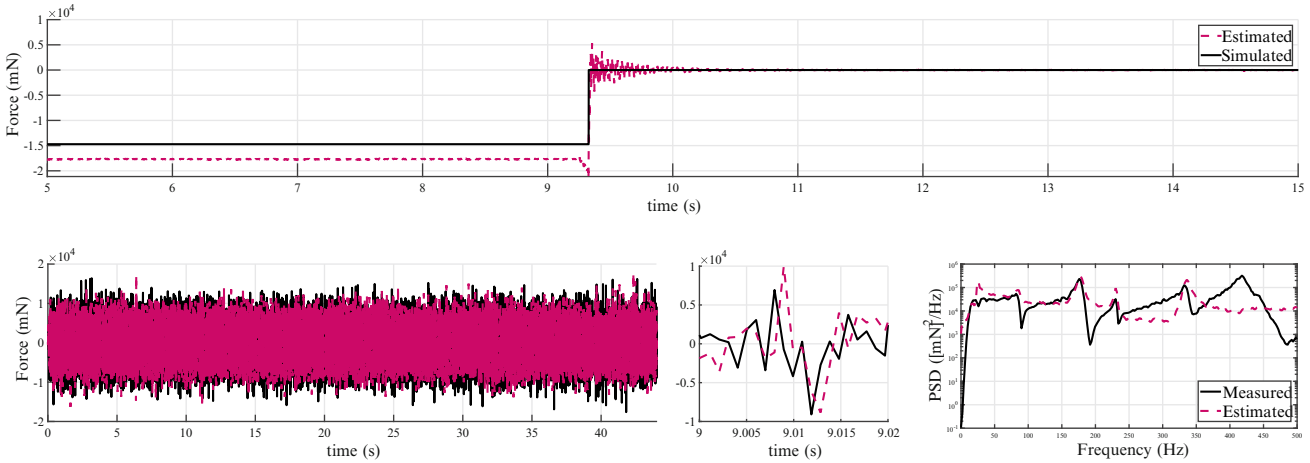

Fig. 4.8 Pull and release excitation history (top). Continuous random excitation time history (bottom, left), detailed time history (bottom, center), and PSD (bottom, right). Actual and predicted signals are, respectively, reported in black and magenta

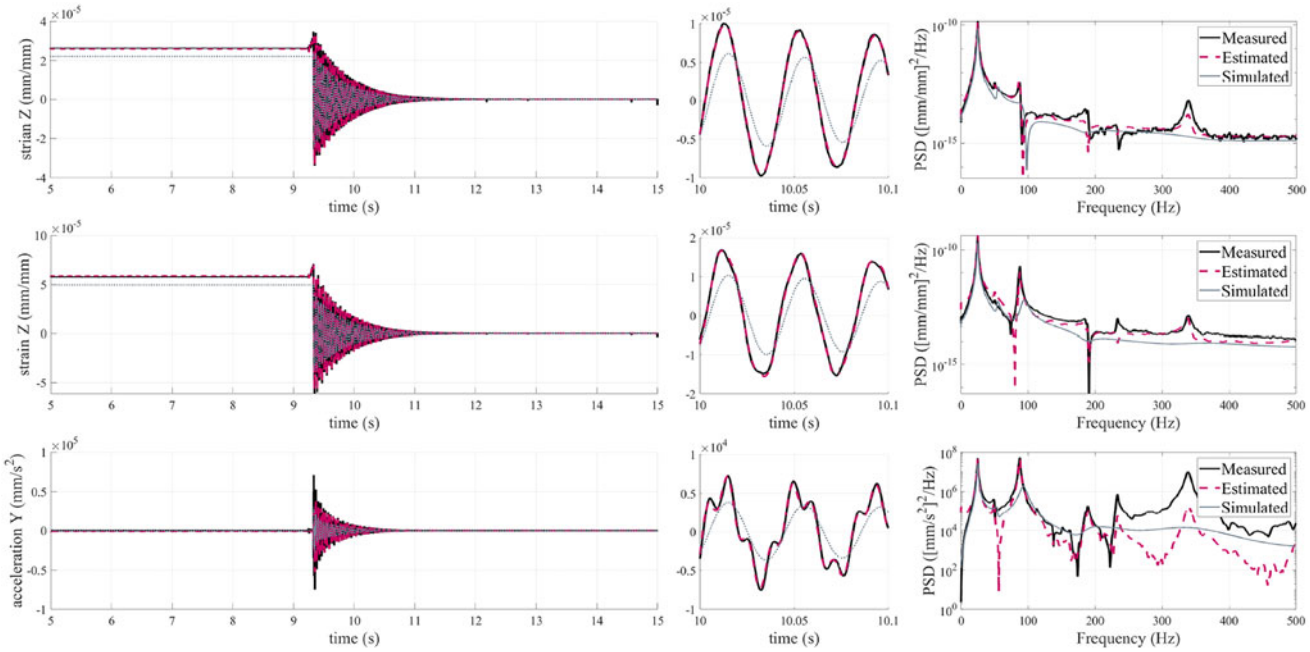

Fig. 4.9 Pull and release time histories (left), detailed time histories (middle), PSD (right) of sensors uni TopSec3, TopSec4, TopSecE2 (respectively, from top to bottom)

shaker has been recorded by a force cell placed between the shaker and the structure. During pull and release tests instead, the static input time history has been reconstructed from the known weight of the mass used to pull the blade. From Fig. 4.8, it can be inferred that the AKF is able to estimate the input during both tests.

For what concerns the pull and release test, an estimate of the prediction error can be computed as the difference between the actual static input and the mean value of the estimated input profile (before and after the blade release), which is equal to 1.32×10^3 mN. The static offset between the actual and the estimated input profiles before the blade release can be ascribed to the assumption of punctual loading made to approximate the input location in the model adopted for the AKF. For what concerns the continuous random test, the algorithm succeeds in estimating the correct input amplitude. On the other hand, the AKF generates an input featuring a flatter PSD with respect to the measured signal. The latter is highly affected by the blade resonances due to the specific BCs between the shaker and the structure. This behavior is difficult to be captured by the filter. The estimated input root mean square error (RMSE) is equal to 4.5126×10^3 mN.

Response estimation results are reported in Fig. 4.9 (pull and release) and in Fig. 4.10 (continuous random) for 3 "unmeasured" locations (a USG, a rosette, and an accelerometer). These plots compare the measured (black), simulated

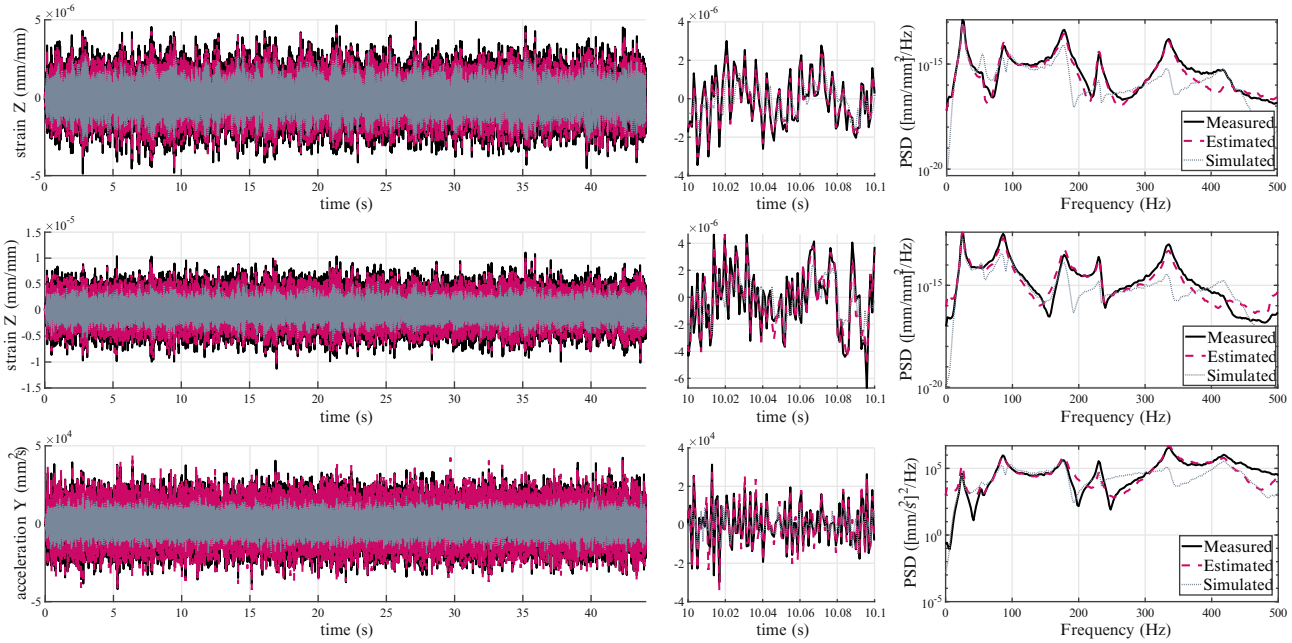

Fig. 4.10 Continuous random time histories (left), detailed time histories (middle), PSD (right) of sensors uni TopSec3, TopSec4, TopSecE2 (respectively, from top to bottom)

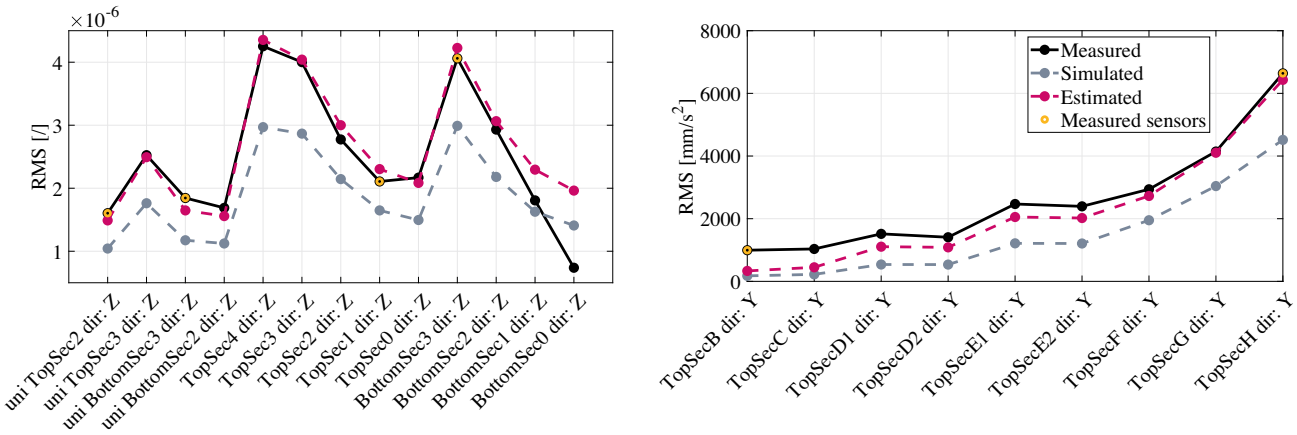

Fig. 4.11 Pull and release strain sensors RMS (left). Pull and release accelerometers RMS (right)

(gray), and estimated (magenta) signals in time and frequency domain. In order to demonstrate the filter performance, the root mean square (RMS) trend over the entire set of sensors along the blade is reported in Figs. 4.11 (pull and release) and 4.12 (continuous random) for the measured (black), simulated (gray), and estimated (magenta) responses. Figures 4.9, 4.10, 4.11, and 4.12 highlight the ability of the filter to correctly estimate the blade response, both in terms of strain and acceleration. Moreover, it is shown how the filter enhances the simulated responses by coupling the FE model with a few physical observations.

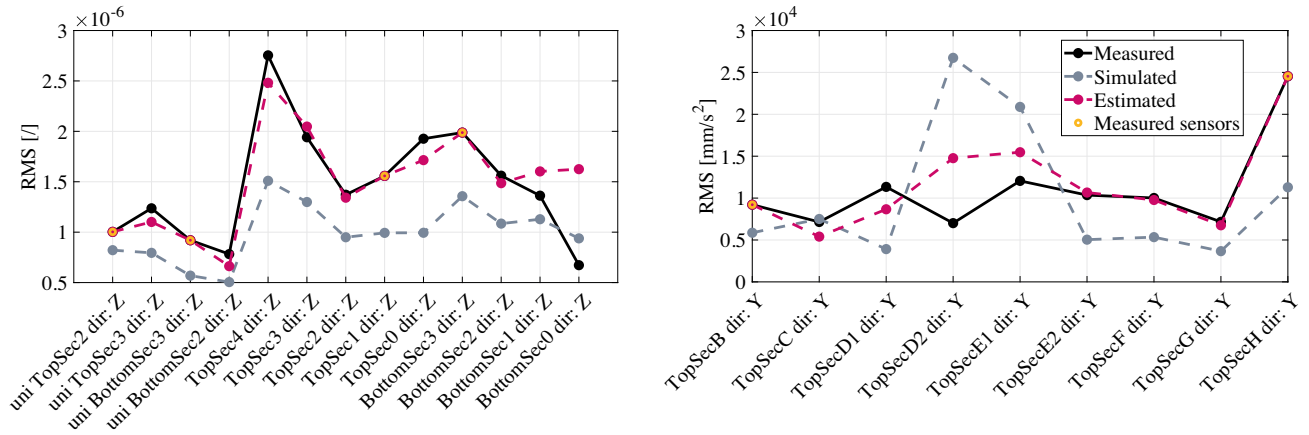

Fig. 4.12 Continuous random strain sensors RMS (left). Continuous random accelerometers RMS (right)

4.5 Conclusions

This chapter reports on the dynamic virtualization process installed for a 3D-printed scaled titanium WT blade. The individual steps of the process consisted in: (1) modeling the WT blade CAD model, (2) manufacturing the blade through an innovative 3D printing process, (3) building a FE model from the available CAD model, (4) testing the blade by means of conventional WT blades testing procedures, (5) validating and updating the FE model using experimentally extracted modal parameters, and (6) extending the information acquired during tests to the full-field response and simultaneously predicting the unknown loads by means of the AKF. This work has proven the effectiveness of the AKF results for both random and pull and release tests when a fusion of strain and acceleration responses is used. The next step could consist in applying other types of Bayesian filters that allow to jointly estimate the system state and parameters, along with the unknown loads. These tools could be used for estimating the defects due to the manufacturing process, e.g., the percentage of pores inside the artifact due to 3D printing.

Acknowledgments The authors gratefully acknowledge the European Commission for its support of the Marie Sklodowska Curie program through the ITN DyVirt project (GA 764547).

The authors would like to also acknowledge DTU Wind Energy and the project "RELIABLADE: Improving Blade Reliability through Application of Digital Twins over Entire Life Cycle," supported by the Danish Energy Agency through the Energy Technology Development and Demonstration Program (EUDP), Grant No. 64018-0068, the support of which is greatly appreciated.

References

1. Azam, S.E., Chatzi, E., Papadimitriou, C., Smyth, A.: Experimental validation of the Kalman-type filters for online and real-time state and input estimation. J. Vibration Control **23**(15), 2494–2519 (2017)
2. Dertimanis, V.K., Chatzi, E.N., Azam, S.E., Papadimitriou, C.: Input-state-parameter estimation of structural systems from limited output information. Mech. Syst. Signal Process. **126**, 711–746 (2019)
3. Papadimitriou, C., Fritzen, C.P., Kraemer, P., Ntotsios, E.: Fatigue predictions in entire body of metallic structures from a limited number of vibration sensors using Kalman filtering. Struct. Control Health Monit. **18**(5), 554–573 (2011)
4. Cumbo, R., Tamarozzi, T., Janssens, K., Desmet, W.: Kalman-based load identification and full-field estimation analysis on industrial test case. Mech. Syst. Signal Process. **117**, 771–785 (2019)
5. Vettori, S., DiLorenzo, E., Peeters, B., Chatzi, E.: Virtual sensing for wind turbine blade full field response estimation in operational modal analysis. In: Proceedings of IMAC2020 International Conference (2020)
6. Avitabile, P., Pingle, P.: Prediction of full field dynamic strain from limited sets of measured data. Shock Vibration **19**(5), 765–785 (2012)
7. Lourens, E., Reynders, E., De Roeck, G., Degrande, G., Lombaert, G.: An augmented Kalman filter for force identification in structural dynamics. Mech. Syst. Signal Process. **27**, 446–460 (2012)
8. Azam, S.E., Chatzi, E., Papadimitriou, C.: A dual Kalman filter approach for state estimation via output-only acceleration measurements. Mech. Syst. Signal Process. **60**, 866–886 (2015)
9. Maes, K.: Filtering techniques for force identification and response estimation in structural dynamics. PhD thesis, KU Leuven, 2016
10. Craig, R.J.: A review of time-domain and frequency-domain component mode synthesis methods. Int. J. Anal. Exp. Modal Anal. **2**(2), 59–72 (1987)

11. Vettori, S., Di Lorenzo, E., Peeters, B., Chatzi, E.: A virtual sensing approach to operational modal analysis of wind turbine blades. In: Proceedings of ISMA2020 International Conference on Noise and Vibration Engineering, Leuven, Belgium (2020)
12. Vettori, S., Lorenzo, E.D., Cumbo, R., Musella, U., Tamarozzi, T., Peeters, B., Chatzi, E.: Kalman-based virtual sensing for improvement of service response replication in environmental tests. In: Model Validation and Uncertainty Quantification, vol. 3, pp. 93–106. Springer (2020)

Chapter 5
Wavelet Energy Features for Damage Identification: Sensitivity to Measurement Uncertainties

Xiaobang Zhang and Yong Lu

Abstract In vibration-based structural parameter identification, wavelet transformation has been widely used for extraction of damage pertinent data for onward identification of structural parameters or the occurrence of anomalies. Among wavelet-based techniques, the use of wavelet packet node energy (WPNE) as damage-sensitive features has attracted much research interest in more recent years. WPNE features contain detailed information which can be highly sensitive to local damages. However, most of the existing studies in the literature on using wavelet energy-based features have been numerical and involved idealised assumptions such as perfect and identical excitations among different tests. This paper presents an investigation into the tolerance of a wavelet packet energy with neural network approach to uncertainties in the input excitations and measurement noises. WPNEs are extracted from vibration signals from impact tests as feature proxies and a back-propagation neural network is used for classification. The method is firstly applied on a beam model using finite element simulations, in which variation in the excitations and measurement noises are incorporated to investigate the susceptibility of the approach to such uncertainties. Subsequently, the method is applied to the experimental data from the laboratory test of a steel beam. The results from both the numerical simulations and the experimental verification demonstrate that the wavelet energy with neural network approach to detecting structural changes is workable, and given a reasonably controlled impact test, it is possible to identify the initiation of damage with good accuracy.

Keywords Early damage detection · Wavelet packet transform (WPT) · WPT node energy features · Digital twin · Machine learning

5.1 Introduction

Wavelet energy-based features are thought to provide comprehensive information that may be extremely sensitive to local damages in vibration-based structural damage detection. Wavelet packet transform (WPT) energy was developed [1] as an alternate method of extracting time-frequency information from vibration signals. In the study by Yen and Lin [1], WPT energy features were used with neural networks for classification. Numerical simulations of a helicopter gearbox were used to test the viability of the classification technique. The findings showed that WPT features outperformed FFT features, and with eight sensors, good classification was achieved. WPT features have since been extensively researched in the identification of damage in civil engineering structures. Wavelet transform-based features have been shown to be effective in detecting, localising, and quantifying damages in many numerical and experimental investigations. Han et al. [2] presented the wavelet energy rate index as a damage measure based on WPT energy derived from 29 acceleration signals and demonstrated the technique on a numerically simulated simply supported beam and an actual steel beam. The index was shown to be sensitive to structural local damage in both simulated and experimental studies. In their research, two assumptions are used: (a) reliable undamaged and damaged structural models are available, and (b) all excitations are identical and repeatable. Mikami et al. [3] utilised the power spectrum density of WPT components as a damage detection index and used computational and experimental data collected from a steel beam to validate the identification technique. The suggested index was shown to be sensitive to damages.

X. Zhang · Y. Lu (✉)
Institute for Infrastructure and Environment, School of Engineering, University of Edinburgh, Edinburgh, UK
e-mail: xiaobang.zhang@ed.ac.uk; yong.lu@ed.ac.uk

Z. Mao (eds.), *Model Validation and Uncertainty Quantification, Volume 3*, Conference Proceedings of the Society for Experimental Mechanics Series, https://doi.org/10.1007/978-3-031-04090-0_5

Damage detection using just the feature proxy often necessitates a large number of sensors providing spatial information. Some research studies have looked at better mapping of the connections between feature proxy and structural state with a small number of signal sources with the use of machine learning techniques in classification and identification. Sun and Chang [4] used numerical simulations of a three-span continuous bridge under impact excitation to explore the application of WPT and the neural network model for damage assessment. The findings revealed that WPT energies derived from a single signal source could identify damage location and levels of severity.

However, the majority of previous research on wavelet energy-based features has been numerical and based on idealised assumptions such as perfect and identical excitations. This paper presents an investigation into the tolerance of a wavelet packet energy with neural network approach to uncertainties in the input excitations and measurement noises. WPNEs are extracted from vibration signals from impact tests as feature proxies, and a back-propagation neural network is used for classification. The method is firstly applied on a beam model using finite element simulations, in which variation in the excitations and measurement noises are incorporated to investigate the susceptibility of the approach to such uncertainties. Subsequently, the method is applied on the experimental data from the laboratory test of a steel beam.

5.2 Background Theories and Methodology

5.2.1 WPT Energy-Based Damage-Sensitive Feature

The wavelet transform (WT) is a signal processing method that has been widely used in a variety of fields. It goes beyond the Fourier transform in that it reveals signal characteristics in both the time and frequency domains. Wavelet transform defines a signal with coefficients that reflect the direct proportions between a basis function called mother wavelet and the original signal by shifting and dilating the mother wavelet [5]. WPT has a tree structure where the original signal is transformed into approximations and details at each level. As a result, a greater frequency domain resolution is obtained. Figure 5.1 shows an example wavelet packet transform tree structure.

The signal is decomposed by the following standard expressions:

$$\begin{cases} u_{2n}^{(j)}(t) = \sqrt{2}\sum_k h(k)u_n^{(j)}(2t-k) \\ u_{2n+1}^{(j)}(t) = \sqrt{2}\sum_k g(k)u_n^{(j)}(2t-k) \end{cases} ; n, k = 0, 1, 2, \ldots \tag{5.1}$$

where $u_0^{(0)}(t) = \varphi(t)$ is the scaling function, $u_1^{(0)}(t) = \varphi(t)$ is the wavelet function, j is the decomposition level, k is the translation parameter, and n is the modulation parameter. The terms $h(k)$ and $g(k)$ are quadrature mirror filters, and the corresponding function sets $H = \{h(k)\}_{k=z}$ and $G = \{g(k)\}_{k=z}$ denote the low-pass filter and the high-pass filter, respectively. After being decomposed for j times, 2^j signal components are obtained. The sum of the component signals can represent the original signal $f(t)$ as:

$$f(t) = \sum_{\mathrm{i}=1}^{2^{\mathrm{j}}} f_{\mathrm{j}}^{\mathrm{i}}(t) \tag{5.2}$$

$$f_j^i(t) = \sum_{i=1}^{2^j} C_j^i(t)\psi_{j,k}^i(t) \tag{5.3}$$

where $f_j^i(t)$ denotes the ith component signal at the jth decomposition level , $C_j^i(t)$ denotes the wavelet packet coefficients, and $\psi_{j,k}^i(t)$ denotes wavelet packet functions. Then, wavelet packet node energies (WPNEs) can be calculated as:

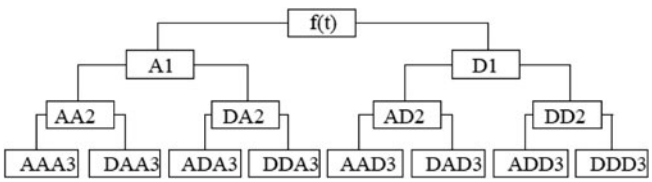

Fig. 5.1 Three-level wavelet packet transform

$$E_j^i = \int_{-\infty}^{\infty} f_j^i(t)^2 dt \tag{5.4}$$

The WPNE denotes the energy content in a specific frequency band without taking into account the time-variant characteristic. Normalised wavelet packet node energy (NWPNE) E_i in i-frequency band is expressed as:

$$E_i = \frac{E_j^i}{E_f} \tag{5.5}$$

where E_f denotes the sum of all terminal WPNEs and it represents the total signal energy. The effects of gross variation, particularly in the magnitudes of the excitations, can be largely eliminated by normalisation. As a result, the NWPNE is selected as the damage-sensitive feature and neural networks are used as inputs. The appropriate level of WPT to be employed is assessed in this research using an entropy-based selection technique [6].

5.2.2 Back-Propagation (BP) Neural Network

Because of strong nonlinearity, the relationship between NWPNE and a structure's dynamic properties is difficult to establish directly. Previous research has shown that back-propagation (BP) neural networks can generally be applied to implement pattern recognition in structural damage identification. In this study, feedforward BP neural networks with an input layer for receiving input data, a hidden layer for processing data, and an output layer for decision-making and outputting results are employed. The NPWNEs are used as inputs. The BP neural network training process includes forward and back propagation. The inputs are sent through levels in forward propagation resulting in an error. The error feedback is used to iteratively change the weights and biases in back propagation. When the loss assessed by validation data stops improving, the training procedure will be completed. Cross entropy loss is used in this case which is defined as:

$$H(p, q) = -\sum_u p(u) \log q(u) \tag{5.6}$$

where $p(u)$ denotes one-hot encoding vector of the true label and $q(u)$ denotes the corresponding output. A scaled conjugate gradient approach is used to train a BP neural network for classification, where each structural state is considered a class. The structural conditions include intact and damaged at various locations. Therefore, the output layer will include representation of the presence and location of the structural damage. In this work, the hidden layers and output layer adopt logistic sigmoid functions and softmax functions, respectively. As a loss function, the cross entropy function is applied to the softmax output. A one-hot encoded vector is employed as a label. For example, a vector of [0,1,0,0,0,0,0,0,0,0] represents the class of damage at segment 2. The number of hidden neurons is estimated by the empirical formula as follows:

$$L = \sqrt{m + n} + k \tag{5.7}$$

where L is the number of hidden layer nodes, m is the number of input nodes, n is the number of output nodes, and k is a constant, $k \in [1, 10]$.

5.2.3 WPT Energy and Neural Network Integrated (WPNE-NN) Approach

The key procedures of WPNE-NN approach are explained as follows. Firstly, vibration signals from the structure under investigation are acquired. The signals are taken in the form of acceleration time histories. Secondly, WPNE features are created from wavelet packet transform of the acquired vibration measurements. Daubechies mother wavelets have been shown to be the optimum choice for analysing acceleration signals [7]. In the present wavelet packet analysis, 'Daubechies 4' is chosen as the mother wavelet. The vibration signals are translated into feature vectors created by WPNEs throughout the feature extraction. Thirdly, supervised neural network training is carried out. With the trained NN, WPNE feature from a new measurement can be used to determine the structural state.

A two-stage strategy for identifying damage is proposed in this study. The challenge of damage detection and localisation is first treated as a classification problem. Once the location is known, the second step treats the damage extent quantification

at the particular location as a fitting problem. Therefore, two distinct neural networks are trained in each stage. The first stage involves training a BP neural network (NN-I) using a scaled conjugate gradient technique to perform classification on each structural state. The structural states include intact and damage at various locations. As a result, the NN-I's output indicates the occurrence and location of a damage. In the second stage of damage quantification, assuming that the location of the damage has been determined in the first stage, the training dataset is reduced to samples taken at the damaged location. Bayesian regularisation is a training function that updates the weight and bias according to Levenberg-Marquardt optimisation and maximises the log probability density towards a correct answer. The output of NN-II will indicate the degree of damage, in the present case the reduced local bending stiffness (or rigidity).

The samples are randomly divided into training, validation, and test sets by a specified proportion. The training set is used to train the neural networks, and the validation set is used to provide an unbiased evaluation of a model fit on the training set. The training, validation, and test data size ratios are set at 70%, 15%, and 15%, respectively. For simplicity in the demonstration of the procedure, it is assumed that damage only occurs in a single segment of the structure, which is consistent with the stated goal of the current approach in detecting incipient damage.

5.3 Numerical Investigation

In this section an investigation into the tolerance of the wavelet-neural network integrated approach to variation in the input excitations and measurement noises is carried out using a finite element beam model. Damages are simulated as stiffness reduction in segments of the structure.

5.3.1 Model Setup

Timoshenko beam elements are used to model an isotropic homogeneous beam in Abaqus. The beam measures 3.2 m in length, 0.15 m in width, and 0.12 m in depth. The material parameters of the beam are as follows: mass density = 2450 kg/m^3; elastic modulus = 38.8 GPa; Poisson's ratio = 0.2; and structural damping in all modes = 0.5%.

The beam is supported at 0.05 m from each end, resulting in a net span of 3.1 m. The beam is meshed into 200 elements throughout its length in the computation to ensure the accuracy of the dynamic analysis. The beam is marked with ten equal-length segments over the net span for the purpose of representing damage to the beam and measurement locations. As illustrated in Fig. 5.2, the ten segments are labelled segment 1–10, and the dividing points between segments are labelled P1 to P9 (excluding the support nodes).

Excitations are modelled as vertical impact point loads at P3. The vertical acceleration response is also recorded for 1 s at P3 (i.e. driving point response) with a sample rate of 2500 Hz. The acceleration signals are imported into MATLAB successively, and the NWPNEs are calculated. As an example, Fig. 5.3 shows a recorded acceleration signal from the beam in its intact state and the corresponding NWPNEs at the seventh WPT level from the signal.

Fig. 5.2 Simply support beam model and segmental divisions

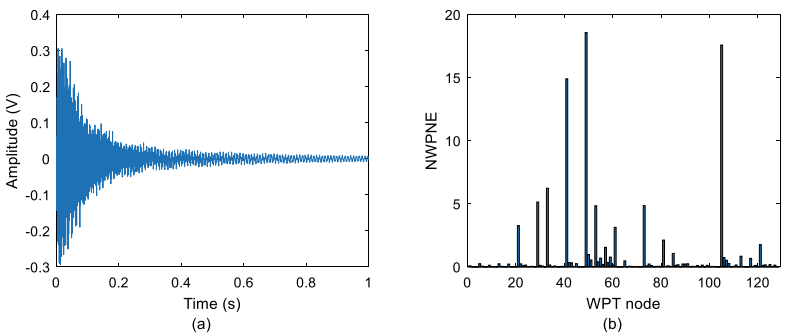

Fig. 5.3 (**a**) Time series of an acceleration signal, (**b**) NWPNE features of the signal

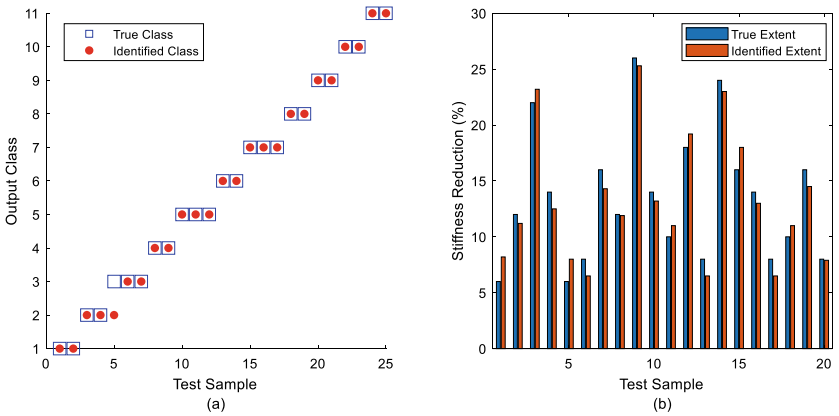

Fig. 5.4 Damage identification result: (**a**) NN-I result, (**b**) NN-II result

5.3.2 Damage Identification Procedure

In the numerical model, ten single damage cases are simulated by a stiffness reduction to segment 1–10, respectively. For each location, 16 levels of stiffness reduction from 0% to 30% at a 2% interval are simulated. The total samples thus amount to 165. Samples are grouped into 11 classes. Ten of these classes represent structural states that damage occurs in one of the ten segments, and the last class represents intact state. The impact excitation is simulated by applying a pulse force downward at point P3 in all cases. The standard pulse force has an isosceles triangle shape in time series with a magnitude of 100 N and a duration of 0.002 s. The acceleration signals collected at P3 are decomposed by WPT with a mother wavelet db4 to seventh levels generating a total of 128 NWPNEs for each signal. The level of WPT is determined through entropy analysis mentioned in Sect. 5.2. Hence, 128-dimensional feature vectors are extracted and employed as input in the neural networks for training and damage identification. The number of hidden neurons is set at 15, as explained in Sect. 5.2. The sizes of training, validation, and test sets are 115, 25, and 25, respectively. The training process of NN-I automatically stops after 42 iterations when generalisation stops improving, as indicated by an increase in the cross-entropy error of the validation samples resulting in a cross-entropy error of 2.17 e^{-7}. Figure 5.4a shows the identification result where the output class of 25 test samples are marked as red dots. It can be seen that only 1 of them fall out of the target classes which are indicated as blue squares. This means 24 out of 25 tests are correct in the structural state identification and the accuracy is 96%.

In damage extent quantification, assuming the damage location is already determined, the training and testing are conducted on that specific class. In order to examine the performance of NN-II on damage quantification at all locations, the same process is repeated on all ten classes. In each class, 11 samples are used for training, 2 for validation, and 2 for testing where samples are randomly selected in each dataset. Therefore, there are 20 tests in total. The result is shown in Fig. 5.4b. The maximum error in estimation of stiffness reduction is within 2.2%. The above results demonstrate that under an ideal condition with identical excitations, the WPNE-NN approach is capable of identifying damage with high accuracy using even just one signal source.

5.3.3 Effect of Measurement Noise

Some explorations in the robustness of the approach to Gaussian white noise have been made in previous numerical studies [8–10]. Under idealised identical excitations, the approach has demonstrated good resistance to noise up to a level of signal to noise ratio (SNR) of 10. However in a real environment, there are more complicated noises contaminating the measured signals due to various interferences, such as ambient vibrations, imperfectness of structures, electrical noises on sensors, etc. Noises from various sources are usually mixed together in the measured signals. They usually come in three common forms, namely, continuous, periodic, and impulsive. Gaussian white noise is an idealised form of continuous noise where the energy in all frequencies are uniform. However, real continuous noises may contain non-uniform frequency contents. Therefore, the effect of noises that could realistically occur in impact vibration tests in a real measurement environment is investigated. Five types of noises are discussed and compared. Figure 5.5 shows time series and power spectrum densities of the normalised noises for example. The noise in Fig. 5.5a is Gaussian white noise whose spectrum is nearly flat across the

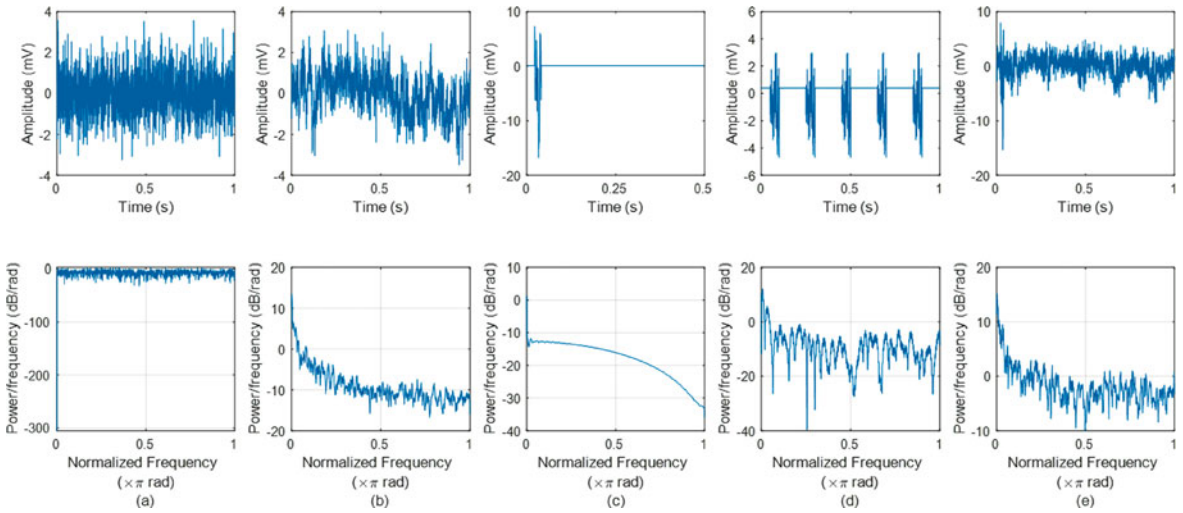

Fig. 5.5 Time series and power density spectrum of noise signals. (**a**) Gaussian white noise. (**b**) Coloured noise. (**c**) Impulsive noise. (**d**) Periodic noise. (**e**) Mixture noise

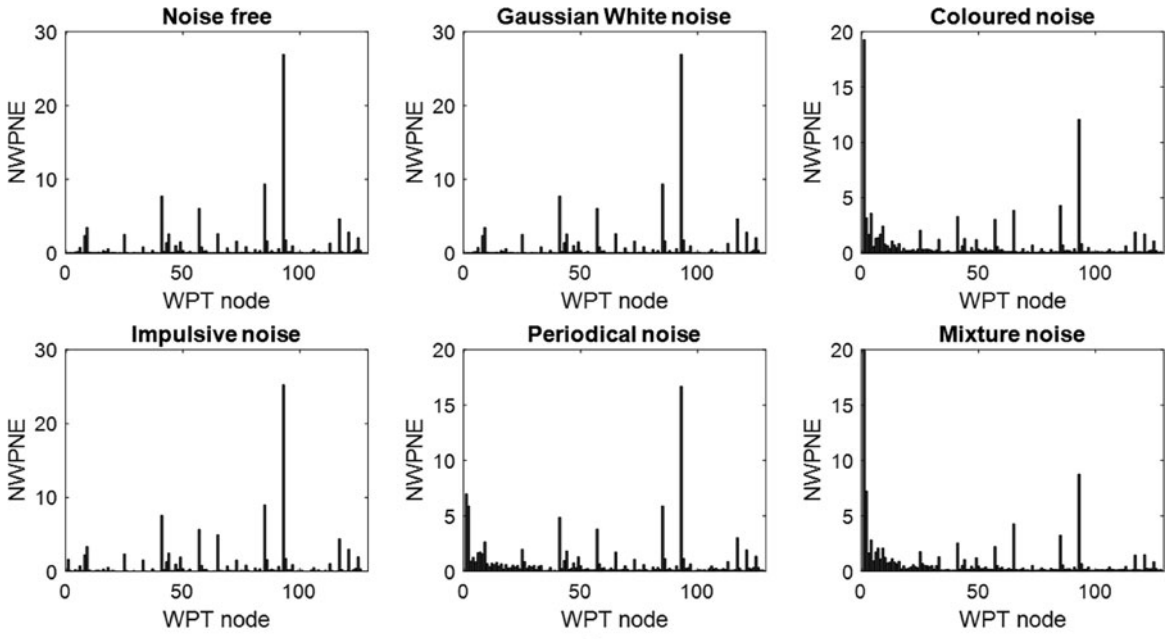

Fig. 5.6 NWPNEs features at SNR 20

frequency range. Figure 5.5b shows a continuous noise whose energy gradually deceases as frequency increases in spectrum. It is also known as a coloured noise. Figure 5.5c shows an impulsive noise which occurs only in a short period of time. Its spectrum is generally flat, and the energy gradually decreases when reaching high-frequency range. Figure 5.5d shows a periodic noise. Due to the complexity of frequency contents, its spectrum appears irregular. In Fig. 5.5e, the abovementioned four noises are combined into a mixture whose spectrum contains all the features of these noises.

The noisy signals are obtained by adding the noise to the 165 samples mentioned above. The noise level is quantified by SNR which is defined in decibel as:

$$\mathrm{SNR} = 20\log_{10}\frac{A_s}{A_n} \tag{5.8}$$

where A_s and A_n denote the root mean squares of the acceleration response and the noise, respectively. Three levels of noises are generated in MATLAB with SNR of 10, 20, and 30. For each type of noise at each SNR level, random noise samples are generated and added into the 165 samples resulting in 15 noise-contaminated datasets. Figure 5.6 shows NWPNE features

Table 5.1 Damage identification results comparison for multiple measurements

Accuracy in damage detection and localisation			
	SNR 30	SNR 20	SNR 10
Gaussian white	96%	96%	96%
Coloured	92%	88%	84%
Impulsive	96%	96%	92%
Periodic	92%	88%	88%
Mixture	92%	88%	80%
Maximum error in damage extent quantification			
	SNR 30	SNR 20	SNR 10
Gaussian white	3.2%	4.3%	7.1%
Coloured	6.6%	7.0%	15.5%
Impulsive	3.8%	4.6%	6.9%
Periodic	5.5%	6.5%	13.5%
Mixture	6.8%	8.5%	18.5%

extracted from clean and various noise-contaminated signals at SNR20. By appearance, Gaussian white noise and impulsive noise barely alter the NWPNE feature, while coloured noise has a significant effect. By comparing to their corresponding spectrum, noises with relatively uniform energy distributions tend to have less impact on the features.

With the same setting of the neural networks and identification procedures, damage localisation and quantification are conducted on the datasets independently. The results are shown in Table. 5.1.

The results show that Gaussian white noises and impulsive noises hardly affect the performance of this approach in damage localisation. However, the accuracy in localisation decreases markedly when coloured noises and periodic noises are introduced; nevertheless the overall performance of the approach may still be considered acceptable. On the other hand, errors in damage quantification increase as noise level increases. Particularly, coloured and periodic noises result in more significant increases in the errors of the damage quantification. The performance under the mixture of the noises is close to the case with coloured noise, which is the major contributor to the errors herein. The approach is more resistant to Gaussian white noise and impulsive noises and less so against noises with non-uniform energy distributions. Therefore, in real application, the latter type of noises should be avoided as much as possible. If such noise components are identified from the measurements, targeted denoising may be required. Up to a noise level with SNR $= 20$, the performance of the approach in damage identification is still satisfactory, even with small (incipient) damages.

5.3.4 Variation in Excitations

In an actual measurement environment, the variation in the impact force may be characterised in three basic aspects, namely, magnitude, duration, and the pulse shape. The variation in the impact duration not only affects the input energy but also the energy distribution in the frequency spectrum, which may result in a more complicated interference to the damage-sensitive features. In the time history of a real excitation signal, it is common to observe more than one peak at the start of the impact due to the imperfectness of the contacting surfaces, and this introduces further complexity in terms of the input energy and frequency contents of the excitation. Therefore, all the three types of variations could potentially have a significant influence on the WPNEs; hence, by incorporating these variations in the impact excitation, it will provide critical insight into the achievable performance of the WPNE-based approach in a real measurement environment. The numerical investigation is carried out to examine the effectiveness of the approach in the following aspects: (1) with variation in the magnitudes of excitations, (2) with variation in the impulse shapes of the excitations, (3) with variation in the duration of the excitation impulse. All the numerical tests are conducted under a Gaussian white noise (SNR 20)-contaminated condition. The state of identical excitations under Gaussian white noise is compared against as benchmark which echoes the conditions commonly adopted in most existing studies.

Variations in magnitudes, shapes, and durations of excitations are introduced step by step. In order to simulate variation in magnitudes of excitations, impulse loads with identical durations of 0.002 s and varying peak values between 100 N and 500 N are employed. All excitations are in isosceles triangle shapes in time history. An example of excitation variations in magnitude is shown in Fig. 5.7a. The 165 samples are simulated again. In each damage case, a unique excitation of 0.002 s duration and a randomly sampled peak force within the above specified range were created.

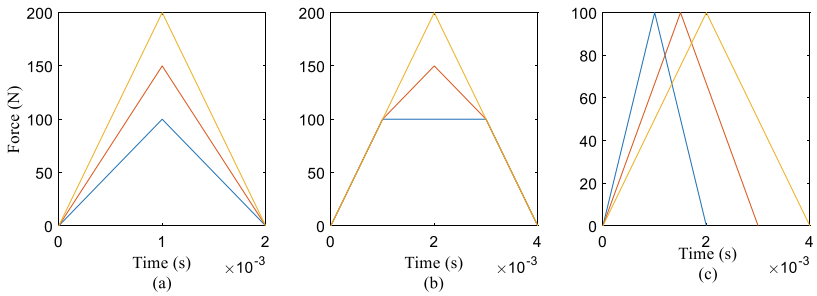

Fig. 5.7 Examples of variations in excitations: (**a**) variation in magnitude, (**b**) variation in shape, (**c**) variation in duration

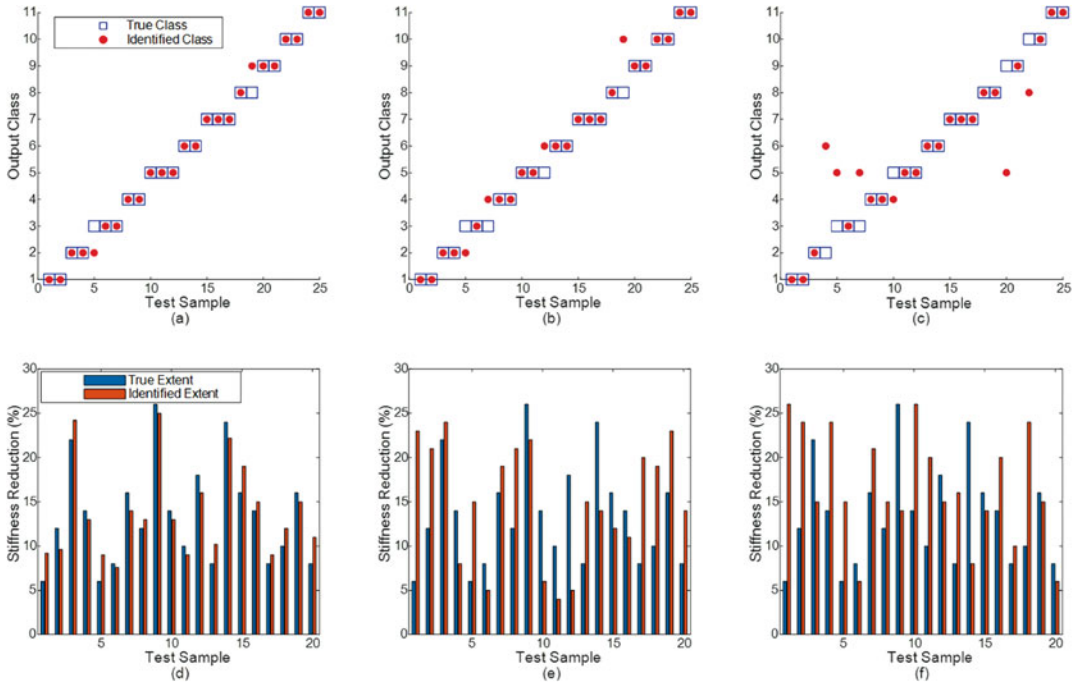

Fig. 5.8 Damage identification results: (**a**) NN-I variation in magnitude, (**b**) NN-I variation in shape, (**c**) NN-I variation in duration, (**d**) NN-II variation in magnitude, (**e**) NN-II variation in shape, (**f**) NN-II variation in duration

It should be pointed out that, despite the variation in magnitude, the power spectra of the impulses are still perfectly flat within the frequency range of interest and it does not disturb frequency distribution remarkably. To further broaden the variability of the excitation, excitation pulse forces varying not only in peak magnitude but also in the pulse shape in the time series are introduced. Figure 5.7b shows the pulse excitation with variable magnitude and pulse shape, while the duration of the excitation is kept at 0.004 s. Different excitations are generated by adjusting the peak value randomly between 100 N and 500 N.

White noises of SNR $=$ 30 are added into the acceleration responses and damage identification is conducted. Next, variation in the excitation duration is introduced which effectively alters the frequency contents (and hence the input energy distribution in the frequency domain). Excitations with identical peak value of 100 N and randomly varying duration between 0.002 s and 0.004 s are created. They are applied respectively in the simulation of the abovementioned 165 samples.

The damage identification results are shown in Fig. 5.8. It can be seen that the variation in the excitation magnitude does not affect markedly the classification (NN-I, detection, and localisation) performance. The variation in the excitation pulse shape causes a decrease in the classification accuracy (NN-I) to 84%. The variation in the duration appears to cause the most significant effect, and the classification accuracy decreases to 76%. In the damage quantification (NN-II), the maximum error increases notably to more than 16% when variations in shape and duration are involved. Therefore in real testing, compared to excitation magnitudes, better control in duration and pulse shape of excitations should be focused on to minimise the uncertainties at the contact point.

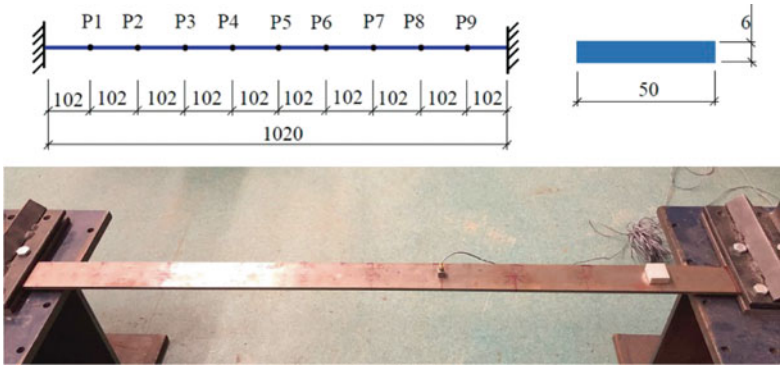

Fig. 5.9 (**a**) Sketch of the flat beam with fixed ends (top). (**b**) Flat steel beam (bottom)

5.4 Experimental Investigation

In order to further examine the performance of the approach in a real measurement condition, an experiment was conducted on a flat steel beam with fixed-end boundaries. Steel clamping plates and bolts were used to fix the two ends of the beam on strong steel supports. The stiffness of the supports is deemed considerably larger than the testing specimen, so that it can be regarded as a fixed support. The beam measured 1020 mm in length and had a cross-sectional area of 50 mm by 6 mm. Figure 5.9 depicts both a sketch and a photograph of the setup.

A measurement array was constructed by dividing the beam into ten segments along its length, resulting in nine joints between the two supports labelled P1 to P9. To avoid a nodal point in any of the first few mode configurations, the excitation was imposed vertically between P4 and P5, and an accelerometer was placed at P6. The duration of the record was set to 6 seconds, and the sampling rate was set at 1650 Hz. All hammer impact locations were controlled within a 2 cm by 2 cm square at midpoint between P4 and P5. All excitation forces were of a peak between 10 N and 20 N. A mass of 12 g was employed as the additional mass, which is equal to 0.5% of the beam weight. By attaching the mass at P1 to P9, respectively, nine structural states were generated. There were a total of ten states including the instance of no mass attached. The beam was excited for 20 times in each state, for a total of 200 samples. For the second stage of the approach for damage quantification, four levels of the magnitude of damage were created by adding masses of 6 g, 12 g, 24 g, and 36 g, respectively, at P3. In each state, the beam was excitated for 5 times, and totally 20 samples were recorded. The 15 samples from cases of 6 g, 24 g, and 36 g are used for training and validation with a dividing ratio of 13:2. The five samples from the case of 12 g are used for testing.

From the measured signals, the 128-dimensional feature vectors consisting of NWPNEs at seventh level of WPT are extracted and used as the inputs of the neural network. The number of neurons in hidden layer is set as 20. The outputs are 10-dimensional one-hot encoded vectors. Thus, the structure of the neural network in terms of neuron numbers in each layer is 128-20-10. The sizes of training, validation, and test datasets in this case are 140, 30, and 30, respectively, based on the same division ratio mentioned above. The training of the neural network completes with 36 iterations, and a cross entropy error is 8.34×10^{-5}.

The test (prediction) result is illustrated in Fig. 5.10 showing a satisfactory accuracy of 93.3% in damage localisation and acceptable maximum error in damage quantification in the real measurement environment.

5.5 Conclusions

Through numerical investigations, this paper demonstrates that the wavelet energy with neural network (WPNE-NN) approach to damage identification is generally impervious to the measurement noises up to a level with SNR = 20. As the noise level further increases, interference from the types of noises with non-uniform energy distributions in the frequency domain becomes more apparent, whereas Gaussian white noise or impulsive noise continue to have a negligible effect. Additionally, variation in the excitation magnitude does not affect markedly the damage identification performance, while the variation in pulse shape and durations of excitations causes more noticeable interference.

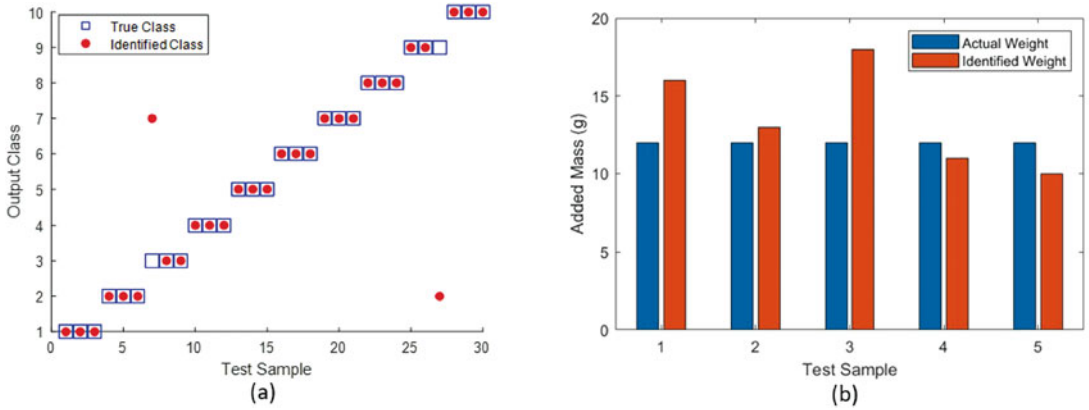

Fig. 5.10 Damage identification result: (**a**) NN-I result, (**b**) NN-II result

The experimental investigation demonstrated that in a real measurement environment with hand controlled excitations, the WPNE-NN approach delivered good accuracy in damage detection and localisation and an acceptable margin of error in damage quantification.

Therefore, it may be concluded that the WPNE-NN approach to detecting structural changes is workable, and with a reasonably controlled impact test, it is possible to identify initiation of damage with good accuracy.

References

1. Yen, G.G., Lin, K.C.: Wavelet packet feature extraction for vibration monitoring. IEEE Trans. Ind. Electron. **47**(3), 650–667 (2000)
2. Han, J.G., Ren, W.X., Sun, Z.S.: Wavelet packet based damage identification of beam structures. Int. J. Solids Struct. **42**(26), 6610–6627 (2005)
3. Mikami, S., Beskhyroun, S., Oshima, T.: Wavelet packet based damage detection in beam-like structures without baseline modal parameters. Struct. Infrastruct. Eng. **7**(3), 211–227 (2011)
4. Sun, Z., Chang, C.C.: Structural damage assessment based on wavelet packet transform. J. Struct. Eng. ASCE. **128**(10), 1354–1361 (2002)
5. Graps, A.: An introduction to wavelets. IEEE Comput. Sci. Eng. **2**(2), 50–61 (1995)
6. Coifman, R.R., Wickerhauser, M.V.: Entropy-based algorithms for best basis selection. IEEE Trans. Inf. Theory. **38**(2), 713–718 (1992)
7. Mallat, S., Peyre, G.: A wavelet tour of signal processing the sparse way preface to the sparse edition. In: Wavelet tour of signal processing: the Sparse Way, 3rd edn. Elsevier (2009)
8. Liu, Y.-Y., Ju, Y.-F., Duan, C.-D., Zhao, X.-F.: Structure damage diagnosis using neural network and feature fusion. Eng. Appl. Artif. Intell. **24**, 87–92 (2011)., 2010.08.011
9. Ghiasi, R., Torkzadeh, P., Noori, M.: A machine-learning approach for structural damage detection using least square support vector machine based on a new combinational kernel function. Struct. Health Monit. **15**(3), 302–316 (2016)
10. Cao, M., Ding, Y., Ren, W., Wang, Q., Ragulskis, M., Ding, Z.: Hierarchical wavelet-aided neural intelligent identification of structural damage in Noisy conditions. Appl. Sci. **7**(4), 391 (2017). 1–20

Chapter 6
Advanced Meta-Modelling Techniques and Sensitivity Analysis for Rotordynamics in an Uncertain Context

E. Denimal and J.-J. Sinou

Abstract It is essential to predict accurately the critical speeds and associated vibration amplitudes of rotating machineries to ensure a correct design to limit noise nuisance and fatigue failure. However, numerous uncertainties are present, due to environmental variations or manufacturing tolerances, e.g. and must be taken into consideration in the design stage to limit their impact on the system dynamics. These uncertainties are usually modelled with a probability law, and the dynamic response becomes stochastic. On the other side, during the design stage, a few key parameters, often called design parameters, are identified and tuned to ensure a robust conception of the rotor w.r.t. the uncertain model parameters. In this context, one must tackle a high-dimension parametric problem but numerous parameters of different nature. The efficiency of an advanced meta-modelling technique that couple polynomial chaos expansion and kriging is demonstrated here. The kriging efficiency is improved by introducing physical properties of the rotor. A finite element model of a rotor subjected to nine uncertain parameters is studied. The hybrid surrogate model gives a direct access to the Sobol indices, exploited to conduct an extensive sensitivity analysis.

Keywords Rotordynamics · Hybrid uncertainties · Kriging · Polynomial chaos expansion · Sobol indices

6.1 Introduction

Rotors are main components in many applications, such as for transports or energy production. They must be able to carry out important loadings, and so their design must be undertaken carefully. More particularly, dramatic accidents and failures may occur due to the vibrational loadings, and so the vibration analysis of such components is primordial to reduce noise and failures due to vibrational loadings. In this context, the prediction of the critical speeds and associated vibration amplitudes are the main concern of engineers during the design to ensure that the vibrations that the rotor will endure are acceptable. Being able to predict accurately and robustly, these critical speeds and vibration amplitudes to detect potential issues are of major concern in the design stage. This task is complex as rotors depend on many parameters (geometry, material, bearings, etc.) making difficult to get a global vision of the dynamic of the structure and the impact of the variability that each component would have on the global response. Thus, one of the most difficult problems nowadays is to develop methods that integrate these uncertainties and are numerically applicable to large and realistic mechanical systems.

When designing such systems, engineers are facing many uncertainties that can be of different natures. They can usually be split into two groups. The first group corresponds to design parameters, i.e. parameters that are usually tuned by engineers and used for the conception of the rotor. They often take value in an interval and parametric studies conducted to tune them. The second group corresponds to uncertain parameters, i.e. parameters that translate a variability or a lack of knowledge due to tolerances, environmental fluctuations, etc. They are often modelled by probability density functions. When many uncertain parameters are present, an efficient strategy consists in the creation of a surrogate model that mimics the behaviour of the full model. Recent strategies have been based on the use of a single method, as PCE [1–3] or kriging [4–6] to predict the critical

E. Denimal (✉)
University of Gustave Eiffel, Inria, Rennes, France
e-mail: enora.denimal@inria.fr

J.-J. Sinou
Labortary Tribologie et Dynamique des Systèmes, Ecully, France

Institut Universitaire de France, Paris, France
e-mail: jean-jacques.sinou@ec-lyon.fr

Z. Mao (eds.), *Model Validation and Uncertainty Quantification, Volume 3*, Conference Proceedings of the Society for Experimental Mechanics Series, https://doi.org/10.1007/978-3-031-04090-0_6

speeds of uncertain rotors. However, none of them is able to deal with both nature of uncertainty at this step. In this context, a recent approach has been developed that combines PCE and kriging to model both random and parametric uncertainties [7]. This method has given good results applied for the prediction of friction-induced vibrations for both academic models and industrial models [7, 8].

This work proposes to predict the dynamic behaviour of a rotor subjected to numerous uncertainties of different natures. More precisely, two of them are parametric and seven others are random. The efficiency of the hybrid surrogate model is demonstrated on this case. The prediction of the mean and variances of the critical speeds and amplitudes is performed, and the formulation avoids costly MCS simulations thus reducing the numerical cost. Moreover, a sensitivity analysis of the rotor is conducted, and complex behaviours are analysed. Finally, the kriging part is improved by introducing the symmetrical properties of the rotor in the formulation.

The paper is organised as follows. First, the model under study is briefly presented. Then the hybrid surrogate model is presented. Specifications on an efficient construction of the kriging are also given. Finally, the efficiency and accuracy of the hybrid surrogate model to predict the critical speeds and associated vibration amplitudes are demonstrated. Additionally, a sensitivity analysis based on the Sobol indices is conducted to get deep insights in the rotor dynamics.

6.2 Description of the Rotor

This section describes briefly the rotor modelling. It is composed of a shaft supported by two bearings and four discs as represented in Fig. 6.1. An unbalanced mass is located on the first disc. For a detailed description of the construction of the model, the interested reader can refer to [5, 9, 10].

The shaft is modelled with a finite element model (FEM) of ten Euler beams. Each node has four degrees of freedom (two displacements and two rotations) and nodal displacements of the element ith are denoted $\mathbf{x}^{(s,i)}$. The EOM of the ith element writes:

$$\left(\mathbf{M}_R^{(s,l)} + \mathbf{M}_T^{(s,l)}\right)\ddot{\mathbf{x}}^{(s,i)} + \left(\mathbf{C}^{(s,l)} + \omega\mathbf{G}^{(s,l)}\right)\dot{\mathbf{x}}^{(s,i)} + \mathbf{K}^{(s,l)}\mathbf{x}^{(s,i)} = \mathbf{0}$$

with $\mathbf{M}_R^{(s,l)}$ and $\mathbf{M}_T^{(s,l)}$ the rotational and translational mass matrices of the element ith, $\mathbf{C}^{(s,l)}$ the damping matrix the element ith, $\mathbf{G}^{(s,l)}$ the gyroscopic matrix the element ith and $\mathbf{K}^{(s,l)}$ the stiffness matrix the element ith. Material properties of the shaft are summarised in Table 6.1.

The discs are modelled as rigid discs and the nodal displacement in the fixed frame is denoted $\mathbf{x}^{(d,j)}$. The EOM writes:

$$\left(\mathbf{M}_R^{(d,j)} + \mathbf{M}_T^{(d,j)}\right)\ddot{\mathbf{x}}^{(d,j)} + \omega\mathbf{G}^{(d,j)}\dot{\mathbf{x}}^{(d,j)} = \mathbf{F}^{(d,j)}$$

with $\mathbf{M}_R^{(d,j)}$ and $\mathbf{M}_T^{(d,j)}$ the rotational and translational mass matrices of the jth disc, $\mathbf{G}^{(d,j)}$ the gyroscopic matrix of the jth disc and $\mathbf{F}^{(d,j)}$ the unbalance of the disc j, of the form:

$$\mathbf{F}^{(d,j)} = \begin{bmatrix} m_u d_u \omega^2 \cos\omega t + \phi & m_u d_u \omega^2 \sin\omega t + \phi & 0 & 0 \end{bmatrix}^T$$

with m_u the unbalanced mass, d_u the eccentricity of the mass, ϕ the initial phase and ω the rotational speed of the rotor. The different properties are summarised in Table 6.1.

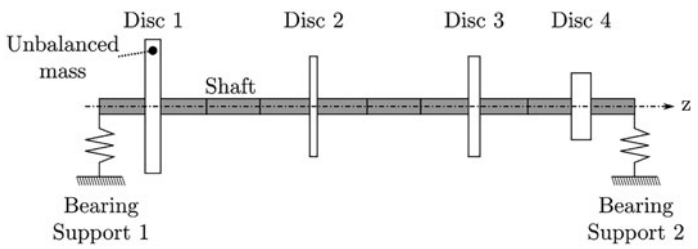

Fig. 6.1 Rotor under study

Table 6.1 Geometrical and material properties of the rotor

Notation	Parameter name	Value
R_1	Outer radius – Disc 1	0.25 m
e_1	Thickness – Disc 1	0.03 m
R_2	Outer radius – Disc 2	0.1875 m
e_2	Thickness – Disc 2	0.015 m
R_3	Outer radius – Disc 3	0.1875 m
e_3	Thickness – Disc 3	0.0225 m
R_4	Outer radius – Disc 4	0.125 m
e_4	Thickness – Disc 4	0.0375 m
E_d	Young modulus of disc material	2.1 10^{11} N/m^2
ρ_d	Density of disc material	7800 kg/m^3
m_u	Mass unbalance – Disc 1	0.01 kg
d_u	Eccentricity of the unbalance mass – Disc 1	0.01 m
$k_h^{b,1}$	Horizontal stiffness – Bearing 1	3 10^6 N/m
$k_v^{b,1}$	Vertical stiffness – Bearing 1	3 10^6 N/m
$k_h^{b,2}$	Horizontal stiffness – Bearing 2	[0.1;2] 10^6 N/m
$k_v^{b,2}$	Vertical stiffness – Bearing 2	[0.1;2] 10^6 N/m

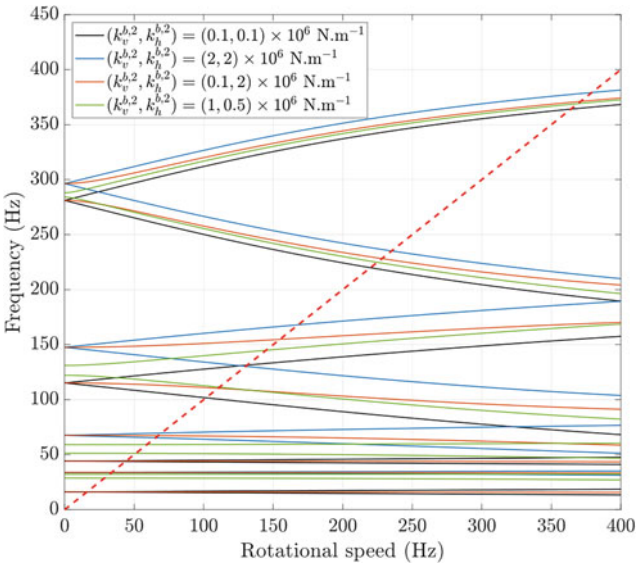

Fig. 6.2 Campbell diagram for different second bearing stiffness

Each flexible bearing supports is modelled as two linear springs, one in each direction of the fixed frame. They are denoted $k_v^{(b,1)}$, $k_h^{(b,1)}$, $k_v^{(b,2)}$ and $k_h^{(b,2)}$. The global matrices are $\mathbf{K}^{(b,1)}$ and $\mathbf{K}^{(b,2)}$.

The general dynamic equation of the rotor is:

$$\mathbf{M}\ddot{\mathbf{x}} + (\mathbf{C} + \omega\mathbf{G})\,\dot{\mathbf{x}} + \mathbf{K}\mathbf{x} = \mathbf{F}$$

where $\mathbf{M}$ groups the mass matrix of the shaft and the discs, $\mathbf{C}$ groups the damping matrix of the shaft, $\mathbf{G}$ groups the gyroscopic of the shaft and the discs, $\mathbf{K}$ groups the stiffness matrix of the shaft and the bearings and $\mathbf{F}$ the vector of the unbalanced forces. For a detailed description of the matrix construction, the interested reader could refer to [5, 10].

Finally, the Campbell diagram of the rotor is given in Fig. 6.2 for different values of bearing stiffness of the second bearing. One can observe the impact of the bearing stiffnesses on the critical speeds.

Table 6.2 Properties of the random parameters

Notation	Parameter name	% variation	Law
E	Young modulus shaft	±5%	Uniform
e_1	Thickness – Disc 1	±10%	Uniform
e_2	Thickness – Disc 2	±10%	Uniform
e_3	Thickness – Disc 3	±10%	Uniform
e_4	Thickness – Disc 4	±10%	Uniform
$k_h^{b,1}$	Horizontal stiffness – Bearing 1	±5%	Uniform
$k_v^{b,1}$	Vertical stiffness – Bearing 2	±5%	Uniform

6.3 Hybrid Surrogate Model

In this section, the uncertain parameters are presented first. Then, the methodology for uncertainty propagation is presented.

6.3.1 Uncertain Parameters

Two types of uncertain parameters are considered here. The first set of uncertain parameters are random parameters and are described by a probability density function (PDF). They might come from manufacturing tolerances or environmental variations, for example. Seven parameters are in this group and are summarised in Table 6.2. Their influence on the model matrices depends on the parameter. They are grouped in the random vector $\boldsymbol{\xi} = \left[\xi_E, \xi_{e_1}, \xi_{e_2}\xi_{e_3}, \xi_{e_4}, \xi_{k_v^{(b,1)}}, \xi_{k_h^{(b,1)}}\right]$.

The second type of uncertain parameters is considered as deterministic and corresponds to the stiffness of the second bearing ($k_v^{(b,2)}$ and $k_h^{(b,2)}$) and can take value in [0.1;2] 10^6 N/m. They are grouped in the vector $\mathbf{x} = \left[k_v^{(b,2)}, k_h^{(b,2)}\right]$.

The final objective is to predict the rotor forward and backward critical speeds and associated vibration amplitudes when these two bearings stiffness vary and by taking into consideration the uncertainty of the seven random parameters. The critical speeds are denoted f^i and the associated vibration amplitudes a^i, for i in [1, 8]. As they depend on $\mathbf{x}$ and $\boldsymbol{\xi}$, they can also be written $f^i(\mathbf{x}, \boldsymbol{\xi})$ and $a^i(\mathbf{x}, \boldsymbol{\xi})$.

6.3.2 Polynomial Chaos

The random part of each quantity of interest (QoI) can be approximated by a convergent PCE of the form [11, 12]:

$$\mathrm{Y}(\boldsymbol{\xi}) = \sum_{k=0}^{P-1} \alpha_k \Phi_{\mathrm{k}}(\boldsymbol{\xi})$$

where Y is the considered QoI (one critical speed or one vibration amplitude), α_k are the weighting coefficients to be determined and Φ_k is the multivariate polynomial basis. The latter is obtained by tensorisation of monovariate polynomial basis given by the Askey Scheme. A hyperbolic norm is adopted to select the PCE terms to keep in the expansion. The coefficients α_k are the solution of a least-square minimisation problem between N evaluations of the expensive model Y and its PCE approximation. For more details, the reader could refer to [7, 10–12].

6.3.3 Kriging

The parametric part of each QoI can be approximated with a kriging surrogate model. In other words, a QoI α that depends on $\mathbf{x}$ can be approximated by [13]:

$$\alpha(\mathbf{x}) = \mathbf{g}(\mathbf{x})^T \boldsymbol{\beta} + Z(\mathbf{x})$$

where $\mathbf{g}$ is a set of regressive functions, often taken as polynomials of low order, $\boldsymbol{\beta}$ are the weighting coefficients and are solution of a least square problem and Z is a zero-mean Gaussian process of variance σ^2, which covariance writes $E[Z(\mathbf{x}), Z(\mathbf{x}')] = \sigma^2 R(\boldsymbol{\theta}, \mathbf{x}, \mathbf{x}')$ with R the spatial correlation function of scaling parameter $\boldsymbol{\theta}$ and $\mathbf{x}$ and $\mathbf{x}'$ two points of the input space. To build the surrogate model, Q evaluations of the expensive model are necessary, i.e. Q inputs $(\mathbf{x}^{(j)})$ and their evaluations $(\alpha^{(j)}) = (\alpha(\mathbf{x}^{(j)}))$. For a detailed description of the Kriging and its practical implementation, the interested reader could refer to [7, 10, 13].

6.3.4 Kriging for a Symmetrical Problem

The possibility to improve the kriging process by taking into consideration the physical properties is discussed here. More specifically, the QoI considered here are symmetrical with respect to $k_v^{(b,2)} = k_h^{(b,2)}$. To consider this, three strategies are investigated in the following:

- A classic strategy: a classic kriging is constructed by choosing a regression function g and a correlation function, and no symmetric properties are considered.
- A half-design space restriction strategy: as the problem is symmetric, only points that satisfy $k_v^{(b,2)} \leq k_h^{(b,2)}$ are used for the kriging construction. For the prediction, half of the design space is directly reconstructed based on the symmetric property.
- A symmetrical regression strategy: the symmetric aspect of the problem introduced in the regression part directly. As an example, in dimension 2, if $\mathbf{g}$ is the second-order polynomial regression function for a classical kriging, the symmetric regression function $\mathbf{g_s}$ would write:

$$\mathbf{g_s}(x_1, x_2) = \begin{cases} \beta_0 + \beta_1 x_1 + \beta_2 x_2 + \beta_3 x_1 x_2 + \beta_4 x_1^2 + \beta_5 x_2^2 & \text{if } x_1 \leq x_2 \\ \mathbf{g_s}(x_2, x_1) & \text{otherwise} \end{cases}$$

with $x_1 = k_v^{(b,2)}$ and $x_2 = k_h^{(b,2)}$.

6.3.5 Hybrid Formulation

The proposed hybrid surrogate model associates PCE and kriging, detailed in [7, 10]. If Y denotes one QoI, i.e. $f^{(i)}$ or $a^{(i)}$, then it writes:

$$Y(\boldsymbol{\xi}, \mathbf{x}) = \sum_{k=0}^{P-1} a_k(\mathbf{x}) \Phi_k(\boldsymbol{\xi}) = \sum_{k=0}^{P-1} \left(\mathbf{g}^{(k)}(\mathbf{x})^T \boldsymbol{\beta}^{(k)} + Z^{(k)}(\mathbf{x}) \right) \Phi_k(\boldsymbol{\xi})$$

Y is obtained by expanding it on a PCE, where PCE coefficients depend on the parametric vector $\mathbf{x}$. These coefficients are then approximated with a kriging surrogate model. Considering the training set, Q points $(\mathbf{x}^{(j)})$ and N points $(\boldsymbol{\xi}^{(j)})$ are generated. The final training set is obtained by tensorisation of these two sets. For each point, the critical speeds and associated amplitudes are computed.

6.3.6 Exploitation of PCE Coefficients

From the PCE expansion, one gets directly access to the mean and variance of the process that depend directly on the vector $\mathbf{x}$ in this case. The interest of the current formulation is that the average and variance can be obtained on the full parametric space without additional MCS (as it would have been the case if a unique kriging surrogate model were built). It writes:

$$E[Y(\mathbf{x})] = a_0(\mathbf{x}) = \mathbf{g}^{(0)}(\mathbf{x})^T \boldsymbol{\beta}^{(0)} + Z^{(0)}(\mathbf{x})$$

$$\sigma^2_{Y(\mathbf{x})} = \sum_{k=1}^{P-1} a_k(\mathbf{x})^2 ||\Phi_k||^2 = \sum_{k=0}^{P-1} \left(\mathbf{g}^{(k)}(\mathbf{x})^T \boldsymbol{\beta}^{(k)} + Z^{(k)}(\mathbf{x})\right)^2 ||\Phi_k||^2$$

Similarly, the Sobol indices $S_i(\mathbf{x})$ are directly related to the PCE coefficients and are equal to [12]:

$$S_i(\mathbf{x}) = \frac{V_i(\mathbf{x})}{V(Y(\mathbf{x}))}$$

where $V_i(\mathbf{x}) = \sum_{j \in v_i} \alpha_j(\mathbf{x})^2 \left|\left|\Phi_j\right|\right|^2$ with v_i the set of multivariate indices for which the only polynomials related to the variable i are present.

6.4 Results

In this section, the results obtained are presented and commented. A first brief part is dedicated to the strategy adopted for the construction and validation of the hybrid surrogate models. Then, the three different kriging strategies are compared. Finally, a variance-based sensitivity analysis is performed.

6.4.1 Construction of the Surrogate Models

For the construction of the training set, the first input set related to the PCE is generated based on an LHS of $N = 250$ points (250 values of $\boldsymbol{\xi}$). For the kriging, Q points are generated based on an LHS maximising a maximin criterion, and four different sizes are considered, namely, $Q = [20, 40, 60, 80]$. The first eight critical speeds and associated vibration amplitudes are computed for the $N \times Q$ configurations.

For 8 values of $\mathbf{x}$, 500 reference points have got to validate the PCE parts. The PCE properties are tuned to ensure the minimum level of relative error over the 8×500 points.

The second step consists in the construction of the kriging surrogate models for each PCE coefficient. To validate this part, the average and variance of the eight critical speeds $f^{(i)}$ and associated vibration amplitudes $a^{(i)}$ are computed over a grid of 100×100, and kriging prediction are compared to these reference values. The comparison of the kriging strategies is presented in the following.

6.4.2 Comparison of the Kriging Strategies

The error on the average and variance of the critical speeds and associated vibration amplitudes over the 100×100 grid is computed. This error is defined as:

$$Error(\mathbf{x}) = \frac{r_p(\mathbf{x}) - r_{ref}(\mathbf{x})}{|\, r_{ref}(\mathbf{x}) \,|}$$

with r_p the prediction of the average (variance resp.) and r_{ref} the reference of the average (variance resp.) of the considered QoI. It is computed for the eight critical speeds $f^{(i)}$ and the associated vibration amplitudes $a^{(i)}$ and for the different cases (four DoE sizes and three kriging strategies). Means and variances of this error over the 100×100 grid are computed. They are displayed for the vibration amplitudes in Fig. 6.3. Results are similar for the critical speeds but are not given here for the sake of concision.

The following conclusions can be drawn:

- Errors vary a lot from one mode to another, and they tend to be lower for forward modes (even number) than for backward modes (odd number). This is explained by the fact that amplitudes for the backward modes are almost zero for equal stiffness $k_v^{(b,2)} = k_h^{(b,2)}$, which tends to increase the relative error.
- When the DoE size increases, the errors decrease on average and variance. The convergence is more or less quick depending on the mode.

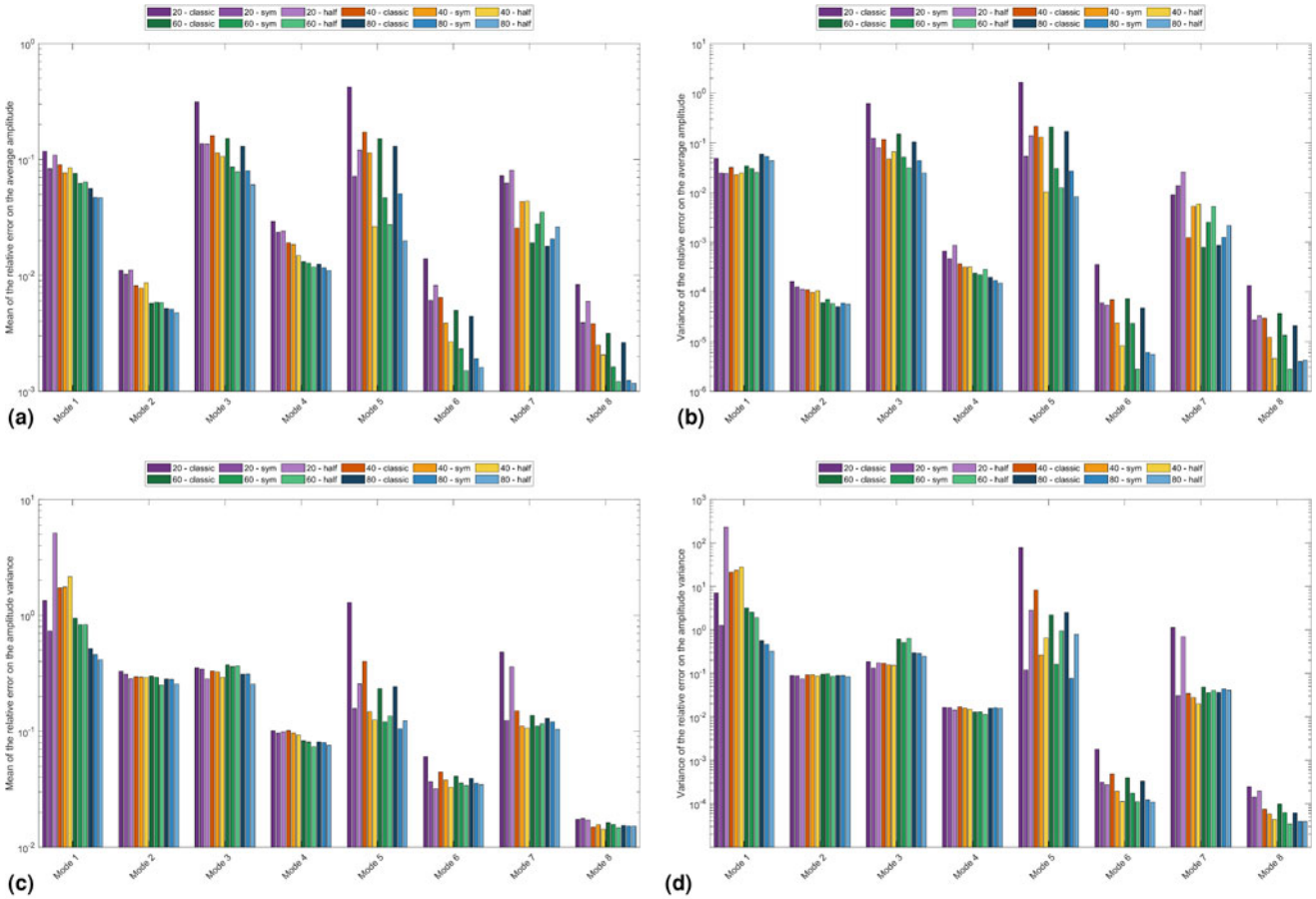

Fig. 6.3 (**a**) Average relative error on the average amplitude (**b**) Variance of the relative error on the average amplitude (**c**) Average error on the amplitude variance (**d**) Variance of the relative error on the amplitude variance

– Globally, the classic kriging strategy is the worst strategy, and the half-design strategy performs better than the others and gives error level that can be several order of magnitude below. It is particularly clear on the average amplitudes for higher modes. Or, for example, for the 20 points case, the symmetric strategy performs better than the others, and it gives better results than the classic strategy with 80 points. This demonstrates the drastic numerical cost reduction such strategy can bring.

When looking at the difference in prediction between the different strategies, it appears that the main differences between the different strategies are around the line $k_v^{(b,2)} = k_h^{(b,2)}$. The classic kriging strategy is in fact unable to catch the sharp evolutions of the amplitudes around this axis, especially for backward modes where amplitudes almost jump to 0 around this line. On the other hand, the two other strategies were able to capture this sharp evolution due to their construction (symmetry imposed either in the regression or in the restriction of the DoE).

As a conclusion, the three strategies perform well globally. However, the half-design and symmetric regression strategies perform better and should be used compared to the classic kriging strategy. Moreover, the half-design strategy required twice less training points and so should be chosen preferably as it represents the best compromise between accuracy and numerical cost. These results demonstrate that adding information about the problem properties in the kriging construction or in the DoE construction improves substantially the kriging efficiency and reduces drastically the size of the required training set.

Finally, the results obtained for prediction the vibration amplitudes and critical speeds are given in Fig. 6.4. Only the first four modes are given for the sake of concision. The coloured surface corresponds to the average value of the QoI, and red and blue surfaces correspond to the average $\pm$ the standard deviation. Results are given with the half-design space strategy with a training set of 30 points for the kriging. One could clearly see here the good agreement between the predictions and the reference case, which illustrates the efficiency of the hybrid meta-model to surrogate the behaviour of the full rotor.

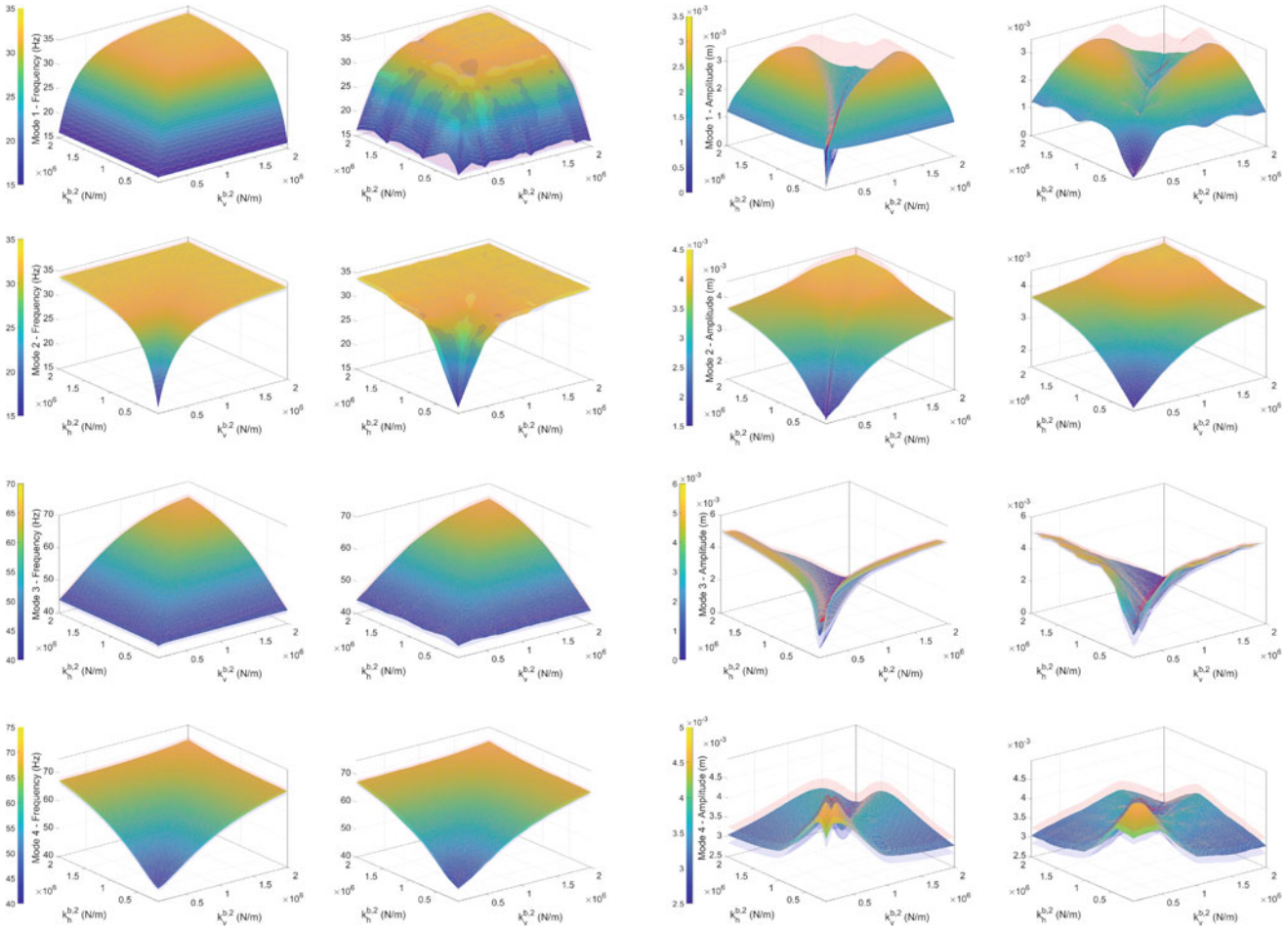

Fig. 6.4 Evolution of the average and average ± standard deviation for the critical speeds (reference, first column; prediction, second column) and associated vibration amplitudes (reference, third column; prediction, fourth column)

6.4.3 Variance-Based Sensitivity Analysis Based on Sobol Indices

A sensitivity analysis is now conducted on the rotor to get insights in the influence played by the different random parameters on the rotor dynamics. The Sobol indices can be deducted directly from the PCE coefficients without any additional cost, which makes this type of analysis very interesting in complement of PCE. As a reminder, Sobol indices are indicator that makes possible to state on the influence of an input variable on the output variance. If the Sobol index associated with one variable is close to 0, then this parameter has no influence on the output variance. On the contrary, if the Sobol index is close to 1, then this parameter is highly influential. First-order Sobol indices are given for the first four modes in Fig. 6.5, for the critical speeds and associated vibration amplitudes.

At a first glance, one could clearly see that the Sobol indices strongly depend on the considered mode. Indeed, one could see that the thickness of the first disc e_1 has a strong influence on the vibration amplitudes associated with the mode 4, whereas it has a low influence on the vibration amplitudes of mode 1. They are also different for the critical speeds and the vibration amplitudes. Indeed, for example, the thickness of the first disc e_1 has a strong influence on the critical speeds of mode 1 (equal to 0.5 over almost the whole domain), whereas it has a limited effect on the vibration amplitude (almost 0 over the whole domain). Then, the Sobol indices also strongly depend on the value of the stiffness $k_v^{(b,2)}$ and $k_h^{(b,2)}$: see, for example, $S_{k_h^{(b,1)}}$ for the vibration amplitude where it has large values for $k_v^{(b,2)} = k_h^{(b,2)}$ and low values otherwise.

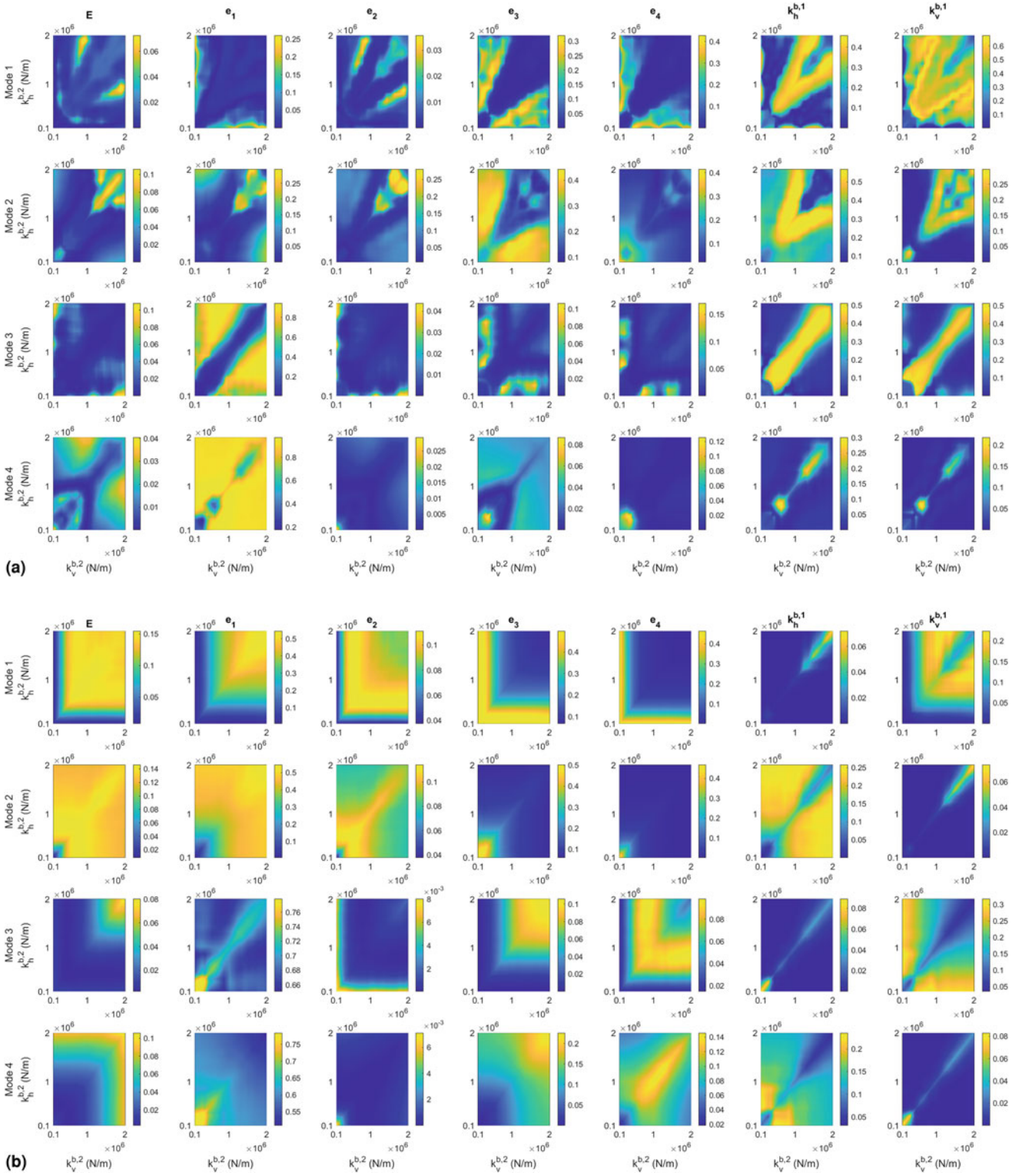

Fig. 6.5 First order Sobol indices for the vibration amplitudes (**a**) and critical speeds (**b**)

More precisely, the following conclusions can be drawn for each mode:

– Mode 1: for low stiffness values, thicknesses of the discs 3 and 4 have a large influence on the critical speed. For higher values, the Young modulus and the thickness of the first disc have the higher influence. Considering the vibration

amplitudes, far from $k_v^{(b,2)} = k_h^{(b,2)}$, the thickness of discs 3 and 4 have the largest contributions. Otherwise, the two stiffness $k_v^{(b,1)}$ and $k_h^{(b,1)}$ are the most influential parameters.
- Mode 2: the parameters that drive the critical speeds are the Young modulus, the thickness of the first disc and the stiffness $k_h^{(b,1)}$. The parameters that drive the vibration amplitudes are the thickness of the disc 3 when far from $k_v^{(b,2)} = k_h^{(b,2)}$ and are the thickness of the first disc, the stiffness $k_h^{(b,1)}$ and the stiffness $k_v^{(b,1)}$ otherwise.
- Mode 3: the critical speed is mostly driven by the thickness of the first disc. The vibration amplitudes are driven by the two stiffnesses when $k_v^{(b,2)} = k_h^{(b,2)}$ and by the thickness of the first disc otherwise.
- Mode 4: the thickness of the first disc drives mostly the critical speed as well as the vibration amplitudes.

More generally, the influence of a disc thickness on a mode depends strongly on its location. If the former is located on a node (anti-node, resp.) of the mode, then it will have a low (high, resp.) influence on the critical speeds. Considering the vibration amplitudes, if $k_v^{(b,2)} = k_v^{(b,2)}$, then stiffness $k_v^{(b,1)}$ and $k_h^{(b,1)}$ drive the symmetrical property of the rotor, and so if they are different then the rotor becomes asymmetric and have large experience important vibrations.

6.5 Conclusion

In the present work, a hybrid surrogate model has been used to predict accurately and efficiently the critical speeds and associated vibration amplitudes of the forward and backward modes of a rotor. The potential of such approach to deal with large models with numerous uncertainties is demonstrated.

Random parameters are modelled through a PCE and parametric parameters with kriging. The combination of the two methods makes possible to consider a high number of uncertainties that can be of different natures. Moreover, as the PCE coefficients are directly predicted with kriging, stochastic properties, as mean and variance, and Sobol indices can directly be estimated without additional costly MCS. This makes the method very efficient to identify the impact of the parametric variables on the stochastic response of the rotor. In a context of design, this approach is very promising. Finally, Sobol indices are used to perform a sensitivity analysis and insights in the rotor dynamics and the influence of the different parameters is assessed.

Three kriging strategies have been compared, and it is shown that introducing known properties about symmetry in the kriging construction improves its efficiency, both in terms of accuracy and convergence speed. It demonstrates the relevance of introducing the expertise that engineers and researchers have gain so far directly in the surrogate model construction and of developing grey-box models for structural dynamics.

Acknowledgement E. Denimal acknowledges the financial support of Rennes Metropole. J-J. Sinou acknowledges the support of the Institut Universitaire de France.

References

1. Sarrouy, E., Dessombz, O., Sinou, J.J.: Stochastic analysis of the eigenvalue problem for mechanical systems using polynomial chaos expansion—application to a finite element rotor. J. Vib. Acoust. **134**(5), 051009 (2012)
2. Didier, J., Faverjon, B., Sinou, J.J.: Analysing the dynamic response of a rotor system under uncertain parameters by polynomial chaos expansion. J. Vib. Control. **18**(5), 712–732 (2012)
3. Garoli, G.Y., de Castro, H.F.: Generalized polynomial chaos expansion applied to uncertainties quantification in rotating machinery fault analysis. J. Braz. Soc. Mech. Sci. Eng. **42**(11), 1–15 (2020)
4. Wang, D., Hua, C., Dong, D., He, B., Lu, Z.: Crack parameters identification based on a kriging surrogate model for operating rotors. Shock. Vib. **2018**, 1–12 (2018)
5. Sinou, J.J., Nechak, L., Besset, S.: Kriging metamodeling in rotordynamics: application for predicting critical speeds and vibrations of a flexible rotor. Complexity. **2018**, 1–26 (2018)
6. Silva Barbosa, J., Campanine Sicchieri, L., Dourado, A.D.P., Cavalini Jr., A.A., Steffen Jr., V.: Kriging approach dedicated to represent hydrodynamic bearings. J. Eng. Gas Turbines Power. **143**(6), 061016 (2021)
7. Denimal, E., Nechak, L., Sinou, J.J., Nacivet, S.: A novel hybrid surrogate model and its application on a mechanical system subjected to friction-induced vibration. J. Sound Vib. **434**, 456–474 (2018)
8. Denimal, E., Sinou, J.J., Nacivet, S.: Prediction of squeal instabilities of a finite element model automotive brake with uncertain structural and environmental parameters with a hybrid surrogate model. J. Vib. Acoust. **144**(2), 021006 (2021)
9. Friswell, M.I., Penny, J.E., Garvey, S.D., Lees, A.W.: Dynamics of Rotating Machines. Cambridge University Press (2010)

10. Denimal, E., Sinou, J.J.: Advanced kriging-based surrogate modelling and sensitivity analysis for rotordynamics with uncertainties. Eur. J. Mech. A/Solids. **90**, 104331 (2021)
11. Xiu, D., Karniadakis, G.E.: The Wiener–Askey polynomial chaos for stochastic differential equations. SIAM J. Sci. Comput. **24**(2), 619–644 (2002)
12. Sudret, B.: Global sensitivity analysis using polynomial chaos expansions. Reliab. Eng. Syst. Saf. **93**(7), 964–979 (2008)
13. Lophaven, S.N., Nielsen, H.B., Søndergaard, J.: DACE: a Matlab Kriging Toolbox IMM, Informatics and Mathematical Modelling, vol. 2. The Technical University of Denmark (2002)

Chapter 7
Variational Filter for Predictive Modeling of Structural Systems

Alana Lund, Ilias Bilionis, and Shirley J. Dyke

Abstract Bayesian inference offers a distinct advantage in predictive structural modeling as it quantifies the inherent epistemic uncertainties that arise due to observations of the system which are both finite in length and limited in representative behavioral information. Current research interest in the field of predictive structural modeling has emphasized analytical and sampling approaches to Bayesian inference, which have the respective advantages of either computational speed or inference accuracy. Recent work in optimization-based inference approaches have created new opportunities to balance these advantages and generate flexible, efficient, and scalable filters for joint parameter-state identification of complex nonlinear structural systems. These techniques, commonly referred to as variational inference, infer the hidden states of a system by attempting to match the true posterior and to a parameterized distribution. In this study we build on the theory of automatic differentiation variational inference to introduce a novel approach to variational filtering for the identification of complex structural systems. We evaluate our method using experimental observations from a nonlinear energy sink device subject to base excitation. Comparison between identification performed using our approach and the unscented Kalman filter reveals the utility of the variational filtering technique in terms of both flexibility in the stochastic model and robustness of the method to poor specification of prior uncertainty.

Keywords System identification · Nonlinear energy sink · Bayesian inference · Unscented Kalman filter · Variational inference

7.1 Introduction

Bayesian filtering approaches have become a powerful tool in predictive structural modeling as they provide a useful framework for interpreting damage and projecting system behavior under the various sources of uncertainty typical in practical structural systems. Current research typically emphasizes analytical or sampling approximations to the Bayesian framework, which, respectively, allow for fast approximations under restrictive modeling assumptions or flexible modeling at a steep computational cost. Recent advances in a third class of approximate Bayesian methods, known as *variational inference*, seek to balance the benefits of the analytical and sampling approximations and have been shown to provide a useful and comparatively efficient alternative to sampling techniques for problems involving complex computational models or large datasets [1].

Research into the adaptation of variational inference for time-series identification problems has most notably resulted in the work of Smidl and Quinn [2], who developed variational Bayesian filtering. Through this approach they coupled variational inference with the particle filter to infer the hidden states of generalized dynamical systems. Other works in this area have coupled variational inference with Kalman filter variants [3, 4]. Each of these approaches has shown some success on computational examples, though their validation on experimental systems with high levels of uncertainty remains to be seen.

A. Lund (✉) · I. Bilionis ·
School of Mechanical Engineering, Purdue University, West Lafayette, IN, USA
e-mail: alund15@purdue.edu; ibilion@purdue.edu

S. J. Dyke
School of Mechanical Engineering, Purdue University, West Lafayette, IN, USA

Lyles School of Civil Engineering, Purdue University, West Lafayette, IN, USA
e-mail: sdyke@purdue.edu

Z. Mao (eds.), *Model Validation and Uncertainty Quantification, Volume 3*, Conference Proceedings of the Society for Experimental Mechanics Series, https://doi.org/10.1007/978-3-031-04090-0_7

In this work, we examine the performance of a novel variational filter (VF) on the identification of an experimental nonlinear energy sink device. The proposed VF steps beyond previous filtering implementations by using state-of-the-art advances in variational inference, such as automatic differentiation variational inference (ADVI) [5] and KL-annealing [6], to enhance modularity and efficiency of the stochastic optimization process. The performance of the proposed filter and its robustness to experimenter uncertainty in the specification of the prior is benchmarked against that of the unscented Kalman filter (UKF).

7.2 Background

The VF algorithm proposed in this study operates in a two-step process aligned with the Bayesian filtering equations for the development of the marginal prior

$$p\left(\mathbf{x}_k, \boldsymbol{\theta} | \mathbf{y}_{1:k-1}, \mathbf{u}_{0:k-1}\right) = \int p\left(\mathbf{x}_k | \mathbf{x}_{k-1}, \boldsymbol{\theta}, \mathbf{u}_{k-1}\right) p\left(\mathbf{x}_{k-1}, \boldsymbol{\theta} | \mathbf{y}_{1:k-1}, \mathbf{u}_{0:k-2}\right) d\mathbf{x}_{k-1}, \tag{7.1}$$

and the marginal posterior

$$p\left(\mathbf{x}_k, \boldsymbol{\theta} | \mathbf{y}_{1:k}, \mathbf{u}_{0:k-1}\right) = \frac{p\left(\mathbf{y}_k | \mathbf{x}_k, \boldsymbol{\theta}\right) p\left(\mathbf{x}_k, \boldsymbol{\theta} | \mathbf{y}_{1:k-1}, \mathbf{u}_{0:k-1}\right)}{p\left(\mathbf{y}_k | \mathbf{y}_{1:k-1}, \mathbf{u}_{0:k-1}\right)}, \tag{7.2}$$

where $\mathbf{x}_k$ are the latent system states, $\boldsymbol{\theta}$ are the constant model parameters, $\mathbf{y}_k$ are the system observations, and $\mathbf{u}_k$ are the open-loop control inputs, measured at the discrete time intervals $t_k = k\Delta t$, where $k = 1, \ldots, \mathrm{K}$. Approximations of the marginal prior and posterior are generated at each filtering step over the batch of observation data $\mathcal{B}_i$. As shown in Fig. 7.1, the marginal prior is approximated by propagating Monte Carlo samples from the posterior of the states in $\mathcal{B}_{i-1}$ to describe the prior uncertainty over the states in $\mathcal{B}_i$. The approximate marginal posterior on $\mathcal{B}_i$ is then developed through ADVI, in which the family of distributions $g_{\mathcal{B}_i}\left(\mathbf{x}_{\mathcal{B}_i}, \boldsymbol{\theta}; \boldsymbol{\phi}\right)$ is optimized against the Kullback-Leibler divergence toward the true marginal posterior.

The performance of the proposed variational filter is compared against that of the UKF [7] in the identification of the states and parameters of an experimental nonlinear energy sink device, which can be modeled by the dynamic equation of motion

$$m\ddot{x} + c_v\dot{x} + c_f \tanh\left(200\dot{x}\right) + kx + zx^3 = -m\ddot{x}_g. \tag{7.3}$$

For the identification problem, the system mass m is assumed known at 0.6637 kg, whereas the viscous damping coefficient (c_v Ns/m), friction damping coefficient (c_f N), stiffness coefficient (k N/m), and nonlinear stiffness coefficient (z N/m^3) are unknown parameters which will be inferred in conjunction with the states. Observations of the system response to a sine wave input with linearly varying amplitude are made in terms of its relative displacement (x) and absolute acceleration ($\ddot{x} + \ddot{x}_g$).

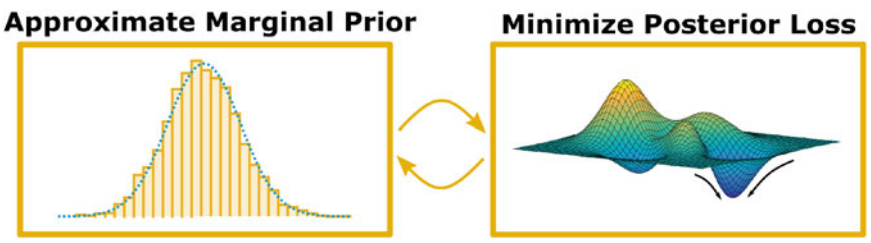

Fig. 7.1 Representation of the operation of the proposed variational filter

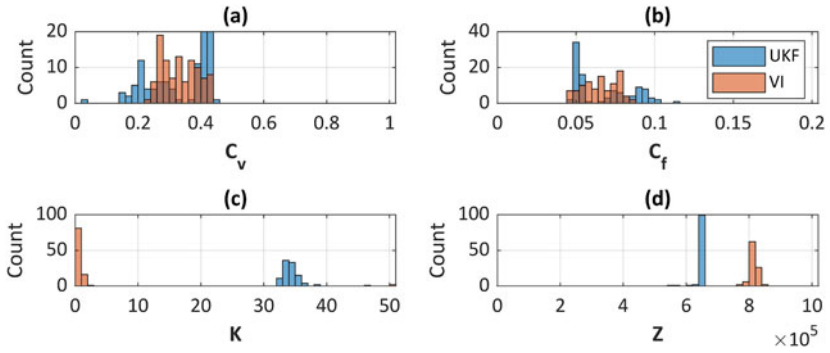

Fig. 7.2 Modes of the (**a**) viscous damping, (**b**) friction damping, (**c**) linear stiffness, and (**d**) nonlinear stiffness for the 100 identified models

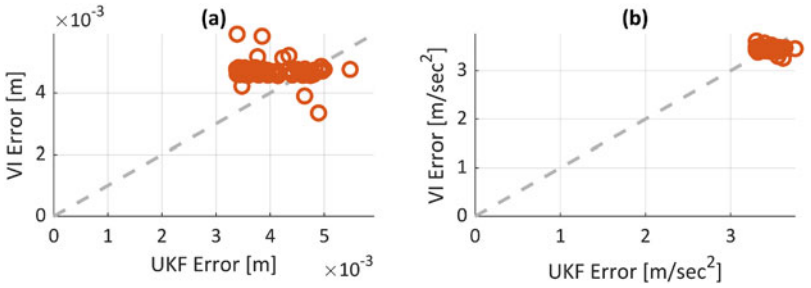

Fig. 7.3 Error in the simulated (**a**) displacement and (**b**) acceleration responses developed from the 100 candidate models

7.3 Analysis

Our objective is to investigate the extent to which variability in the prior distribution produces variability in the candidate model obtained from the Bayesian identification algorithm. To this end, we compare the relative performance of the VF and UKF algorithms on a series of inference trials run using 100 possible prior distributions on the parameters. These distributions were selected to represent the variability with which different experimentalists might approach the specification of prior uncertainty. The results of these inference trials are given with respect to the modes of the posterior distributions on the parameters (Fig. 7.2) and the root-mean-square (RMS) error of the simulated displacement and acceleration responses of the generated candidate models over the observed system responses (Fig. 7.3).

The results in Fig. 7.2 show a similar concentration in the parameters developed through the candidate models between the VF an UKF approaches. Though the algorithms generate different interpretations of the stiffness parameters, these differences do not correlate to large differences in the resulting RMS error values, as one might expect. Rather, these results demonstrate the gap between the computational model form selected for the experimental system and the actual response behavior of that system. Both approaches employ slightly different modeling assumptions and tune the identification process for slightly different objectives, resulting in two high-quality, but different, calibrated models.

7.4 Conclusion

The results of this study reveal that the proposed VF algorithm experiences similar levels of success in identification as the more commonly used UKF, though the two converge to different high-quality models. The key functional difference between these algorithms in the identification of models of similar complexity to the nonlinear energy sink system described herein then becomes their respective computational efficiencies, where the UKF currently runs orders of magnitude faster the VF. This computational constraint in the VF has the potential for improvement in future work.

Acknowledgments We gratefully acknowledge support from NASA's Space Technology Research Grant Program, Grant #80NSSC19K1076.

References

1. Blei, D.M., Kucukelbir, A., Mcauliffe, J.D.: Variational inference: a review for statisticians. J. Am. Stat. Assoc. **112**, 859–877 (2017). https://doi.org/10.1080/01621459.2017.1285773
2. Šmídl, V., Quinn, A.: Variational Bayesian filtering. IEEE Trans. Signal Process. **56**, 5020–5030 (2008). https://doi.org/10.1109/TSP.2008.928969
3. M.J. Beal, Z. Ghahramani, The Variational Kalman Smoother, 2001
4. Auvinen, H., Bardsley, J.M., Haario, H., Kauranne, T.: The variational Kalman filter and an efficient implementation using limited memory BFGS. Int. J. Numer. Methods Fluids. **64**, 314–335 (2010). https://doi.org/10.1002/fld
5. Kucukelbir, A., Tran, D., Ranganath, R., Gelman, A., Blei, D.M.: Automatic differentiation variational inference. J. Mach. Learn. Res. **18**, 430–474 (2017)
6. Huang, C.W., Tan, S., Lacoste, A., Courville, A.: Improving explorability in variational inference with annealed variational objectives. Adv. Neural Inf. Proces. Syst. **2018**, 9701–9711 (2018)
7. Wan, E.A., Van Der Merwe, R.: The unscented Kalman filter for nonlinear estimation. In: IEEE 2000 Adaptive Systems for Signal Processing, Communications, and Control Symposium, pp. 153–158. IEEE, Lake Louise, Alberta, Canada (2000)

Chapter 8
Optimal Sensor Configuration Design for Virtual Sensing in a Wind Turbine Blade Using Information Theory

Tulay Ercan, Konstantinos Tatsis, Victor Flores Terrazas, Eleni Chatzi, and Costas Papadimitriou

Abstract Optimal sensor placement (OSP) strategies in complex engineering systems aim to maximize the information gain from data by optimizing the location, type and number of the sensors or the actuators. It is used as a guide for assessing the structural condition, detecting damages and supporting the decision-making regarding structural health, safety and performance. In this work, a Bayesian optimal experimental design framework is used to optimize the type, location and number of sensors in composite wind turbine blades (WTB) excited by wind loads. The framework is based on a modal expansion technique for virtual sensing under output-only vibration measurements and on information theory for quantifying the information contained in a sensor configuration. The optimal sensor configuration optimizes a utility function associated with the expected Kullback-Leibler divergence (KL-div) between the prior and posterior distribution of the predictions at the virtual sensing (Ercan and Papadimitriou, Sensors 21:3400, 2021). The design variables include the location, type and number of sensors.

Keywords Bayesian optimal experimental design · Information gain · Virtual sensing · Modal expansion · Wind turbines

8.1 Analysis

Employing the Gaussian nature of the response estimates for a linear model of the WTB, the utility function is formulated in terms of the prior and posterior covariance matrices of the error in the estimates of the response predictions. The optimal sensor placement theory and tools are presented in reference [1]. Specifically, using the expected KL-div between the prior and posterior distribution of the output quantities of interest (QoI) to be reliably predicted using the measurements, the utility function which quantifies the information gained from a sensor configuration is finally derived in the form

$$U\left(\underline{\delta}\right) = -\frac{1}{2}\sum_{i=1}^{n_z} \ln\left[\underline{\psi}_i^T\left[\Phi^T L^T\left(\underline{\delta}\right) Q_e^{-1}\left(\underline{\delta}\right) L\left(\underline{\delta}\right)\Phi + S^{-1}\right]^{-1}\underline{\psi}_i + Q_{\varepsilon_i}\right] / \left[\underline{\psi}_i^T S\underline{\psi}_i + Q_{\varepsilon_i}\right] \tag{8.1}$$

where $\Phi \in R^{n \times m}$ is the full displacement modeshape matrix associated with all degrees of freedom (DOF) of the model, $L\left(\underline{\delta}\right)$ is the observation matrix that maps the displacements at all n DOF to the measured displacement or strain quantities indicated in the sensor location vector $\underline{\delta} \in R^{N_0}$ containing the sensor "location" information (DOF for displacement sensors; positions and directions for strain sensors), $\underline{\psi}_i$ is the i-th row of the modeshape matrix $\Psi \in R^{n_z \times m}$ associated with the type of predictions (e.g. strain modeshapes for the case of strain predictions), $\Psi \in R^{n_z \times m}$ contains the modeshape components at the

T. Ercan · C. Papadimitriou (✉)
Department of Mechanical Engineering, University of Thessaly, Volos, Greece
e-mail: ercan@uth.gr; costasp@uth.gr

K. Tatsis · E. Chatzi
Department of Civil, Environmental and Geomatic Engineering, Institute of Structural Engineering, Zürich, Switzerland
e-mail: tatsis@ibk.baug.ethz.ch; chatzi@ibk.baug.ethz.ch

V. F. Terrazas
Department of Civil and Environmental Engineering, The Hong Kong University of Science and Technology, Hong Kong, China
e-mail: vft@connect.ust.hk

Z. Mao (eds.), *Model Validation and Uncertainty Quantification, Volume 3*, Conference Proceedings of the Society for Experimental Mechanics Series, https://doi.org/10.1007/978-3-031-04090-0_8

n_z locations where predictions are made, m is the number of contributing modes and N_0 is the number of sensors involved in the sensor configuration. The quantity $Q_e = s^2 I + \sigma_e^2 \tilde{Q}_y$ represents the covariance matrix of the total predictions error with s accounting for the intensity of the measurement error and σ_e accounting for the intensity of the model error with respect to the intensity of the responses at the measured locations, and $\tilde{Q}_y$ is the diagonal matrix containing at the diagonals the variances of the measured responses $\underline{y}(t) \in R^{N_0}$ at the measured locations. The quantity $Q_{\varepsilon_i} = \sigma_\varepsilon^2 \tilde{Q}_{z_i}$ denotes the variance of the prediction error expected for the predicted response quantity $z_i(t)$, where $\tilde{Q}_{z_i}$ is the diagonal matrix containing at the diagonals the variances of the predicted time history $z_i(t)$. The quantity $S = \alpha^2 \tilde{Q}_\xi$ is the covariance of the prior distribution assumed for the modal quantities $\underline{\xi}(t)$, where α quantifies the extent of uncertainty in the prior distribution. The optimal $\underline{\delta}$ is selected as the one that maximizes $U\left(\underline{\delta}\right)$. Both a genetic algorithm (GA) and alternative heuristic sequential sensor placement (SSP) algorithms are used to solve the optimization problem in an effort to provide computationally efficient solutions.

8.2 Application

The OSP methodology is applied to a small-scale composite WTB structure. The structure with its structural and geometrical properties as well as the monitoring campaign performed at ETH Zurich is presented in detail in references [2, 3]. A simple representation of the WTB can be seen in Fig. 8.1. The blade model is fixed at the left edge and the outer surface consists of 6189528 nodes and 242930 six-degree-of freedom thin shell elements. OSP analysis is performed to optimize the location and number of strain sensors for strain response prediction on the locations marked with red dots in Fig. 8.1. For illustration purposes, it is assumed that the blade is subjected to a point load defined as a white noise input with a sampling period $\Delta t = 0.0025$ sec at the location shown in Fig. 8.1. The OSP design is performed assuming eight contributing modes. Model and measurement error parameters σ_e and s (see [1] for details) are selected according to the intensities of responses (of the observed QoI) and given in Table 8.1 with the prior parameter α and the prediction error parameter $\sigma_\varepsilon = \sigma_e$. The values in Table 8.1 correspond to small model error of the order of 1%, as well as medium to small measurement error ranging from 20% to 0.4% measurement error for the minimum and maximum reported strain in the structure.

The OSP results for strain sensors are presented in Fig. 8.2. The expected information gain (utility values) as a function of the number of sensors placed at their optimal (or worst) locations is shown in Fig. 8.2a, while the optimal positions of eight sensors are shown in Fig. 8.2b. The maximum utility value ($U_{max} = 9.17$) which can be reached with 245 strain sensors is shown as a grey horizontal line in Fig. 8.2a. For less than eight sensors (the number of contributing modes), the problem of OSP is unidentifiable, and subjective information for placing sensors is borrowed from the prior PDF.

As a result, the information gain for a configuration up to 7 sensors is significantly less than the maximum information gain that can be achieved with 245 strain sensors uniformly spread over the blade surface. Including eight sensors in the sensor configuration leads to a sharp increase in the information gain, reaching a value which is very close to the maximum information gain. Adding more than eight sensors at the optimal locations results in a relatively small increase in information gain. From the optimal sensor configuration results in Fig. 8.2b, it can be seen that the strain sensors are well distributed along the blade for reliable response prediction. For validation purposes, strain responses at the 245 locations shown in Fig. 8.1 are predicted from the modal expansion technique by using the best, worst and an arbitrary sensor configuration, all involving eight sensors. For this, simulated measurement data are generated at all 245 strain locations using white noise input

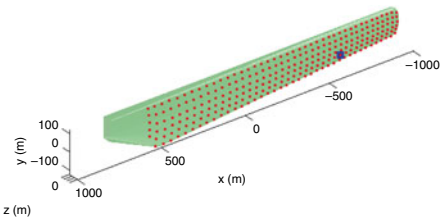

Fig. 8.1 Location of input (blue), predictions and possible sensors (red)

Table 8.1 Prior, prediction error, model and measurement error parameters

Sensor type	α	σ_ε	σ_{em}	s	$\sim s/\varepsilon_{min}$	$\sim s/\varepsilon_{max}$
Strain	10^2	10^{-2}	10^{-2}	10^{-7}	2×10^{-1}	4×10^{-3}

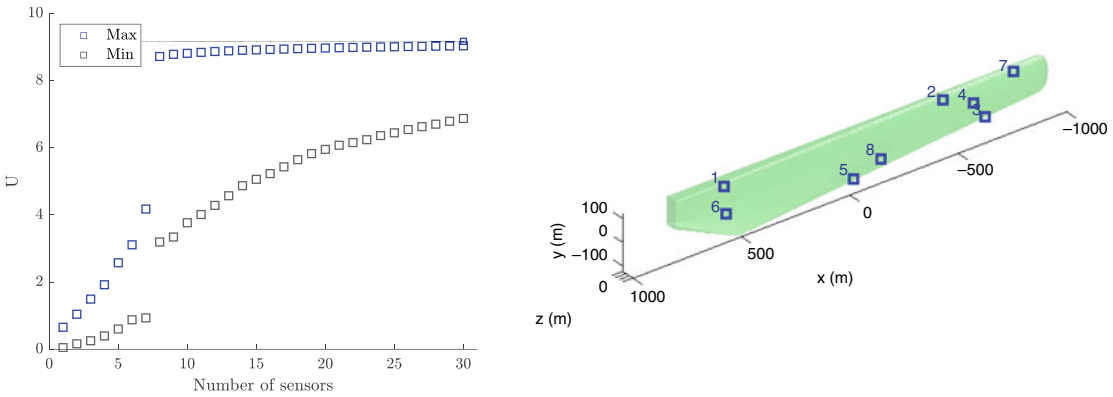

Fig. 8.2 OSP results – utility values (**a**), best sensor positions (**b**)

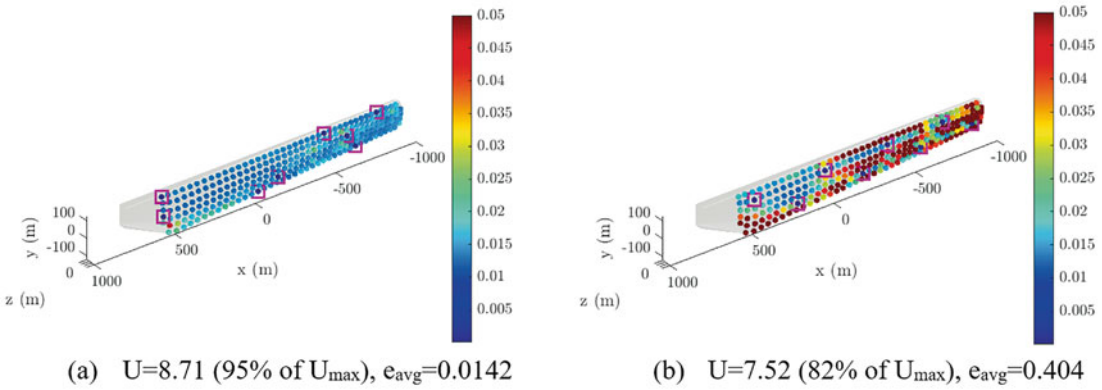

Fig. 8.3 Relative error in response prediction locations using best (**a**) and arbitrary (**b**) sensor locations. Magenta shows measured locations

at the input location shown in Fig. 8.1. 1% of the intensity of the strains is added as Gaussian noise in the simulated response time histories to include model and measurement error. Given these simulated measurements, the OSP methodology is used to predict responses in measured and unmeasured locations from the three different sensor configurations involving eight strain sensors. Relative root mean square (RRMS) errors between the predictions and the simulated measurements for the two sensor configurations (with their utility values) are presented in Fig. 8.3.

Very good predictions with average RRMS error equal to 0.0142 and maximum RRMS error less than 0.03 are obtained with the optimal sensor configuration. With the worst sensor locations, the average RRMS error (not shown in the figure) in the unmeasured locations is 180%, much higher than the one found with the best locations. The results also indicate that the selected arbitrary sensor layout, corresponding to a utility value that is approximately 20% less than the utility value for the optimal sensor configuration, also give a higher average RRMS error of 40% in the response prediction in the unmeasured locations.

8.3 Conclusions

The OSP approach is applicable for studying the effects of uncertainties in measurement and model errors, the temporal and spatial distribution of loads and the prior distribution on the optimal sensor configuration design. These studies are important to demonstrate the capabilities of the proposed OSP framework for WTB operating in a highly dynamic and uncertain environment. The proposed framework is applicable to optimize the experimental design for a wide variety of systems that require comprehensive use of limited resources in the experiment due to the high cost of maintenance and inspection.

Acknowledgements This project has received funding from the European Union's Horizon 2020 research and innovation programme under the Marie Skłodowska-Curie grant agreement No 764547.

References

1. Ercan, T., Papadimitriou, C.: Optimal sensor placement for reliable virtual sensing using modal expansion and information theory. Sensors. **21**(10), 3400 (2021)
2. Ou, Y., Tatsis, K.E., Dertimanis, V.K., Spiridonakos, M.D., Chatzi, E.N.: Vibration-based monitoring of a small-scale wind turbine blade under varying climate conditions. Part I: an experimental benchmark. Struct. Control. Health Monit. **28**(6), e2660 (2021)
3. Tatsis, K., Ou, Y., Dertimanis, V.K., Spiridonakos M.D., Chatzi, E.N.: Vibration-based monitoring of a small-scale wind turbine blade under varying climate and operational conditions. Part II: a numerical benchmark. Struct. Control. Health Monit. **28**, e2734 (2021)

Chapter 9
Probability Bounds Analysis Applied to Multi-purpose Crew Vehicle Nonlinearity

Daniel C. Kammer, Paul Blelloch, and Joel Sills

Abstract The Multi-purpose Crew Vehicle (MPCV) Program Orion finite element model (FEM) was updated based on a modal test performed by Lockheed Martin. Due to nonlinearity observed in the test results, linear low force level (LL) and high force level (HL) FEMs were developed for use during various Space Launch System (SLS) flight regimes depending on expected forcing levels. Uncertainty models were derived for the combined MPCV and MPCV Stage Adaptor LL and HL Hurty/Craig-Bampton (HCB) components based on the MPCV structural test article Configuration 4 modal test-analysis correlation results. Subsequently, system-level uncertainty quantification analyses were performed using both models for various SLS flight configurations to determine the impact of the nonlinearity on important system metrics. The system metrics included both transfer functions associated with attitude control and dynamic loads associated with aerodynamic buffeting during ascent. In each case, an independent Monte Carlo (MC) analysis was performed, and no attempt was made to combine the results. The hybrid parametric variation (HPV) method was used to develop the LL and HL MPCV HCB uncertainty models. The HPV method provides both parametric and non-parametric components of uncertainty. The non-parametric uncertainty accounts for the difference in model form between the linearized analytical model and the corresponding linearized component test results in the form of mode shapes and frequencies at that force level. This linear model-form uncertainty is implemented in the HPV method using random matrix theory. However, the HPV uncertainty models developed for the linear LL and HL MPCV components do not account for the nonlinearity in the MPCV. With respect to the linearized models, this nonlinearity is also an uncertainty in model form, but in this case, it must be treated independently as an epistemic uncertainty. It represents a lack of knowledge, in contrast to an aleatory uncertainty due to the randomness of a variable. In the case of an epistemic variable, the true value is unknown, only the interval within which it lies is known. Epistemic uncertainty can be reduced with increased knowledge, while in general, aleatory uncertainty cannot. This work combines the epistemic uncertainty due to the MPCV nonlinearity with the parametric and non-parametric uncertainty within the HPV method using a second-order propagation approach. The LL and HL test data is augmented with surrogate test data derived from a nonlinear MPCV representation. The impact of the MPCV nonlinearity on system response statistics is determined using a series of cumulative distribution functions in the form of a horsetail plot, or p-box. This results in an interval of probabilities for a specific response value or an interval of response values at a specific probability.

Keywords Uncertainty quantification · Hurty/Craig-Bampton · Random matrix · Model form

Acronyms

C4	Configuration 4
CCDF	Complementary cumulative distribution function
CDF	Cumulative distribution function
CLA	Coupled loads analysis
CMA	Crew module adapter

D. C. Kammer (✉) · P. Blelloch
ATA Engineering, Inc, San Diego, CA, USA
e-mail: daniel.kammer@wisc.edu; paul.blelloch@ata-e.com

J. Sills
NASA Johnson Space Center, Houston, TX, USA
e-mail: joel.w.sills@nasa.gov

Z. Mao (eds.), *Model Validation and Uncertainty Quantification, Volume 3*, Conference Proceedings of the Society for Experimental Mechanics Series, https://doi.org/10.1007/978-3-031-04090-0_9

CS	Core stage
dB	Decibel
DCGM	Diagonal cross-generalized mass
DOF	Degree of freedom
FI	Fixed-interface
FEM	Finite element model
HCB	Hurty/Craig-Bampton
HL	High load
HPV	Hybrid parametric variation
Hz	Hertz
itRGA	Intertank rate gyro assembly
lbf	Pound force
lbf-in	Pound-force inch
LAS	Launch abort system
LL	Low load
MC	Monte Carlo
MPCV	Multi-purpose Crew Vehicle
MSA	MPCV Stage Adapter
PDF	Probability distribution function
QOI	Quantity of interest
RMS	Root mean square
SLS	Space Launch System
SOP	Second-order propagation
UQ	Uncertainty quantification

9.1 Introduction

The Multi-Purpose Crew Vehicle (MPCV) Program Orion finite element model (FEM) was updated based on a modal test performed at the Lockheed Martin facility in Denver, from October 2017 to July 2018. Due to nonlinearity observed in the test results, linear low force level (LL) and high force level (HL) FEMs were developed for use during various Space Launch System (SLS) flight regimes depending on expected forcing levels. Uncertainty models were developed for the combined MPCV and MPCV Stage Adaptor (MSA) LL and HL Hurty/Craig-Bampton (HCB) [1] components based on the MPCV structural test article (STA) Configuration 4 (C4) modal test-analysis correlation results. Subsequently, system-level uncertainty quantification (UQ) analyses were performed using both models for various SLS flight configurations to determine the impact of the nonlinearity on important system metrics. The system metrics included both transfer functions associated with attitude control at 120 s after liftoff and dynamic loads associated with aerodynamic buffeting at 50 s after liftoff. In each case, an independent Monte Carlo (MC) analysis was performed, and no attempt was made to combine the results.

The hybrid parametric variation (HPV) method [2–4] was used to develop the LL and HL MPCV/MSA HCB uncertainty models. The HPV method provides both parametric and non-parametric components of uncertainty. The non-parametric uncertainty accounts for the difference in model form between the linearized analytical model and the corresponding linearized component test results in the form of mode shapes and frequencies at that force level. This linear model-form uncertainty is implemented within the HPV method using random matrix theory. The parametric part of HPV treats the modal frequencies as uncertain parameters and layers that on top of the random matrices. However, the HPV uncertainty models developed for the linear LL and HL MPCV/MSA components do not directly account for the nonlinearity observed in the MPCV. With respect to the linearized models, this nonlinearity can be considered an uncertainty in model form, but in this case, it must be treated independently as an epistemic uncertainty since the structure will be exercised at a range of input levels during flight. It represents a lack of knowledge, in contrast to an aleatory uncertainty due to the randomness of a variable. In the case of an epistemic variable, the true value is unknown, only the interval within which it lies is known. Epistemic uncertainty can be reduced with increased knowledge, while in general, aleatory uncertainty cannot. In an MC analysis, an aleatory variable is sampled according to a designated probability distribution, while an epistemic variable cannot, not even when using a uniform distribution [5, 6]. Doing so can produce incorrect and misleading results [5].

This work combines the epistemic uncertainty due to the MPCV nonlinearity with the parametric and non-parametric uncertainty within the HPV method using a second-order propagation approach (SOP). Initially, only the LL and HL test data are considered in the analysis. However, the LL and HL test data are then augmented with surrogate test data derived from a simulation using a nonlinear MPCV representation. The impact of the MPCV nonlinearity on system response statistics is determined through the use of a series of cumulative distribution functions (CDF) in the form of a horsetail plot, or p-box. This results in an interval of probabilities for a specific response value or an interval of response values at a specific probability.

9.2 Combining Epistemic and Aleatory Uncertainty

Epistemic and aleatory variables can be combined within a single UQ analysis using an SOP approach [6, 7]. Within this technique, there are two loops, as shown in Fig. 9.1. In the outer loop, the epistemic variables are sampled from within their respective intervals. Their values are then passed as deterministic variables to the inner loop, where the aleatory variables are sampled from their respective probability distributions. For each set of epistemic variable values, an MC analysis is performed on the aleatory variables, resulting in a corresponding CDF for each selected quantity of interest (QOI). The complete UQ analysis produces an ensemble of CDFs, sometimes called a horsetail plot [6]. The interpretation is that each CDF within the ensemble has no relative probability of occurrence, only that each is possible [7]. Bounds on the ensemble of CDFs are called a probability box (p-box) [8]. Figure 9.2 illustrates a general p-box with bounds $L(x)$ and $U(x)$ for uncertain QOI x.

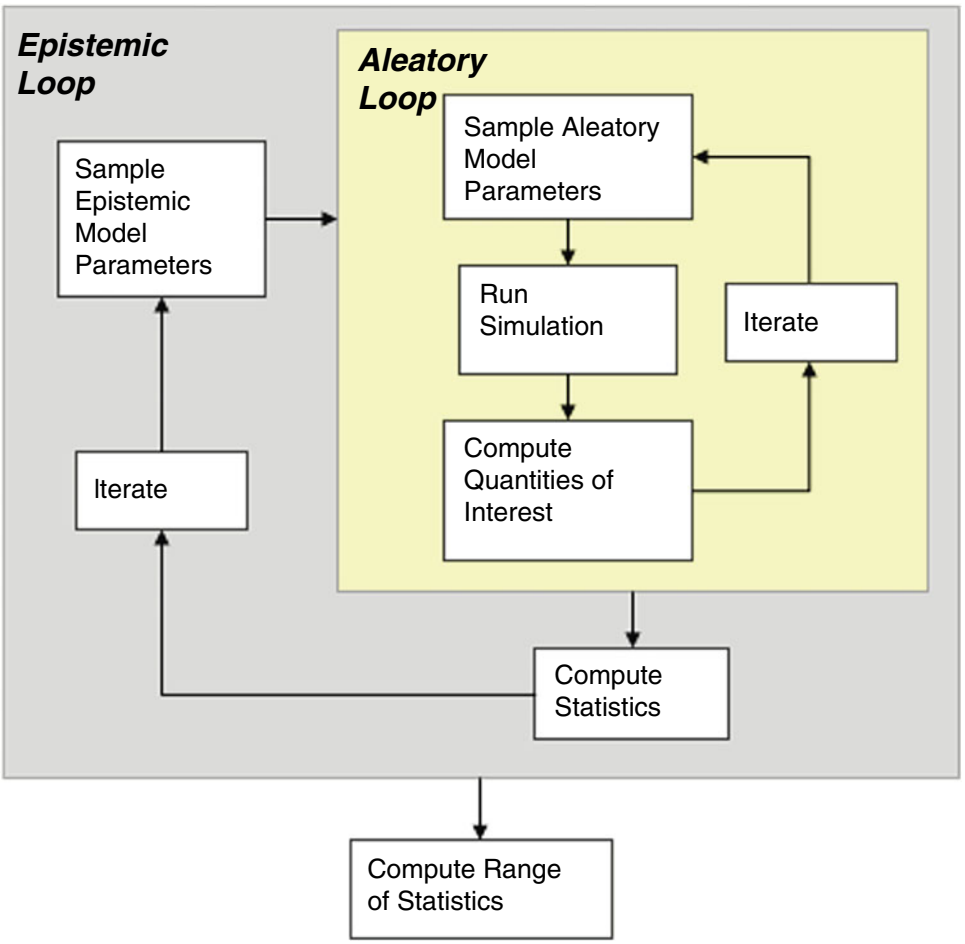

Fig. 9.1 Flow diagram for SOP [8]

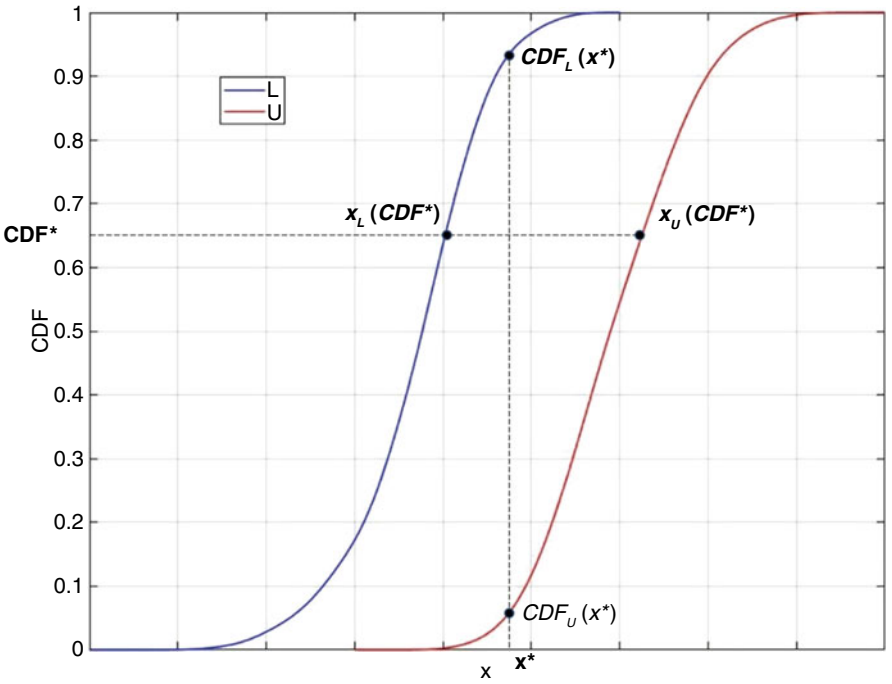

Fig. 9.2 General p-box for uncertain variable x

For a horizontal line drawn at a selected value CDF*, the p-box provides an interval of plausible variable x values. This means that the response at a specific probability level lies within a range of response values, not just at a single value [6]. The CDF value is deterministic, and all the uncertainty is in the variable x [9]. Conversely, for a vertical line at the selected variable value x*, the p-box gives an interval of plausible probabilities. In this case, the variable is deterministic, and the uncertainty lies in the CDF. Combining epistemic and aleatory uncertainty in this fashion determines the range of the QOI that corresponds to a certain percentile and the range of percentiles that corresponds to a specific value of the QOI [8].

9.3 SOP UQ Applied to SLS

In the case of the SLS, the individual HPV UQ assessments are performed using MPCV models that can be thought of as linearizations of the nonlinear model representing the true MPCV. There are no specific epistemic variables that govern the observed nonlinearity or model from uncertainty that can be sampled in the SOP outer loop. Instead, the MPCV nonlinearity can be thought of as being simplistically represented by a slider that gives the mapping from the nonlinear model into the linearized model at a specific forcing level. Discretely adjusting the slider over the forcing level interval of interest would produce an outer loop represented by an ensemble of linear models that approximate the nonlinear model at a corresponding ensemble of input force levels. For each linearized model, the SOP inner loop corresponds to the application the HPV UQ method using an MC analysis. In the case of the MPCV nonlinearity, there are only two members in the ensemble of linearized system models: one containing the LL MPCV and one containing the HL MPCV. Therefore, the SOP consists of two MC analyses, one using the LL system model and one using the HL model. Ideally, these two models would provide CDFs that would bound the effects of the MPCV nonlinearity for the QOIs, but there is no guarantee that is the case.

This method is approximate in the sense that no linear model exactly captures the nonlinear behavior, even at a fixed input level. This is due to the fact that even the behavior of a single degree of freedom system with a nonlinear spring can only be approximated by a linear spring and also because a complex system has many modes, each of which will result in different behavior at nonlinear joints. This is addressed in the current approach by finding the linear model that best captures the nonlinear behavior at each force level and then adding uncertainty to that best fit linear model to represent the fact that it only approximates the nonlinear behavior at that force level.

To perform the system level UQ, the SLS system is broken into five primary "components." These are the two solid rocket booster (SRBs), the core stage, the 2nd stage, and the MPCV/MSA. Uncertainty models based on modal test results are

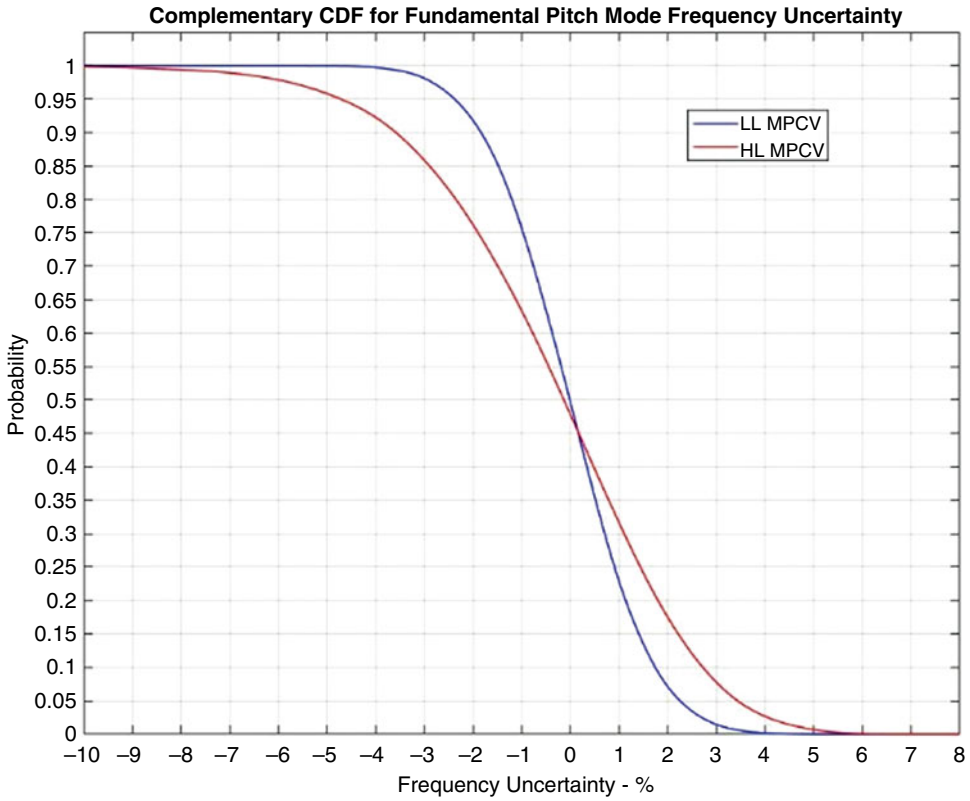

Fig. 9.3 Complementary CDFs for LL and HL MPCV pitch frequency uncertainty

applied to all five components. Details related to these components and their uncertainty models can be found in references [2, 3]. In this work, only the MPCV/MSA component is treated as an epistemic uncertainty to cover nonlinear response.

9.3.1 Guidance Navigation and Control

The first application of the SOP approach is to the guidance, navigation, and control attitude stability conditions for the SLS configuration corresponding to ascent at liftoff T0 + 120 s, prior to booster separation. The uncertainty in the fundamental bending mode frequencies must be greater than −10%, and the corresponding frequency response gain uncertainty must be less than 4 dB to guarantee control system stability. Figure 9.3 shows the complementary CDFs (CCDFs) (i.e., cumulative probability of being greater than) for the uncertainty in the LL and HL fundamental pitch frequencies based on an inner-loop MC analysis with 10,015 iterations. Figure 9.4 presents an expanded view of Fig. 9.3. If a vertical line is drawn at the lower bound for frequency uncertainty (i.e., −10%), then the plausible range in probability is between P99.8 and P100. At a frequency uncertainty of −5%, a vertical line indicates a plausible range in probability of between P95.8 and P100. Conversely, drawing horizontal lines at probability values of P90, P95, and P99 produces plausible ranges of pitch frequency uncertainty, as listed in Table 9.1. These plausible ranges of probability and QOI are due to the model-form uncertainty represented by the linearized LL and HL MPCV models. At the lower bound of allowed frequency uncertainty, the MPCV nonlinearity produces almost no uncertainty.

Figure 9.5 presents the CCDFs for the uncertainty in the LL and HL fundamental yaw bending frequencies. The order of the CCDFs is the opposite of what it was in the case of pitch because the PDF for the LL yaw frequency has a greater standard deviation than that for the HL PDF. The spread in frequency uncertainty between the LL and HL models for yaw is not as great as it is in the case of pitch, shown in Fig. 9.3. If a vertical line is drawn at the lower bound for frequency uncertainty (i.e., −10%), there is no plausible range in probability. If a vertical line is drawn at −5%, the plausible range in probability is between P95.7 and P97.7. Conversely, drawing horizontal lines at probability values of P90, P95, and P99 produces plausible ranges of yaw frequency uncertainty listed in Table 9.2. The plausible ranges of probability and frequency uncertainty for

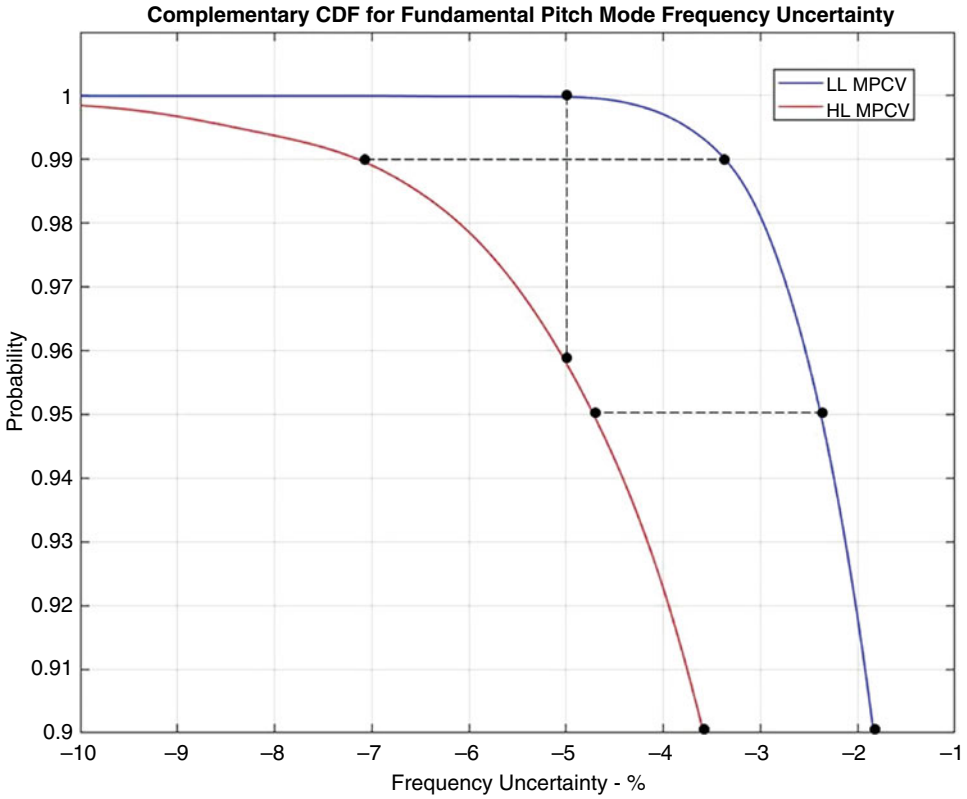

Fig. 9.4 Expanded view of CCDFs for LL and HL MPCV pitch frequency uncertainty

Table 9.1 Plausible range of pitch frequency uncertainty

	Range of uncertainty – %		Delta – %
Probability	HL	LL	abs([HL-LL]/LL)
90	−3.60	−1.85	94.59
95	−4.70	−2.40	95.83
99	−7.15	−3.35	113.43

yaw are smaller than for pitch, indicating that the MPCV nonlinearity has a greater impact on the system fundamental pitch bending frequency than the fundamental yaw bending frequency.

Uncertainty in pitch and yaw rate gains can be examined in the same way. Figure 9.6 illustrates the CDFs for the uncertainty in the pitch rate gain at the core stage intertank rate gyro assembly (itRGA) for the ascent at T0 + 120 s configuration. If a vertical line is drawn at the 4 dB upper bound for gain uncertainty, the corresponding plausible range in probability is between P99.9 and P100. Drawing horizontal lines at probability values of P90, P95, and P99 produces plausible ranges of pitch rate gain uncertainty listed in Table 9.3. Figure 9.7 shows the CDFs for the corresponding uncertainty in the yaw rate gain at the itRGA. In this case, the CDFs do not intersect. Drawing a vertical line at the upper bound of 4 dB uncertainty in gain produces a probability of approximately P98.8. There is essentially no range of plausible probabilities for 4 dB uncertainty in pitch or yaw rate gain. This implies that the MPCV nonlinearity has little impact on the percentile corresponding to the 4 dB rate gain uncertainty stability requirement. Table 9.4 lists the plausible ranges of yaw rate gain uncertainty for probabilities P90, P95, and P99. The widths of the plausible ranges for yaw rate gain are smaller than those for pitch, indicating that the nonlinearity in the MPCV has a smaller impact on yaw rate gain than pitch.

9.3.2 Buffet

An SOP analysis was also applied to the SLS core stage (CS) section loads due to buffet at ascent T0 + 50 s. In the original work, it was found that there were appreciable differences in nominal CS peak moments about Y and in peak shear along

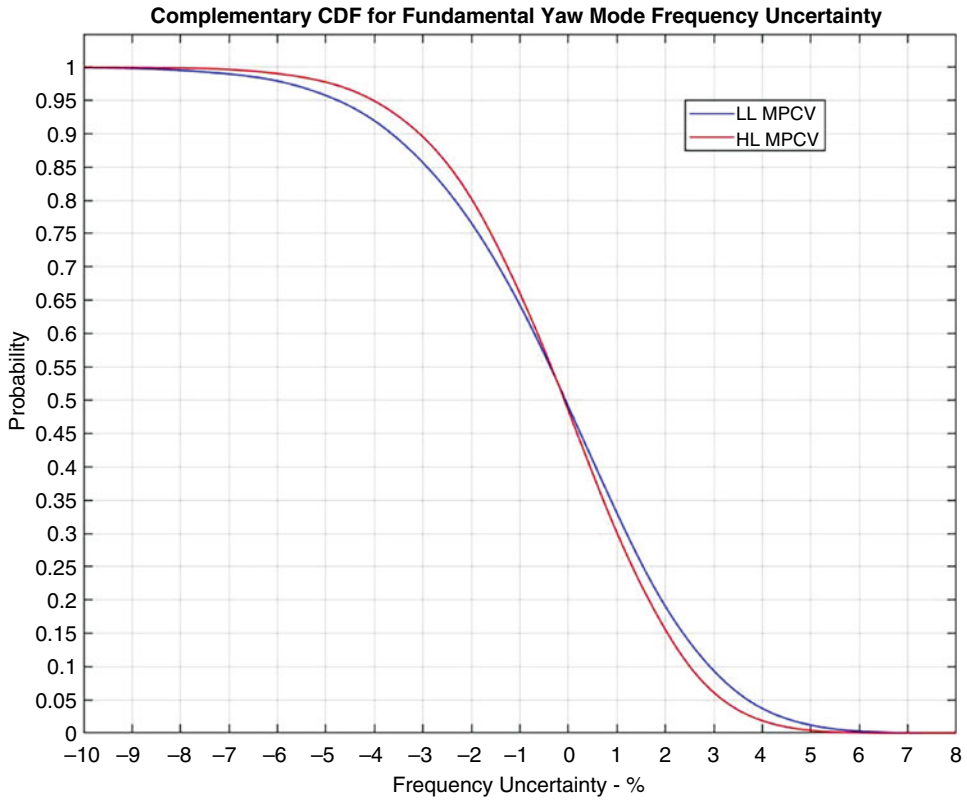

Fig. 9.5 Complementary CDFs for LL and HL MPCV yaw frequency uncertainty

Table 9.2 Plausible range of yaw frequency uncertainty

	Range of uncertainty – %		Delta – %
Probability	LL	HL	abs([HL-LL]/LL)
90	−3.65	−3.05	16.44
95	−4.75	−4.00	15.79
99	−7.05	−6.00	14.89

Z predicted using the LL MPCV model versus the HL MPCV model. The peak moment about Y for the LL MPCV model occurs at section $x = 2754.99$ inches and is approximately 15% higher than that predicted by the HL model. Figure 9.8 illustrates the LL and HL CDFs for the normalized peak moments about Y at $x = 2754.99$ inches for an ensemble of 1000 random systems. No critical value of CS section moment was specified,[1] but as an example, drawing a vertical line at the specific normalized peak moment of 1.4 produces the plausible range of probabilities P34–P95. The MPCV nonlinearity has a large influence on the probability of this specific peak CS moment value. Horizontal lines at probabilities P50 and P90 produce plausible ranges of peak moment about Y listed in Table 9.5.

The peak CS shear along Z occurs at section $x = 2862.71$ inches using the HL MPCV model. It is approximately 11% larger than the value predicted using the LL MPCV. Figure 9.9 presents the LL and HL CDFs for the normalized peak shear along Z. As an example, picking a specific normalized peak shear of 2.4 produces a range of plausible probabilities between P57 and P97. Picking probabilities P50 and P90 yield ranges of peak shear values listed in Table 9.6. Based on these results, the MPCV nonlinearity has a substantial effect upon the statistics for the peak CS moment about Y and the peak CS shear along Z from buffet loading. Percentage wise, the impact is greater on the peak section shear along Z.

[1] Vehicle bending moments during atmospheric flight are typically dominated by static aeroelastic loads and gust, with buffet playing a secondary role. The uncertainty in buffet responses, therefore, does not reflect an equivalent uncertainty in peak bending moments experienced by the vehicle.

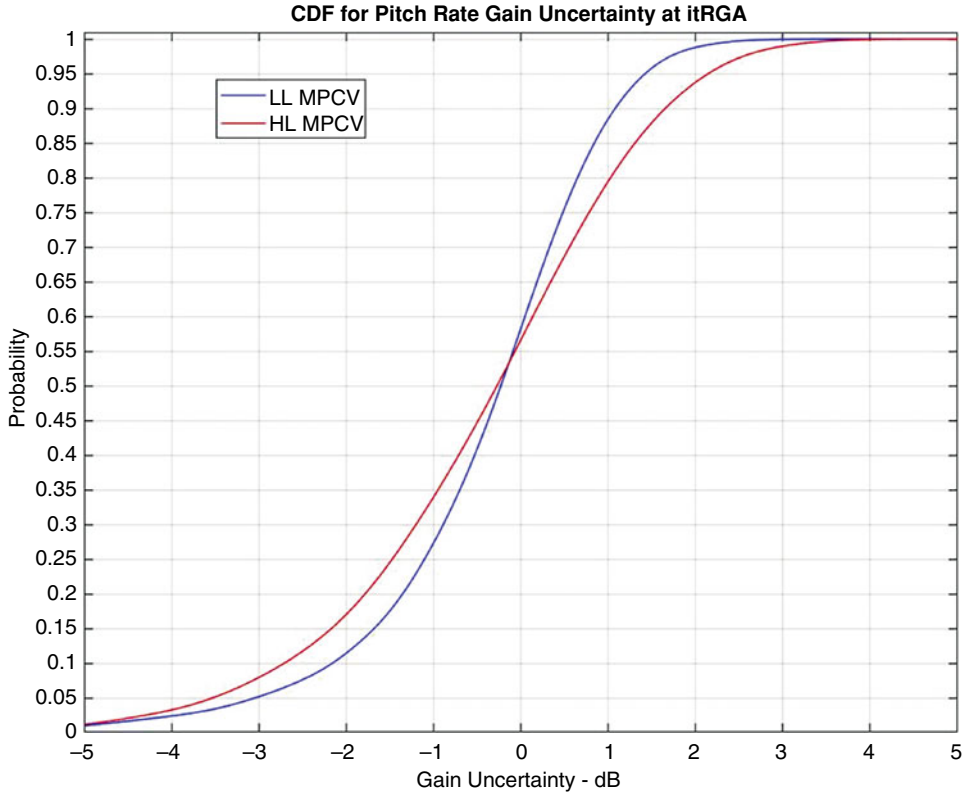

Fig. 9.6 CDFs for LL and HL MPCV pitch rate gain uncertainty

9.4 SOP Analysis of SLS Using Surrogate Test Data

The drawback of the previous analysis is that there are only two sets of C4 test data, one at low input levels and one at high input levels. The two sets of test data were used to generate corresponding LL and HL linear MPCV models. In the LL MPCV model, the nonlinear joints are fixed with respect to relative motion, while in the case of the HL model, they are modeled with relatively low stiffness and are effectively free to slip. The corresponding model ensemble describing the SOP outer loop contains only two models. This results in response horsetail plots that contain only two CDFs, which assumes that the LL and HL responses bound the corresponding p-boxes. While the original program goal was to bound the response of the nonlinear MPCV by using both the LL and HL linear MPCV models, there is no guarantee that this is the case.

Ideally, additional C4 modal test data would have been measured at intermediate loading levels in order to study MPCV nonlinearity. Since this was not done, this work augments the C4 test data with surrogate test data generated using a nonlinear model of the MPCV that captures the friction behavior of the joints. Eight additional linear MPCV models were generated based on simulated response to enforced base sine inputs of amplitudes 0.1, 1, 2, 3, 5, 7.5, 10, and 20 in/s^2. At the input level of 0.1 in/s^2, the nonlinear joints are essentially fixed, as in the LL MPCV. In contrast, at an input level of 20 in/s^2, the joints are freely slipping, as in the HL MPCV. SOP UQ analysis is performed for each of the additional eight models in the ensemble. The goal is to determine how well the LL and HL MPCV models bound the response of the actual nonlinear MPCV based on linearized models.

9.4.1 Generation of Linear MPCV Models Based on Surrogate Test Data

Since actual test data was only available for the LL and HL responses, surrogate test data was developed by running a nonlinear MPCV model. This model was initially based on reducing a NASTRAN FEM to the sliding interfaces along with additional nodes for recovery of responses in an HCB format. This was then transformed to an ABAQUS substructure using the *MATRIX INPUT format. The slipping joints were modeled as 204 *CONNECTOR elements corresponding to

Table 9.3 Plausible range of pitch rate gain uncertainty

	Range of uncertainty – dB		Delta – %
Probability	LL	HL	abs([HL-LL]/LL)
90	1.08	1.64	51.85
95	1.42	2.14	50.70
99	2.07	3.01	45.41

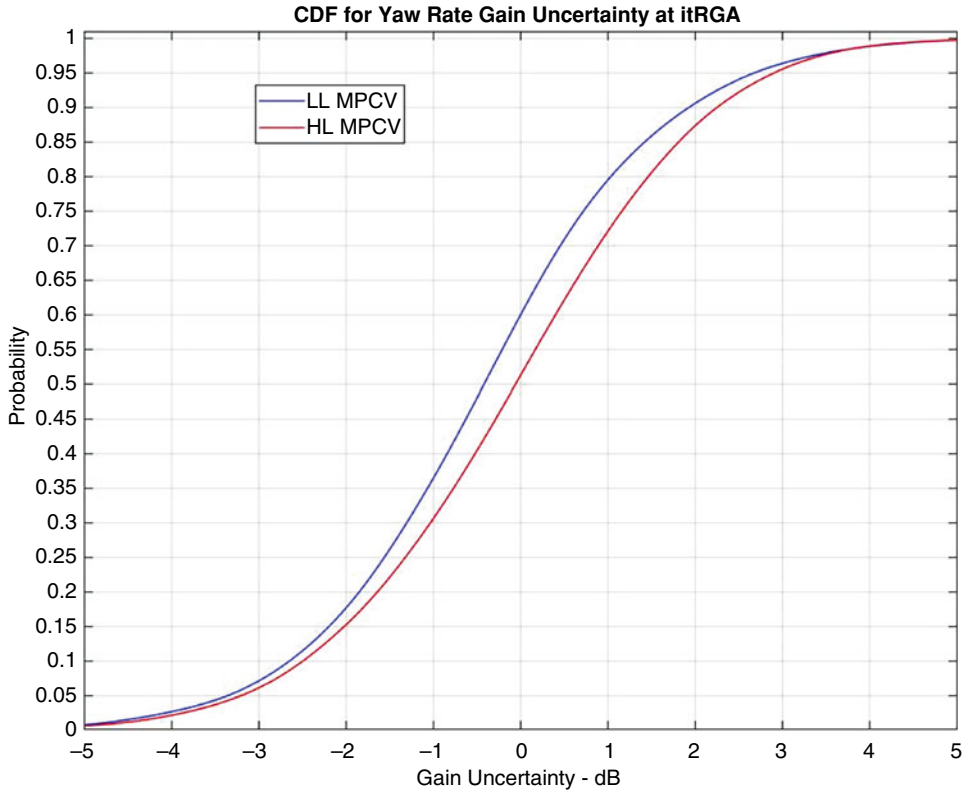

Fig. 9.7 CDFs for LL and HL MPCV yaw rate gain uncertainty

Table 9.4 Plausible range of yaw rate gain uncertainty

	Range of uncertainty – dB		Delta – %
Probability	LL	HL	abs([HL-LL]/LL)
90	1.93	2.25	16.58
95	2.68	2.91	8.58
99	4.10	4.14	0.98

the airfoils between the crew module adaptor (CMA) and fairing and 114 *CONNECTOR elements corresponding to the aerodeflectors between the launch abort system (LAS) and CMA, as illustrated in Fig. 9.10. All other connections were assumed to be linear. Each joint is a two degrees of freedom (DOFs) sliding joint in the 2 and 3 directions. Since all the corresponding elements are defined in a cylindrical coordinate system, this is a joint that's fixed radially and sliding tangentially and vertically.

The ABAQUS connector elements represent a sliding interface like the one illustrated in Fig. 9.11, where K1 is the "sliding stiffness," K2 is the "stick stiffness," and μ is the "friction force," which is the product of the normal force and the coefficient of friction. Different K1, K2, and m values were used for the airfoil and the aerodeflector joints, based on tuning the nonlinear model to modal test results. Note that the ABAQUS connector elements are two-dimensional versions of the system illustrated in Fig. 9.12, since they slide in the tangential/vertical plane. The parameters were originally tuned to approximately fit the nonlinear behavior observed at the LL and HL excitation levels. Initially the goal was to use the ABAQUS model directly and exercise it at different input levels. However, 10 s of simulation took up to 10 days of run time, so it was not feasible to generate the data required for this study using that approach.

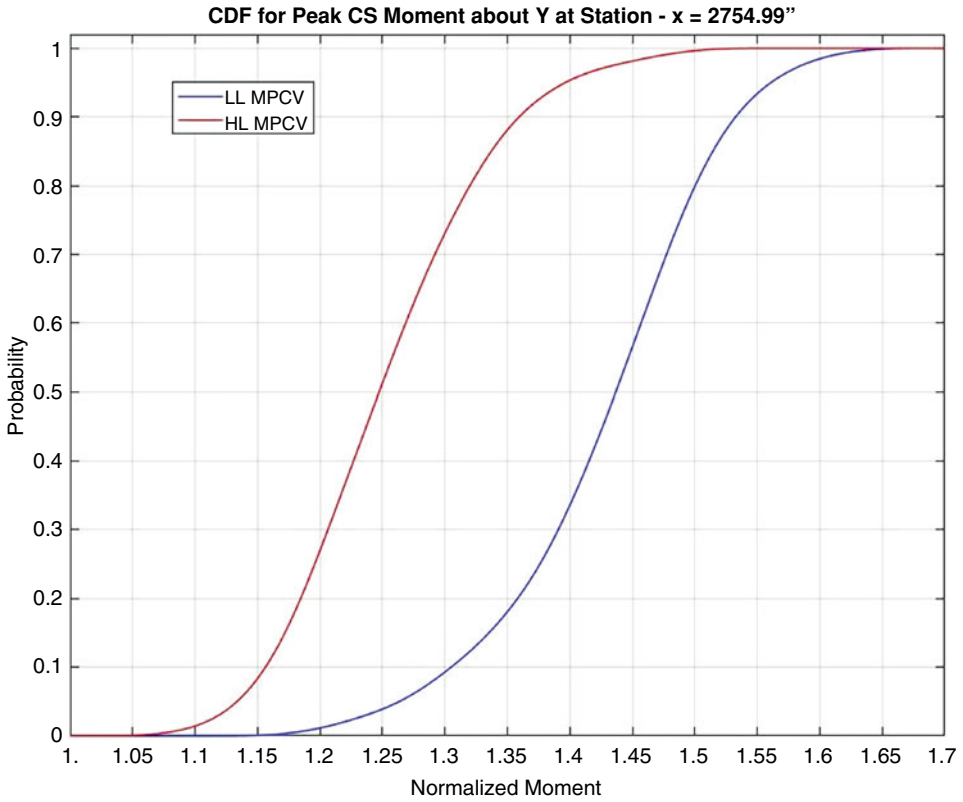

Fig. 9.8 CDFs for LL and HL MPCV peak CS moment about Y at $x = 2754.99$ inches

Table 9.5 Plausible range of peak moment about Y at $x = 2754.99$ inches

	Range – %
Probability	abs([HL-LL]/LL)
50	11.61
90	9.99

An alternate approach was developed using ATA's internal Matlab nonlinear integration algorithm. This code was developed to support coupled loads analysis (CLA) and other dynamic response calculations where local nonlinearities are critical to the response. It uses a Chapman algorithm [10] to integrate the equations along with a user supplied function to represent the nonlinear forces. This approach is based on modal properties calculated in Nastran, with residual vectors at the nonlinear joints to accurately capture local compliance. A user supplied routine was developed and checked that captured the one-dimensional version of the sliding joint illustrated in Fig. 9.11. In this case the sliding stiffness (K1) was included in the Nastran model, while the friction force (μ) and the stick stiffness (K2) were included in the user supplied routine. Each two-dimensional joint was represented by two one-dimensional elements. This is not identical to the representation in ABAQUS, but it captures the observed behavior as the input is increased. A total $2 \times (204 + 114)$ sliding elements were included in the model.

Behavior of the joints was validated by first exercising the function directly and then exercising it in the context of the MPCV model and examining the force/deflection curves over a range of input levels. Force/deflection curves for all the sliding elements at various input levels are illustrated in Fig. 9.12. At the lowest level input, the joints are acting as stiff linear springs, with a spring constant equal to the stick stiffness of each joint. As the input level is increased, each joint travels in a hysteretic loop, with increasing slip, but with a force that never exceeds the friction force in the joint. While the exact behavior of the pairs of one-dimensional joints is a little different from the two-dimensional joint modeled in ABAQUS, the expected behavior from fully stuck to fully sliding and the corresponding shift in frequency was captured using this approach. Run times were reduced to approximately 2 h for 50 s of simulation or a 600X improvement over the ABAQUS run times.

Initially, scaled versions of the random buffet forcing functions were applied at the base of the MPCV to exercise the nonlinear joints at different levels of excitation. However, the random buffet input resulted in very poor frequency response

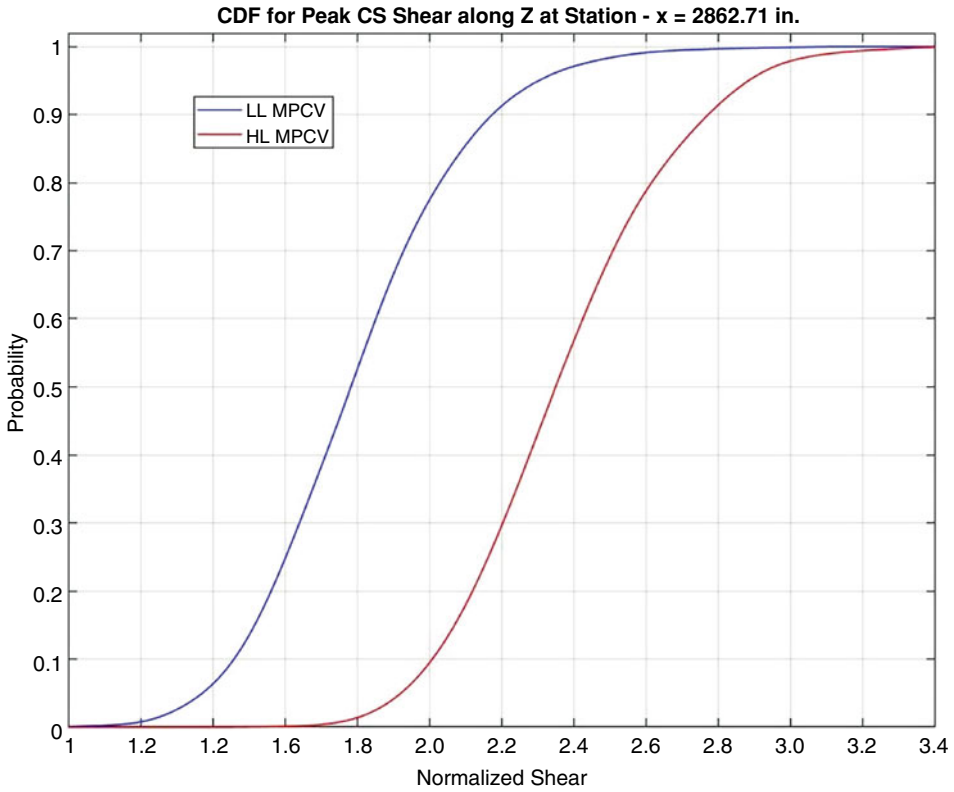

Fig. 9.9 CDFs for LL and HL MPCV peak CS shear along Z at $x = 2862.71$ inches

Table 9.6 Plausible range of peak shear along Z at $x = 2862.71$ inches

	Range – %
Probability	abs([HL-LL]/LL)
50	13.46
90	13.03

function estimates, so a wrapped frequency multi-sine swept input applied as an enforced acceleration in all three directions at the base was used instead. The sweeps are logarithmic from 20 Hz to 1 Hz. The first axis (X) starts at 20 and sweeps down to 1 Hz; the second axis (Y) starts at 8 Hz, sweeps down to 1 Hz, starts back up at 20 Hz, and sweeps down to 8 Hz; the third axis (Z) starts at 3 Hz sweeps down to 1 Hz, starts back up at 20 Hz, and sweeps down to 3 Hz. The signal frequencies vs. time are illustrated in Fig. 9.13. This approach results in three independent signals that can be separated from each to calculate transfer functions from each of the three inputs to 1029 response accelerations on the MPCV.

Each simulation used a constant amplitude sine input as a function of frequency, so the only variation was in the amplitude of the signal. Several different amplitudes were applied to examine the behavior of the joints and find a range of amplitudes that would exercise the joints through their full range. An input amplitude of 0.1 in/s^2 was found to result in linear behavior as illustrated in Fig. 9.12. As the amplitude was increased, modal properties reached asymptotic limits as the input approached roughly 20 in/s^2. Based on this observation, the MPCV nonlinear model was simulated at input amplitudes of 0.1, 1, 2, 3, 5, 7.5, 10, and 20 in/s^2. Transfer functions from the three inputs to 1029 outputs were calculated for each input level. The transfer function from Y input to Y response on the LAS ballast node is illustrated in Fig. 9.14. Results are similar in the X and Z direction.

Next the OPOLY™ modal fitting algorithm was used to estimate a set of linear modes associated with each set of transfer functions. To maintain consistency across force levels, a total of eight modes were fit to each level. These included the 1st axial mode, the 1st four Y-bending modes,[2] and the 1st three Z-bending modes. The variation in frequency of these eight modes as a function of input level is illustrated in Fig. 9.15. The frequency variations were like those observed in

[2] All levels identified a pair of fairly closely spaced bending modes in the Y-direction, which were not observed in the Z-direction, resulting in 4 Y-bending and 3 Z-bending modes in the frequency range.

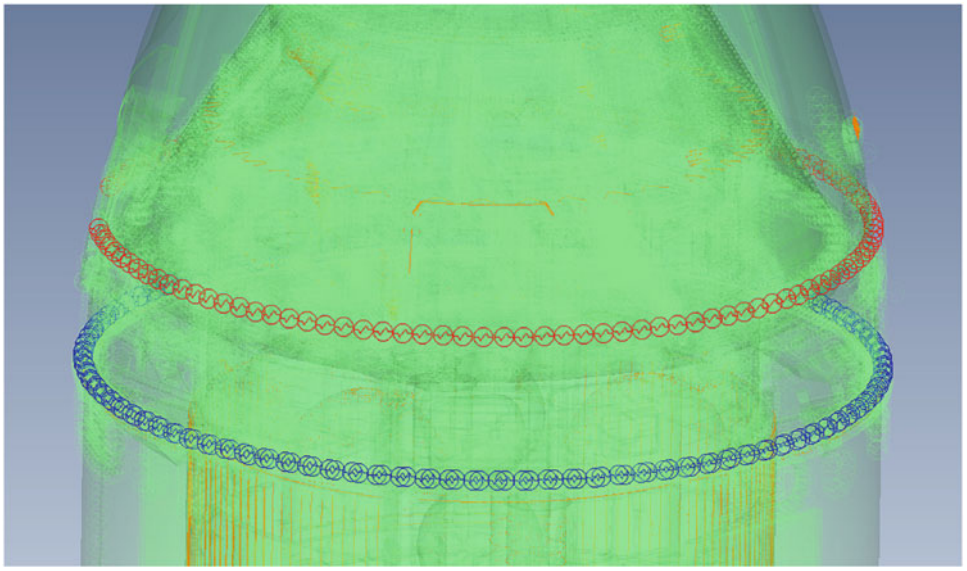

Fig. 9.10 Location of 204 airfoil (blue) and 114 aerodeflector (red) nonlinear joints in MPCV FEM

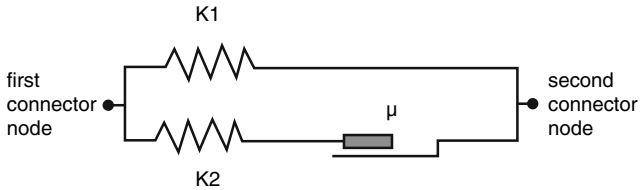

Fig. 9.11 Nonlinear model for airfoil and aerodeflector joints

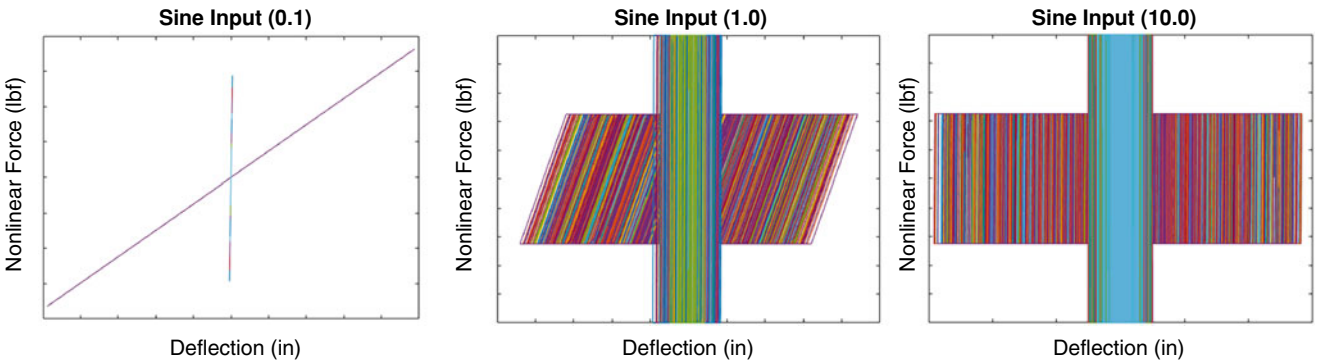

Fig. 9.12 Force/deflection curves for MPCV sliding joints at various input levels

the correlation study for the MPCV LL and HL loads. The axial frequency drops by about 11%. The 1st bending mode frequencies in the Y and Z directions drop by 14% and 25%, respectively. All other bending modes drop in frequency, though by different amounts.

The final step was to "tune" a FEM to match the observed results at each input level. This was done by parameterizing the FEM using the axial and tangential stiffness values at each of the two joint types. ATA's ATTUNE™ software, which uses a genetic algorithm to find a set of FEM properties that best match the measured frequencies, was then applied to find optimal values of the four parameters. Since the individual joints are not necessarily slipping identically, and since the joints slip differently in different modes, it isn't possible to find one set of spring values that will match all frequencies at each input level. The algorithm uses a sum of squares error metric to find an optimal solution, and the lower frequency modes were weighted a little more heavily than the higher frequency modes. The normalized values of the optimally tuned spring stiffnesses for each input level are plotted in Fig. 9.16. In this case 0% is the "slipping" value, while 100% is the "stick" value.

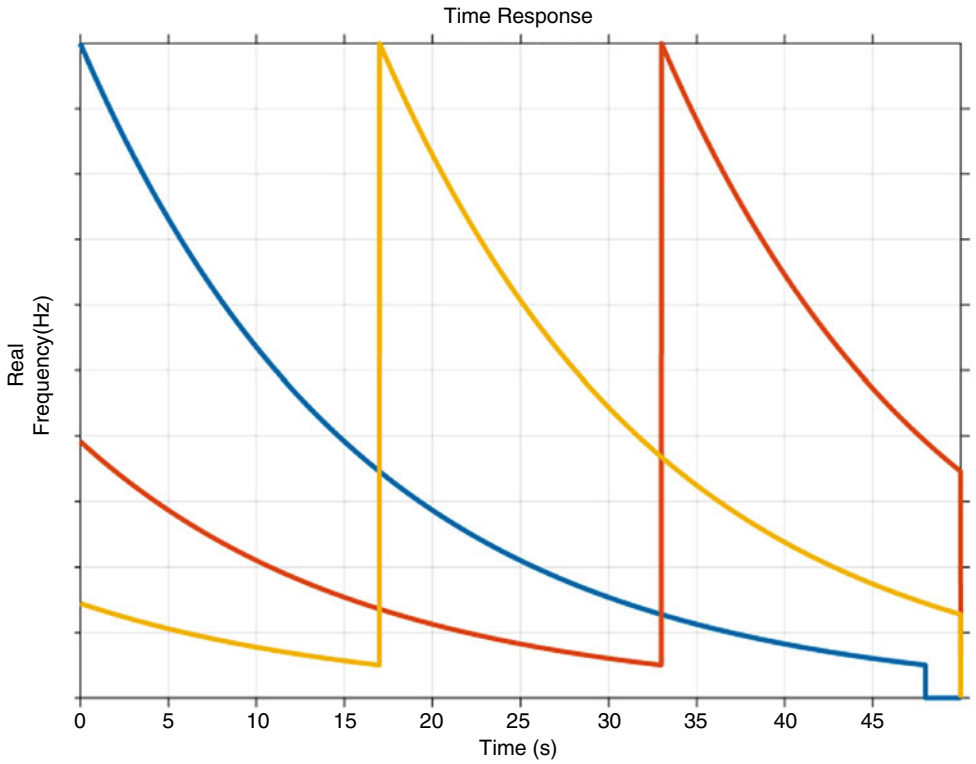

Fig. 9.13 Input base shake frequencies in X, Y, and Z direction as a function of time

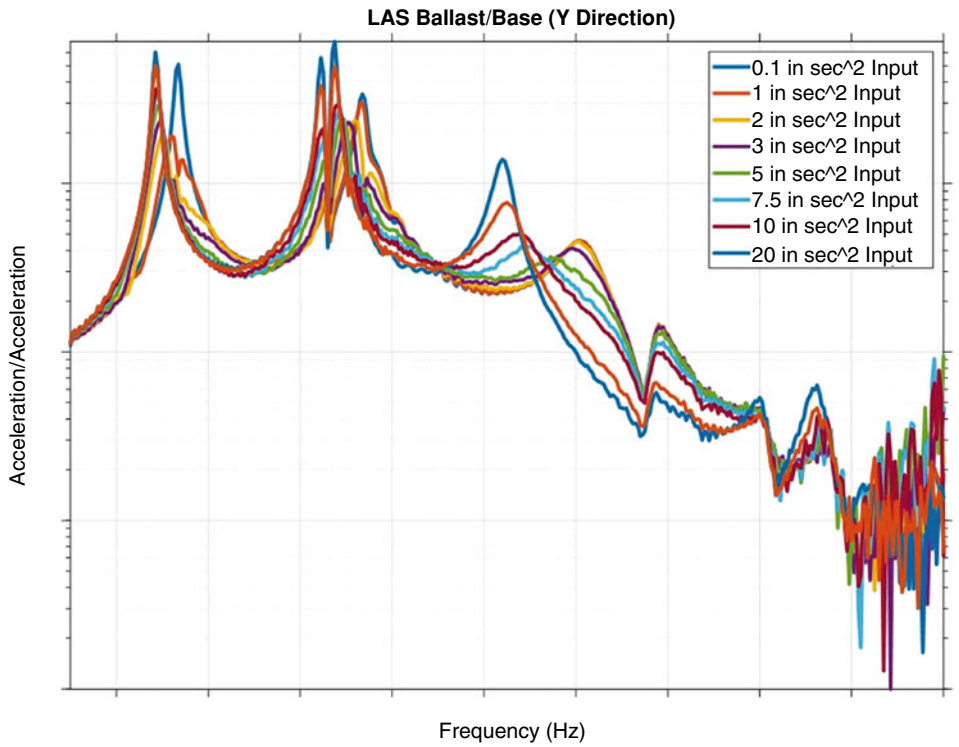

Fig. 9.14 Y Direction transfer functions for different input levels

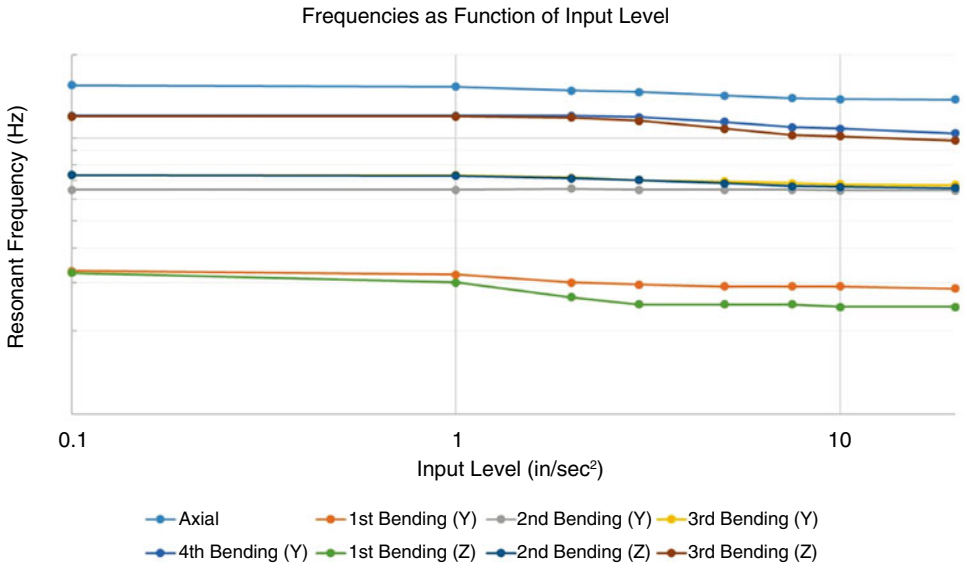

Fig. 9.15 Variation in frequency as a function of base acceleration input level

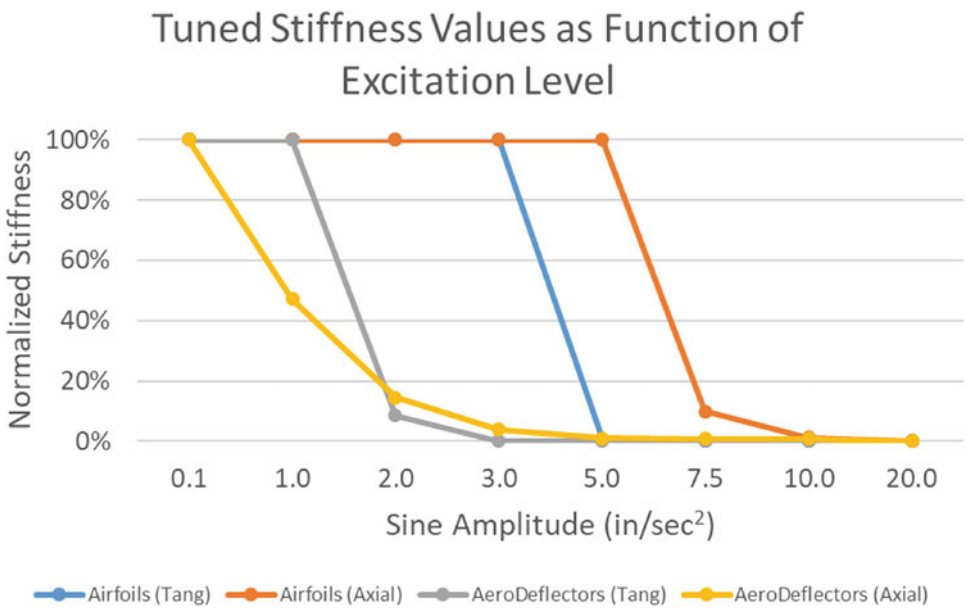

Fig. 9.16 Optimal normalized spring stiffness as a function of base acceleration input level

It is interesting to note that the optimal fits suggest that the joints begin to slip at different input levels. The aerodeflectors slip first in the axial direction and then tangential direction. The airfoils, on the other hand, don't begin to slip until an input level of 5 in/s^2, first axially and then tangentially. All spring values have reached their asymptotic "slipping" values by an input level of 10 in/s^2. In all cases the slipping behavior is approximate because the joints behave differently in different modes at different frequencies. This means that no one spring stiffness can capture even the linearized behavior of all the modes. This is addressed by finding a compromise solution that matches the target modes as well as possible "on the average" and then accounting for the fact that it does not match all modes in the uncertainty model.

The MPCV FEM was reduced to the 1029 "measured" DOFs in order to provide an orthogonality metric to match modes and calculate a mode shape error. Because no one set of the four spring stiffness parameters can match all modes, the modal error varies from level to level, and this was used to inform the uncertainty models described in the next section.

Table 9.7 Test-analysis frequency error (%) for first nine test modes

	Input level – in/s^2							
Test mode	0.1	1	2	3	5	7.5	10	20
1	0.52%	0.12%	1.31%	1.93%	0.70%	0.74%	0.64%	0.60%
2	0.05%	1.51%	1.73%	0.22%	0.49%	0.03%	0.18%	0.11%
3	0.25%	0.40%	0.23%	1.74%	1.36%	1.35%	1.04%	0.01%
4	0.99%	0.94%	0.43%	2.61%	1.87%	1.42%	0.96%	0.08%
5	1.36%	4.45%	10.30%	12.06%	9.55%	4.92%	3.32%	0.06%
6	1.03%	3.33%	8.06%	10.22%	9.23%	5.42%	3.72%	0.04%
7	0.27%	0.94%	1.25%	1.39%	1.35%	1.30%	1.04%	0.01%
8	0.36%	0.76%	1.20%	2.86%	1.04%	0.27%	0.42%	0.56%
9	0.81%	1.89%	2.24%	1.09%	0.99%	0.93%	0.34%	0.38%
Mean	0.63%	1.59%	2.97%	3.79%	2.95%	1.82%	1.30%	0.20%

9.4.2 Uncertainty Models for MPCV/MSA HCB Components

An HPV component uncertainty model is based on the HCB component representation. Uncertainty in the HCB fixed-interface (FI) eigenvalues is based upon component test/analysis frequency error, and the dispersion of the HCB stiffness matrix is based on the root mean square (RMS) value of the diagonal of the corresponding cross-orthogonality matrix (DCGM). Details of the process can be found in reference [2]. The LL MPCV model, discussed previously, was based on matching eight test modes derived from low level C4 test data. The median frequency error was 4.65%, and the corresponding DCGM value was 93.87 out of a perfect value of 100. The HL MPCV model was also based on eight test modes, but derived from high level C4 test data. The median frequency error was 5.50%, and the corresponding DCGM value was 96.66. The frequency correlation gets worse going from the LL to the HL model, while the cross-orthogonality gets better.

The absolute percentage frequency error between the ensemble of updated linear MPCV models, described in the previous section, and the surrogate test data for the first nine test modes, relative to the FEM values, is listed in Table 9.7. The test-analysis correlation results between the surrogate test data and the updated linear ensemble models assume that the surrogate test data corresponds to the truth, which it does not. The test data is based upon a nonlinear version of a linear MPCV model; therefore the correlation results are artificially accurate. Note that the absolute mean error is very low at load levels 0.1 and 20 in/s^2, where the joints are essentially totally locked and free, respectively. There is essentially no frequency uncertainty for these two extreme load levels where the MPCV behaves in a more linear fashion. At the intermediate load levels, there is more mixed joint slipping and sticking, leading to more nonlinear behavior. This makes it more difficult to fit linear models, leading to increased frequency errors.

An effort was made to add uncertainty to the test-analysis frequency errors listed in Table 9.7 to reflect the fact that the nonlinear model used to generate the surrogate test data does not match reality. As mentioned, the LL and level 0.1 MPCV models both have the same fixed joint state, while the HL and level 20 MPCV models both have a free joint state. Actual test data from the C4 STA produced a median frequency error of 4.65% in the LL MPCV model and a median frequency error of 5.50% in the HL model. Therefore, 4.65% error was added to all of the frequency errors for level 0.1, and 5.50% error was added to all of the frequency errors in level 20 to account for the difference between the surrogate test data and reality. The median frequency uncertainty was used instead of the mean such that no one mode would have an undue influence. For lack of actual test data at the intermediate load levels, the median frequency error was assumed to vary linearly with load level between the 0.1 and 20 in/s^2 load levels. These intermediate values, listed in Table 9.8, were then added to the frequency errors for each load level listed in Table 9.7. The median frequency error was assigned to all other HCB FI modes that were not matched to a test mode for each load level.

The same approach was used to add uncertainty to the HCB mode shapes for stiffness matrix dispersion. Test-analysis cross-orthogonality between the ensemble of MPCV models and the surrogate test data produced the DCGM values listed in the third column of Table 9.8. As mentioned, these values are artificially high. Based on C4 test-analysis cross-orthogonality, the LL MPCV model had a DCGM value of 93.87, while the HL MPCV model had a DCGM value of 96.66. Assuming that the intermediate load level DCGM values vary linearly between the LL and HL levels, and including the small degradation in DCGM from column 3, produces DCGM values for all eight load levels that account for uncertainty in the surrogate test data, as listed in column 4 of Table 9.8.

The dispersion of the stiffness matrix for each of the HCB MPCV components in the model ensemble was determined by assigning the corresponding component FI frequency uncertainties discussed previously and then assigning a stiffness

Table 9.8 Frequency and mode shape error assigned to account for surrogate test data uncertainty

Load level	Median Freq. Error (%)	Surrogate DCGM	Assumed Test DCGM
0.1	4.65	99.60	93.47
1.0	4.69	99.10	93.09
2.0	4.73	98.42	92.56
3.0	4.77	97.91	92.18
5.0	4.86	98.61	93.22
7.5	4.97	99.20	94.11
10.0	5.07	99.20	94.45
20.0	5.50	99.89	96.55

Table 9.9 Assumed MPCV HCB stiffness matrix dispersions for ascent +50 and ascent +120 s

Load level	A50 Dispersion (%)	A120 Dispersion (%)
0.1	3.25	2.25
1.0	3.00	2.00
2.0	2.90	1.75
3.0	2.75	1.75
5.0	1.25	1.00
7.5	0.00	0.00
10.0	0.00	0.00
20.0	0.00	0.00

dispersion value. Using that uncertainty model, a MC analysis with 3000 iterations was used to generate an ensemble of nominal-random cross-orthogonality matrices, which produced an ensemble of random DCGM values corresponding to the selected dispersion value. The most probable DCGM value corresponding to the first 64 free-free elastic non-slosh modes with frequencies less than 20 Hz. was computed over the ensemble and compared to the assumed test values listed in column 4 of Table 9.8. The stiffness dispersion value for the component was adjusted until the most probable and test DCGM values agreed. Details of the process can be found in reference [2].

Ascent at T0 + 50 and T0 + 120 s were considered in the subsequent buffet and GNC SOP analyses, respectively. The stiffness dispersion values selected for each of the MPCV HCB models in the ensemble are listed in Table 9.9. Note that the dispersion values decrease as the load level increases, to the point where no stiffness dispersion is required to obtain the desired component mode shape uncertainty. This is consistent with the previous uncertainty models derived for the LL and HL MPCV components. As mentioned previously, there are four other HCB components within the SLS system models. The corresponding uncertainty models were derived using component modal test results. Details related to these components and their uncertainty models can be found in references [2, 3].

9.4.3 SOP UQ Analysis for Additional Model Ensemble Members

The SOP analysis for the guidance, navigation, and control stability conditions was repeated for the eight additional systems, each containing one of the MPCV ensemble models. The uncertainty in the fundamental bending mode frequencies must be greater than −10%, and the corresponding frequency response gain uncertainty must be less than 4 dB for control system stability. Figure 9.17 corresponds to Fig. 9.3 for pitch frequency uncertainty, but with the CCDFs from the eight additional models. Only two of the CCDFs, load level 0.1 and load level 1 in/s^2, lie slightly outside the region bounded by the CCDFs corresponding to the LL and HL MPCV models. This implies that if a linear MPCV model is a valid representation of the nonlinear MPCV at a specific load level, then the LL and HL MPCV models essentially bracket the effect of the MPCV nonlinearity on the fundamental pitch frequency. Figure 9.18 presents an expanded view of Fig. 9.17 for the critical region of negative frequency uncertainty. It can be seen that within this region, all of the CCDFs are to the right and above the CCDF corresponding to the HL MPCV model. This implies that for a specific negative frequency uncertainty, like the critical value of −10%, the HL model yields a lower probability that the actual pitch frequency uncertainty is greater than that value. Therefore, in terms of control system stability, using the HL MPCV model, and its corresponding uncertainty model, produces a statistically more conservative result with respect to pitch frequency uncertainty.

Figure 9.19 is analogous to Fig. 9.5 for yaw frequency uncertainty, but with the additional eight model CCDFs. In this case, three of the CCDFs, corresponding to load levels 0.1, 1, and 2 in/s^2, lie outside the region bounded by the LL and HL MPCV

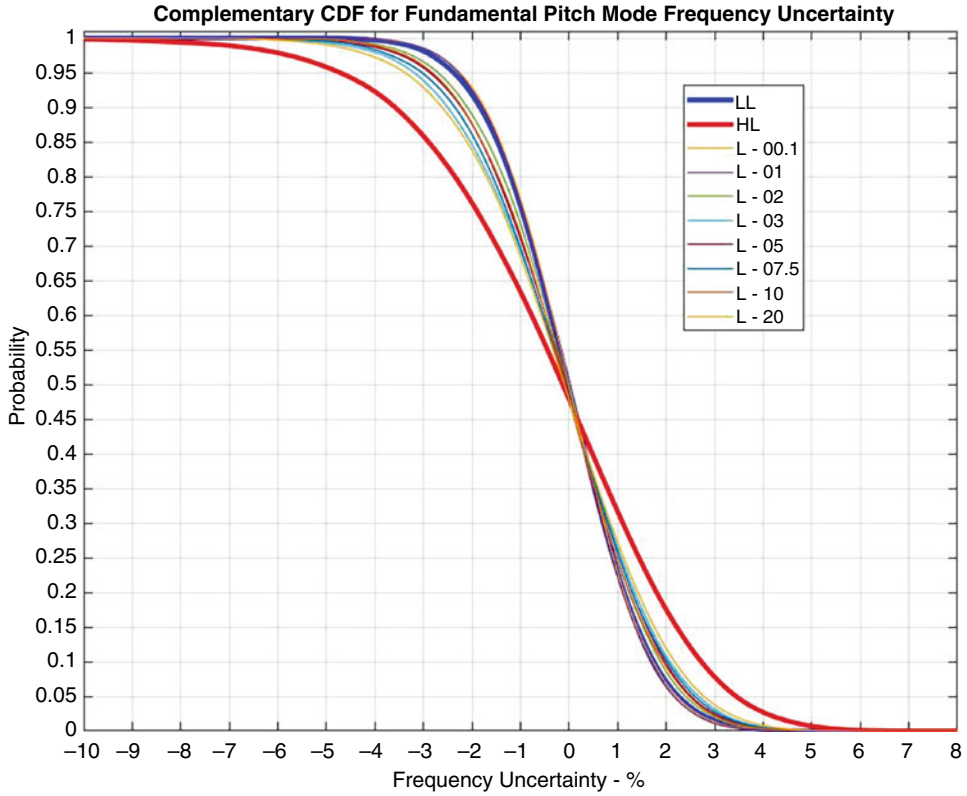

Fig. 9.17 Complementary CDFs for pitch frequency uncertainty

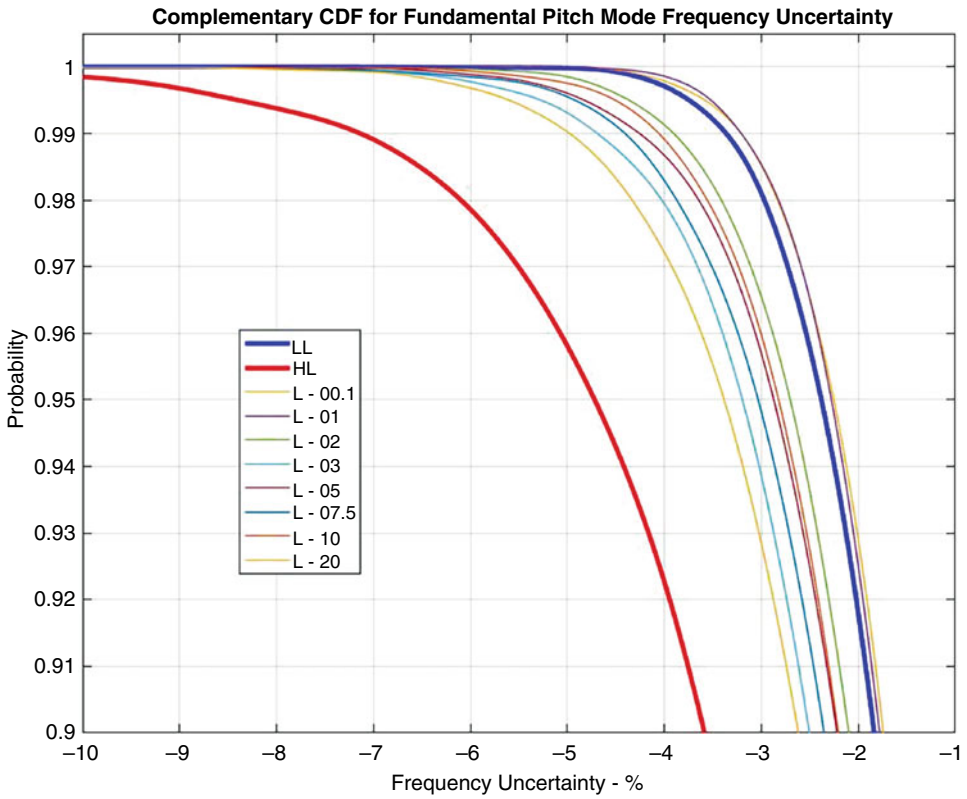

Fig. 9.18 Expanded view of complementary CDFs for pitch frequency uncertainty

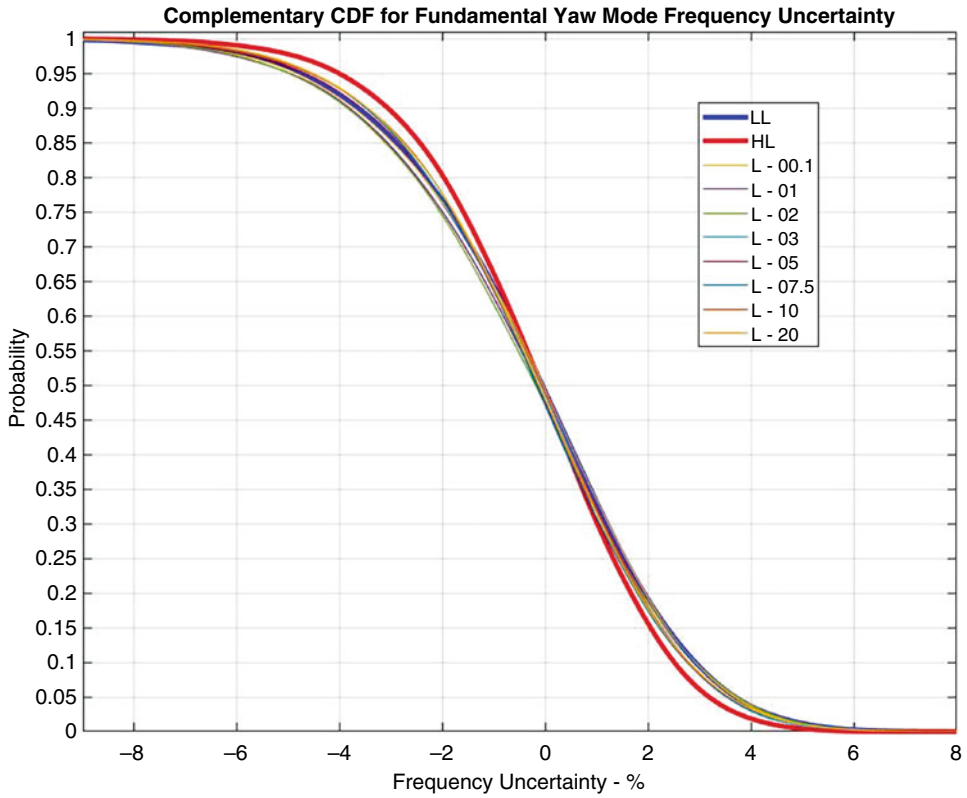

Fig. 9.19 Complementary CDFs for yaw frequency uncertainty

CCDFs. Figure 9.20 presents an expanded view of Fig. 9.19 for the critical region of negative frequency uncertainty. In this case, within the region of negative frequency uncertainty, all the CCDFs are to the left and below the CCDF corresponding to the HL MPCV model. This implies that for a specific negative frequency uncertainty, the HL model yields a higher probability that the actual yaw frequency uncertainty is greater than that value. Therefore, in terms of control system stability, using the HL MPCV model produces a statistically less conservative result with respect to yaw frequency uncertainty.

Figure 9.6 shows the LL and HL MPCV model CDFs for pitch rate gain uncertainty at the itRGA. Figure 9.21 presents the expanded view of Fig. 9.6 for the critical region of positive gain uncertainty, including the CDFs for the ensemble of MPCV models. As in the case of pitch frequency uncertainty, all of the ensemble CDFs lie between the LL MPCV and HL MPCV CDFs, with the exception of the CDFs corresponding to the 0.1 and 1 in/s^2 load levels, which are outside, but close to the LL CDF. The figure shows that all of the CDFs are to the left and above the CDF corresponding to the HL MPCV. This indicates that for a specific value of positive rate gain uncertainty, such as the critical value of 4 dB for control system stability, the probability of that uncertainty value being exceeded is greater using the HL MPCV model than when using the other MPCV representations. This implies that using the HL MPCV and its corresponding uncertainty model is statistically more conservative than the other models with respect to pitch rate gain uncertainty at the itRGA. Figure 9.22 illustrates the expanded view of Fig. 9.7 for the region of positive yaw rate gain uncertainty at the itRGA but including the CDFs for the ensemble of eight MPCV models. For the most part, the ensemble CDFs lie between the LL and HL MPCV CDFs. At probabilities below 2% and above 90%, the ensemble CDFs venture outside the LL/HL CDF interval, but the departure is never very great. Also, for the most part, the HL MPCV CDF lies to the right and below the other MPCV CDFs within the positive rate gain uncertainty region. This indicates that using the HL MPCV model is also statistically conservative with respect to the yaw rate gain uncertainty stability criterion at the itRGA.

The application of the SOP approach to the buffet CS section loads for the LL and HL versions of the SLS at ascent T0 + 50 s configuration was described in the previous section. As discussed, the original analysis [3] found that there were substantial differences in nominal CS peak moments about Y and in peak shear along Z predicted using the LL versus the HL MPCV models. The maximum peak moment about Y occurs at section $x = 2754.99$ inches using the LL MPCV model. The SOP analysis was repeated for the eight additional systems, each containing one of the MPCV ensemble models. Figure 9.23 illustrates the LL and HL CDFs, as well as the CDFs from the eight additional ensemble models, for the peak moment about Y at $x = 2754.99$ inches for 1000 random systems. Apart from very low probabilities, all but two of the ensemble

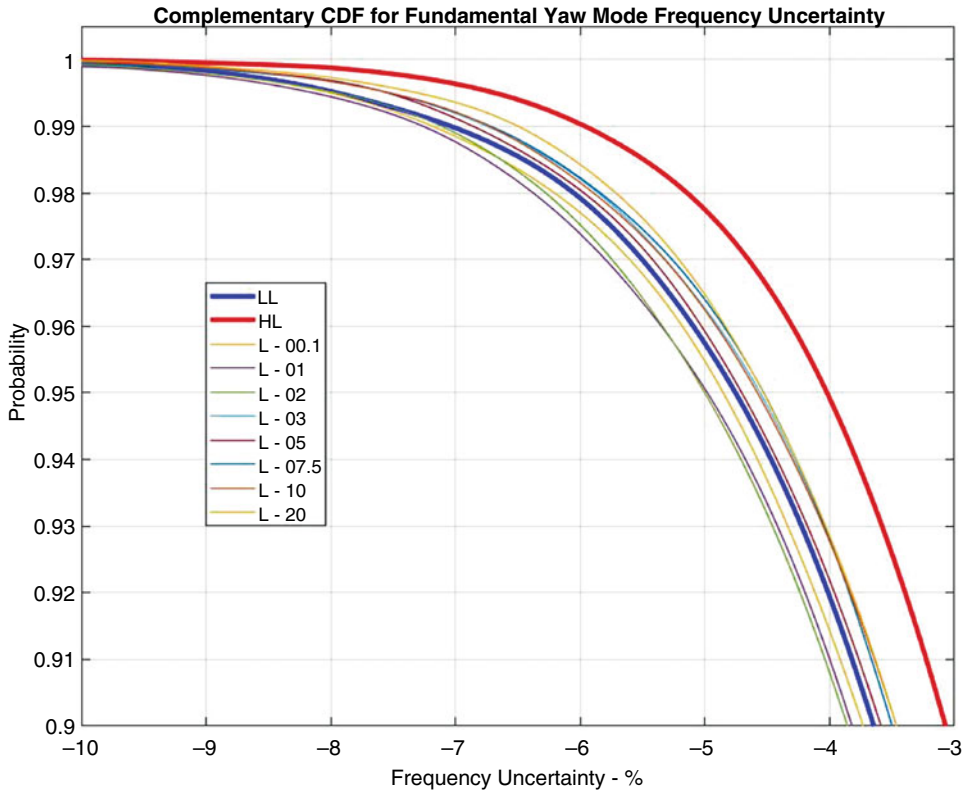

Fig. 9.20 Expanded view of complementary CDFs for yaw frequency uncertainty

model CDFs, levels 0.1 and 1 in/s^2, are bounded by the LL and HL MPCV CDFs. With the same exception, the HL MPCV CDF lies to the left and above all other CDFs. This indicates that for a specific value of peak CS section moment about Y, the probability that the value is exceeded is smaller for the HL MPCV model than all other models. The HL MPCV model is therefore less conservative statistically with respect to CS peak section moment about Y at the specific section $x = 2754.99$ inches.

The maximum peak CS shear along Z occurs at section $x = 2862.71$ inches using the HL MPCV model. Figure 9.24 presents the LL and HL CDFs, as well as the CDFs from the eight additional ensemble models, for the peak shear along Z at that section. Up to a probability of P99.6, only two of the ensemble model CDFs, levels 0.1 and 1 in/s^2, are not bounded by the CDFs of the LL and HL MPCV models. The corresponding excursions are small, and for the most part, only the level 0.1 CDF is outside the region between the LL and HL CDFs. In addition, the HL MPCV model CDF lies to the right and below all other MPCV model CDFs. This indicates that for a specific value of peak CS section shear along Z, the probability that the value is exceeded is larger for the HL MPCV model than all other models. The HL MPCV model is therefore conservative statistically with respect to CS peak section shear along Z at the specific section $x = 2862.71$ inches.

While only a small number of SLS response items were considered in this assessment, the HL MPCV and corresponding uncertainty models produced statistically conservative results most, but not all of the time. Statistical conservatism implies here that, for example, if there is a particular response item that is not to be exceeded, using the HL MPCV and uncertainty models produces a greater probability than other possible models that it will be exceeded.

9.5 Conclusion

Epistemic and aleatory uncertainty cannot be handled in the same manner within a UQ analysis. However, epistemic and aleatory variables can be combined within a single UQ analysis using a SOP approach. The nonlinearity within the MPCV is a model-form or epistemic uncertainty. In this assessment, it is assumed that the MPCV nonlinearity can be represented by an ensemble of linear MPCV models, one for each forcing level of interest. Sampling the ensemble of MPCV models and then performing an HPV UQ analysis produces an ensemble of CDFs for the associated QOIs. A p-box analysis of the

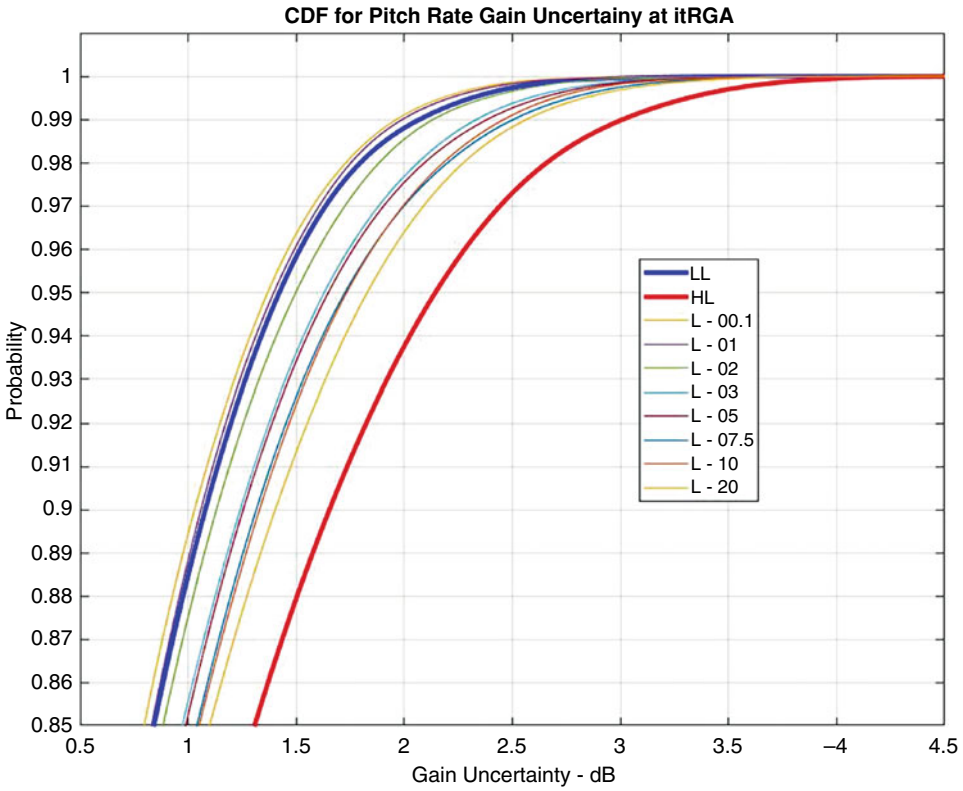

Fig. 9.21 Expanded view of CDFs for pitch rate gain uncertainty

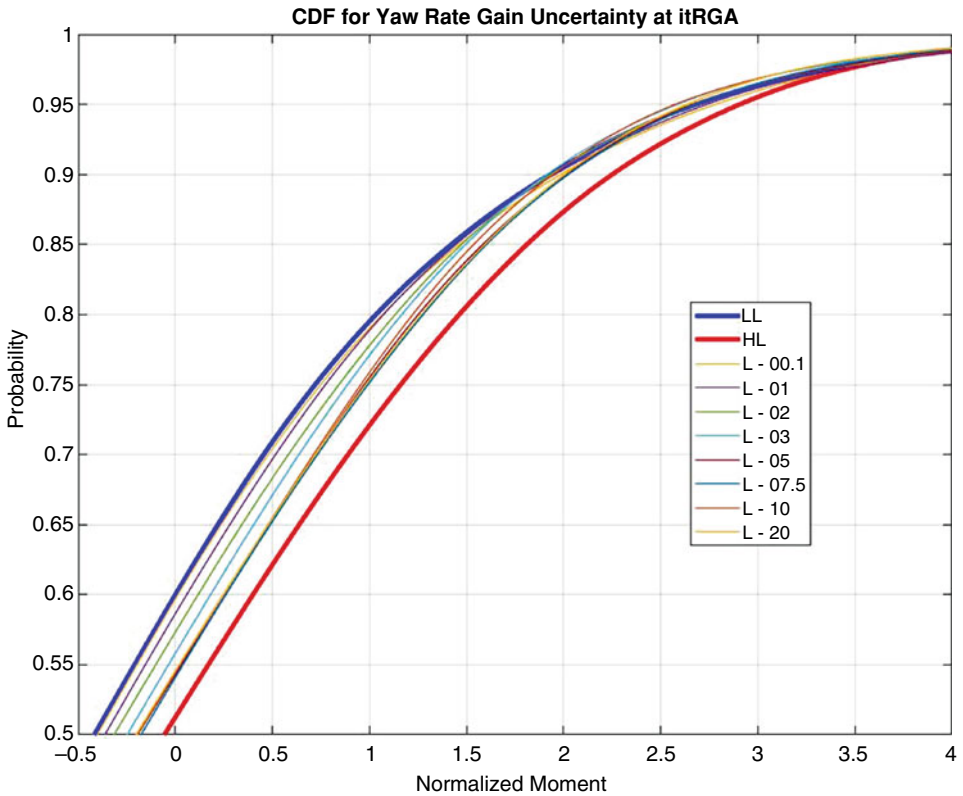

Fig. 9.22 Expanded view of CDFs for yaw rate gain uncertainty

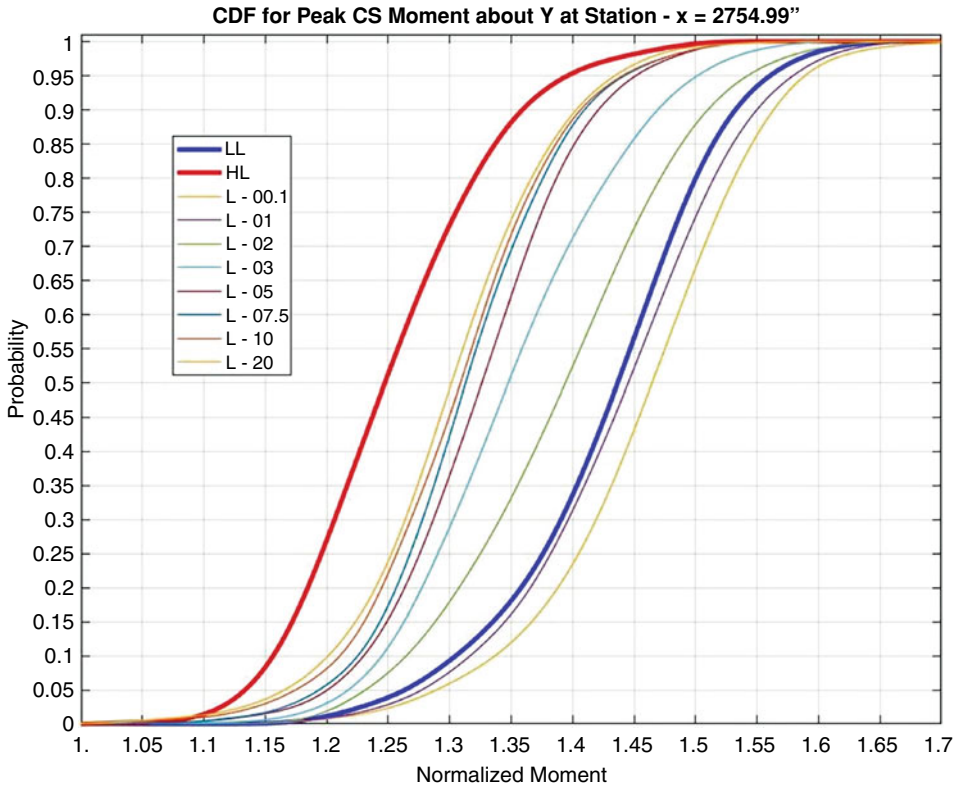

Fig. 9.23 CDFs for peak CS moment about Y at $x = 2754.99$ inches

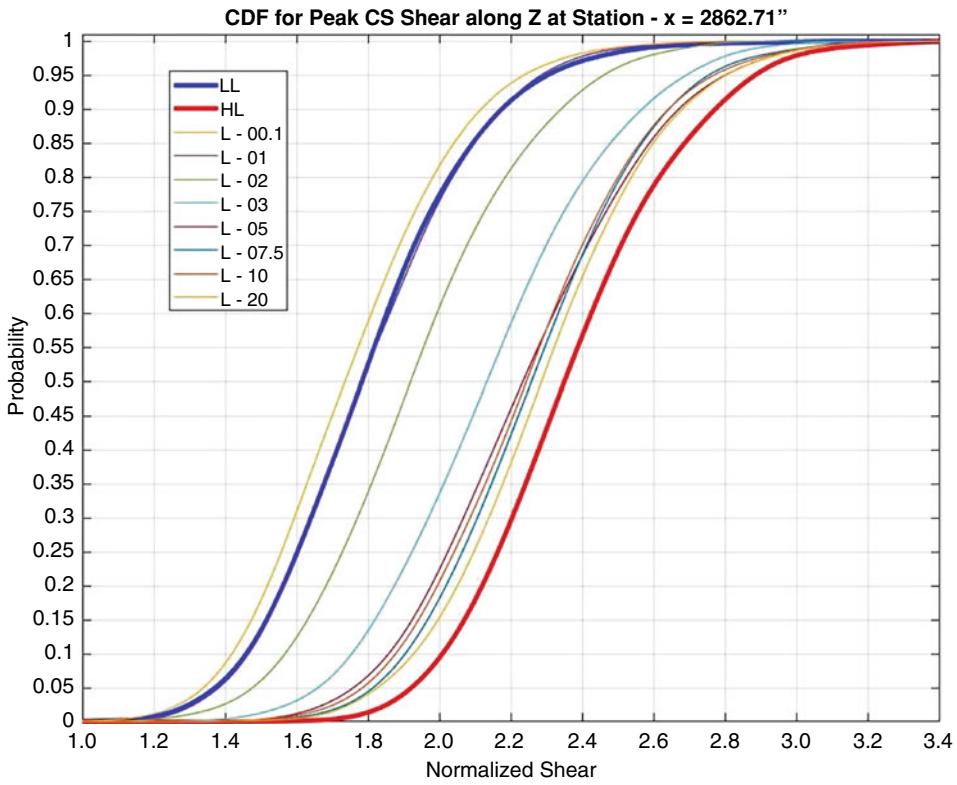

Fig. 9.24 CDFs for peak CS shear along Z at $x = 2862.71$ inches

upper and lower bound CDFs produces plausible ranges of probability for specific QOI values and plausible ranges of QOIs for specific probabilities. The larger the ranges, the greater the impact of the MPCV nonlinearity upon the QOIs.

In the case of the SLS, there were initially only two MPCV models within the SOP outer loop ensemble corresponding to low and high C4 test forcing levels. Using the CDFs from these two models, a p-box analysis was performed for selected QOIs to assess the influence of MPCV nonlinearity. However, there was no guarantee that the LL and HL MPCV models represent the true bounds of the model-form uncertainty due to the nonlinearity. Ideally, additional C4 modal test data would have been measured at intermediate loading levels. To determine how well the LL and HL MPCV models bound the response of the actual nonlinear MPCV, the C4 test data was augmented with surrogate test data generated using a nonlinear model of the MPCV. Eight additional linear MPCV models were derived based on simulated response to enforced base sine inputs. SOP UQ analysis was performed for each of the additional eight models in the ensemble. The UQ analysis also included uncertainty models of all the other SLS components that had previously been derived using modal test data. The corresponding horsetail plots showed that for the specific QOIs selected, at least six of the eight additional intermediate model CDFs were bounded by the LL and HL MPCV model CDFs. When an intermediate load level CDF was outside the interval, it was only slightly outside the boundary formed by the LL MPCV CDF. Therefore, if it can be assumed that a linear MPCV model can adequately represent the response of the nonlinear MPCV at a specific load level, then the ensemble of linear models in the outside SOP loop spans the response of the nonlinear MPCV. The p-box formed by the ensemble CDFs bracket the response of the nonlinear system. In the cases examined, the LL and HL MPCV CDFs for the selected QOIs are close to bracketing the nonlinear system response and representing the associated model-form uncertainty. The HL model CDFs always bounded the other models, while up to three intermediate level models had CDFs outside the region bounded by the LL model. It was also found that the HL MPCV model does not always give statistically conservative results.

This assessment shows that the SOP approach combined with the HPV UQ method can provide an effective means of determining the impact of component nonlinearities upon the uncertainty in system level results.

References

1. Craig, R.R., Bampton, M.C.C.: Coupling of substructures for dynamic analysis. AIAA J. **6**, 1313–1319 (1968)
2. Kammer, D., Blelloch, P., Sills, J.: Test-based uncertainty quantification and propagation using Hurty/Craig-Bampton substructure representations. In: IMAC, Orlando, FL (2019)
3. Kammer, D., Blelloch, P., Sills, J.: Variational coupled loads analysis using the hybrid parametric variation method. In: IMAC, Houston, TX (2020)
4. Kammer, D., Blelloch, P., Sills, J.: SLS integrated modal test uncertainty quantification using the hybrid parametric variation method. In: IMAC (2020)
5. Ferson, S., Ginzberg, L.: Different methods are needed to propagate ignorance and variability. Reliab. Eng. Syst. Saf. **54**, 133–144 (1996)
6. Peterson, L.D., Mobrem, M.: A Comparison of Uncertainty Quantification Methods on Benchmark Problems for Space Deployable Structures, 2018 AIAA Spacecraft Structures Conference, Kissimmee, FL, January (2018)
7. Eldred, M., Swiler, L.: Efficient Algorithms for Mixed Aleatory-Epistemic Uncertainty Quantification with Application to Radiation-Hardened Electronics-Part I: Algorithms and Benchmark Results, Sandia Report: SAND2009_5805, September (2009)
8. Bailey, E., Peterson, L.: Ignorance vs. Variability: Considerations for UQ Analysis, Joint GN&C and L&D Uncertainty Quantification Workshop, Marshall Space Flight Center, January 17, (2018)
9. Moderes, M., Bergerson, J.: Dynamic analysis of uncertain structures using imprecise probability. Int. J. Reliab. Saf. **9**(2/3), 203–219 (2015)
10. Chapman, J.M.: Incorporating a Full Damping Matrix in the Transient Analyses of Nonlinear Structures, Damping '93 Conference, San Francisco, (1993)

Chapter 10
A Physics-Based Reduction with Monitoring Data Assimilation for Adaptive Representations in Structural Systems

Konstantinos Vlachas, Konstantinos Tatsis, Carianne Martinez, and Eleni Chatzi

Abstract Digital twin representations have become an indispensable tool for delivering data-informed virtualizations of operating systems, especially in structural health monitoring applications. In this context, challenges arise when the response often shifts beyond regular operating conditions due to extreme events such as earthquakes or structural damage. Our work proposes a reduced order modeling for adaptive digital twins, for systems undergoing damage, condition deterioration, or experiencing stochastic excitation. Our approach initiates by featuring a projection-based reduced order model (ROM), relying on proper orthogonal decomposition (POD) and local subspaces to form a low-cost surrogate of the parametrized high-fidelity system that retains a physical connotation. However, extreme events induce loading conditions and model states that challenge the accuracy of such representations. To this end, we propose adopting the derived ROM as a forward simulator and adapt the projection basis on-the-fly during operation via a Gaussian processes regressor (GPR) scheme. During operation, the ROM framework receives response monitoring information from a sparse number of nodes. It employs a suitable condition indicator to highlight the potential low precision of the initial surrogate. Subsequently, the GPR-based scheme utilizes the monitoring input to reconstruct the current deformed configuration of the whole system in an online manner. In turn, this approximation serves as a damaged mode that enriches the projection-based ROM and enables online adaptivity. This coupling yields a ROM equipped with critical features for health monitoring applications such as (near) real-time basis refinement, signaling potentially irreversible consequences, and estimation of the uncertainty in the enrichment mode and the adapted ROM prediction.

Keywords Adaptive GPR-ROM · Monitoring data assimilation

10.1 Introduction

Dynamical systems may experience complex nonlinear phenomena, which extend beyond behavior that is expected during operational conditions. For tackling loading and response regimes that correspond to unusual or extreme events, data assimilation techniques, driven by availability of monitoring observations, could provide a form of performance adaptivity, either on-the-fly or afterward.

This notion of adaptivity in a ROM context has already been discussed, for example, in [1, 2], where suitable error estimators are utilized in the input parameter space to assemble an adaptive basis construction scheme. Performance enrichment and basis update techniques during the online phase have also been suggested in [3] via low-rank matrix updates, in [4, 5] by means of full-order simulations, or in [6, 7] employing local refinements and vector sieving strategies.

Our approach proposes an alternative methodology that relies on online monitoring information from sparse structural degrees of freedom, as opposed to assuming knowledge over the entire response vector. Our work features ROMs as efficient surrogates and attempts to address the aforementioned challenge of adaptive response prediction under extreme events like structural damage or state deterioration. In essence, we utilize an initially deployed ROM and then adopt a Gaussian processes

K. Vlachas (✉) · K. Tatsis · E. Chatzi
Department of Civil, Environmental, and Geomatic Engineering, ETH Zurich, Zurich, Switzerland
e-mail: vlachas@ibk.baug.ethz.ch; tatsis@ibk.baug.ethz.ch; chatzi@ibk.baug.ethz.ch

C. Martinez
Applied Machine Intelligence, Sandia National Laboratories, Albuquerque, NM, USA
e-mail: cmarti5@sandia.gov

Z. Mao (eds.), *Model Validation and Uncertainty Quantification, Volume 3*, Conference Proceedings of the Society for Experimental Mechanics Series, https://doi.org/10.1007/978-3-031-04090-0_10

regressor (GPR) to adapt the projection basis during operation. This fusion allows for an adaptive ROM through an online projection basis refinement while estimating the uncertainty involved.

10.2 Framework Formulation

As a first step, to derive the adaptive framework, our work follows the approach described in [8] to assemble an initial ROM. In short, we formulate a low-order system equivalent to the full-order model (FOM) through a Galerkin projection and proper orthogonal decomposition (POD).

The constructed ROM is equipped with an indicator representing an alarm. The condition indicator is constructed on the basis of the noisy response of a few selected system degrees of freedom (dofs). The discrepancy between the measurement and the respective ROM prediction at the selected dofs is utilized to indirectly evaluate the precision of the ROM approximation. In our work, the Mahalanobis distance is employed as a comparative measure, applied on the residuals between the ROM prediction and the actual response on the monitored dofs. The alarm threshold is defined exploiting the respective chi-distribution statistics with a suitable significance level for each case.

Based on the previous work in [9], artificial measurement data at the chosen sensor locations are produced, and the corresponding vector $\mathbf{d}_k \in \mathrm{R}^{n_d}$ from the selected dofs is polluted with Gaussian white noise to generate the noisy output $\tilde{\mathbf{d}}_k \in \mathrm{R}^{n_d}$ at every timestep k following:

$$\tilde{\mathbf{d}}_k = \mathbf{d}_k + \delta \sigma_d \mathbf{r}_k, \tag{10.1}$$

where n_d is the number of measured quantities, δ denotes the noise level, $\sigma_d \in \mathrm{R}^{n_d \times n_d}$ is a diagonal matrix containing the standard deviations of the signals, and $\mathbf{r}_k \in \mathrm{R}^{n_d}$ is a vector of random values drawn independently from the standard normal distribution. This setup aims to account for modelling and measurement noise in an actual system.

In an alarm event, the Gaussian processes regression (GPR) receives the noisy residuals as input and estimates the residual response on the entire physical space. In turn, the output is utilized as an additive correction to the ROM prediction. The resulting approximation represents an instance of a damaged configuration of the system, equivalent to some sort of POD mode, and functions as a projection basis enrichment that captures the system's behavior during a damage event.

The ROM subspace is thus updated on-the-fly delivering an adaptive GPR-ROM. The GPR scheme is trained similar to the ROM, relying on a radial basis function kernel. Additionally, the training leverages local correlations between coordinates representing physical response correlations between neighboring degrees of freedom. This implies that the response in each coordinate is approximated, exploiting information from the most suitable monitoring channels.

10.3 Analysis

The adaptive nature of the proposed ROM is validated using the following proof of concept case studies: The first is a 10 m steel cantilever beam, whereas the second is a two-story plane frame out of steel with a story height of 4 m and a width of 10 m. Both structures are discretized using beam elements and excited using Gaussian noise. In all the couplings of the frame and in the boundary node of the cantilever beam, Bouc–Wen springs are assembled, enforcing a hysteretic behavior based on the following:

$$\mathbf{R} = \mathbf{R}_{linear} + \mathbf{R}_{hysteretic} = \alpha k \mathbf{x} + (1-\alpha) k \mathbf{z} \qquad \dot{\mathbf{z}} = \frac{A\dot{\mathbf{x}} - (1.0 + \delta_v \int_0^t \mathbf{z}\dot{\mathbf{x}} dt)(\beta |\dot{\mathbf{x}}| \mathbf{z} |\mathbf{z}|^{w-1} - \gamma \dot{\mathbf{x}} |\mathbf{z}|^w)}{1.0 + \delta_\eta \int_0^t \mathbf{z}\dot{\mathbf{x}} dt}, \tag{10.2}$$

where $\mathbf{R}$ denotes the restoring forces, $\mathbf{x}$ the displacements, and $\mathbf{z}$ represents the hysteretic term. The rest are characteristic parameters of the Bouc–Wen spring, controlling the shape of the response curve. A detailed description can be found in [8].

Regarding the cantilever beam, a linear ROM is initially deployed. Subsequently, the Bouc–Wen spring is activated during operation representing damage. This process is controlled by varying parameters a and k. Figure 10.1b highlights the ability of the GPR-ROM to capture the response of the damaged structure by performing on-the-fly adaptations of the projection basis. On the contrary, the initially deployed healthy ROM fails to capture the damage effect in Fig. 10.1a.

For the plane frame, the initial ROM is trained based on the nonlinear behavior of the structure. During operation, stiffness degradation and strength deterioration effects are activated by tweaking δh and δv. In this more advanced case study, the

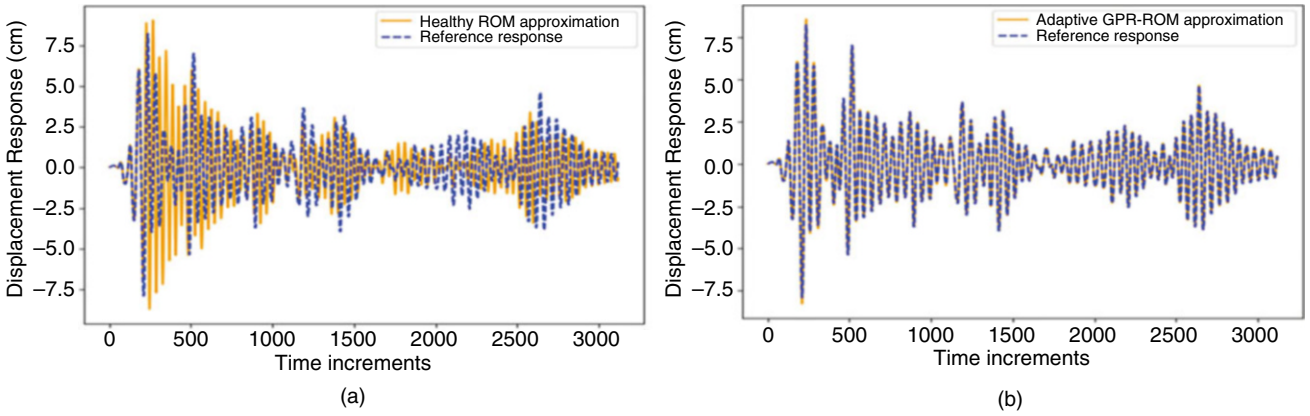

Fig. 10.1 Performance of the adaptive GPR-ROM in capturing the response under a damage scenario. (**a**) Healthy ROM approximation. (**b**) Adaptive GPR-ROM approximation

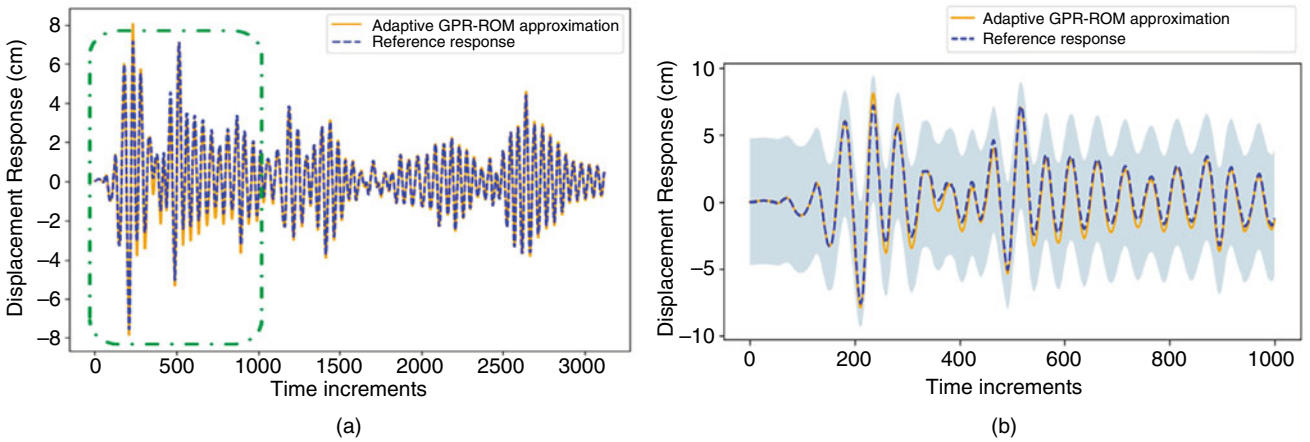

Fig. 10.2 Performance of the adaptive ROM in capturing the response under a condition deterioration scenario. (**a**) Adaptive GPR-ROM approximation. (**b**) Magnified view and confidence bounds of the prediction

GPR-ROM provides a sufficiently accurate approximation as depicted in Fig. 10.2a. Additionally, the confidence bounds of the prediction in Fig. 10.2b offer an initial uncertainty estimation and function as envelope curves for the actual response.

10.4 Conclusions

In our work, we derive an adaptive low-order representation with the ability to update its projection basis on-the-fly to address challenges of response estimation during operational conditions that extend beyond expected behavior. This is achieved utilizing a condition indicator and a Gaussian processes regressor that reconstructs the residual response in all physical nodes of the system by relying on sparse monitoring measurements. The output approximation is subsequently used for basis enrichment. This fusion allows for an adaptive ROM, able to perform basis refinement, signaling of potentially irreversible consequences, and uncertainty estimation features critical for health monitoring. Potential extensions involve utilizing the ROM as a forward simulator assembled in an inverse setup that aims to estimate features of the system's state [10].

Acknowledgments This research has been funded from the Sandia National Laboratories, under SAND Number: SAND2022-1357 C. Sandia National Laboratories is a multimission laboratory managed and operated by National Technology and Engineering Solutions of Sandia, LLC, a wholly owned subsidiary of Honeywell International Inc., for the U.S. Department of Energy's National Nuclear Security Administration under contract DE-NA0003525. This paper describes objective technical results and analysis. Any subjective views or opinions that might be expressed in the paper do not necessarily represent the views of the U.S. Department of Energy or the United States Government.

References

1. Chellappa, S., Feng, L., Benner, P.: Adaptive basis construction and improved error estimation for parametric nonlinear dynamical systems. Int. J. Numer. Methods Eng. **121**(23), 5320–5349 (2020)
2. Cortinovis, A., Kressner, D., Massei, S., Peherstorfer, B.: Quasi-optimal sampling to learn basis updates for online adaptive model reduction with adaptive empirical interpolation. In: 2020 American Control Conference (ACC), pp. 2472–2477. IEEE (2020)
3. Peherstorfer, B., Willcox, K.: Online adaptive model reduction for nonlinear systems via low-rank updates. SIAM J. Sci. Comput. **37**(4), A2123–A2150 (2015)
4. Rocha, I., van der Meer, F., Sluys, L.J.: An adaptive domain-based POD/ECM hyper-reduced modeling framework without offline training. Comput. Methods Appl. Mech. Eng. **358**, 112650 (2020)
5. Rocha, I.B., Van Der Meer, F.P., Mororó, L.A., Sluys, L.J.: Accelerating crack growth simulations through adaptive model order reduction. Int. J. Numer. Methods Eng. **121**(10), 2147–2173 (2020)
6. Carlberg, K.: Adaptive h-refinement for reduced-order models. Int. J. Numer. Methods Eng. **102**(5), 1192–1210 (2015)
7. Etter, P.A., Carlberg, K.T.: Online adaptive basis refinement and compression for reduced-order models via vector-space sieving. Comput. Methods Appl. Mech. Eng. **364**, 112931 (2020)
8. Vlachas, K., Tatsis, K., Agathos, K., Brink, A.R., Chatzi, E.: A local basis approximation approach for nonlinear parametric model order reduction. J. Sound Vibration **502**, 116055 (2021)
9. Tatsis, K., Lourens, E.: A comparison of two Kalman-type filters for robust extrapolation of offshore wind turbine support structure response. In: Life-Cycle of Engineering Systems, pp. 209–216. CRC Press (2016)
10. Agathos, K., Tatsis, K.E., Vlachas, K., Chatzi, E.: Parametric reduced order models for output-only vibration-based crack detection in shell structures. Mech. Syst. Signal Process. **162**, 108051 (2022)

Chapter 11
Comprehensive Testing Environment to Evaluate Approaches in Uncertainty Quantification for Passive and Active Vibration Isolation

Roland Platz

Abstract This contribution introduces a one-mass oscillator subject to passive and active vibration isolation. In this context, passive means that the vibration isolation behavior only depends on preset inertia, damping, and stiffness properties. Active means that additional controlled forces change and adapt the damping properties to enhance the vibration isolation behavior. The purpose of the system is, eventually, to assess diverse measures in quantifying model form uncertainty of various mathematical models of the passive and active vibration isolation configuration in a consistent and comparable way. On the one hand, the one-mass oscillator is simple enough to be modeled analytically to establish a reference model. With its realization as an experimental test environment, it also allows more complex models such as a two-mass oscillator, which is still modeled analytically, and numerical finite and multi-body modeling. The test environment guarantees a consistent and comparable discussion about different approaches to quantify model form uncertainty in an uppermost comprehensive and extended way. First, the author derives the mathematical model for numerical simulation and explains the real test environment. An impulse excites the mass, and the mass responds with vibrations, given by velocity and acceleration responses. Second, preliminary studies for different passive and active damping cases identify the differences between numerical and experimental outcomes from simulation and test. The contribution closes with an invitation to continue and extend the work by a round robin within IMAC's *Model Validation and Uncertainty Quantification MVUQ* community.

Keywords Vibration isolation · One-mass oscillator · Active damping force · Model form uncertainty · Round robin

11.1 Introduction

Awareness and quantifying uncertainty in mathematical modeling, experimental test, and model verification and validation in early design stage are essential in structural dynamic application. The author recognizes the fact that, not rarely, uncertainty quantification approaches and documentation tend to lack transparency and comprehensibility, together with reluctance in consistently consolidating mathematic, stochastic, and engineering terminology. This makes it often impractical or too difficult and time consuming to transfer and apply uncertainty quantification measures to common and real engineering problems faced by the industry.

Model form uncertainty expresses unknown, incomplete, inadequate, or unreasonable functional relations between the model input and output, between model parameters and state variables when compared to observations from real experimental test [11]. The scope and complexity of the model also have an impact on the severity of the uncertainty. The dilemma the designer encounters in early stage design, before calibration, verification, and validation processes start, is to assess the extent of uncertainty for different models. With that, the designer is not sure if a simple model with minor efforts in modeling may be adequate enough with tolerable uncertainty, compared to a more complex model with major efforts in modeling and with, probably, less uncertainty.

The works [1] and [3] introduce a general relation between a real observation from experiments and a mathematical model to identify model form uncertainty. An observation reflects the measured physical outcome, mostly as states like forces, displacement, accelerations, etc. A model must reflect the same outcome, which depends on data and the chosen functional relations. The difference between the outcome of the observation and the model is a combination of quantified

Roland Platz (✉)
Department Mechanical Engineering and Mechatronics, Deggendorf Institute of Technology, Deggendorf, Germany
e-mail: roland.platz@th-deg.de

Z. Mao (eds.), *Model Validation and Uncertainty Quantification, Volume 3*, Conference Proceedings of the Society for Experimental Mechanics Series, https://doi.org/10.1007/978-3-031-04090-0_11

model deviation and measurement uncertainty, including noise. Deterministic or non-deterministic approaches estimate the deviation, for example, as a discrepancy function.

This chapter initially identifies qualitatively the basic deviations between experimental and numerical simulated outcomes of a one-mass oscillator's passive and active vibration isolation capability for different damping cases. The investigated one-mass oscillator is equipped with a velocity feedback controller that realizes passive and active damping. Considering this particular structural dynamic example, Platz et al. so far investigated the influence of data uncertainty on the vibrational behavior in frequency domain by numerical simulations in [8–10]. Lenz et al. [4] conducted experimental investigations with regard to data uncertainty of the same system, introduced in [7] and [11]. The investigations also identified data uncertainty in frequency domain. Data includes model parameters and state variables, and a model determines the functional relation of data. Data uncertainty may appear as *stochastic uncertainty* or *incertitude* [6]. In case of stochastic uncertainty, probabilistic measures such as BAYES-inferred MONTE CARLO simulations process known or assumed distribution functions of data. In case of incertitude, non-probabilistic measures such as FUZZY and interval analysis process membership functions and intervals. *Ignorance* of uncertainty prevails if neither stochastic uncertainty nor incertitude is taken into account.

First, the author gives a brief overview about the scope and limits of the one-mass oscillator, followed by introducing a linear, fully axiomatic analytical low-fidelity model as the simplest virtual representation possible with linear functional relations between model parameters and state variables. The model includes mass, damping, stiffness, and a gain factor for velocity feedback control in case of active vibration isolation as the only model parameters considered so far. In case of passive vibration isolation, the gain factor is zero. Second, a description of the experimental test rig explains the realization of the one-mass oscillator system with options to vary mass, damping, stiffness, and active gain properties for passive and active vibration isolation. Third, different damping case studies used in the mathematical and experimental model give first insights about the different numerical and experimental dynamic responses from impulse excitation. The test results show a rising shift of the system's resonance frequency for higher passive damping rates that is not predicted by the analytical model. Obviously, the current model is too simple, inadequate, or incomplete.

11.2 Analytical Model

A one-mass oscillator is the most simple representation of a vibrating rigid body system to describe linear passive and active vibration isolation for many structural dynamic systems [11]. For example, it is often used for first numerical estimation of a driving car's vertical dynamic behavior [12], Fig. 11.1.

The analytical mathematical model represents only one fourth of the car's chassis and one suspension leg, with the chassis mass m and the suspension leg's damping and stiffness properties: damping coefficient b and the stiffness k in passive configuration. For active configuration, a velocity feedback with gain g is added to provide an active force, Fig. 11.1c. The absolute vertical displacement $z(t)$ of the mass and the base point displacement excitation function $w(t)$ depend on time t. In this most simple analytical model, the base point is assumed without inertia, represented only by a horizontal line. For example, $w(t)$ represents driving on an uneven, bumpy road.

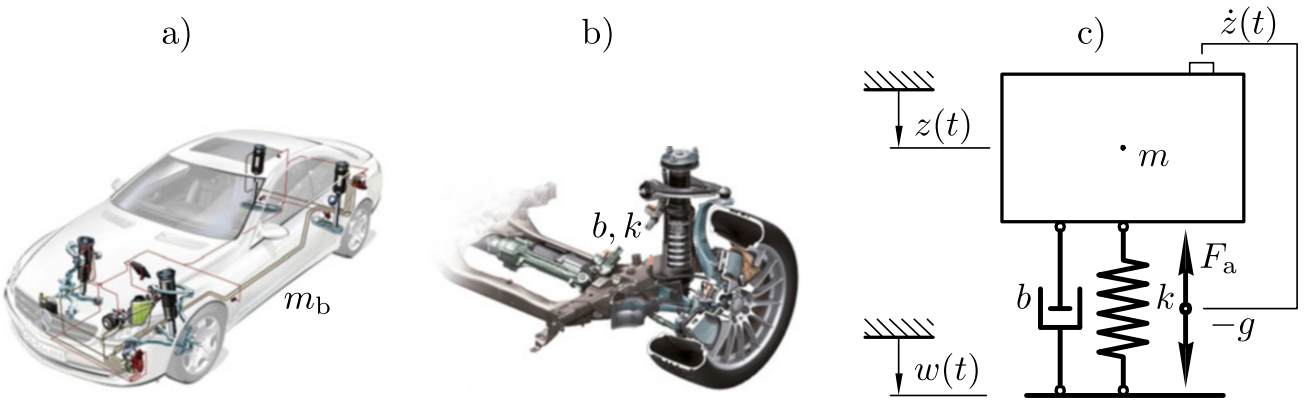

Fig. 11.1 Derivation of a one-mass oscillator, (**a**) automobile (© Auto Reporter/Mercedes Benz) with total mass m_b, (**b**) front suspension leg (Mercedes Benz) with damping b and stiffness k, mass of suspension leg neglected, (**c**) one-mass oscillator model with position excitation $w(t)$ of a massless base point, and active vibration isolation by active velocity feedback control force $F_\mathrm{a} = -g\,\dot{z}$ [11]

The inhomogeneous differential equation of motion for mass m

$$\ddot{z}(t) + \left[2\, D_\mathrm{p}\, \omega_0 + \frac{g}{m}\right] \dot{z}(t) + \omega_0^2\, z(t) = 2\, D_\mathrm{p}\, \omega_0\, \dot{w}(t) + \omega_0^2\, w(t) = \omega_0^2\, r(t) \tag{11.1}$$

of the one-mass oscillator includes the damping ratio D_p from passive damping, $0 < D_\mathrm{p} < 1$, as well as the angular eigenfrequency ω_0, with

$$2\, D_\mathrm{p}\, \omega_0 = \frac{b}{m}, \text{ and } \omega_0^2 = \frac{k}{m}. \tag{11.2}$$

The term $r(t)$ in (11.1) is the general expression of the excitation function multiplied by ω_0^2. In this particular case, it is the linear combination of a damper–spring base point excitation [2].

Vibration Response in Time Domain

In the experimental investigation, see the following chapter, a step excitation following an impulse excitation by a modal hammer on a frame structure excites the oscillating mass, Fig. 11.2 [11]. The unit step function

$$\sigma(t - t_0) = \begin{cases} 0 & \text{for } t < t_0 \\ 1/2 & \text{for } t = t_0 \\ 1 & \text{for } t > t_0 \end{cases} \tag{11.3}$$

is an ideal excitation model of the sudden change from the state 0 for $t < t_0$ to state 1 for $t > t_0$ before or after a certain point of time t_0 [5]. The dynamic system's vibration response

$$z(t) = r_0 \left\{1 - e^{-D\, \omega_0\, t} \left[\cos \omega_D\, t - D \frac{\omega_0}{\omega_D} \sin \omega_D\, t\right]\right\} \tag{11.4}$$

for $t > t_0$ is the sum of the system's free vibration response solution $z_\mathrm{h}(t)$ of the homogeneous equation of motion (11.1), with initial conditions $w(t_0) = 0$ and $\dot{w}(t_0) = 0$, and the forced vibration response

$$r_0 = \frac{1}{\omega_0} 2\, D_\mathrm{p}\, \dot{w}_0 + w_0. \tag{11.5}$$

Equation (11.5) is the assumptive particular solution $z_\mathrm{ih}(t)$ of the inhomogeneous equation of motion (11.1) for $w_0 = w(T_\mathrm{i}) \neq 0$ and $\dot{w}_0 = \dot{w}(T_\mathrm{i}) \neq 0$, when the impulse ends at time T_i [2].

The unit step function applied on the oscillating mass m is assumed being transferred from an impulse on a connected frame structure with mass m_f that realizes the base point shown in the following chapter. Generally, an initial impulse force

$$\check{F} = \int_{t_1}^{t_2} F(t)\, \mathrm{d}t \tag{11.6}$$

is the integral of a force function $F(t)$ within a short time period between t_1 and t_2. Ideally, $F(t)$ reaches infinity if the duration ΔT between t_1 and t_2 becomes infinitesimal small with $\Delta T \to 0$ at $t = t_0$. In this case, it follows the DIRAC-impulse function, also known as DELTA-function

$$\delta(t - t_0) = \begin{cases} 0 & \text{for } t \neq t_0 \\ \infty & \text{for } t = t_0, \end{cases} \tag{11.7}$$

with

$$\int_{-\infty}^{\infty} \delta(t - t_0)\,\mathrm{d}t = 1. \tag{11.8}$$

The impulse to the rigid frame m_f by the hammer impact, Fig. 11.2, is

$$m_\mathrm{f}\,\vec{v}(t_2) - m_\mathrm{f}\,\vec{v}(t_1) = \int_{t_1}^{t_2} \vec{F}(t)\,\mathrm{d}t = \breve{F}, \tag{11.9}$$

with the velocity vectors $\vec{v}(t_1)$ and $\vec{v}(t_2)$ at times t_1 and t_2. For $\Delta T \to 0$ at $t = t_0$, it is assumed that $t_1 = 0$ and $t_2 = t_0$. According to the notation in Fig. 11.2, $\vec{v}(t_0) = \dot{w}(t_0)$, the relation (11.9) leads to

$$m_\mathrm{f}\,\dot{w}(t_0) = \breve{F}(t_0) \tag{11.10}$$

as the impulse applied on the rigid frame m_f. Therefore, the frame's initial velocity, used in (11.5), after impact becomes

$$\dot{w}(t_0) = \frac{\breve{F}(t_0)}{m_\mathrm{f}}. \tag{11.11}$$

Eventually, a force function determines the impulse force $\breve{F}(t_0)$ in (11.6). From experimental tests, the force function

$$F(t) = \begin{cases} \dfrac{\widehat{F}}{2}\left[\sin\left(\Omega_\mathrm{i} t - \dfrac{\pi}{2}\right) + 1\right] & \text{between } 0 \le t \le T_\mathrm{i} \\ 0 & \text{for } t > T_\mathrm{i} \end{cases} \tag{11.12}$$

is approximated with the force amplitude $\widehat{F}$ and a sine function for one short period $\Delta T = 0 \le t \le T_\mathrm{i}$.

Vibration Response in Frequency Domain

The frequency content of the step excitation used in the experiments, and following an impulse on the rigid frame mass m_f in Fig. 11.2, determines the amplitude frequency and phase frequency response [11]. Using

$$\zeta = \frac{\Omega}{m\,\omega_0^2} \quad \text{and} \quad \eta = \frac{\Omega}{\omega_0} \tag{11.13}$$

results in the complex magnifying function

$$\underline{V}(\eta) = \frac{\underline{\widehat{z}}_\mathrm{ih}}{\underline{\widehat{w}}} = \frac{i\,2\,D_\mathrm{p}\,\eta + 1}{1 - \eta^2 + i\,(2\,D_\mathrm{p}\,\eta + g\,\zeta)}, \tag{11.14}$$

with the complex and constant excitation amplitude magnitude $\underline{\widehat{z}}_\mathrm{ih}$ and the complex response amplitude magnitude $\underline{\widehat{w}}$, leading to the amplitude response

$$|\underline{V}(\eta)| = \sqrt{\frac{(2\,D_\mathrm{p}\,\eta)^2 + 1}{(1 - \eta^2)^2 + (2\,D_\mathrm{p}\,\eta + g\,\zeta)^2}} \tag{11.15}$$

and phase response

$$\psi(\eta) = \arctan\,\frac{-2\,D_\mathrm{p}\,\eta^3 - g\,\zeta}{1 - \eta^2 + (2\,D_\mathrm{p}\,\eta)^2 + 2\,D_\mathrm{p}\,\eta\,g\,\zeta}. \tag{11.16}$$

11.3 Experimental Test Setup

Figure 11.2 explains the real test setup concept, with the one-mass oscillator model in Fig. 11.1c embedded in a frame with a relatively heavy mass $m_\mathrm{f} \gg m$. It contains the physical and real representation of the base point for experimental testing. The frame is excited by the force $F(t)$ due to an impulse using a modal hammer; it is connected to the ground via an elastic support with relatively low damping $b_\mathrm{f} \ll b$ and low stiffness $k_\mathrm{f} \ll k$. These properties lead to a quasi-static dynamic response of the frame after the impulse, with a relatively low first eigenfrequency $\omega_{0,\mathrm{f}} \approx 2\pi\ 1/\mathrm{s} \ll \omega_0$, compared to the first eigenfrequency ω_0 of the mass m. It is fair to assume that the forced vibration response $z(t)$ is the result of an assumed one-mass oscillator.

The rigid frame model with mass m_f in Fig. 11.2 is fixed by an idealized gliding support assumed to have no friction perpendicular to the z-direction. The support permits a frame movement only in the z-direction. The frame is constrained by an idealized damper with the damping coefficient b_f and a spring with the stiffness k_f in the z-direction. The frame suspends from a rigid mount via elastic straps vertical to the z-direction, allowing low-frequency pendulum motion of the frame in the z-direction, Fig. 11.3. This motion is the translational absolute excitation displacement $w(t)$ in the z-direction, when the frame is excited by a hammer impulse.

The frame in Figs. 11.2 and 11.3 retains two supports that fix a leaf spring at its ends at A and C, with the effective bending length l on sides A-B and B-C, and with the rigid mass m in the center position at B. The leaf spring is the practical realization of the spring elements in Fig. 11.1c. Its cross-section area is $d\,h$, with the cross-section width d and height h; its stiffness k is a function of the bending stiffness EI; E is the elastic or YOUNG'S modulus of the leaf spring made from carbon fiber reinforced polymer (CFRP); I is the area moment of inertia. The two supports at A and C are adjustable along l to tune the leaf spring's bending deflection and eventually its effective stiffness k. A voice coil actuator (VCA) provides the passive and active damping forces F_b and F_a as the electromotive force

$$F_{\mathrm{S_{VCA}}} = F_b + F_\mathrm{a} = b\,(\dot{z} - \dot{w}) + g\,\dot{z} = r\,l_\mathrm{c}\,i \cdot B = \Psi\,i \tag{11.17}$$

detected via the sensor $\mathrm{S_{VCA}}$, Fig. 11.3, [11] and [7]. It is expressed by the force constant Ψ, the length of the coil l_c, and the ratio r of the effective coil length, the magnetic flux density B, and the electrical current i, if B and i are perpendicular to each other. The VCA's driving electrical power is

$$P = u_\mathrm{VCA}\,i = F_{\mathrm{S_{VCA}}}\,v \tag{11.18}$$

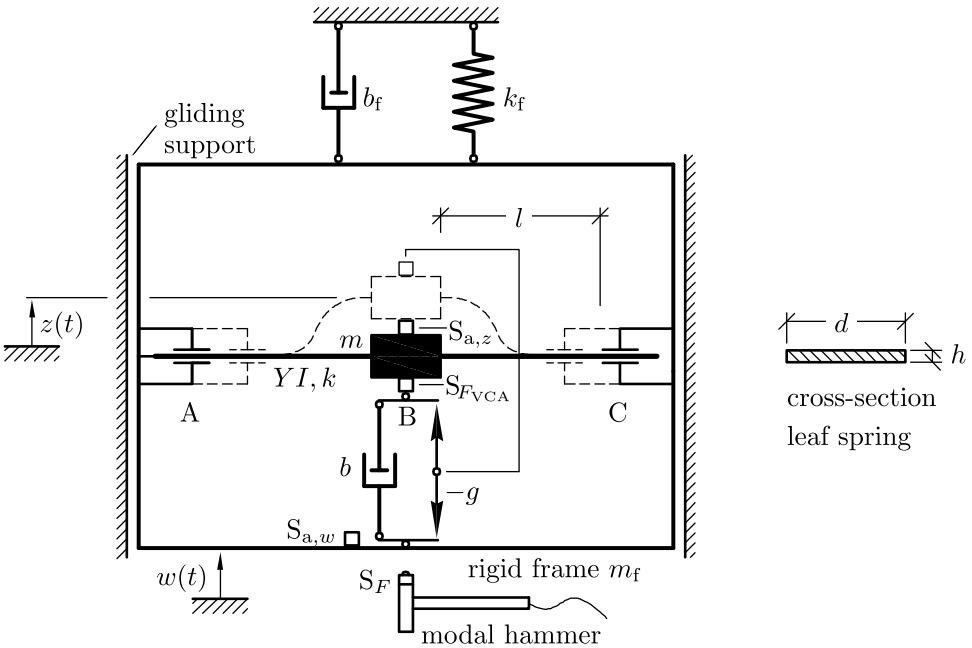

Fig. 11.2 One-mass oscillator—schematic diagram of real test setup with an additional rigid frame mass m_f excited by a modal hammer

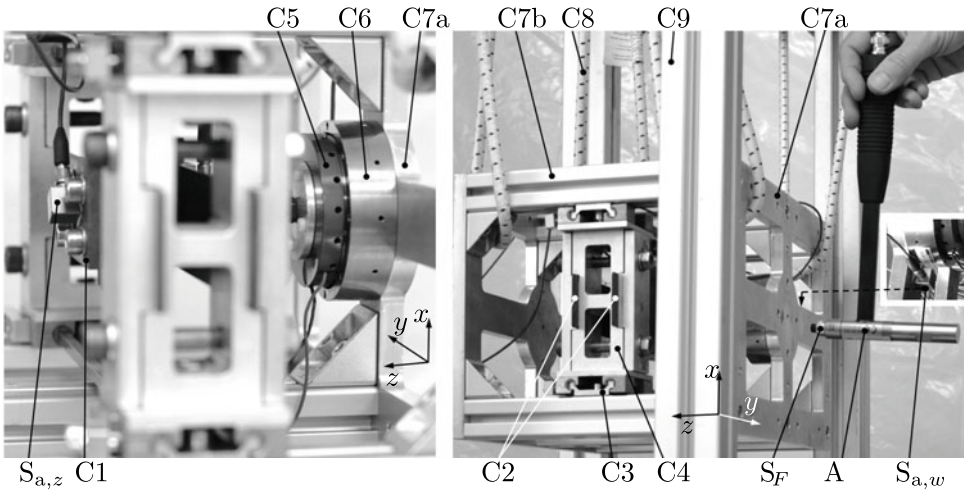

Fig. 11.3 Physical test setup—left: assembly of leaf spring and VCA; right: hammer impulse on frame; the components are: acceleration sensor $S_{a,z}$ attached to the oscillating mass C1, two leaf springs C2 with partial stiffness $k/2$ on each side of C1, glide support C3, fixed leaf spring support C4, VCA coil support/holder C5, VCA stator, magnet outer ring C6, front/side structure of rigid frame C7a/b with total mass m_f, elastic strap C8, mount C9 to suspend the frame with elastic straps, acceleration sensor $S_{a,w}$ (hidden behind the frame) on the frame mass m_f, and force sensor S_F measuring the impulse force from the model hammer A

and equivalent to the driving mechanical power $F_{S_{VCA}}\, v$. The driving voltage $u_{VCA} = \Psi\, v$ initiates the electromotive force $F_{S_{VCA}}$. The VCA's properties such as inductance L, Ohmic resistance R, and force constant Ψ lead to the control voltage

$$u = \Psi\, v + \frac{\mathrm{d}i}{\mathrm{d}t} L + i\, R. \tag{11.19}$$

Eventually, the applied control voltage

$$u = \left\{ \Psi\, (\dot{z} - \dot{w}) + \frac{\mathrm{d}}{\mathrm{d}t} \left[\frac{1}{\Psi} \left(b(\dot{z} - \dot{w}) + g\dot{z} \right) \right] L + \frac{1}{\Psi} \left(b(\dot{z} - \dot{w}) + g\dot{z} \right) R \right\} \tag{11.20}$$

depends on the relative velocity $\dot{z} - \dot{w}$ between the frame and the mass to provide the passive damping force, and on the absolute velocity $\dot{z}$ of the mass to provide the active force F_a. It depends directly on b and g.

The stiffness

$$k^* = \frac{12\, E\, I}{l^3} \tag{11.21}$$

derives from one leaf spring's flexural bending stiffness $E\, I$ with respect to the length l between A and B, and between B and C, Fig. 11.2. The effective stiffness with four leaf springs becomes $k = 4 \cdot k^*$. It is the sum of four added stiffnesses, linearity assumed, with two leaf springs at each side A–B and B–C of the mass m.

Two acceleration sensors $S_{a,z}$ and $S_{a,w}$ measure the absolute accelerations $\ddot{z}(t)$ and $\ddot{w}(t)$ of the mass and the frame. The absolute accelerations are transformed into absolute velocities $\dot{z}(t)$ and $\dot{w}(t)$ by numerical integration in the SIMULINK-DSPACE™environment. The masses of the sensors $S_{a,z}$, $S_{F_{VCA}}$, and of the leaf spring, are considered parts of the oscillating mass m. Gravitational forces are neglected, and the directions of $z(t)$ and $w(t)$ of the test rig are perpendicular to gravitation.

The amplitude and phase estimation

$$|\underline{V}_e(\Omega)| = |H_2(\Omega)| = \left| \frac{S_{\tilde{\ddot{z}},\, \tilde{\ddot{z}}}(\Omega)}{S_{\tilde{\ddot{z}},\, \tilde{\ddot{w}}}(\Omega)} \right|, \quad \psi_e(\Omega) = \angle\, H_2(\Omega) \tag{11.22}$$

process the auto-power and cross-power spectral densities $S_{\tilde{\ddot{z}},\, \tilde{\ddot{z}}}(\Omega)$ and $S_{\tilde{\ddot{z}},\, \tilde{\ddot{w}}}(\Omega)$ from the measured mass acceleration response $\tilde{\ddot{z}}(t)$, and from the frame acceleration excitation $\tilde{\ddot{w}}(t)$ from hammer excitation, averaged 5 times. The signals take into account normal perturbations from inexact and manual handling of the impulse hammer during averaging, marked by

the tilde $\tilde{}$. The well-known estimator $H_2(\Omega)$ leads to relatively small response errors in resonance compared to higher errors for anti-resonances. The coherence evaluates the quality of the measurements and is further explained in [11].

11.4 Numerical and Experimental Vibration Isolation Responses

As the results of numerical simulation and experimental test, Figs. 11.4 and 11.5 show the simulated and measured excitation forces $F(t)$ (11.12) and $F_e(t)$, as well as the simulated velocity and acceleration responses $\dot{z}(t)$ and $\ddot{z}(t)$ as first and second time derivations of (11.4), and the measured responses $\dot{z}_e(t)$ and $\ddot{z}_e(t)$ from six different damping cases in time domain. For both numerical simulation and experimental test, the damping cases are:

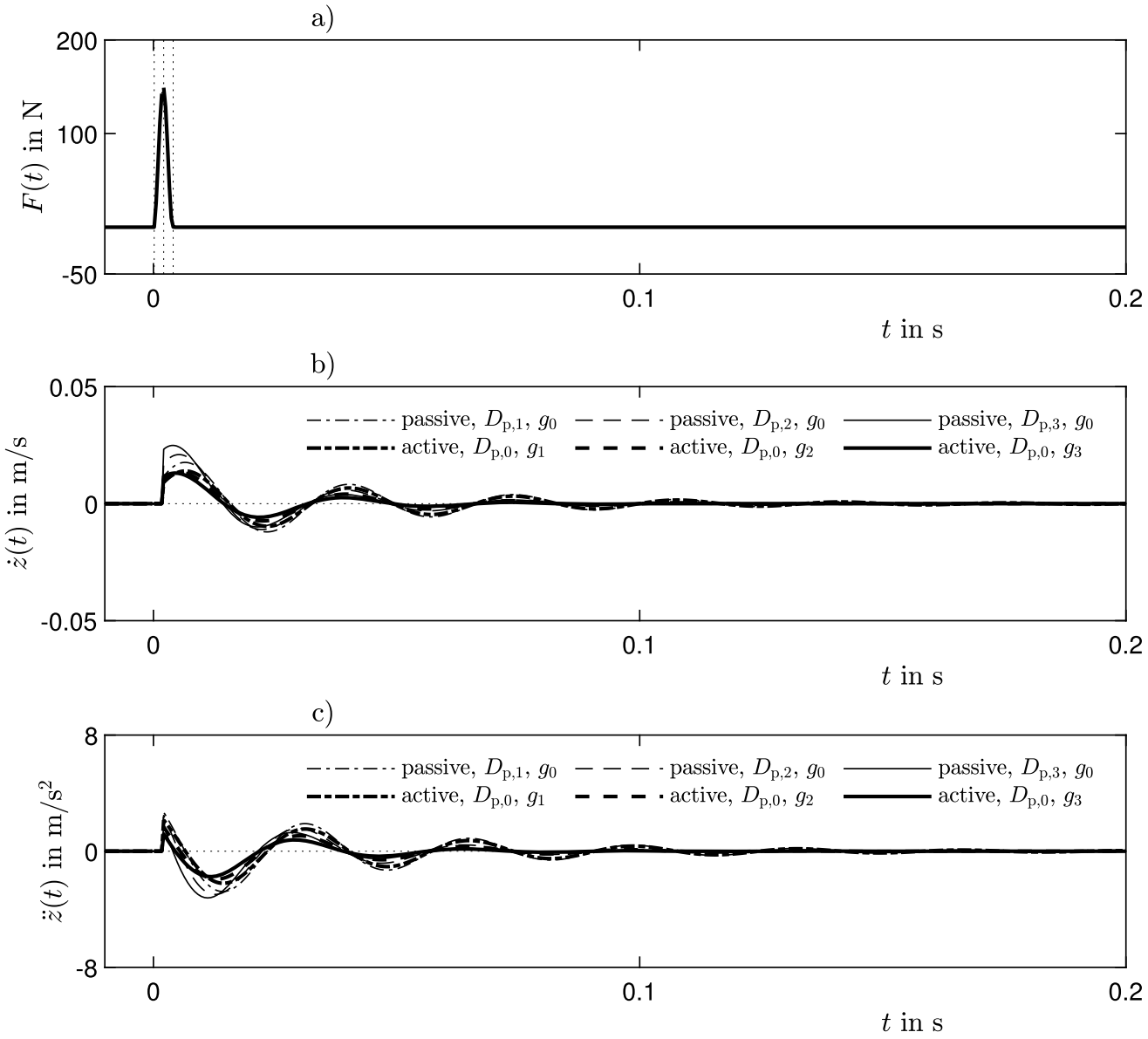

Fig. 11.4 Enforced vibration responses of the mass m in time domain after *numerical simulation* due to (**a**) force $F(t)$ from an impulse, (**b**) velocity response $\dot{z}(t)$, (**c**) acceleration response $\ddot{z}(t)$, responses with three passive damping cases (i) b_1, g_0, (ii) b_2, g_0, and (iii) b_3, g_0, and three active damping cases (iv) b_0, g_1, (v) b_0, g_2, and (vi) b_0, g_3

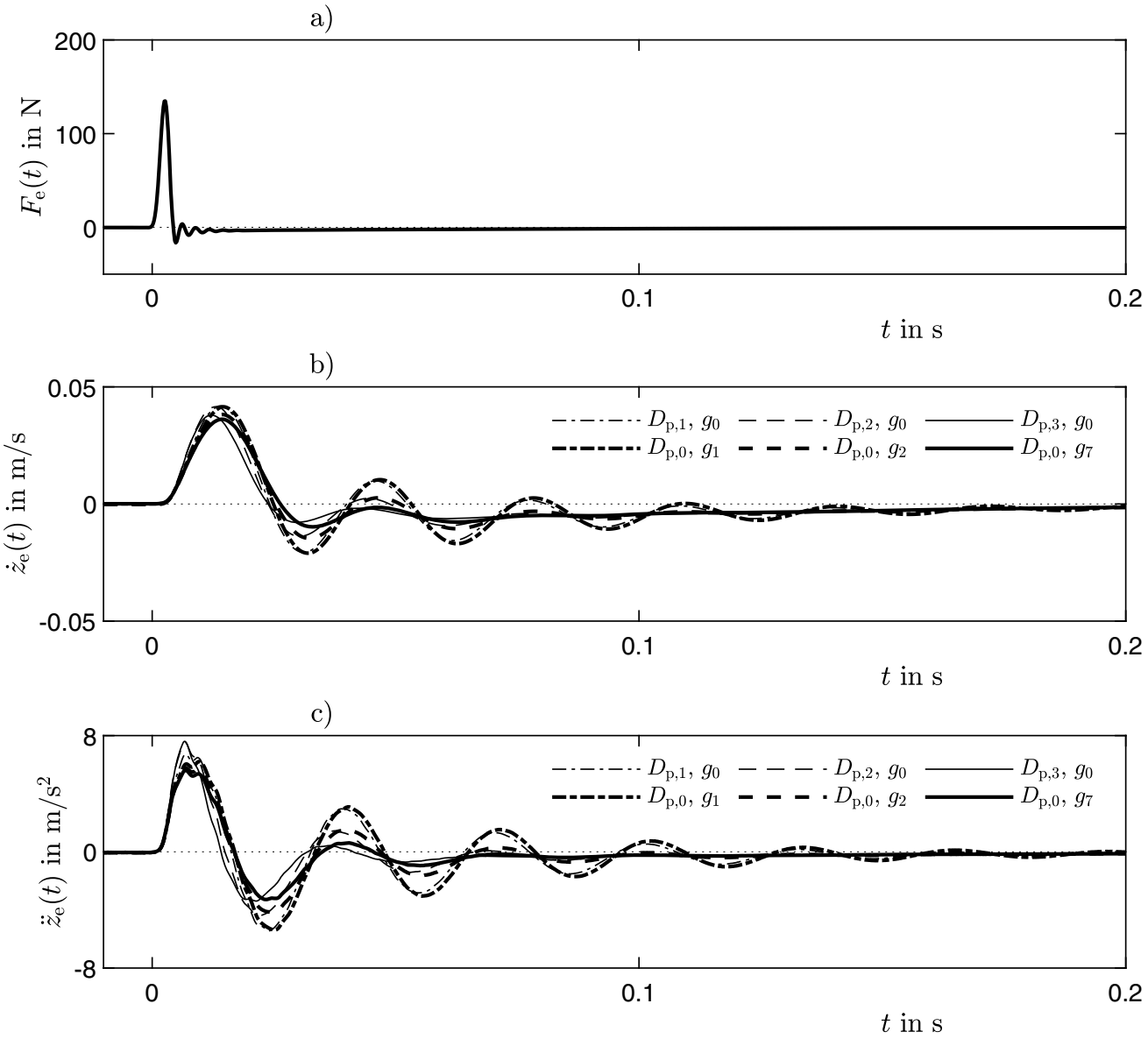

Fig. 11.5 Enforced vibration responses of the mass m in time domain after *experimental test* due to (**a**) force $F_e(t)$ from an impulse, (**b**) velocity response $\dot{z}_e(t)$, (**c**) acceleration response $\ddot{z}_e(t)$, responses with three passive damping cases (i) b_1, g_0, (ii) b_2, g_0, and (iii) b_3, g_0, and three active damping cases (iv) b_0, g_1, (v) b_0, g_2, and (vi) b_0, g_3

- (i) $D_{p,1}$, g_0, (ii) $D_{p,2}$, g_0, (iii) $D_{p,3}$, g_0,
  with $D_{p,1} < D_{p,2} < D_{p,3}$ and $g_0 = 0$ Ns/m for passive damping.
- (iv) $D_{p,0}$, g_1, (v) $D_{p,0}$, g_2, (vi) $D_{p,0}$, g_3,
  with $g_1 < g_2 < g_3$ and $b_0 = 18.3$ Ns/m for active damping.

The passive damping ratios are assumed $D_{p,0} = 0.053$, $D_{p,1} = 0.120$, $D_{p,2} = 0.200$, and $D_{p,3} = 0.280$. The active gain factors are $g_1 = 22$ Ns/m, $g_2 = 46$ Ns/m, and $g_3 = 68$ Ns/m.

For the same damping cases, Figs. 11.6 and 11.7 show the phase frequency responses $\psi(\eta)$ (11.16) and $\psi_e(\eta)$ (11.22), as well as the amplitude frequency responses $|\underline{V}(\eta)|$ (11.15) and $|\underline{V}_e(\eta)|$ (11.22) after numerical simulation and experimental test.

First of all, it is worth noting that the numerical and experimental results in frequency domain in Fig. 11.6 and 11.7 confirm the improved vibration isolation effect for the active damping cases (iv), (v), and (vi). A strong vibration isolation effect for frequencies higher than resonance frequencies is present with increasing active damping, compared to the passive

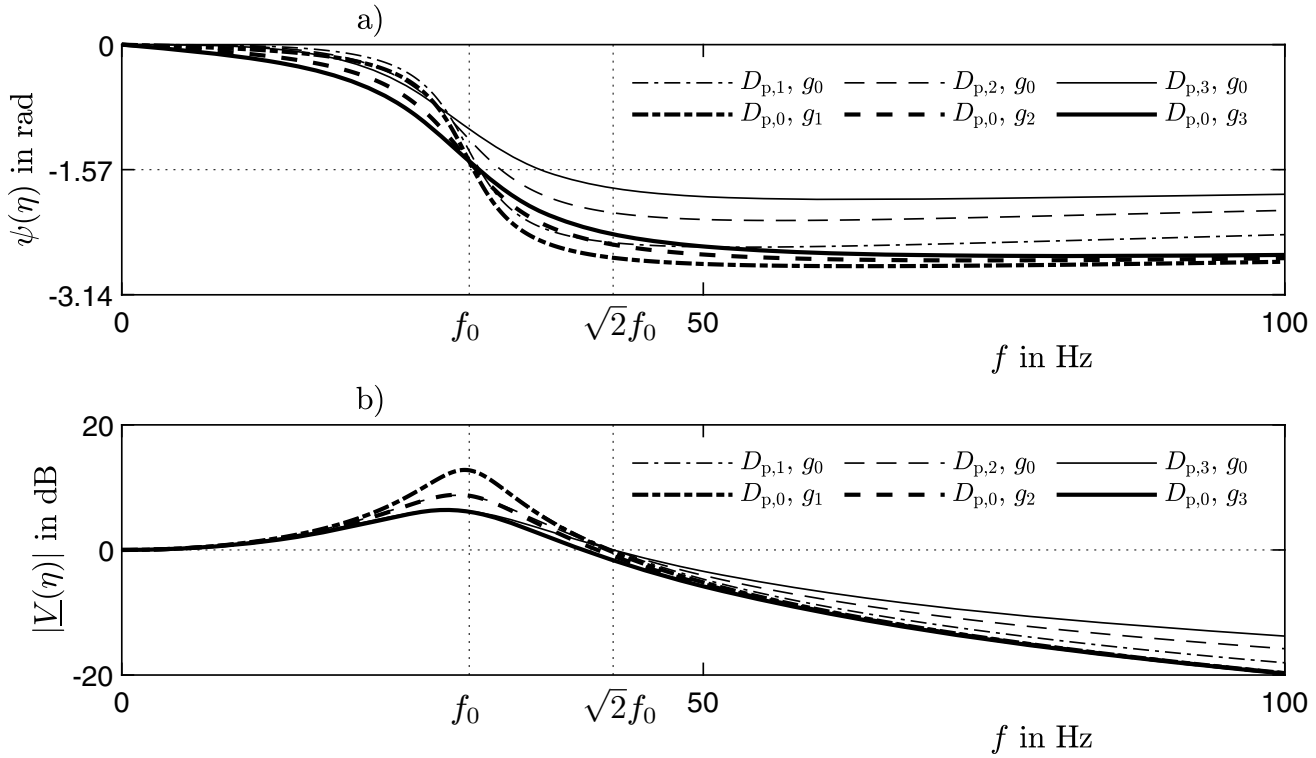

Fig. 11.6 Enforced vibration responses of the mass m in frequency domain after *numerical simulation*, (**a**) phase frequency response $\psi(\eta)$, (**b**) amplitude frequency response $|\underline{V}(\eta)|$, responses with three passive damping cases (i) b_1, g_0, (ii) b_2, g_0, and (iii) b_3, g_0, and three active damping cases (iv) b_0, g_1, (v) b_0, g_2, and (vi) b_0, g_3

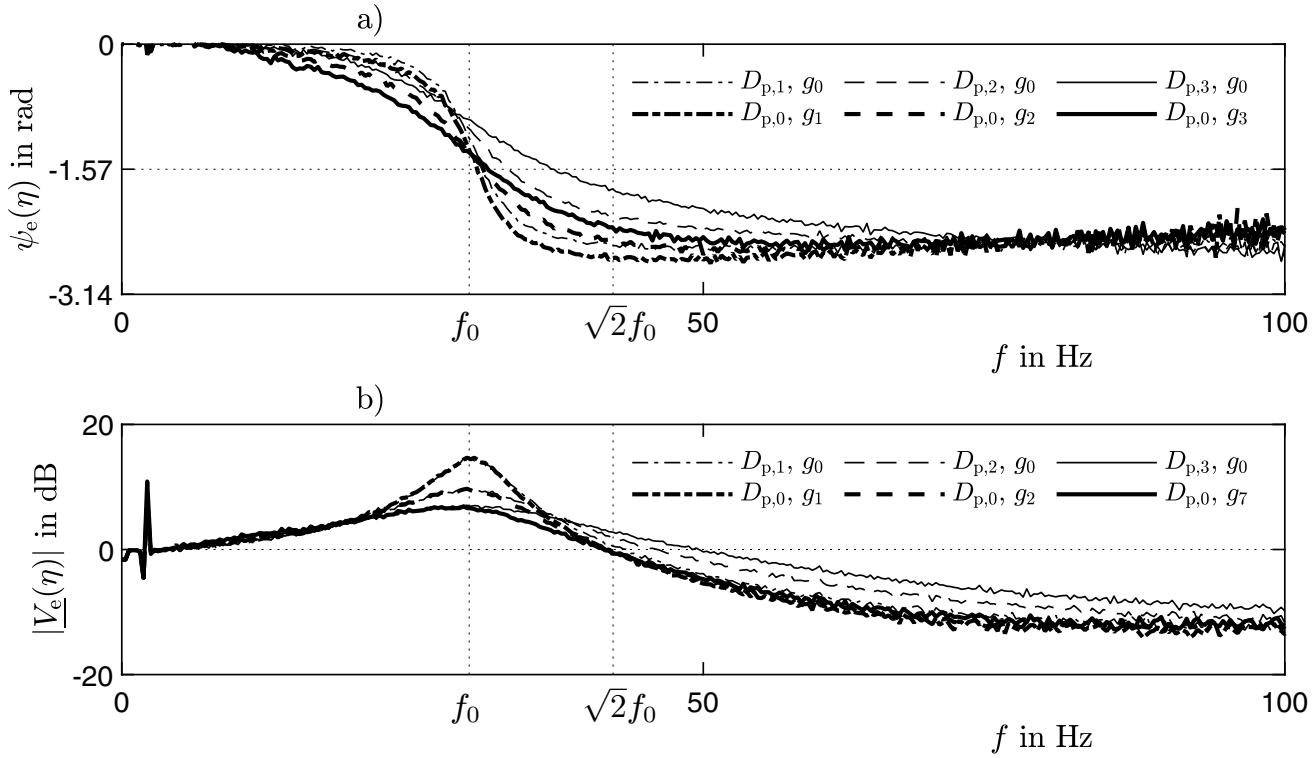

Fig. 11.7 Enforced vibration responses of the mass m in frequency domain after *experimental test*, (**a**) phase frequency response $\psi_e(\eta)$, (**b**) amplitude frequency response $|\underline{V}_e(\eta)|$, responses with three passive damping cases (i) b_1, g_0, (ii) b_2, g_0, and (iii) b_3, g_0, and three active damping cases (iv) b_0, g_1, (v) b_0, g_2, and (vi) b_0, g_3

cases (i), (ii), and (iii). Second, increasing passive damping leads to a shift in the system's eigenfrequency to the right. With increasing gain in the active configuration, this shift does not appear as strong. Even after calibration of model parameters as shown in [11], relatively high deviation in both the calibrated damping coefficient and active gain compared to the initially guessed values remains.

11.5 Summary and Outlook

This current state of investigation is the basis for successive and extensive research on evaluating the model form uncertainty. The current analytical, linear, and fully axiomatic model is considered being the simplest model form possible. It represents the modeling reference state. Alternative models use additional empirical correction factors, use a priori both axiomatic and empiric functional relations, use finite elements or a multi-body approach, and use more degrees of freedom. These high-fidelity models are expected to gradually lower model form uncertainty. However, due to their higher complexity, modeling efforts are costly. Therefore, the author pursues a new measure to quantify model form uncertainty. It takes the costs of modeling as well as the efforts in model verification and validation into consideration and compares them to the gain in reducing model form uncertainty.

The existing test environment allows reproducible, consistent, and comparable validation of different models of always the very same oscillator. It also allows to assess differences between the passive and active vibration isolation with respect to uncertainty to reach the desired isolation effect. For a comprehensive and sufficient study of model form uncertainty considering the one oscillator, a great variety of low- and high-fidelity models are possible. The author proposes a round robin approach within the track *Model Validation and Uncertainty Quantification MVUQ* offered by the SOCIETY OF EXPERIMENTAL MECHANICS SEM. The members are invited to use the experimental data and contribute with own approaches to quantify model form uncertainty using their own models of the very same one-mass oscillator for passive and active vibration isolation. They are asked to share their results and being part of a broad research collaboration. The outcomes are presented in a separate session within MVUQ at the following IMAC conferences.

Acknowledgments This research was funded by the Deutsche Forschungsgemeinschaft (DFG, German Research Foundation) within the Sonderforschungsbereich (SFB, Collaborative Research Center) 805 "Control of Uncertainties in Load-Carrying Structures in Mechanical Engineering"—project number: 57157498.

References

1. Higdon, D., Gattiker, J., Williams, B., Rightley, M.: Computer model calibration using high-dimensional output. J. Am. Stat. Assoc. **103**(482), 570–583 (2008). https://doi.org/10.1198/016214507000000888
2. Irretier, H.: Basics in Vibration Technology (Grundlagen der Schwingungstechnik). Studium Technik (2000)
3. Kennedy, M.C., O'Hagan, A.: Bayesian calibration of computer models. J. R. Stat. Soc. B (Stat. Methodol.) **63**(3), 425–464 (2001). https://doi.org/10.1111/1467-9868.00294
4. Lenz, J., Platz, R.: Quantification and evaluation of parameter and model uncertainty for passive and active vibration isolation. In: IMAC–bXXXVII A Conference and Exposition on Structural Dynamics, Jan. 28–31, 2019, Orlando, Fl, pp. 135–147 (2020)
5. Markert, R.: Strukturdynamik (Structural Dynamics). Textbook. Shaker Verlag (2013)
6. Melzer, C.M., Platz, R., Melz, T.: Comparison of methodical approaches to describe and evaluate uncertainty in the load-bearing capacity of a Truss structure, in *Fourth International Conference on Soft Computing Technology in Civil Engineering, Sept. 1–4, Prague* (2015)
7. Perfetto, S., Rohlfing, J., Infante, F., Mayer, D., Herold, S.: Test rig with active damping control for the simultaneous evaluation of vibration control and energy harvesting via piezoelectric transducers. J. Phys. Conf. Ser. **744**, 012010 (2016)
8. Platz, R., Ondoua, S., Enss, G.C., Melz, T.: Approach to evaluate uncertainty in passive and active vibration reduction, in *IMAC–XXXII A Conference and Exposition on Structural Dynamics, Feb. 3–6, Orlando, FL*, pp. 345–352 (2014)
9. Platz, R., Enß, G.C.: Comparison of uncertainty in passive and active vibration isolation. In: IMAC–XXXIII A Conference and Exposition on Structural Dynamics, Feb. 2–5, Orlando, FL, pp. 15–25 (2015)
10. Platz, R., Melzer, C.: Uncertainty quantification for decision making in early design phase for passive and active vibration isolation. In: ISMA 2016 Including USD 2016 International Conference on Uncertainty in Structural Dynamics, Sept. 19–21, Leuven, pp. 4501–4513 (2016)
11. Platz, R.: Approach to assess basic deterministic data and model form uncertainty in passive and active vibration isolation. In: Pelz, P.F., Groche, P. (eds.), Uncertainty in Mechanical Engineering, pp. 208–223. Springer International Publishing, Cham (2021)
12. Vöth, S.: Dynamik schwingungsfähiger Systeme (Dynamics of vibrations systems). Vieweg & Sohn Verlag, Wiesbaden (2006)

Chapter 12
An Optimal Sensor Network Design Framework for Structural Health Monitoring Using Value of Information

Mayank Chadha, Zhen Hu, Charles R. Farrar, and Michael D. Todd

Abstract A structural health monitoring (SHM) system is essentially an information-gathering mechanism. The information accumulated via an SHM system is crucial in making appropriate maintenance decisions over the life cycle of the structure. An SHM system is feasible if it leads to a greater *expected reward* (by making data and risk-informed decisions) than the intrinsic cost (or *investment risk*) of the information-acquiring mechanism incurred over the lifespan of the structure. In short, the *value of information* acquired through a feasible SHM system manifest into net positive expected cost savings over the life cycle of the structure. Traditionally, the cost-benefit analysis of an SHM system is carried out through pre-posterior decision analysis that helps one evaluate the benefit of an information-gathering mechanism using the expected value of information (EVoI) metric. EVoI is a differential measure and can be mathematically expressed as a difference between the *expected reward* and *investment risk*. Therefore, by definition, EVoI fails to capture the compounded savings over the life cycle of the structure (since it quantifies absolute savings). Unlike EVoI, we quantify the economic advantage of installing an SHM system for inference of the structural state by using a normalized expected-reward (benefit of using an SHM system) to investment-risk (cost of SHM over the life cycle) ratio metric (also called a risk-adjusted reward in short) as the objective function to quantify the value of information (VOI). We consider monitoring of a miter gate as the demonstration example and focus on the inference of an unknown and uncertain state parameter(s) (i.e., damage from loss of contact between gate and wall, the "gap") from the acquired sensor data. This paper proposes a sensor optimization framework that maximizes the net expected compounded savings achieved as a result of making SHM system-acquired data-informed life cycle management decisions. We also inspect the impact of various risk intensities of decision-makers on the optimal sensor design.

Keywords Value of information · Bayesian optimization · Behavioral psychology · Structural health monitoring · Sensor design

12.1 Introduction

This paper briefly describes a sensor optimization framework with a target of maximizing the net savings as a consequence of using an SHM system over the life cycle of the structure. Conventionally, the cost-benefit analysis of an SHM system is carried out through pre-posterior decision analysis using the expected value of information (EVoI) metric (a differential metric). We use *expected value of information* (EVoI) (a differential metric) and *risk-adjusted reward* (a normalized metric) as an optimality criterion. Finally, the goal of this research is to obtain the optimal sensor network design that maximizes the value of information over the life cycle of the structure.

M. Chadha · M. D. Todd (✉)
Department of Structural Engineering, University of California San Diego, La Jolla, CA, USA
e-mail: machadha@ucsd.edu; mdtodd@eng.ucsd.edu

Z. Hu
Department of Industrial and Manufacturing Systems Engineering, University of Michigan-Dearborn, Dearborn, MI, USA
e-mail: zhenhu@umich.edu

C. R. Farrar
Engineering Institute, Los Alamos National Laboratory, Los Alamos, NM, USA
e-mail: farrar@lanl.gov

Z. Mao (eds.), *Model Validation and Uncertainty Quantification, Volume 3*, Conference Proceedings of the Society for Experimental Mechanics Series, https://doi.org/10.1007/978-3-031-04090-0_12

12.2 Value of Information Metric

Consider an SHM-based decision-making problem. Let the state of the structure at time $t \in \Omega_T$ be defined by an uncertain state-parameter vector denoted by $\Theta(t)$ with a realization $\theta(t) \in \Omega_{\Theta(t)}$. The data acquired by the SHM system $z \in \Omega_Z$ at time t is defined by a random variable $X_z(t)$, where $x_z(t) \in \Omega_{X_z(t)}$ denote an observed realization. The goal of an SHM system is to recommend a maintenance strategy selected from a set of predefined choices $\Omega_D = \{d_0, d_1, \ldots, d_n\}$. For a risk profile of the decision-maker parameterized by (γ, ξ), let $L(d_i, \theta_{\text{true}}; \gamma, \xi)$ denote the consequence cost/regret/loss function that defines the total perceived loss as a consequence of making the decision d_i when the true state of the structure is $\theta_{\text{true}}(t)$ at time t (see [1, 2]). To obtain the benefit of an SHM system in the design phase, we require the following:

1. We need a probabilistic state-parameter evolution model (see [2]). Let $\Theta(t)$ denote a random variable representing the state parameter at a time instance $t \in \Omega_T$. The prior state-parameter evolution model is then quantified by $f_{\Theta(t)}(\theta(t))$.
2. We need an inflation-adjusted cost function. The factor $(r(t)+1)^t$ adjusts for the future inflation, where $r(t)$ is the assumed future monthly rate of inflation at time t in months. We consider four types of costs:

- **Cost A**: The inflation-adjusted consequence-cost of decision making at time t, denoted by $\tilde{L}\left(d_j, \theta_{\text{true}}(t), t; \gamma, \xi\right) = L\left(d_j, \theta_{\text{true}}(t); \gamma, \xi\right).(r(t)+1)^t$. The inspection and maintenance decisions are usually carried out at discrete time steps.
- **Cost B and Cost C:** The maintenance (cost B) and operation (cost C) cost of the SHM system, denoted by $C_M(t) = C_M.(r(t)+1)^t$ and $C_O(t) = C_O.(r(t)+1)^t$, respectively. Here, C_M denotes the current estimated cost for one instance of maintenance of the system, and C_O denotes the currently estimated operation cost per month. We assume that the maintenance is done periodically.
- **Cost D:** The cost of design and initial installation of an information gathering system $C(z)$. We assume this to be an initial cost and hence time-independent.

When new data/measurement $x_z(t) \in \Omega_{X_z(t)}$is obtained, the state of the structure is updated by obtaining the posterior distribution of the state parameter, denoted by $f_{\Theta|\mathrm{X_z}}(\theta|x_z)$, using Bayesian inference (see [3]). The updated posterior state-parameter evolution model, denoted by $f_{\Theta(t)|\mathrm{X_z}(t)}(\theta(t)|x_z(t))$, is obtained by using Bayesian inference utilizing the measurement data simulated by a finite element model that is assumed to be the ground truth.

The EVoI of the design z for a risk profile (γ, ξ) at a given time instance is defined as:

$$\text{EVoI}(z, t; \gamma, \xi) = C_{\text{save}}(z; \gamma, \xi) - C(z) \tag{12.1a}$$

$$C_{\text{save}}(z, t; \gamma, \xi) = E_{X_z(t)}\left[\min_{d_i} \tilde{L}\left(d_j, \theta_{\text{true}}(t), t; \gamma, \xi\right)\right] - \min_{d_i} E_{\Theta(t)}\left[\tilde{L}\left(d_j, \theta_{\text{true}}(t), t; \gamma, \xi\right)\right] \tag{12.1b}$$

Here, $C_{\text{save}}(z, t; \gamma, \xi)$ gives the expected cost saved by making a better decision based on newly acquired measurements through the mechanism z at time t for the risk profile (γ, ξ). The EVoI over the life cycle for an SHM system z for the risk profile (γ, ξ), denoted by $\text{EVoI}_{\text{LC}}(z; \gamma, \xi)$, and the risk-adjusted reward, denoted by $\lambda_{\text{LC}}(z; \gamma, \xi)$ is then defined as (derived in Chadha et al. [3]):

$$\text{EVoI}_{\text{LC}}(z; \gamma, \xi) = C_{\text{saveLC}}(z; \gamma, \xi) - (C(z) + C_{M\&O}(z)) \tag{12.2a}$$

$$\lambda_{\text{LC}}(z; \gamma, \xi) = \frac{C_{\text{saveLC}}(z; \gamma, \xi)}{(C(z) + C_{M\&O}(z))} \tag{12.2b}$$

The quantity $C_{\text{saveLC}}(z; \gamma, \xi)$ denotes the expected savings over the life cycle of the structure as a consequence of making data-informed decision-making for the risk profile (γ, ξ), such that:

$$C_{\text{saveLC}}(z;\gamma,\xi) = \sum_{n=1}^{N_A}\left(\min_{d_i} E_{\Theta(t_{A_n})}\left[\tilde{L}\left(d_j,\theta_{\text{true}}\left(t_{A_n}\right),t_{A_n};\gamma,\xi\right)\right]\right) - \sum_{n=1}^{N_A}\left(E_{X_z(t_{A_n})}\left[\min_{d_i} E_{\Theta(t_{A_n})|X_z(t_{A_n})}\left[\tilde{L}\left(d_j,\theta_{\text{true}}\left(t_{A_n}\right),t_{A_n};\gamma,\xi\right)\right]\right]\right) \tag{12.3}$$

An SHM system is feasible if it satisfies either of these equivalent conditions:

$$\text{EVoI}_{\text{LC}}(z) \geq 0, \text{ or } \lambda_{\text{LC}}(z) \geq 1. \tag{12.4}$$

Among many SHM system designs, optimal designs z_{EVoI} and z_λ are obtained as:

$$z_{\text{EVoI}} = \arg\max_{z\in\Omega_Z} \text{EVoI}_{\text{LC}}(z), \text{ and } \; z_\lambda = \arg\max_{z\in\Omega_Z} \lambda_{\text{LC}}(z) \tag{12.5}$$

We obtain the optimal sensor design using $\text{EVoI}_{\text{LC}}(z)$ and $\lambda_{\text{LC}}(z)$ as the objective functional by deploying the Bayesian optimization algorithm described in Yang et al. [3].

12.3 Application to Miter Gates

Let the state of the miter gate be completely defined by the loss of boundary contact (or a "gap") between the gate and the concrete wall at the bottom of the gate, such that $\theta \in \Omega_\Theta = [\theta_{\min} = 0, \theta_{\max} = 180 \text{ in}]$. Consider a binary decision-space $\Omega_D = \{d_0, d_1\}$, such that d_0 is a decision to not do specified maintenance and d_1 is a decision to perform some specified maintenance. Figure 12.1a below shows the optimal sensor network design z_{EVoI} obtained using Eq. (12.5) and the optimization algorithm delineated in Yang et al. [3]. It was observed that the Bayesian algorithm picked two sensors close to the gap (encircled with red) leading to maximum $\text{EVoI}_{\text{LC}}(z_{\text{EVoI}})$. However, for comparison purposes, we consider the optimal design z_{EVoI} and the random design z_{random} to have five sensors. This shows that effectively, the optimal design would consist of a smaller number of sensors.

We observe that the optimal sensor design leads to a higher expected value of information at an intermediate time period (5–30 months). Beyond this time period, the structural damage is high enough that a conservative decision-maker (the

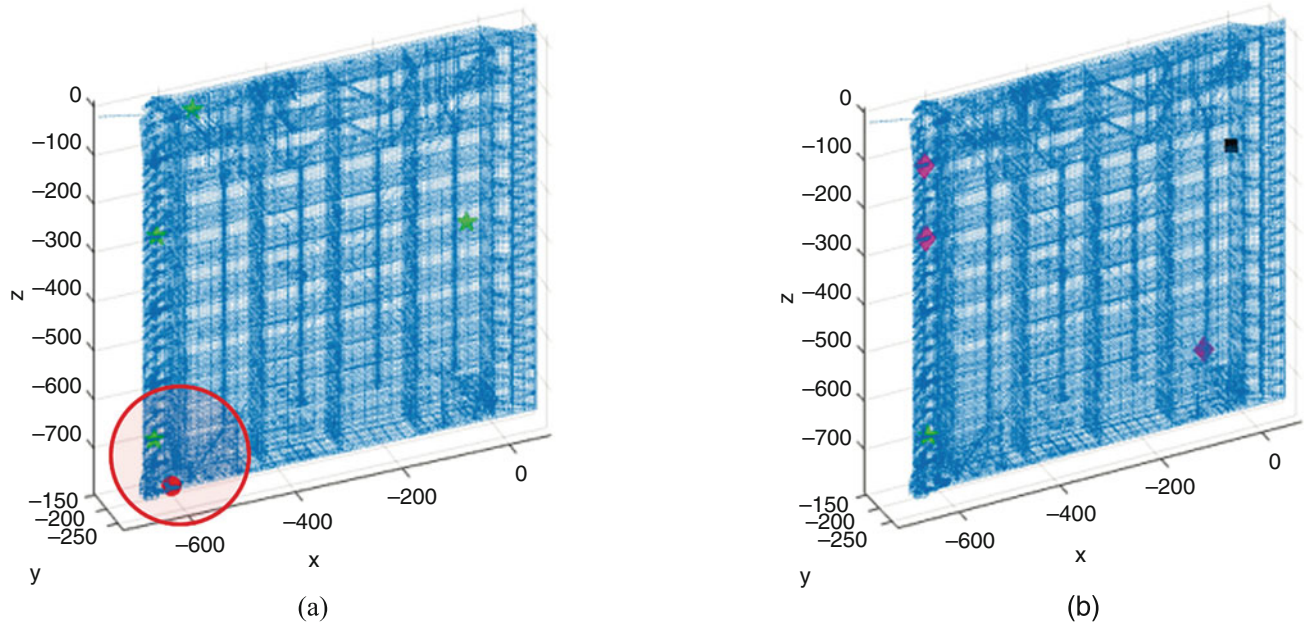

Fig. 12.1 Miter gate and the sensor network design considering conservative decision profile. (**a**) Optimal sensor design z_{EVoI}. (**b**) Random design z_{random}

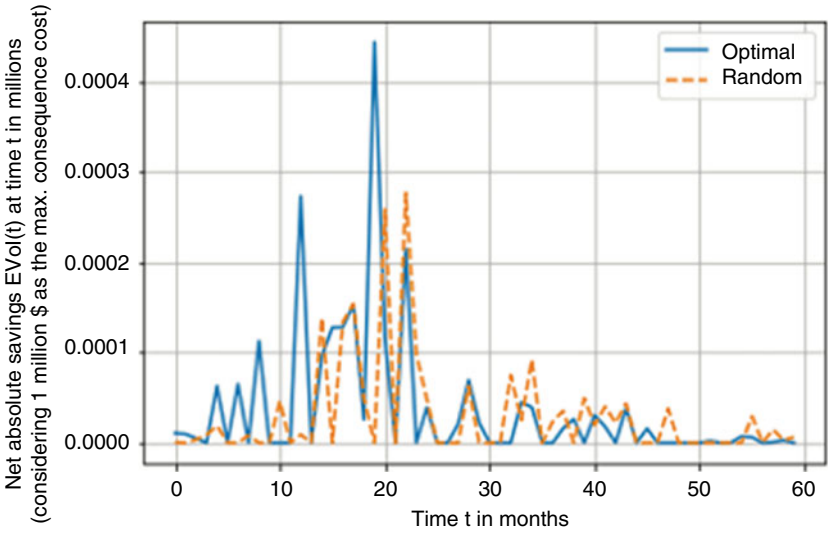

Fig. 12.2 Comparison of EVoI$(z, t; \gamma, \xi)$ for optimal and random design at various time instances

considered profile for the simulation) would recommend maintenance be carried out irrespective of the SHM design used to obtain the measurements. Therefore, for higher damage levels, decisions obtained using optimal design and random design are the same. The EVoI$(z, t; \gamma, \xi)$ is not smooth in Fig. 12.2 because lower particle numbers were used for Bayesian inference using the particle filter technique. This was done to reduce computational costs.

12.4 Conclusions

This paper briefly details the mathematical formulation behind a sensor optimization framework that aims at maximizing the net cost saving over the life cycle of the structure. The idea targets the core of an SHM system and attempts to come up with the most optimal data acquisition system design. This is currently ongoing research.

References

1. Chadha, M., Ramancha, M.K., Vega, M.A., Conte, J.P., Todd, M.D.: The role of risk profile in state determination of structures. In: Proceedings 10th International Conference on Structural Health Monitoring (SHMII-10 Conference), Porto, Portugal, June 30–July 2 (2021)
2. Chadha, M., Hu, Z., Todd, M.D.: An alternative quantification of the value of information in structural health monitoring. In: Structural Health Monitoring: Value of Information Perspective. Sage (2021)
3. Yang, Y., Chadha, M., Hu, Z., Parno, M., Todd, M.D.: A probabilistic sensor design approach for structural health monitoring using risk-weighted f-divergence. Mech. Syst. Signal Process. **161**, 107920 (2021)

Chapter 13
Uncertainty Effects on Bike Spoke Wheel Modal Behaviour

E. Bonisoli, A. D. Vella, and S. Venturini

Abstract In bicycles, one of the components which mostly influences the global system dynamics is the wheel-tyre subsystem. In this paper, the modal behaviour of a bike spoke wheel is numerically and experimentally investigated focusing on the characterisation of the spoke pretension effect, role of boundary conditions and parameter uncertainties.

A linearised parametric finite element model (FEM) is developed with the open-source code LUPOS in Matlab® environment. A detailed description of the model which includes several components, i.e. rim, hub, spokes and hub gears, is given. The FEM model is based on a reduced set of key nodes belonging to the wheel cross section profile, material and geometrical characteristic assignment and automated meshing procedure, allowing reduced computational effort and high model accuracy.

Experimental modal analysis is conducted on the wheel, and critical issues in the pole identification are highlighted, due to the high modal density given by the spokes and uncertainties. A further numerical investigation based on a variational approach is applied to investigate the role of system uncertainties on the modal parameters. The analysis shows that the identification issues are mainly related to spoke pretension, cross contact and boundary conditions. Moreover, the spoke pretension uncertainty induces a mistuning in the structure and the corresponding loss of axial symmetry. The fine model updating of the preliminary model is then achieved optimising geometrical and material properties of the components as well spoke pretension.

Keywords Parametric modal analysis · Uncertainty quantification · Boundary conditions · Model updating · Stress stiffening

13.1 Introduction

In wheeled vehicle applications, the wheel subsystem acts as support for the tyre and is directly or indirectly (by means of a suspension system) connected to the vehicle chassis. The interactions between the road surface and the tyre thread, which can be distinguished into impacts and adhesion mechanisms, produce radial and tangential vibrations [1]. These phenomena constitute the main noise source over 40 km/h in passenger car and 60 km/h in trucks [2]. It can be taken for granted that the wheel subsystem represents also a relevant part in the vibration transmission chain, from the ground irregularities to the vehicle passengers [3].

Since tyre and wheel are strictly correlated to vibration and acoustic ride comfort, the state-of-the-art extensively investigates tyre and tyre-wheel assembly modal behaviour, from both experimental and numerical point of view. In [4, 5] the effect of the angular velocity, vertical load and air pressure on the tyre dynamics was studied. Doria et al. [6] identified the first five out-of-plane mode shapes of motorcycle tyres to estimate the relaxation length. FTYRE model was discussed in [7]. Pinnington et al. [8] showed that tyre belt can be considered rigid in tangential direction above 500 Hz. The first air cavity resonance in the unloaded configuration occurs between 200 Hz and 250 Hz [9]. It was experimentally proved that interior noise below than 400 Hz is related to forces at the spindle [7]. In automotive field, frequency ranges to evaluate whole-body and hand-transmitted vibration discomfort are, respectively, up to 80 Hz and 1000 Hz [10].

E. Bonisoli (✉) · A. D. Vella · S. Venturini
Department of Mechanical and Aerospace Engineering, Politecnico di Torino, Torino, Italy
e-mail: elvio.bonisoli@polito.it; angelo.vella@polito.it; simone.venturini@polito.it

Z. Mao (eds.), *Model Validation and Uncertainty Quantification, Volume 3*, Conference Proceedings of the Society for Experimental Mechanics Series, https://doi.org/10.1007/978-3-031-04090-0_13

Several analytical and FEM models were developed in order to study specific frequency ranges and tyre phenomena. Flexible ring with an elastic foundation can describe in-plane dynamics but not the cross-sectional dynamics. Flat model is used to describe road deformation and phenomena higher than 400 Hz.

If on one hand the tyre was deeply discussed, on the other hand, a limited amount of available data deals more closely to the wheel subsystem, both in automotive and in other applications. In order to validate a simplified tyre model to predict structure-borne interior noise, Kindt et al. [1] showed the first four natural frequencies identified on 205/55 R16 steel wheel in the clamped configuration: the axial mode occurs at 393.2 Hz while the first and the second bending mode shapes, respectively, at 167.5 Hz and 440.7 Hz. Steel wheel is a relatively simple system to study since it is constituted by a disc mated to a rim by interference fit. In [11] the authors discussed a novel non-destructive method to evaluate the fitting force starting from stiffening effect and experimental data.

On the other side, the bike spoke wheel which is discussed in this work is an example of complex subsystem to investigate because of its several potential uncertainties. The case study deals with the analysis of the modal behaviour of a bike spoke wheel, focusing on structure uncertainties and stiffening effect due to spoke preload. The presence of the spokes undoubtedly plays the key role since each of them is clamped with a certain axial preload on the rim, tangentially pulled through the rim holes and then again clamped on the rim. Moreover, the spokes are in contact with each other. The nominal preload may also decrease in a different amount after a certain working period. Spoke contacts, different levels of preload and peculiar boundaries together with geometrical and material properties of the rim and the hub make the bike spoke wheel a challenging case to study and to model. To do so, model updating (MU) techniques can be exploited.

Eigenvalue sensitivity to parameters uncertainties was used in [12, 13] to evaluate the stress-stiffening effect in aluminium frame. MU techniques can be also based on optimisation problems: for instance, in [14–16], the target was the evaluation of residual stress from dynamic measurements. An alternative to take advantage from eigenvalue sensitivity to uncertainties is represented by the methodology proposed by Bahra and Greening [17] which monitored the Modal Assurance Criterion (MAC) [18, 19]. The variability in dynamic behaviour due to constraint uncertainties [20] is a well-known issue in industrial field. In automotive manufacturing, frequency response function (FRF) variability is usually considered. In [21–24] geometrical and material uncertainties were introduced in FEM models to reproduce the FRF variability experienced in the experimental analysis. In this case study, a minimisation problem is solved varying uncertain parameters to tune the FEM model in terms of natural frequency similarity. The mode tracking is performed with MAC.

The paper is organised as follows:

In Sect. 13.1 the required theoretical background and the case study are defined.
Sect. 13.2 deals with the modelling phase with a specific focus on the assumption made and implementation in LUPOS [25] software.
In Sect. 13.3 the experimental modal analysis (EMA) on the wheel is described. Results and numerical-experimental comparison are shown.
In Sect. 13.4 the optimisation problem to achieve the FEM model tuning is discussed and results are presented.

13.2 Model Updating by Mode Shape Tracing

The proposed method aims at efficiently characterising the effect of uncertainties on the dynamics of a mechanical component. The uncertainties in the geometrical and material properties are exploited to tune the finite element (FE) model: the component pre-stress induced in the structure during the assembly phase is also considered.

The starting point of the presented approach is the modal analysis of the full assembly. Modal analysis is nowadays a robust and diffused technique to perform dynamic behaviour prediction both exploiting finite elements analysis (FEA) with commercial software and laboratory testing with experimental modal analysis (EMA).

Once the modal properties of the assembly are known, the tuning is performed by design to modal analysis (DMA) approach [26–28] exploiting the influence of uncertain parameter variability on the global structural mode shapes. The fine model updating is automatically performed by the optimisation problem based on the aforementioned method. The DMA approach was introduced for investigation, re-design and improvement purposes by exploiting the Modal Assurance Criterion (MAC) introduced by Allemang in 1982 [18]; in summary, it consisted in an index defined in the $[0 \div 1]$ interval computed between mode shapes j and k whose value is as higher as the two mode shapes are identical based on the original index; the MACW2 correlation index is adopted to include eigenvalue contribution (gap or proximity) in the mode shape correlation

assessment. This index is the instrument to distinguish similar mode shapes with spaced natural frequencies. Equation 13.1 represents the MACW2 between eigenvectors φ_j and φ_k, where ω_j^2 and ω_k^2 are the related eigenvalues:

$$MACW2_{j,k} = \frac{\left[\boldsymbol{\varphi}_j^T \ \boldsymbol{\varphi}_k\right]^2}{\left[\boldsymbol{\varphi}_j^T \ \boldsymbol{\varphi}_j\right]\left[\boldsymbol{\varphi}_k^T \ \boldsymbol{\varphi}_k\right]} e^{-\sqrt{2\left|\frac{\omega_j^2-\omega_k^2}{\omega_j^2+\omega_k^2}\right|}} \tag{13.1}$$

Starting from consistent experience in optimisation processes for MU, gradient-based Matlab tool *fmincon* [29] is used in the methodology. The optimisation is performed by following the reported steps:

- Preliminary analysis on the model to estimate expected nominal properties and parameter sensitivity.
- Optimisation run with initial optimising parameters slightly shifted from nominal condition.

The objective function is developed as a composition of the error in terms of MACW2 and the discrepancy on the model weight as shown in Eq. 13.2:

$$\begin{aligned} \text{ObjFnc} &= \text{RE}\,(\text{MACW2}) + \text{RE}(m) \\ \text{RE}\,(\text{MACW2}) &= \frac{n - \sum_{r=1}^{n} \max\left(\text{MACW2}_{r,k} | \forall \ k\right)}{n} \\ \text{RE}(m) &= \frac{\left|m_{ref} - m\right|}{m_{ref}} \end{aligned} \tag{13.2}$$

where:

- n are the number of experimental modes considered in the updating
- m_{ref} is the reference mass of the structure
- m is the mass of the updating structure.

The objective function solution is defined in $[0 \div 2]$ interval and has to be minimised. The weights of eigenvectors and eigenvalues are identical and collected in the MACW2 term (see Eq. 13.1), while the relative error on the mass guarantees that the properties are not changed without physical meaning.

13.3 Rear Bike Spoke Wheel in Free-Free Conditions

In this section, the development of the preliminary FE model of a rear bike spoke wheel is discussed. The system under analysis is a prestressed structure in which the spoke preload is imposed during the assembly procedure. The wheel can be theoretically considered as an axisymmetric structure composed by several components. In the bike wheel, typically the hub is linked to the rim by a set of spokes which are tensioned by acting on nipples, i.e. rivets located in the rim. In this case study, transmission gears are also included. Depending on the type of wheel, spoke pretension can be modified directly acting on the nipples. The wheel under analysis is based on the rim Rigida X-PLORER Safety Line 26″ 559–19 with 36 spoke holes [30] in aluminium material. The wheel involves a Shimano HB-TS30 hub in aluminium. The spokes are made of steel and consist of rod elements whose diameter is equal to 2 mm: their purpose is linking the hub to the rim. The maximum allowable pretension of the spokes is equal to 1300 N [30]. The spokes pattern is usually classified by the number of in-plane intersections between the spokes. In this case study, the pattern is classified as a "3X" [31] which is based on a 4spokes connection between the rim and the inner and outer hub flanges. This configuration involves spoke contact.

In Fig. 13.1 it is shown the resulting developed preliminary FE model.

The FE model is developed in LUPOS open source FE code in Matlab. The model is parametrically built by revolution of a cross-sectional pattern of nodes and then assigning material and geometry properties to the two main subsystem, i.e. the rim and the hub. On the contrary, the spokes are procedurally introduced in the FE model by imposing the "3X" pattern [31]. Spoke contact spots are automatically identified by the code, and spherical joints are introduced between the interface nodes supposing the contact as a constraint. The hub and the rim are described with 4-node shell element with constant thickness while the spokes with 1D Euler-Bernoulli rod elements and the gears as 1D elements. The model stands a total of 2146

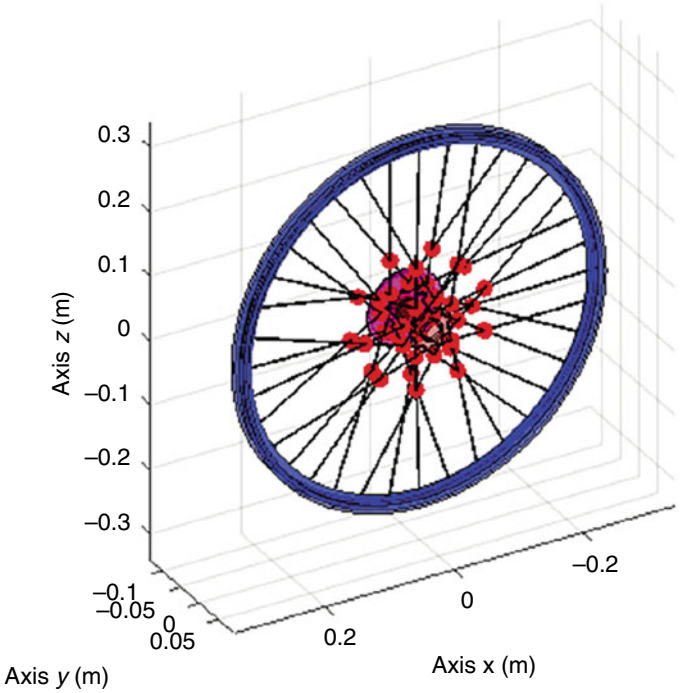

Fig. 13.1 FE model

Table 13.1 Geometrical and material properties

Component	Parameter	Value
Rim	E, Young Modulus [GPa]	70
	ρ, density [kg/m^3]	2700
	t, thickness [mm]	0.8–2.0
Hub	E, Young Modulus [GPa]	70
	ρ, density [kg/m^3]	2700
	t, thickness [mm]	3–8
Spokes	E, Young Modulus [GPa]	210
	ρ, density [kg/m^3]	7800
	$\varnothing$, diameter [mm]	2
	N, pretension [N]	1200
Gear	E, Young Modulus [GPa]	210
	ρ, density [kg/m^3]	7800

nodes, with 1036 1D elements and 1440 2D elements for a total amount of 12876 degrees of freedom in free-free conditions. The mass of the starting model is 1.5253 kg, while 1.5774 kg is the mass of the real assembly.

In Table 13.1, the main geometrical and material data are reported.

MoGeSeC methodology [32] is applied to the starting model in order to define the master nodes for roving hammer EMA. In total, four PCB 356A15 tri-axial accelerometers whose masses are equal to 14.2 g are placed on the wheel, three distributed on the rim flanges and one on the hub. 50 hammer locations are identified, and 48 nodes are circumferentially located at angular positions multiple of $\pi/2$, $\pi/4$, $\pi/6$ for the axial and radial response, while 2 nodes are located on the outer hub flange for the axial response only. In Fig. 13.2, the sensor locations and the hammered points are sketched.

13.3.1 Effect of Spoke Pretension

The spoke tension could be operatively defined during the mounting procedure of the bike wheel. Nevertheless, the preload of the bike wheel under analysis is considered an unknown parameter since it is not possible to regulate or easily measure. From a preliminary study of the modal behaviour of the system, a high density of modes related to spokes local dynamics is

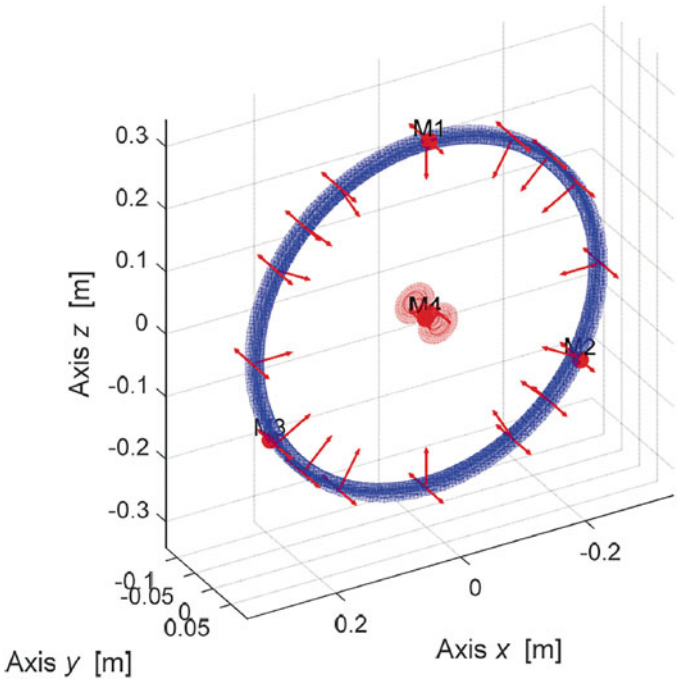

Fig. 13.2 Accelerometers and hammered locations

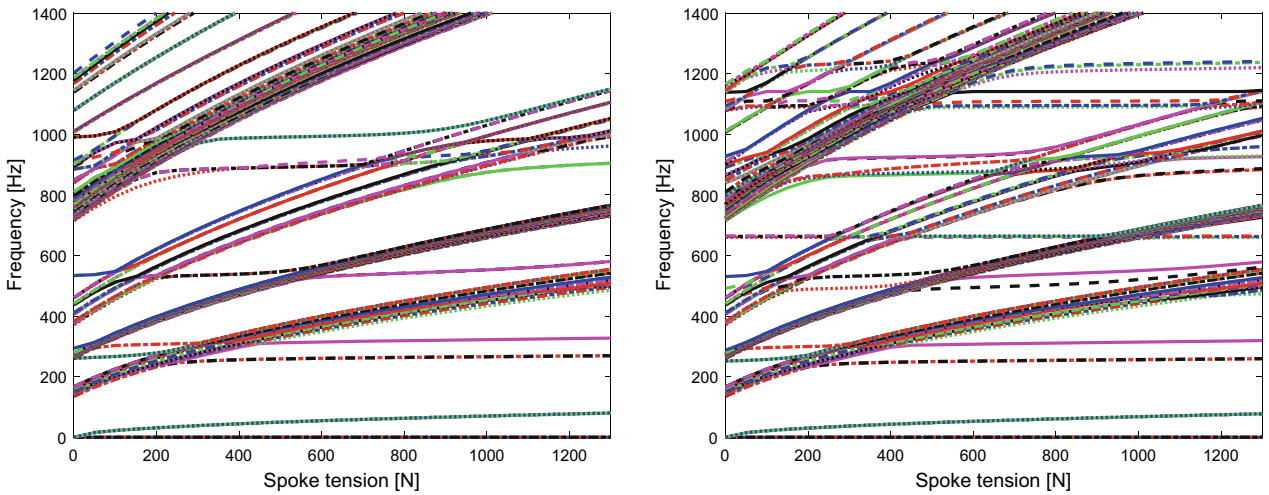

Fig. 13.3 Parametric real modal analysis, first 200 modes: without accelerometers (left) and with accelerometers (right)

expected. This property is mainly caused by the high difference in thickness between spokes and the rim. A parametric real modal analysis is performed on the FE model assuming the same tension on all the spokes. The first 200 natural frequencies are identified by varying the spoke tension T = [0: 50: 1200] N.

In Fig. 13.3, on the left, the aforementioned density of mode shapes is already emphasised: applying spoke pretension equal to 0 N, the first 100 modes occur in the first 600 Hz, and it is very challenging to distinguish local spoke modes and structure modes. Moreover, it is possible to identify subsets of modes which are strongly affected by the pretension and monotonically increasing in frequency: these modes are related to spoke local dynamics. On the other hand, single mode shapes or couples of mode shapes, not so influenced by the pretension, can be associated with the rim and the hub dynamics. Multiplicity equal to 2 of some mode shapes is due to the pseudo-axisymmetric. In the experimental campaign, the introduction of accelerometers makes the structure no more axisymmetric: some of the coupled eigenvalues are spaced, while some couple of eigenvectors are split in more than two mode shapes on a certain frequency range.

Figure 13.3, on the right, shows how the density increases following the first 200 modes: the addition of accelerometers is almost marginal on the structure, while the hardest difficulty in correlating the model to experimental results will be caused by correct estimation of the spoke tension which couples spoke and wheel modes.

13.3.2 Experimental Modal Analysis

In this subparagraph, the experimental setup, the mode shapes and the natural frequencies coming from the numerical and the experimental results are reported.

In the experimental campaign, the bike wheel is hanged by an elastic rubber band to a pneumatic crane, to perform roving hammer EMA in free-free conditions. The rubber band is passed through the hollow shaft of the wheel. The folded rubber band under static deformation induced by the bike wheel weight has a vertical length of 0.61 m. The wheel does not enter in contact with the rubber band during the entire measuring activity. As previously mentioned, four tri-axial accelerometers PCB 356A15 are placed in the identified master node locations using MoGeSeC technique. The impact hammer PCB 086C03 is used to excite the structure. All 40 locations are hammered on the wheel. The locations are radially distributed every 30 ° and 45 ° to describe 2-lobe and 3-lobe mode shapes at best and 4-lobe ones with compromises. The radial locations on the rim follow the rim features, deviating from nipple hole locations (Fig. 13.4).

Siemens LMS SCADAS Mobile was used to acquire and post-process the hammer and accelerometer signals. The EMA is performed in bandwidth 0÷4096 Hz with an acquisition time of 1 s (frequency resolution of 1 Hz) and linear average measure of five repetitions; the force-exponential window is used for the hammer input signal over 0.6% of samples, while an exponential window with a decay of 30% is applied to accelerometer output signal. H1 is used as FRF estimator. The identification is performed in the bandwidth 0÷2000 Hz.

In Fig. 13.5 the sum of all the FRFs is reported in red line. Black dot-dot lines represent the identified 19 poles.

Since the pole identification was hard to achieve, the frequency range is divided in 400 Hz intervals, then the identified subsets of poles are grouped. The main structure mode shapes, in correspondence of the higher peaks, are evident. At the same time, except for the first couple of mode shapes (at almost 190 Hz) and the first single mode shape (at almost 230 Hz), the amplitude curve is highly rugged: minor peaks in correspondence of structural mode shapes are due to the presence of the same mode shapes, sometimes mixed each other, many times because of the asymmetries caused by unbalanced masses and different spoke pretensions. Other peaks are probably due to local spoke mode shapes and cannot be identified.

Fig. 13.4 Experimental setup

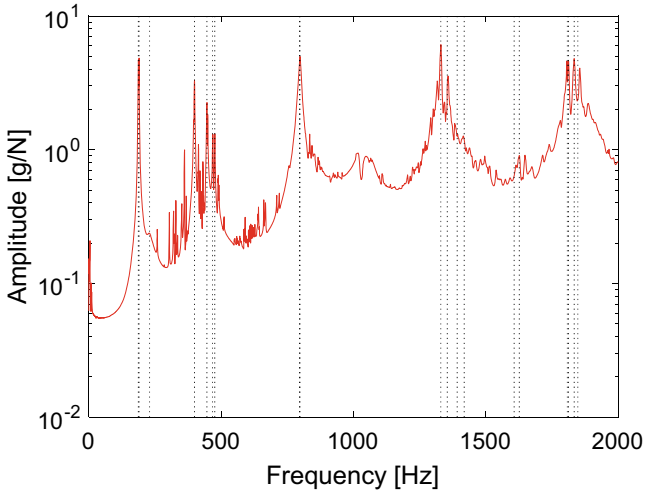

Fig. 13.5 Sum of all the experimental FRFs

13.3.3 Numerical to Experimental Comparison

In this subparagraph, the comparison between the experimental and the numerical results is carried out. The comparison is carried out considering the FE primary model and only the subset of degrees of freedom (DOFs) experimentally used for forcing or measuring the hammer response. Figure 13.6 represents the MAC computed between the experimental mode shapes (along y-axis) and the first 214 numerical mode shapes (along x-axis). The rigid body motions are deleted from both the numerical and the experimental mode shape sets.

As highlighted by Fig. 13.6, some experimental mode shapes are well-correlated to more than one numerical mode shape: this phenomenon is due to the fact that all the local spoke mode shapes involve a small rim deformation which can be more or less similar to other structural mode shapes. It was not possible to monitor spoke response during the experimental activity to isolate this issue. As mentioned in Sect. 13.2, the identification is also performed using MACW2 index to track mode shapes in function of the corresponding eigenvalue.

Figure 13.7 represents MAC index (experimental along y-axis, numerical along x-axis) between all the identified experimental mode shapes and the most interesting numerical mode shapes in function of the relative natural frequencies.

The dash-dot black line represents the iso-frequency line on which occurs the perfect similarity between EMA and FEA results. As it is clear, the preliminary FE model can catch the principal mode shapes experimentally identified, but it tends to overestimate the frequencies. The model seems to be more rigid than the real bike wheel.

Now some details are given on the identification of the 19 experimental structural mode shapes related to the modal deformation of the whole rim and the axial displacement of the hub. The first three mode shapes refer to the 1st bending and the axial mode shape. Secondly, there is a group of four identified mode shapes which refer to the 2nd bending. Then there is a couple of mode shapes around 800 Hz which represents the 3rd bending. Then there are four mode shapes from 1330 Hz to 1420 Hz which are the 4th bending and the in-plane 2-lobe mode shapes. At almost 1600 Hz the in-plane 3-lobe mode shapes are detected. Finally, there are four peaks representing the 5th bending. The 4-lobe in-plane mode shapes are not experimentally found, probably because of the frequency bandwidth. In Fig. 13.7, very good correlation can be remarked for the 1st and the 2nd bending mode shapes (higher than 90%) as well as for the axial mode shape (97%). A bit smaller MAC correspond to the 2nd and the 4th bending mode shapes, respectively higher than 75% and 62%. The 2-lobe in-plane mode shapes own a poor correlation, almost 25%, while the MAC increases in the 3-lobe case. Even the 5th bending mode shapes are well correlated.

In Table 13.2, an overview of the numerical and the experimental frequencies is proposed. In the second and in the third columns, natural frequencies numerically achieved with and without the mass addition due to accelerometer are reported, while in the fourth column the experimental frequencies of the identified mode shapes are shown.

From the numerical-experimental comparison shown in this section, a very high modal density is achieved performing the modal analysis of the model due to the presence of the several rods with different pretensions. The defined hammering locations allow to mainly identify bending mode shapes, and the proposed MACW2 approach is suitable for correlation when

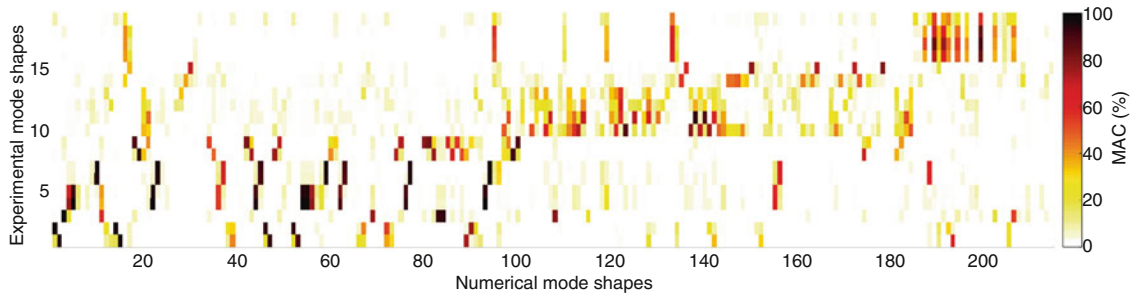

Fig. 13.6 MAC between experimental mode shapes and the first 214 numerical mode shapes

Fig. 13.7 MAC between EMA and preliminary FE model with coarse tuning

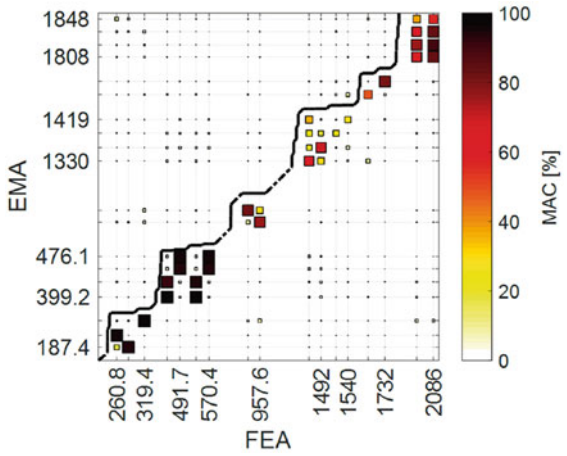

Table 13.2 Experimental and numerical (with and without accelerometer masses) natural frequencies

	Frequency [Hz]		
	Numerical		
Mode description	Without accelerometers	With accelerometers	Experimental
1st bending	268.3–268.3	260.8–260.9	187.4–190.3
1st axial	325.7	319.4	230
2nd bending	491.8–491.8570.6–570.6	476.6–491.7553.4–570.4	399.2–446.3468.2–476.1
1st membrane	692.5–692.5	691.6–691.7	–
1st torsional	705.4	703.8	–
2nd membrane	792.7–792.7	787.4–787.8	–
2nd torsional	952.7	952.3	–
3rd bending	989.7–989.7	957.3–957.6	796.1–797.9
3rd membrane	1472–1472	1469–1470	–
3rd torsional	1472	1471	–
4th torsional	1530	1530	–
4th bending	1535–1535	1490–1492	1330.2–1354.3
In-plane 2-lobe	1568–1568	1539–1540	1392.1–1418.7
In-plane 3-lobe	1738–1738	1660–1732	1607.2–1626.6
4th membrane	1797–1798	1764–1764	–
In-plane 4-lobe	1949–1949	1895–1903	–
5th bending	2217–2217	2017–2086	1808–18131834–1848

high modal density occurs. The lack of correlation for some modes can be attributed to the variability in pretension which not only alters the mode natural frequencies by removing structure axial symmetry but also modal deformation. The model is suitable to describe the dynamics of the bike wheel but is too stiffer since all the frequencies are over estimated. Hence, MU is introduced to obtain a finely tuned FE model.

13.4 Optimisation

For the optimisation process, it is decided to track the first seven experimental mode shapes (first and second bending and axial mode shapes) since the identification and the multiplicity of the other modes at higher frequency is strongly affected by lack of axial symmetry in the prestressed structure. The optimisation is performed by considering the main geometrical and material properties affected by uncertainties. In Table 13.3 the design parameters are listed:

For material properties, the boundaries are imposed for ±50% of the nominal value; on the contrary, a range of two orders of magnitude is supplied to the $t_{mult,rim}$ term, i.e. a multiplier of the rim thickness assumed to be wider since modelisation was based on catalogue data. The pretension N is ranged between 0 N and 3000 N, despite the rim producer maximum spoke tension requirement is 1300 N. In the optimisation algorithm, the first guess is based on nominal values reported in Table 13.1 but reduced of the 25% in order to allow the optimisation tool to start far from sub-optimal condition.

The reliability of the values obtained with the optimisation is checked by running a second process with higher guess (+25%). The aim is to verify that the minimisation of the objective function reached a global minimum.

In Fig. 13.8 the results of the optimisation process are shown.

The process lasts 178 iterations reaching a minimum at 0.183. As can be seen from Fig. 13.8 on the right, the process almost confirmed the Young moduli, while biggest modifications occur to densities. The optimisation process principally redistributes the masses in order to reduce exponential term of MACW2.

MAC in function of EMA and FEA frequencies is plotted in Fig. 13.9.

The identification confirms the effectiveness of the adopted optimisation approach based on mode tracking and frequency weighting. A very good correlation can be remarked for the first and the second bending mode shapes (higher than 93%) as well as for the axial mode shape (97%). A bit smaller MAC correspond to the second bending mode shapes (higher than 94%). Consequently, the MAC correlation is quite high also for modes not tracked in the optimisation: the third bending mode shape is well correlated (at least 90%), while the fourth bending mode ha MAC higher than 51%. Instead, the 2-lobe

Table 13.3 Design parameters for the optimisation with boundaries

Parameter	Lower bound	Starting point	Upper bound	Optimal
E_{rim}, Young Modulus [GPa]	35	52.5	105	68.30
ρ_{rim}, density [kg/m^3]	1350	2025	4050	3589
$t_{mult,rim}$, thickness multiplier [–]	0.1	0.75	10	1.497
E_{spokes}, Young Modulus [GPa]	105	157.5	315	163.3
ρ_{spokes}, density [kg/m^3]	3900	5850	11700	7204
$\varnothing_{spokes}$, diameter [mm]	1	1.5	3	1.617
N, pretension [N]	0	900	3000	529
ρ_{gear}, density [kg/m^3]	3900	5850	11700	6010
ρ_{hub}, density [kg/m^3]	1350	2025	4050	2302

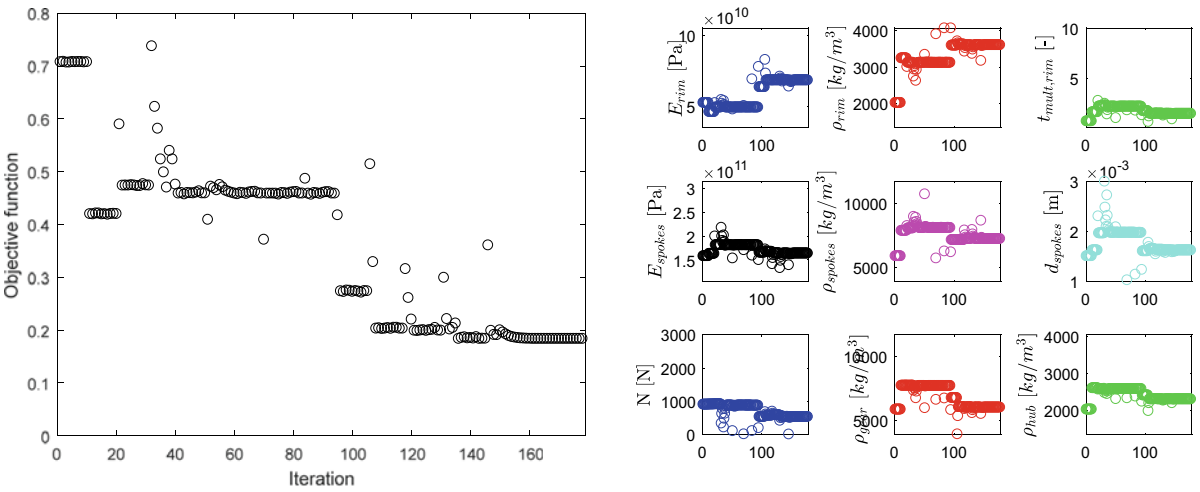

Fig. 13.8 Objective function (left) and parameters (right) trends with respect to the iterations for *fmincon* algorithm

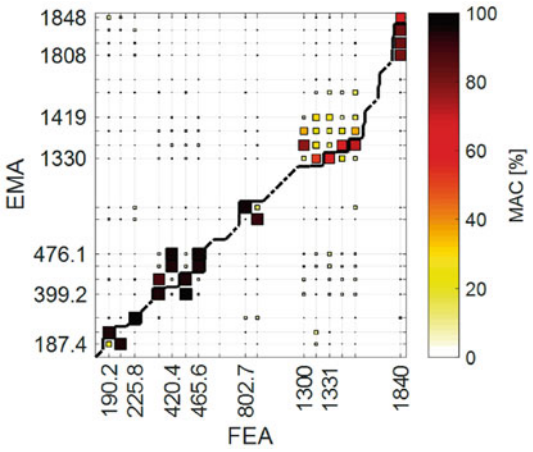

Fig. 13.9 MAC between EMA and preliminary FE model with fine-tuning

Table 13.4 Experimental-numerical comparison of FE finely tuned model

	Frequency [Hz]	
Mode description	Numerical	Experimental
1st bending	190.2–190.3	187.4–190.3
1st axial	225.8	230
2nd bending	403.6–420.4453.6–465.6	399.2–446.3468.2–476.1
3rd bending	802.7.3–803.5	796.1–797.9
4th bending	1306.8–1364.7	1330.2–1354.3
In-plane 2-lobe	–	1392.1–1418.7
In-plane 3-lobe	–	1607.2–1626.6
5th bending	1840	1808–18131834–1848

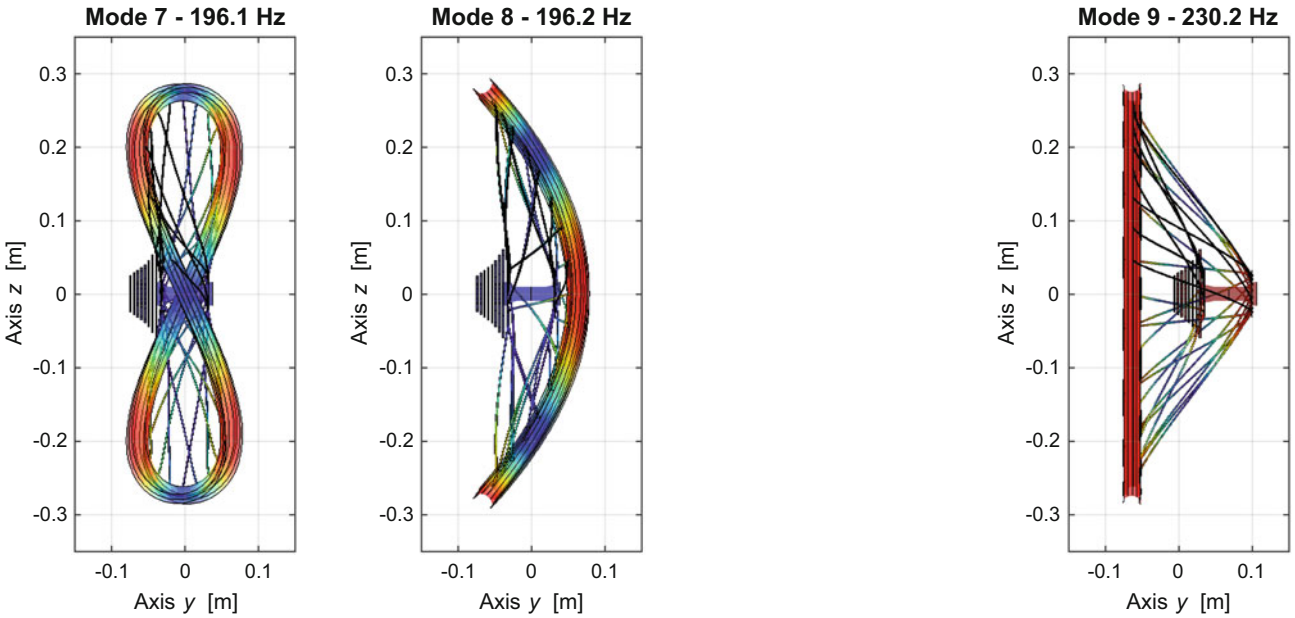

Fig. 13.10 1st bending mode shapes (left and middle), 1st axial mode shape (right)

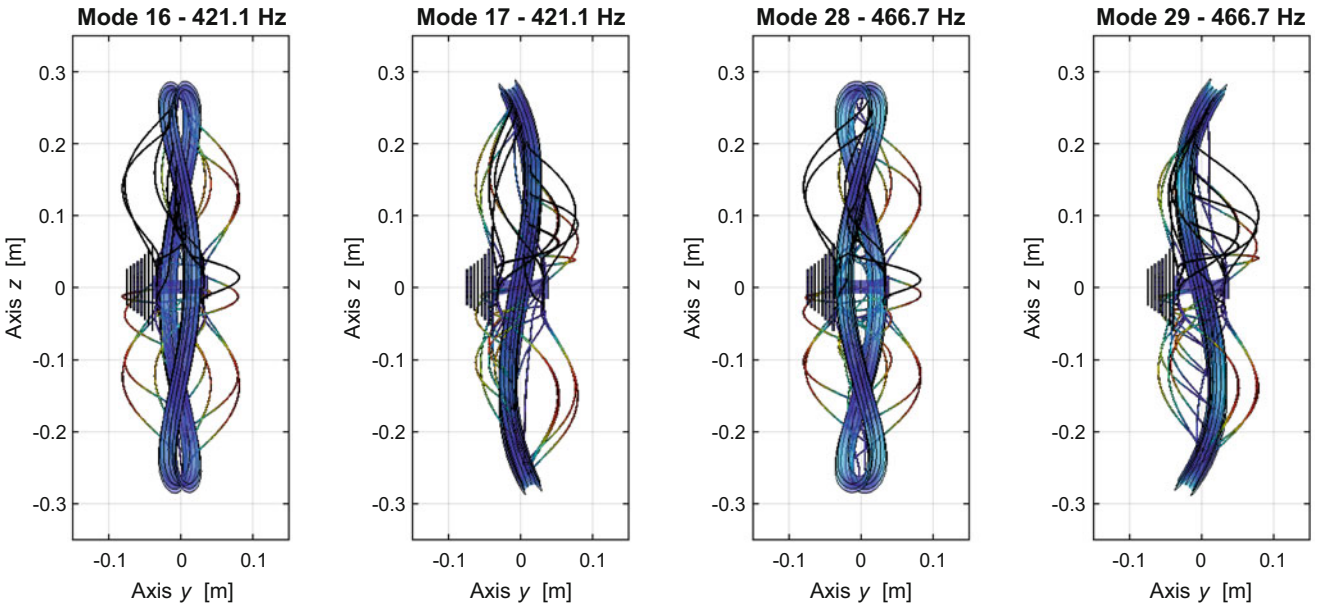

Fig. 13.11 2nd bending mode shapes

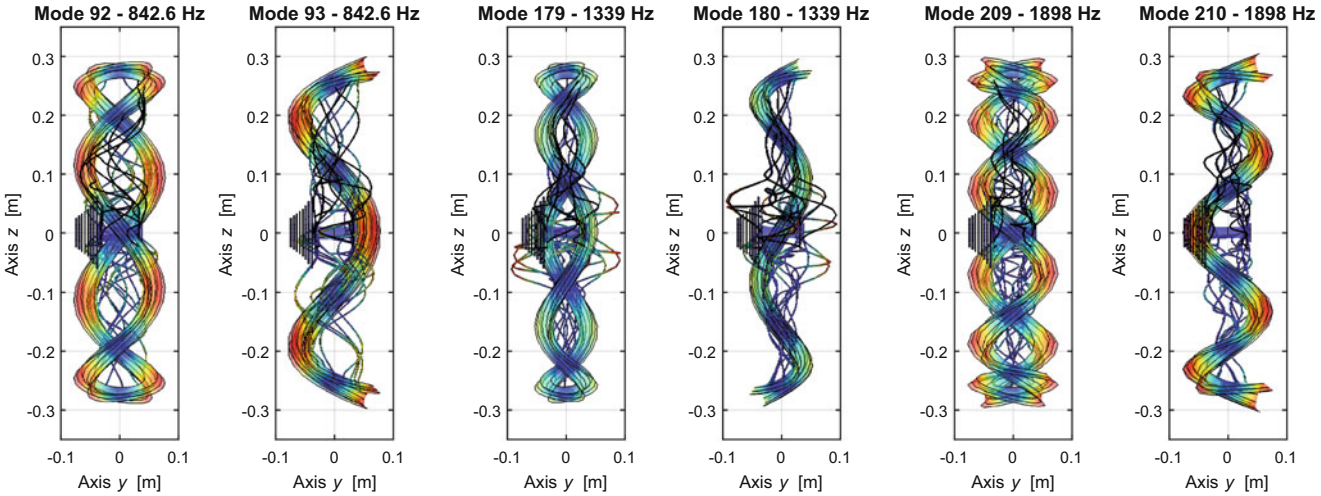

Fig. 13.12 Bending mode shapes from left to right: 3rd modes (1st and 2nd), 4th modes (3rd and 4th), 5th modes (5th and 6th)

in-plane mode shapes own a very poor correlation, almost 10%. The fifth bending mode shapes are well correlated at 80%. The details of the comparison are listed in Table 13.4, considering accelerometer inertial effect.

In the following figures, the numerical mode shapes achieved on the final FE model, without accelerometer adding masses, are shown. In Fig. 13.10 the 1st bending mode shape set and the 1st axial mode shape are shown. In Fig. 13.11 the 2nd bending mode shape set is shown. Finally, in Fig. 13.12 the 3rd, 4th and 5th bending mode shape sets are respectively shown.

13.5 Conclusion

The target of this research activity was the investigation of the modal behaviour of a bike spoke wheel from both experimental and numerical points of view and the application of optimisation algorithm to exploit uncertainties for the model tuning. EMA procedure resulted to be suitable for the identification of the principal structural mode shapes. Good agreement between the primary FE model and experimental result can be highlighted, as for the axial and the bending mode shapes. Between the poles, the identification of in-plane eigenvalues was particularly complex. The model, defined by reference parameters,

results to be stiffer than it was expected. Moreover, high modal density is evidenced both in the FEA and in the EMA. The gap in terms of natural frequencies remarked the presence of a relevant amount of uncertainties. In order to reduce the numerical-experimental mismatching, MU technique is applied, keeping constant the model topology and varying geometrical and material properties. The definition of an objective function to minimise in which overall mass contribution and the difference in terms of eigenvectors and eigenvalues of a mode shape subset was proved to be a robust strategy. Between the parameters, the most relevant variation with respect to the nominal values occurs for inertial properties and spoke thickness.

References

1. Kindt, P., Sas, P., Desmet, W.: Development and validation of a three-dimensional ring-based structural Tyre model. J. Sound Vib. **326**(3–5), 852–869 (2009)
2. Brinkmeier, M., Nackenhorst, U., Petersen, S., Estorff, O.: A finite element approach for the simulation of Tyre rolling noise. J. Sound Vib. **309**, 20–39 (2008)
3. Vella, A.D., Tota, A., Vigliani, A.: On the Road Profile Estimation from Vehicle Dynamics Measurements, SAE Paper 2021-01-1115 (2021)
4. Diaz, C.G., Kindt, P., Middelberg, J., Vercammen, S., Thiry, C., Close, R., Leyssens, J.: Dynamic behaviour of a rolling Tyre: experimental and numerical analyses. J. Sound Vib. **364**, 147–164 (2016)
5. Diaz, G.., Vercammen, S., Middelberg, J., Kindt, P., Thiry, C., Leyssens, J..: Numerical prediction of the dynamic behaviour of rolling tyres. In: Proceedings of ISMA (2012)
6. Doria, A., Taraborrelli, L., Urbani, M.: A modal approach for the study of the transient behavior of motorcycle and scooter Tyres. In: Proceedings of ASME, Buffalo, New York, USA, pp. 29–37. (2014)
7. Dorfi, H.R., Wheeler, R.L., Keum, B.B.: Vibration modes of radial tyres: application to non-rolling and rolling events, SAE Paper 2005-01-2526 (2005)
8. Pinnington, R.J., Briscoe, A.R.: A wave model for a pneumatic Tyre belt. J. Sound Vib. **253**, 941–959 (2002)
9. Kindt, P., Berckmans, D., De Coninck, F., Desmet, W.: Experimental analysis of the structure-borne Tyre/road noise due to road discontinuities. Mech. Syst. Signal Process. **23**, 2557–2574 (2009)
10. Vella, A.D., Vigliani, A., Tota, A., Lisitano, D.: Experimental Ride Comfort Analysis of an Electric Light Vehicle in Urban Scenario, SAE Paper 2020-01-1086 (2020)
11. Bonisoli, E., Marcuccio, G., Venturini, S.: Interference fit estimation through stress-stiffening effect on dynamics. Mech. Syst. Signal Process. **160**, 107919 (2021)
12. Mottershead, J.E., Mares, C., Friswell, M.I., James, S.: Selection and updating of parameters for an aluminium space-frame model. Mech. Syst. Signal Process. **14**(6), 923–944 (2000)
13. Kyprianou, A., Mottershead, J.E.: Uncertain systems: Modelling and updating. In: Proceedings of the 18th ICSV, pp. 995–1002 (2011)
14. Greening, P.D., Lieven, N.A.J.: Identification and updating of loading in frameworks using dynamic measurements. J. Sound Vib. **260**(1), 101–115 (2003)
15. Flores, J.E.R., Viana, F.A.C., Rade, D.A., Steffen Jr., V.: Identification of external forces in mechanical systems by using LifeCycle model and stress-stiffening effect. Mech. Syst. Signal Process. **21**(7), 2900–2917 (2007)
16. Bahra, A.S., Greening, P.D.: Identifying axial load patterns using space frame FEMs and measured vibration data. Mech. Syst. Signal Process. **23**(4), 1282–1297 (2009)
17. Bahra, A.S., Greening, P.D.: Identifying multiple axial load patterns using measured vibration data. J. Sound Vib. **330**(15), 3591–3605 (2011)
18. Allemang, R.J.: A correlation coefficient for modal vector analysis. In: Proceedings of the 1st International Modal Analysis Conference, pp. 110–116. (1982)
19. Allemang, R.J.: The modal assurance criterion–twenty years of use and abuse. Sound Vib. **37**(8), 14–23 (2003)
20. Kranjc, T., Slavič, J., Boltežar, M.: An interface force measurements-based substructure identification and an analysis of the uncertainty propagation. Mech. Syst. Signal Process. **56**, 2–14 (2015)
21. Durand, J.F., Soize, C., Gagliardini, L.: Structural-acoustic modeling of automotive vehicles in presence of uncertainties and experimental identification and validation. J. Acoust. Soc. Am. **124**(3), 1513–1525 (2008)
22. Hinke, L., Dohnal, F., Mace, B.R., Waters, T.P., Ferguson, N.S.: Component mode synthesis as a framework for uncertainty analysis. J. Sound Vib. **324**(1–2), 161–178 (2009)
23. Scigliano, R., Scionti, M., Lardeur, P.: Verification, validation and variability for the vibration study of a car windscreen modeled by finite elements. Finite Elem. Anal. Des. **47**(1), 17–29 (2011)
24. Gallina, A., Lisowski, W., Pichler, L., Stachowski, A., Uhl, T.: Analysis of natural frequency variability of a brake component. Mech. Syst. Signal Process. **32**, 188–199 (2012)
25. Bonisoli E.: LUPOS – LUmped Parameters Open Source FEM code, Tutorial v.2021-09-16
26. Bonisoli, E., Marcuccio, G., Rosso, C.: Crossing and veering phenomena in crank mechanism dynamics. In: Topics in Model Validation and Uncertainty Quantification, vol. 5, pp. 175–187. Springer, New York (2013)
27. Bonisoli, E., Brino, M., Delprete, C.: Numerical-experimental comparison of a parametric test-rig for crossing and veering phenomena. Mech. Syst. Signal Process. **128**, 369–388 (2019)
28. Bonisoli, E., Lisitano, D., Dimauro, L., Peroni, L.: A proposal of dynamic behaviour design based on mode shape tracing: numerical application to a motorbike frame. In: Dynamic Substructures, vol. 4, pp. 149–158. Springer, Cham (2020)
29. https://it.mathworks.com/help/optim/ug/fmincon.html. Available in 2021-10-18

30. https://www.ryde.nl/x-plorer-r. Available in 2021-06-03
31. https://www.purecycles.com/blogs/bicycle-news/156387911-speaking-of-spokes-spoke-patterns. Available in 2021-06-03
32. Bonisoli, E., Delprete, C., Rosso, C.: Proposal of a modal-geometrical-based master nodes selection criterion in modal analysis. Mech. Syst. Signal Process. **23**(3), 606–620 (2009)

Chapter 14
Probabilistic Assessment of Footfall Vibration

Chase Hibbard, Karly J. Vial, Aliz Fischer, Nick Sherrow-Groves, Jean M. Franco Lozada, Juan Caicedo, and Zhaoshuo Jiang

Abstract As one of the serviceability limit states of structural design, excessive vibration has attracted more attention in recent years, with the design trend moving toward lighter and more slender structures. Footfall vibration contains high uncertainties in nature, with significant variations in walker weight, walking speeds, and dynamic load factor. Since conservative designs can often lead to significant cost premiums, this study focuses on the stochastic assessment of footfall vibration of on a composite steel floor to better understand the variation in performance of various design factors and better inform the ultimate decision-makers. To close the knowledge gap between academia and industry in this area, San Francisco State University and the University of South Carolina partnered with Arup through an NSF-funded Research Experience for Undergraduates (REU) program. A composite steel structure was modeled to resemble a typical office bay. The model was developed and analyzed in Oasys GSA. Monte Carlo simulation was used to quantify the probability of exceeding certain common vibration criteria. The results of this study would provide actionable guidance to stakeholders to weigh the benefits and costs between performance targets.

Keywords Footfall vibration · MC · Academia and industry collaboration

14.1 Introduction

With the design trend moving toward lighter and more slender structures, excessive vibration, as one of the serviceability limit states of structural design, has attracted more attention in recent years. Two of the most famous and publicized cases of vibration serviceability problem caused by footfall vibration are probably the pont de Solférino in Paris [1] and London Millennium Bridge [2, 3]. While the vibration serviceability problem of bridges is well studied, the vibration serviceability for floor design is less regulated as the primary concern is typically focused on the ultimate limit state [4]. Several design guidelines, such as ATC Design Guide 1 [5], the National Building Code of Canada [6], the AISC Design Guide 11 [7], and A Design Guide for Footfall Induced Vibration of Structures (CCIP-016) [8], were developed to guide designers through the process. Several studies have tried to model the footfall problem by representing human behavior based on different assumptions (e.g., the traditional mass model [9, 10]), and recent studies have shown that the human body can be modeled

C. Hibbard
University of Oklahoma, Norman, OK, USA
e-mail: chasehibbard@ou.edu

K. J. Vial
Oregon State University, Corvallis, OR, USA
e-mail: vialk@oregonstate.edu

A. Fischer · N. Sherrow-Groves
Arup US Inc., San Francisco, CA, USA
e-mail: Aliz.Fischer@arup.com; nick.sherrow-groves@arup.com

J. M. Franco Lozada · J. Caicedo
University of South Carolina, Columbia, SC, USA
e-mail: FRANCOLJ@email.sc.edu; CAICEDO@cec.sc.edu

Z. Jiang (✉)
San Francisco State University, San Francisco, CA, USA
e-mail: zsjaing@sfsu.edu; zsjiang@sfsu.edu

Z. Mao (eds.), *Model Validation and Uncertainty Quantification, Volume 3*, Conference Proceedings of the Society for Experimental Mechanics Series, https://doi.org/10.1007/978-3-031-04090-0_14

using different approaches as a mass-damper-spring (MDS) systems [11, 12] or more recently as a PID controller system which can react to varying levels of excitation [13]. Floor vibration serviceability is commonly addressed at the design stage by either putting a constraint on the minimum fundamental frequency of the floor to avoid resonance induced by footfall [14] or using a performance-based approach by setting an upper bound for the floor vibration response based on certain design criteria [4]. In either approach, the evaluation process is in a deterministic fashion in current practice. Based on the authors' experience in the design practice, the design could vary largely when adopting the different design guidelines, and it is currently unclear how that affects the probability of excess footfall-induced floor vibrations. Variability of factors, such as walker weight, speed, or walker style as well as unreliable prediction of modal properties, could be some of the reasons in the design stage that contribute to the uncertainties in the results.

14.2 Proposed Solution

Currently, footfall analysis is performed with a given walking frequency and walker weight. These two singular values are used in the calculations to return a response factor. A response factor (RF) is used to describe the intensity of vibration felt by an occupant; it is a scaled value with an RF = 1 being the threshold of human perception [8]. Through the opportunity provided by an NSF-funded Research Experience for Undergraduates (REU) program established by San Francisco State University and the University of South Carolina, the REU participants (the first two authors) were working together with faculty advisors in academia and industrial mentors from Arup, a leader in engineering consulting and structural design, to start exploring floor vibrations in a probabilistic way. In this study, Monte Carlo simulation was used to obtain the probability of exceeding common RF criteria. The simulation combined normal distributions of walker frequency and walker weight to evaluate the ability of the model to meet RF criteria. This project utilized a typical central bay of a composite steel structure, the structural type that is more vulnerable to floor vibration problem, to simulate different design configurations through Oasys GSA - Structural Design & Analysis Software and evaluate each design's performance in achieving RF criteria through Monte Carlo simulation. Probabilistic analysis was performed in MC Walker, an Arup internal software extension for GSA. Different parameters were varied in the simulations such as beam and girder section sizes, concrete weight and thickness, and the number of beams per bay. The results from the simulations were analyzed to find which design factors had the greatest impact on footfall vibration within the structure.

14.3 Methodology

In order to evaluate the effects of the various parameters mentioned above, a large number of simulations needed to be run. To avoid tedious adjustment of parameters, an automated framework was developed to facilitate the process. Figure 14.1 below shows the framework that was followed throughout this project.

The steel composite model was first developed in Rhino (Fig. 14.2), a computer-aided design software, after which GSA was used to perform dynamic modal analysis and dynamic response footfall analysis (Fig. 14.3). Compared to the current practice of analyzing structures for footfall vibration, this study includes a probabilistic approach by utilizing MC Walker, which accounts for the walker weight and walking frequency. The parameters in MC Walker are shown in Table 14.1. To meet a certain RF value, certain structural properties such as section size, concrete weight, and the number of beams per bay were adjusted to find the optimal design. A script was set up via Python to alter the beam and girder section sizes of the composite steel model. For each section size changed, a footfall analysis was performed using calculations set forth in the design guide CCIP-016, and the model and its results were stored. A total of 220 beam/girder configurations were analyzed for each change of concrete thickness. This amounted to 1320 models for the 2-beam structure (two interior beams between column lines; see Fig. 14.2) and another 1320 models for the 3-beam structure (three interior beams between column lines), respectively. Note that a 9-bay model was created for each model, while only the middle bay was analyzed to mitigate the effects on the support boundaries.

After the pool of outputs were collected, two models were selected for each of the following RF design criteria: RF 6, 4, 2, and 1. The two models were selected based on a large difference in steel weight (psf) and a similar maximum response factor, within 0.10 of one another. The steel weight was calculated by summing the weight of all beams and girders and dividing by the area of the 9-bay model (8100 ft^2). The RF for each of the selected models had to be within 0.20 of the RF design criteria (e.g., 5.85 max RF for the RF 6 Design would suffice). For each model, a Monte Carlo simulation was performed to assess the probability of exceeding RF 8, 6, 4, 2, and 1. The simulation randomized the walking frequency and

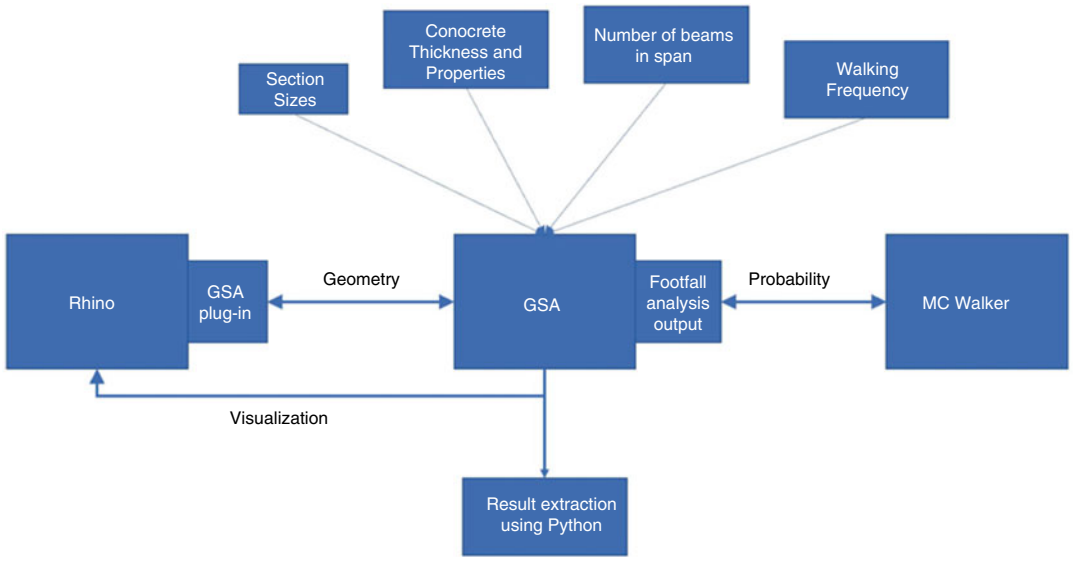

Fig. 14.1 Framework for designing, constructing, and analyzing structural testbed models

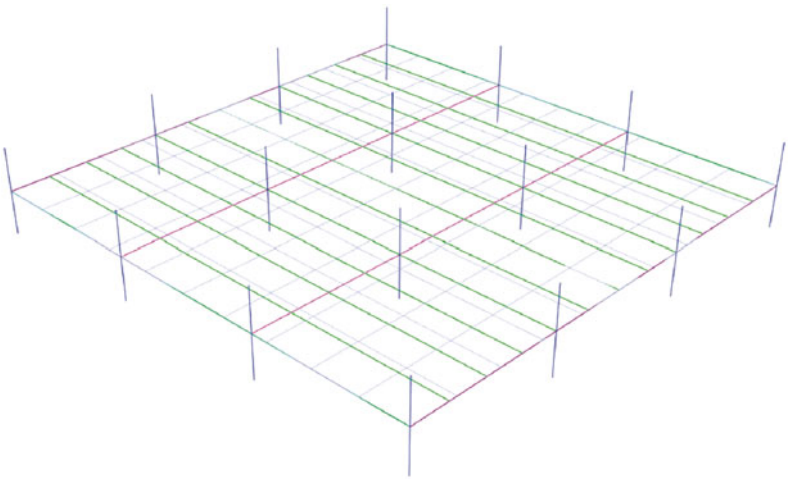

Fig. 14.2 Three beam steel model construct in Rhino 3D designing software

walker weight for each of the models through 750 cycles using Latin hypercube sampling. The walking frequency followed a normal distribution with a median of 2.0 Hz and standard deviation of 0.25 Hz in accordance with the research by Stuart Kerr [15]. The walker weight was randomized following a standard deviation with a mean of 74.5 kg and a standard deviation of 13.5 kg, with values based on research by the Australian Bureau of Statistics [16].

14.4 Results

Following each property change made on the model in GSA, specific outputs such as max response factor and fundamental frequency were extracted using Python and stored into a data frame. By tracking the many iterations performed on the steel model, relationships could easily be identified between a multitude of factors. Figure 14.4 shows the relationship between section size and RF as changes were made to the beams and girders within the model. Although the model varied in section sizes, the 2-beam structure's concrete slab was held constant at 4.5 inches thick of normal weight concrete (150 pcf). As section size increases, the structure gains more mass and does a better job absorbing the footfall vibration. As section size increases, the structure gets stiffer and gains more mass resulting in smaller footfall vibration.

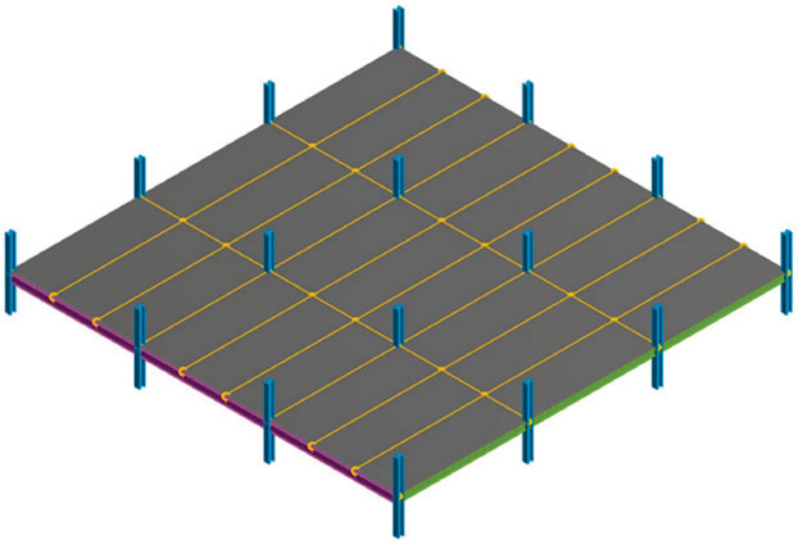

Fig. 14.3 Two beam steel model in GSA structural analysis software

Table 14.1 MC walker parameters

MC Walker parameter (assumed normal distribution)		
Statistics	Walker frequency (Hz)	Weight of walker (kg)
Mean	2.00	74.5
Standard deviation	0.25	13.5
Minimum	1.00	20.0
Maximum	3.00	200.0

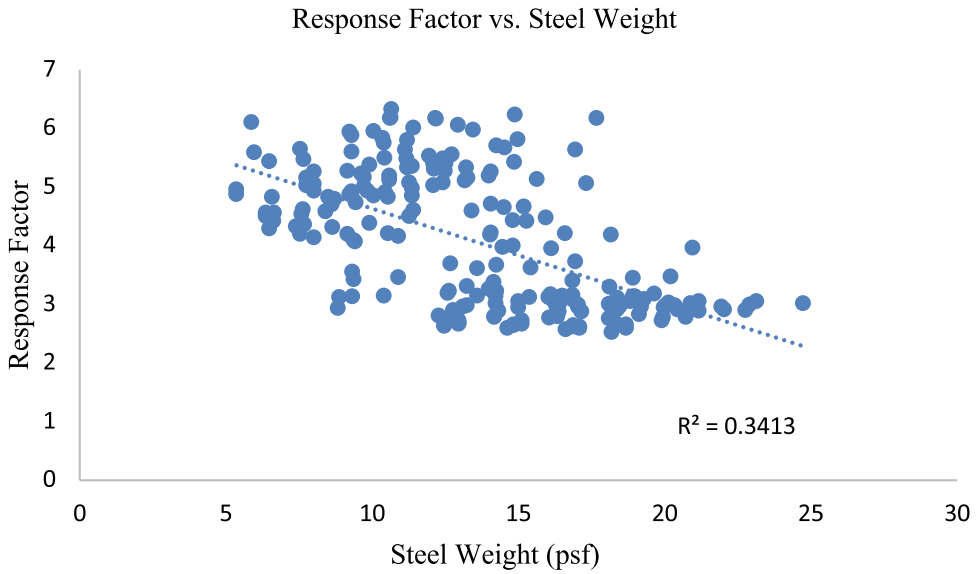

Fig. 14.4 The effect increasing section sizes has on RF for a 2-beam structure with a 4.5 in. NWC slab

Increasing the weight of the structure can also decrease footfall vibration. Concrete is an effective tool to so increase mass. Figure 14.5 shows the effect concrete thickness had on the RF for a given model with beams sized at W18 × 60 and girders sized at W21 × 44 to maintain a constant steel weight. As can be seen from Fig. 14.5, concrete has an approximately linear relationship with the RF and is an efficient way to reduce footfall vibration, if that design intervention is possible.

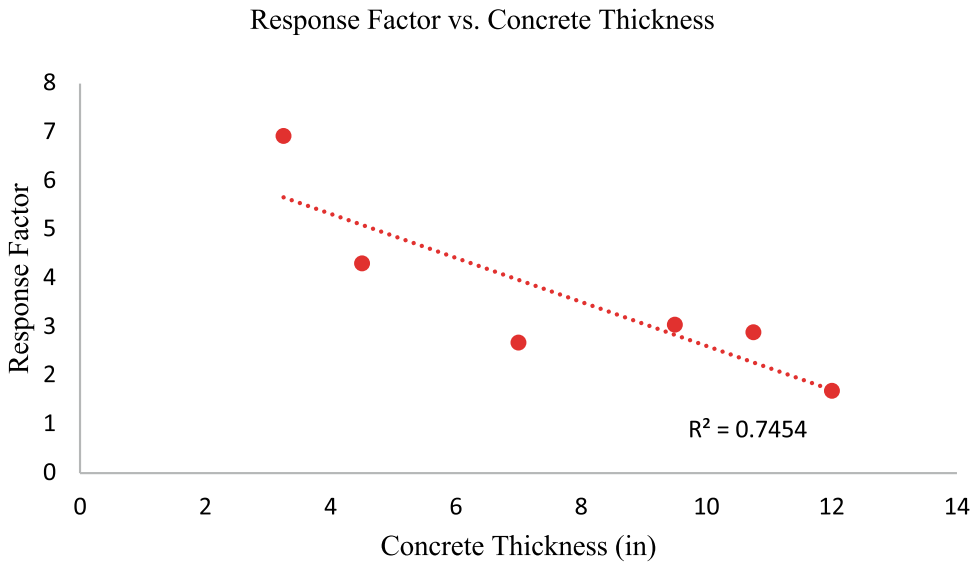

Fig. 14.5 The effect increasing concrete slab thickness has on RF for a 2-beam structure with W18 × 35 beams and W21 × 44 girders

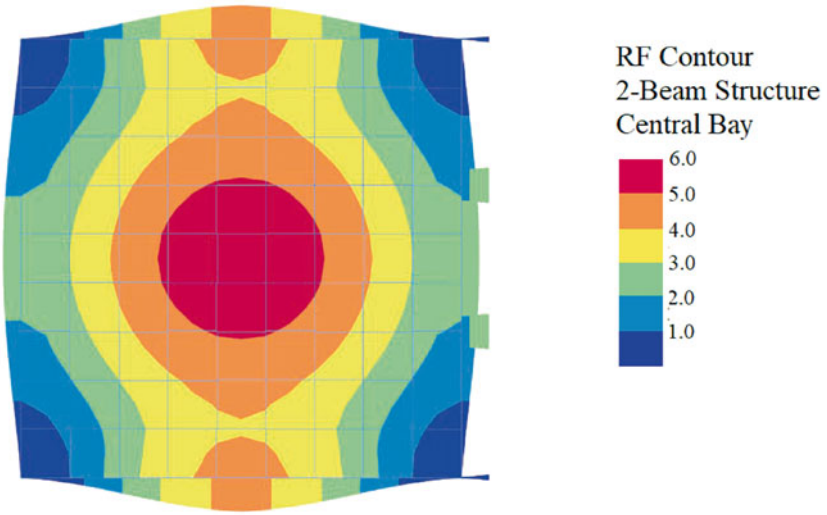

Fig. 14.6 Contour plot of response factor for composite steel bay

The results use the standard RF as a measure for the floor vibration. The output from GSA can be seen as a contour plot of the central office bay in Fig. 14.6. This image shows the magnitude of the RF across the entire bay with the most severe vibration occurring at the center.

After the footfall analysis in GSA, a Monte Carlo simulation was used to calculate the probability of exceeding a specific RF. The simulation repeated the footfall analysis for 750 samples by varying the walking frequency and walker weights as discussed in the methodology section. Figure 14.7 reveals the contour plot generated by the Monte Carlo simulation. The bay shown was designed to meet RF 6 criteria and has only a 5% chance of exceeding RF 6 at the center of the bay.

Throughout the course of this project, more questions arose regarding the probability of a specific design exciding different multiple RF criteria. A test matrix was developed to include all parameters that were tested and evaluated for the steel model. Table 14.2 contains models for a two beams per bay model (2-beam structure) and their respective probabilities of exceeding certain response factors. The highlighted cells indicate the probability of exceeding the vibration criteria required for that specific design. For each RF design, the two models that were chosen had similar maximum RF values within 0.10 of one another and were within 0.20 of the design criteria. The difference in steel weight was around 8–10 psf for the two models. A light steel structure was able to have a similar maximum RF to the heavy steel structure because of an increase in concrete thickness. Table 14.2 shows the difficulty in achieving perfect design of low RF criteria. There was a slight challenge in

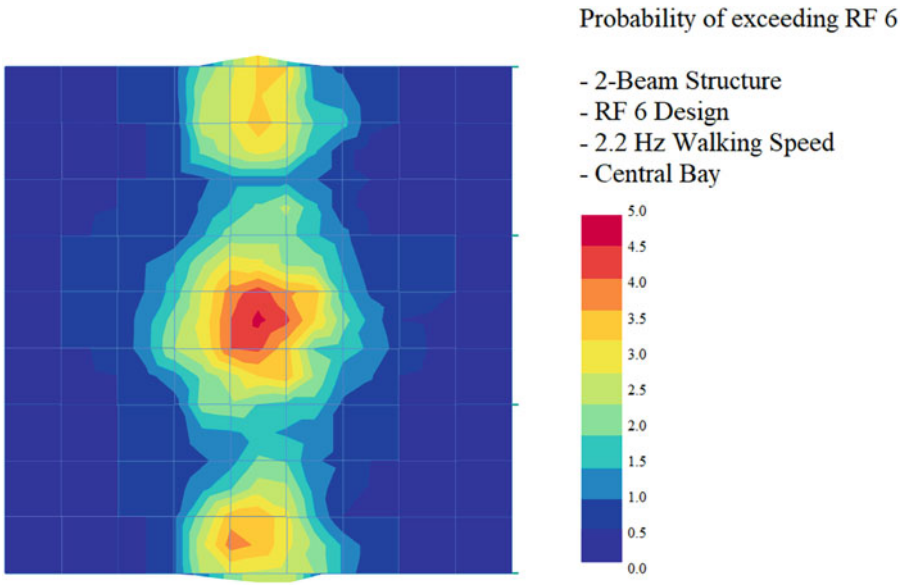

Fig. 14.7 Contour plot showing the probability of exceeding a response factor of 6

Table 14.2 Properties and probabilities of exceedance for two beams per bay composite steel models

Two beams per bay model						
		Probability of exceeding RF (MC Walker)				
RF design criteria	Model type	RF 8	RF 6	RF 4	RF 2	RF 1
RF 6	Light steel	9.2	16.8	31.6	68.0	90.3
	Heavy steel	5.2	10.0	21.6	58.7	81.3
RF 4	Light steel	1.5	3.2	8.9	25.5	52.5
	Heavy steel	1.3	2.9	9.7	25.5	53.5
RF 2	Light steel	0.1	0.3	1.6	12.8	40.5
	Heavy steel	0.0	0.8	2.8	16.1	41.2
RF 1	Light steel	0.0	0.1	1.9	9.2	27.2
	Heavy steel	0.0	0.0	0.0	1.5	12.9

designing a structure to not exceed RF 4 more than 10% of the time, but an RF 1 design would still exceed its limit more than a quarter of its lifespan.

Figure 14.8 below shows the comparison of the 2-beam structure and 3-beam structure models using a 2.2 Hz design walking frequency. The 3-beam models seem to be generally more efficient design especially for low RF as design with similar steel weight achieves lower RF compared to the 2-beam structure.

Figures 14.9a, 14.9b, and 14.9c represent the extended probability of exceeding various design criteria after running the MC Walker Monte Carlo simulation on three different models. The model in Fig. 14.9a is 2-beam structure that was analyzed with a maximum walking frequency of 1.6Hz in GSA. Figure 14.9b also has a 2-beam structure, but the maximum frequency was set to 2.2 Hz. Figure 14.9c shows a 3-beam model with a maximum walking frequency of 2.2 Hz.

14.5 Conclusion

Regarding the factors influencing the analysis, the relationship between structural steel weight and RF was consistent, as increasing section sizes provided more mass and stiffness to the structure allowing a better absorption of the vibration. The increase in slab thickness proved to be a more effective tool in mitigating floor vibration. The slab of the concrete spanning the entirety of the bay added more mass than that of steel members and had a stronger relationship with lowering RF. The heavier concrete design generally performs similar or better, primarily the 3-beam model for design criteria. Another key takeaway is the rapid increase in the probability of exceeding various RF criteria for a specific design. The 3-beam design

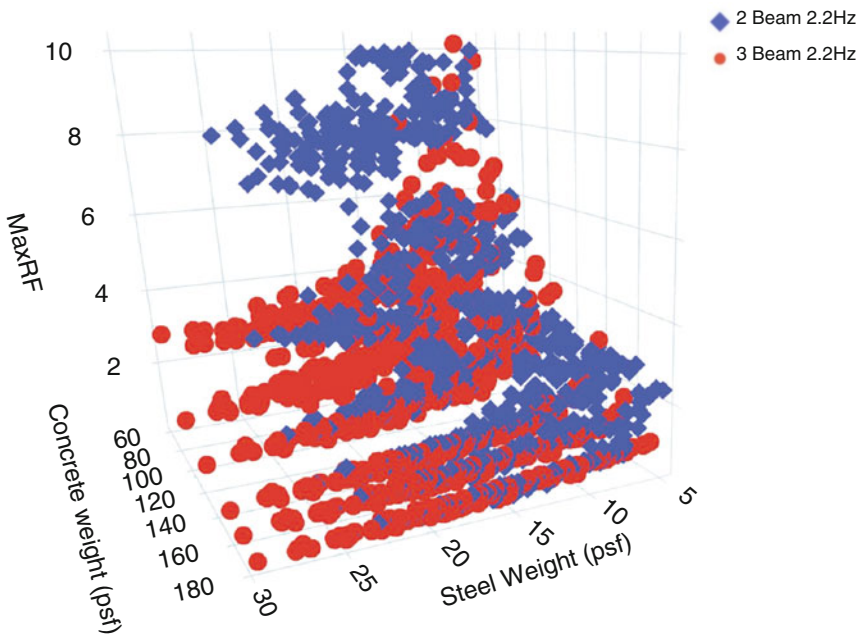

Fig. 14.8 3-beam and 2-beam comparison of steel weight and concrete weight vs max RF at a walking speed of 2.2Hz

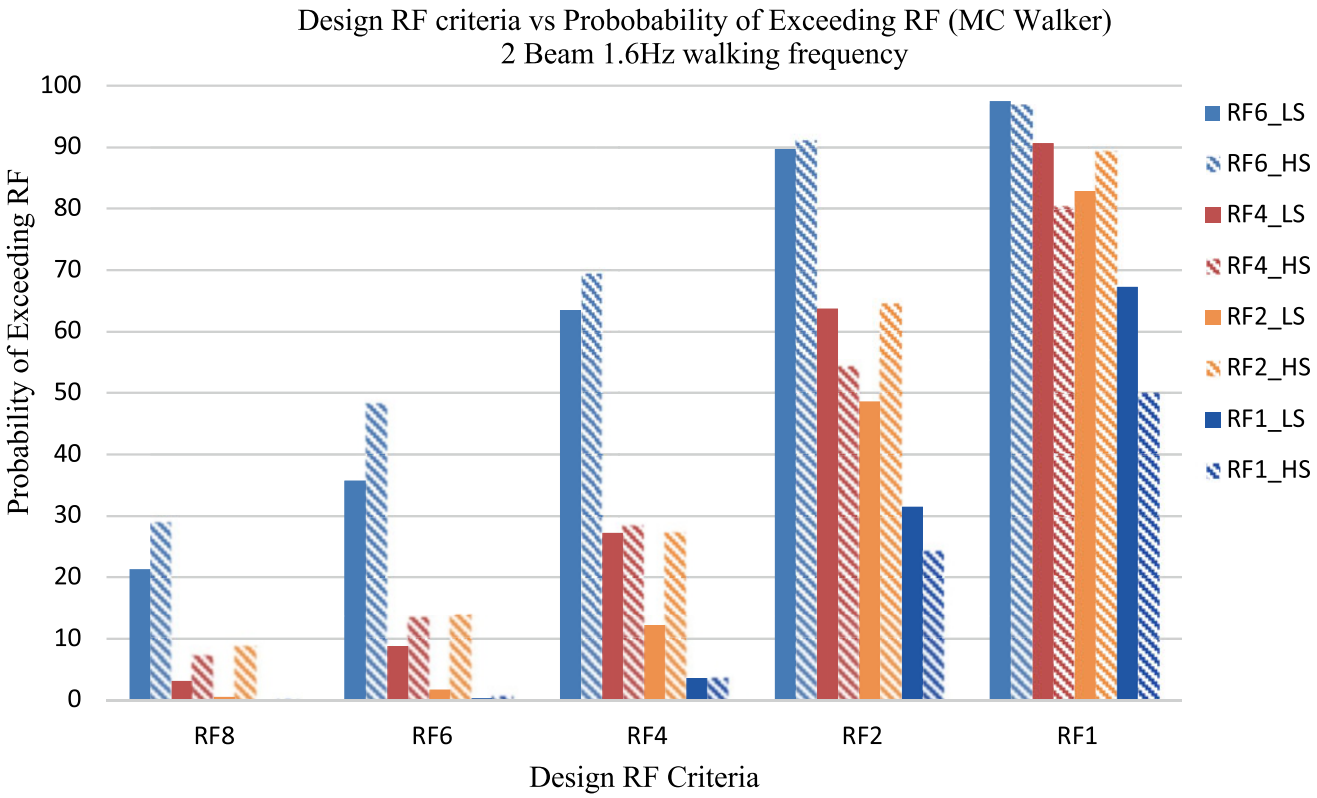

Fig. 14.9a Probability of exceeding certain design criteria with 2-beam 1.6Hz walking frequency model (*LS* light steel design and *HS* heavy steel design)

was more efficient for more stringent criteria without sacrificing performance. Designing to a 1.6 Hz vs 2.2 Hz can result in significant difference in probability of exceeding criteria, especially for the designs targeting more stringent criteria. There is an exponential trend upward as a design is tested against lower RF criteria. It is important to note that there is no single

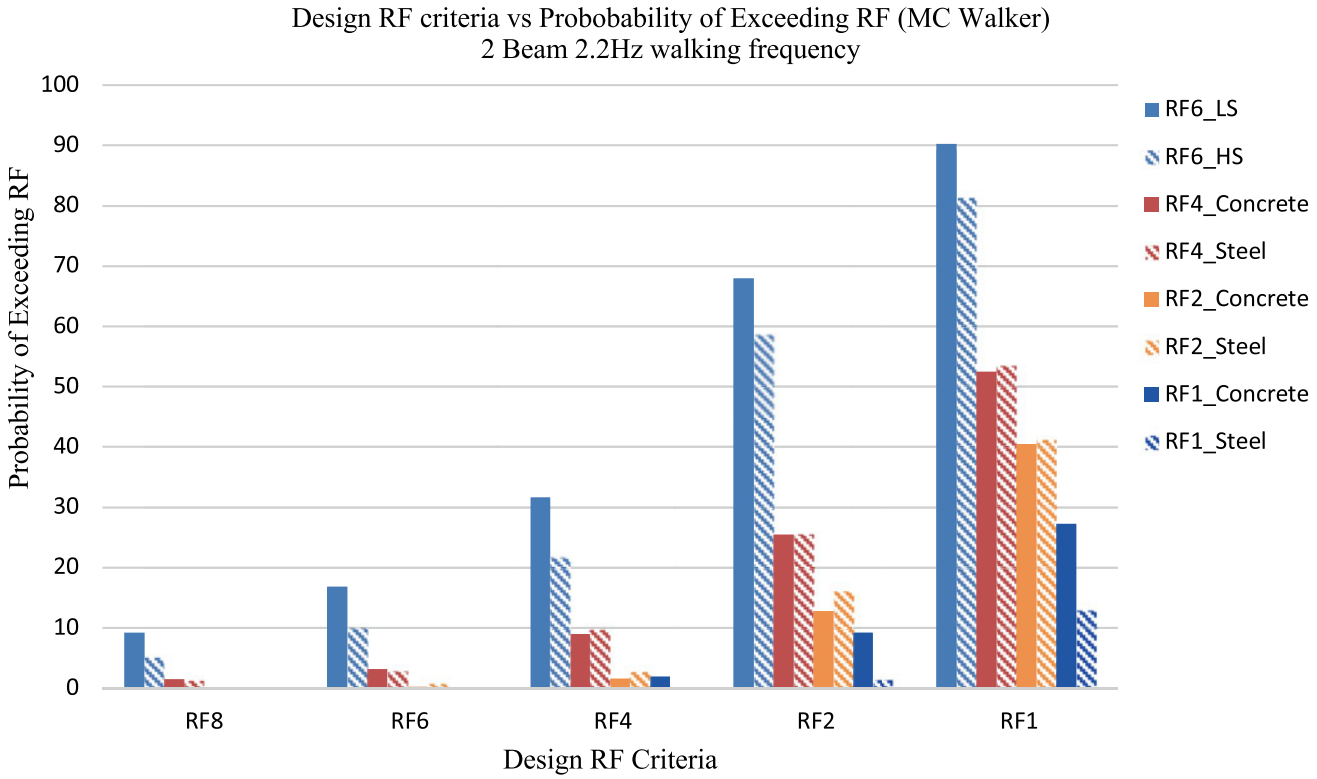

Fig. 14.9b Probability of exceeding certain design criteria with 2-beam 2.2Hz walking frequency model

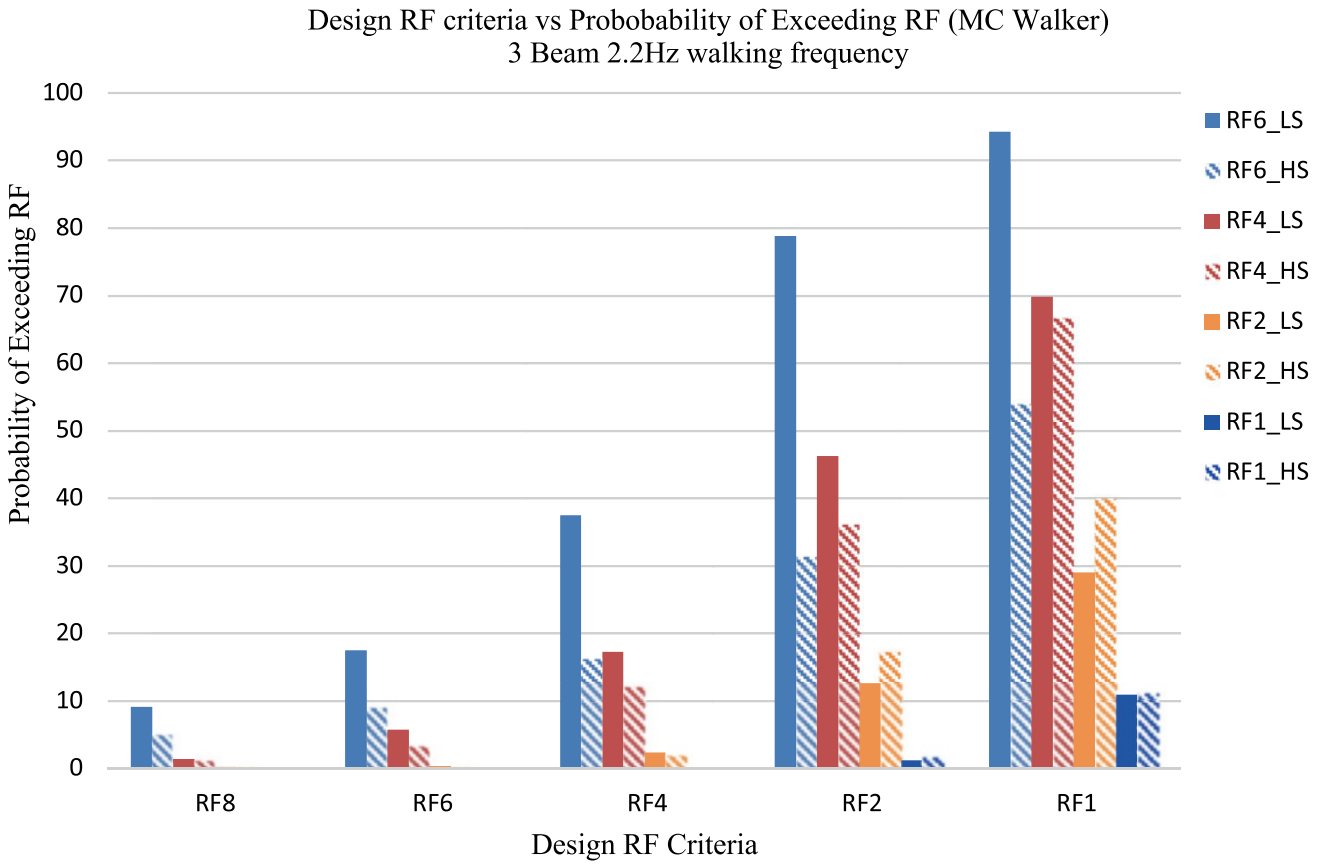

Fig. 14.9c Probability of exceeding certain design criteria with 3-beam 2.2Hz walking frequency model (*LS* light steel design and *HS* heavy steel design)

absolute design in reducing footfall vibration, and many methods can be used to meet a specific constraint set by the client. The results from this study give reason to believe a heavier concrete structure performs better at reducing footfall-induced vibration; however, it may not always be feasible due to its higher seismic mass. The results gathered from this research can be useful for engineering firms to design for footfall vibration and will become more applicable as the focus on vibration increases. As this research continues, more trends between structure properties and floor vibration will be discovered outside of steel weight and concrete weight.

Acknowledgments The authors would like to acknowledge the supports from National Science Foundation EEC-1659877/ECC-1659507, the College of Science and Engineering and the School of Engineering at San Francisco State University, and College of Engineering and Computing at the University of South Carolina. Supports from the industrial collaborator, Arup Us Inc, are also appreciated. The authors would also like to thank Mark Arkinstall and Andreanna Tzortzis in Arup for their advice and supports to the project.

References

1. Sétra: Assessment of vibrational behaviour of footbridges under pedestrian loading Technical guide SETRA. SETRA, Paris (2006)
2. Dallard, P., Fitzpatrick, A.J., Flint, A., Le Bourva, S., Low, A., Ridsdill Smith, R.M., Willford, M.: The London millennium footbridge. Struct. Eng. **79**(22), 17–21 (2001)
3. Ingólfsson, E.T., Georgakis, C.T., Jönsson, J.: Pedestrian-induced lateral vibrations of footbridges: a literature review. Eng. Struct. **45**, 21–52 (2012)
4. Brownjohn, J., Racic, V., Chen, J.: Universal response spectrum procedure for predicting walking-induced floor vibration. Mech. Syst. Signal Process. **70**, 741–755 (2016)
5. Allen, D.E.: Building vibrations from human activities. Concr. Int. **12**(6), 66–73 (1990)
6. NBCC: Users' Guide – National Building Code of Canada (NBCC 2005): structural commentaries – commentary D: deflection and vibration criteria for serviceability and fatigue limit states, 2nd edn. Canadian Commission on Building and Fire Codes – National Research Council of Canada, Ottawa (2010)
7. Murray, T.M., Allen, D.E., Ungar, E.E.: Floor Vibrations Due to Human Activities Steel Design Guide Series-11. AISC/CISC, Chicago (2016)
8. Willford, M.R., Young, P., CEng, M.: A design guide for footfall induced vibration of structures. Concrete Society for The Concrete Centre, Surrey (2006)
9. Wei, L., Griffin, M.J.: Mathematical models for the apparent mass of the seated human body exposed to vertical vibration. J. Sound Vib. **212**(5), 855–874 (1998)
10. ASCE: Minimum design loads for buildings and other structures. American Society of Civil Engineers, Oct 2013
11. Sachse, R., Pavic, A., Reynolds, P.: Human-structure dynamic interaction in civil engineering dynamics: a literature review. Shock Vib. Dig. **35**(1), 3–18 (2003)
12. Institution of Structural Engineers (Great Britain): Dynamic performance requirements for permanent grandstands subject to crowd action: interim guidance on assessment and design. Institution of Structural Engineers, London (2001)
13. Ortiz, A.R.: Modeling human-structure interaction using a controller system, 1st edn. Universidad del Valle, Bogota (2020)
14. Ebrahimpour, A., Sack, R.L.: A review of vibration serviceability criteria for floor structures. Comput. Struct. **83**(28–30), 2488–2494 (2005)
15. Kerr, S.C., Bishop, N.W.M.: Human induced loading on flexible staircases. Eng. Struct. **23**(1), 37–45 (2001)
16. Australian Bureau of Statistics: How Australians measure up. Australian Bureau of Statistics, Canberra (1995)

Chapter 15
Digital Twinning of Modeling for Offshore Wind Turbine Drivetrain Monitoring: A Numerical Study

Vahid Jahangiri, Mohammad Valikhani, Hamed Ebrahimian, Sauro Liberatore, Babak Moaveni, and Eric Hines

Abstract Failures in wind turbine drivetrain system including gearbox, bearings, and generator accounts for more than 60% of total wind turbine downtime. In this study, a mechanics-based digital twin technology is proposed to update drivetrain models parameters using measured data and predict the mechanics-based demand in drivetrain components. With the proposed mechanics-based digital twin, the alternations in the structural model parameters can be monitored and identified for damage diagnosis purposes. The proposed technology is implemented on a numerical torsional model of a wind turbine drivetrain system to update the drivetrain model using simulated data and predict the mechanics-based demand in drivetrain components. Implementation of this approach is used to update the failure models and estimate the remaining useful life of drivetrain components including gears and shafts.

Keywords System identification · Remaining useful life · Wind turbine drivetrain · Digital twin technology · Bayesian model updating

15.1 Introduction

More than 60% of total wind turbine downtime is caused by failures in wind turbine drivetrain system including gearbox, generator, and bearings [1]. The overall costs for failure in wind turbines are much higher in offshore wind turbines which are farther from the shore making the maintenance more costly and increasing the downtime. Unexpected failures can occur due to the difference in dynamic demands in wind turbine drivetrain systems and the values used in the design. This shows the importance of remote monitoring for damage identification and condition monitoring in wind turbine drivetrains.

Different studies have been carried out for model identification and damage detection of wind turbine drivetrain systems. Perisic et al. [2] used an augmented Kalman filter with fading memory to measure the drivetrain shaft torque indirectly using the measurements from the rotor angular velocity, generator torque, and generator angular velocity. Also, the authors compared the robustness of the proposed augmented Kalman filter with fading memory with augmented Kalman filter, by adding noise to the simulated wind turbine data. It was concluded that, the proposed algorithms provide an acceptable matching between the predicted and the simulated shaft torque signals. In another study, Moghaddam et al. [3] proposed an algorithm for near real-time estimation of wind turbine torsional drivetrain parameters. The authors compared their model responses with a high-fidelity model [4], and it was shown that the proposed digital twin approach is computationally fast and can be used for online monitoring of wind turbine drivetrain components.

In the present study, a Bayesian model updating approach is used for mechanics-based model updating approach, which has been previously implemented and validated through numerically simulated data for earthquake engineering applications [5] and for digital modeling of wind turbine tower [6] is modified for the application of wind turbine drivetrain systems in the present study. The proposed model updating approach is implemented on a numerical torsional model of a wind turbine drivetrain system to update the drivetrain model parameters using simulated data and predict the mechanics-based demand in drivetrain components.

V. Jahangiri (✉) · M. Valikhani · H. Ebrahimian
Department of Civil and Environmental Engineering, University of Nevada, Reno, NV, USA
e-mail: vjahangiri@unr.edu; mvalikhani@nevada.unr.edu; hebrahimian@unr.edu

S. Liberatore · B. Moaveni · E. Hines
Department of Civil and Environmental Engineering, Tufts University, Medford, MA, USA
e-mail: sauro.liberatore@tufts.edu; babak.moaveni@tufts.edu; eric.hines@tufts.edu

Z. Mao (eds.), *Model Validation and Uncertainty Quantification, Volume 3*, Conference Proceedings of the Society for Experimental Mechanics Series, https://doi.org/10.1007/978-3-031-04090-0_15

15.2 Analysis

The Bayesian model updating approach previously used for earthquake engineering applications [5] and for digital modeling of wind turbine tower [6] is being used for the application of wind turbine drivetrain systems. In a Bayesian model updating approach, the uncertain model parameters of the system (θ) are updated using sensor measurements (y) via the Bayes theorem:

$$p(\theta|\boldsymbol{y}) = \frac{p(\boldsymbol{y}|\theta)\, p(\theta)}{p(\boldsymbol{y})} \tag{15.1}$$

where $p(\theta|\boldsymbol{y})$ represents the posterior probability density function, $p(\theta)$ is the prior probability density function which shows the previous knowledge of the parameter, $p(\boldsymbol{y}|\theta)$ is the likelihood function, and $p(\boldsymbol{y})$ is the evidence.

The proposed technology is implemented on a numerical torsional model of a wind turbine drivetrain system to update the drivetrain model using simulated data and predict the mechanics-based demand in drivetrain components. In this regard, the NREL 5MW reference wind turbine drivetrain is selected as the case study, whereas only the torsional behavior of the drivetrain is considered. A schematic model of the wind turbine drivetrain with two planetary gearbox stages and one parallel gearbox stage is illustrated in Fig. 15.1. In this figure, *R*, *C*, *S*, *W*, and *G* represents the rotor, carrier, sun gear, wheel gear, and the generator, respectively. Also, *LSS*, *IS*, and *HSS* denote the low-speed shaft, intermediate shaft, and high-speed shaft, respectively. The overall gearbox ratio is 1:97 [7], whereas the gearbox ratio for the first stage planetary gearbox is 1:3.947, the second stage planetary gearbox ratio is 1:6.167, and the third stage parallel gearbox ratio is 1:3.958 [4].

The rotor, generator, and gearbox components including planet carrier, gears, and the shafts are modeled as a one torsional degree of freedom. The wind turbine drivetrain is modeled numerically, and the equations of motion can be written in a matrix format as follows:

$$J\ddot{\theta} + K\theta = T \tag{15.2}$$

where J is the mass inertia matrix, K is the stiffness matrix, and T is the external torques applied to the drivetrain system. $\ddot{\theta}$ and θ are the nodal acceleration and displacement vectors.

Using the Bayesian model updating approach, the aerodynamic input torque can be estimated jointly with the LSS stiffness and rotor mass moment of inertia only based on generator torque and speed measurements. As it can be seen from Fig. 15.2 (a)–(b), the LSS stiffness and rotor polar mass moment of inertia converge to the true values and can be estimated after a few iterations. Also, the time-history of measured generator speed and estimated aerodynamic torque can be seen in Fig. 15.2 (c)–(d). It can be observed that the measured generator speed matches the predicted generator speed.

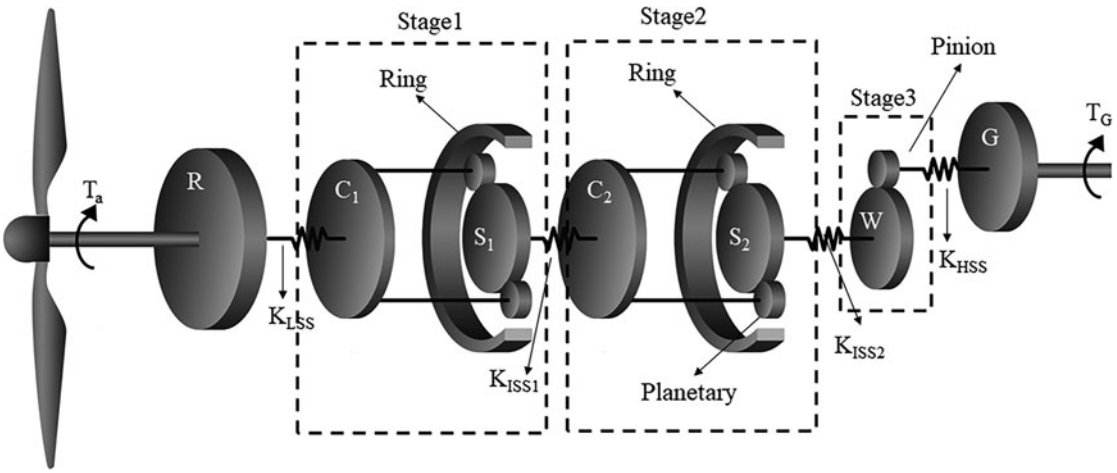

Fig. 15.1 Schematic model of the wind turbine drivetrain with two planetary gearbox stages and one parallel gearbox stage

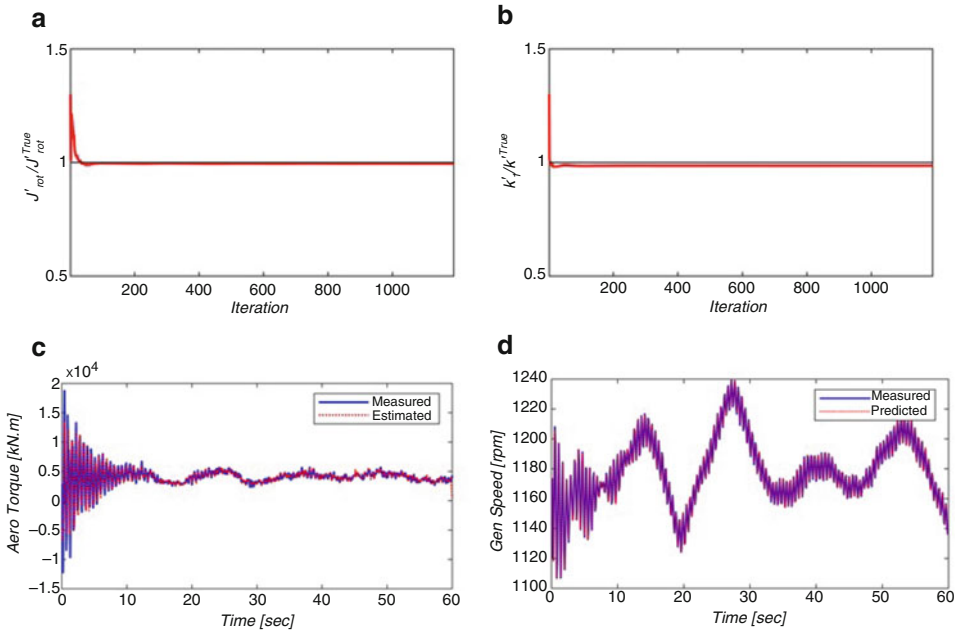

Fig. 15.2 Convergence history of normalized (**a**) rotor mass moment of inertia and (**b**) LSS stiffness; (**c**) time-history of measured and estimated aerodynamic torque; (**d**) Measured and predicted responses of generator from the updated model

15.3 Conclusion

A mechanics-based digital twin technology is used to update wind turbine drivetrain model using measured data and predict the mechanics-based demand in drivetrain components. The changes in structural model parameters can be identified and monitored for damage diagnosis purposes of the wind turbine drivetrain system. In this regard, a numerical torsional model of the wind turbine drivetrain system, including the rotor, gearboxes, generator, and corresponding shafts, is established to update the drivetrain model using simulated data and predict the mechanics-based demand in drivetrain components. Implementation of this approach is used to update the failure models and estimate the remaining useful life of drivetrain components including gears and shafts. It has been shown that, using the developed Bayesian model updating approach the aerodynamic input torque can be estimated jointly with LSS stiffness and rotor mass moment of inertia using only measurements from the generator.

Acknowledgments This work was supported by National Offshore Wind Research and Development Consortium (NOWRDC). The authors are grateful for all the support.

References

1. Pfaffel, S., Faulstich, S., Rohrig, K.: Performance and reliability of wind turbines: a review. Energies. **10**(11), 1904 (2017)
2. Perišić, N., Kirkegaard, P.H., Pedersen, B.J.: Cost-effective shaft torque observer for condition monitoring of wind turbines. Wind Energy. **18**(1), 1–19 (2015)
3. Moghadam, F.K., Rebouças, G.F.d.S., Nejad, A.R.: Digital twin modeling for predictive maintenance of gearboxes in floating offshore wind turbine drivetrains. Forschung im Ingenieurwesen. **85**(2), 273–286 (2021)
4. Nejad, A.R., Guo, Y., Gao, Z., Moan, T.: Development of a 5 MW reference gearbox for offshore wind turbines. Wind Energy. **19**(6), 1089–1106 (2016)
5. Ebrahimian, H., Astroza, R., Conte, J.P., Papadimitriou, C.: Bayesian optimal estimation for output-only nonlinear system and damage identification of civil structures. Struct. Control Health Monit. **25**(4), e2128 (2018)
6. Nabiyan, M.-S., Khoshnoudian, F., Moaveni, B., Ebrahimian, H.: Mechanics-based model updating for identification and virtual sensing of an offshore wind turbine using sparse measurements. Struct. Control Health Monit. **28**, e2647 (2021)
7. Jonkman, J., Butterfield, S., Musial, W., Scott, G.: Definition of a 5-MW reference wind turbine for offshore system development No. NREL/TP-500-38060. National Renewable Energy Lab. (NREL), Golden (2009)
8. Jonkman, J.M., Buhl Jr, M.L.: FAST user's guide, vol. 365, p. 366.8. National Renewable Energy Laboratory, Golden (2005)

Chapter 16
Prediction of Footbridge Vibrations and Their Dependence on Pedestrian Loads

Lars Pedersen and Christian Frier

Abstract Prediction of structural vibrations due to vertical loads generated by pedestrians is an assignment that many engineers involved with footbridge design have encountered. Often, the problem matter is not ultimate limit-state-requirements, but concern is on serviceability-limit-state requirements in the form of potential excessive structural vibrations. The nature of human locomotion dictates that the action of pedestrians on footbridges is random. This also has the effect that the footbridge vibrational response is random and potentially depends on a set of walking parameters (pacing speed, load amplifications factors, pedestrian weight, etc.) and the stochastic nature of these parameters. The paper will address issues of predicting footbridge vibrations in this context, taking offset in artificial footbridges. Monte Carlo simulations and Newmark time integration will be employed for determining footbridge vibrations.

Keywords Footbridge · Vibrations · Walking · Serviceability

Nomenclature

a	Bridge acceleration	f_1	Bridge fundamental frequency	f_s	Step frequency
i	Integer	m_1	Bridge modal mass	l_s	Step length
v	Pacing speed	t	Time	F	Walking load
L	Bridge length	Q	Modal load	W	Weight of pedestrian
α	Dynamic load factor	ζ_1	Bridge damping ratio	μ	Mean value
σ	Standard deviation	θ	Phase	Φ	Mode shape

16.1 Introduction

It is well known that footbridges can be flexible and that this can be of concern. An example of this is the Millennium Bridge vibrations [1] that occurred as a result of human locomotion.

The bridge turned out unfit for its intended use. The problem was not the ultimate-limit-state but the serviceability-limit-state. Persons passing the bridge felt uncomfortable, and it was due to the actions of pedestrians generating forces onto the bridge bringing it into vibration. The general problem was resonant excitation.

The present paper also addresses vibrations generated by pedestrians based on the modelling of walking loads. A lot of works done previously have addressed modelling walking loads, for instance [2–4]. In these works, walking loads were modelled in a deterministic manner.

However, by nature, human locomotion is stochastic. This is recognised in [5–10] either by modelling the walking parameters as random variables or by setting up a stochastic framework for computing footbridge vibrations.

L. Pedersen (✉) · C. Frier
Department of Civil Engineering, Aalborg University, Aalborg Ø, Denmark
e-mail: lp@civil.aau.dk; cf@civil.aau.dk

Z. Mao (eds.), *Model Validation and Uncertainty Quantification, Volume 3*, Conference Proceedings of the Society for Experimental Mechanics Series, https://doi.org/10.1007/978-3-031-04090-0_16

In this paper the probabilistic/stochastic approach is adopted. Since walking parameters will be modelled as random variables, also the bridge acceleration response will be stochastic. The bridge response in focus in the paper will be the 95% quantile of midspan bridge accelerations.

This property (a_{95}) will be estimated using Newmark time integration combined with the use of Monte Carlo simulation methods for a set of artificial single-span pin-supported bridges.

The aim of the paper is on examining how a selected subset of possible load model assumptions influences estimates of a_{95}, basically to test how sensitive the outcome of calculations is to different load model assumptions.

Section 16.2 outlines the main structure of the load model and assumptions made in terms of the stochastic nature of walking parameters. Section 16.3 presents two different studies exploring how sensitive a_{95} is to different load model assumptions. Section 16.4 summarises the conclusions.

16.2 Modelling of Walking Loads

The modelling of walking loads is based on Eq. (16.1).

$$Q(t) = \Phi(t)F(t) \tag{16.1}$$

In this equation, $Q(t)$ represents the modal load, and $F(t)$ represents the vertical force generated by the pedestrian. $\Phi(t)$ is the mode shape function assumed to take on values calculated from Eq. (16.2).

$$\Phi(t) = \sin(\pi v t/L) \tag{16.2}$$

Hence, it is assumed that it is the first bending mode that governs the response.

In Eq. (16.2), v is the pacing speed of the pedestrian, calculated from Eq. (16.3).

$$v = f_s l_s \tag{16.3}$$

In this equation, f_s is the step frequency, and l_s is the step length of the pedestrian.

These two parameters will be modelled as random variables with the parameters shown in Table 16.1. Gaussian assumptions are made for the parameters f_s and l_s.

In the table, also W is introduced, and it represents the static weight of the pedestrian. As can be seen, this property is handled as a deterministic property.

As for the load $F(t)$, it is modelled in the way described by Eqs. (16.4, 16.5, and 16.6).

$$F(t) = \sum_{i=1}^{5} F_i(t) + \sum_{i=1}^{5} F_i^S(t) \tag{16.4}$$

$$F_i(t) = W\alpha_i \cos(2\pi i f_s t + \varphi_i) \tag{16.5}$$

$$F_i^S(t) = W\alpha_i^S \cos(\pi\,(2i-1)\,f_s t + \varphi_{i+5}) \tag{16.6}$$

Table 16.1 Mean values (μ) and standard deviations (σ)

–	μ	σ	Reference
W	750 N	0 N	[9]
l_s	0.71 m	0.071 m	[9]
f_s	1.87 Hz	0.186 Hz	[9]

Table 16.2 Mean values (μ) and standard deviations (σ) [7, 9]

–	α_2	α_3	α_4	α_5
μ	0.07	0.05	0.05	0.03
σ	0.030	0.020	0.020	0.015

Table 16.3 Modal properties of bridge and bridge length (L)

Property	f_1	ζ_1	m_1	L
Value	1.875	0.5	44.9	45.9
Unit	Hz	%	10^3 kg	m

The load model was first introduced in [10]. In its basic form, it assumes five main harmonics (entering by Eq. (16.5)) and five subharmonics (entering by Eq. (16.6)). The model assumes no leakage of energy to other frequencies outside the excitation frequencies.

As for the dynamic load factors, α_i, they are modelled as random variables and assumed to follow a Gaussian distribution.

For the first harmonic, α_1, its mean value, μ, and standard variation, σ, are calculated from Eq. (16.7).

$$\mu = -0.2649 f_S^3 + 1.3206 f_S^2 - 1.7597 f_S + 0.7613; \quad \sigma = 0.16\mu \tag{16.7}$$

Table 16.2 defines the assumptions made for the remaining main dynamic load factors.

The subharmonic dynamic load factors α_i^S (in Eq. 16.6) are calculated from the main harmonic load factor, α_1, according to the procedure outlined in [9], which also outlines procedures for determining the phases in Eqs. (16.5 and 16.6).

16.3 Studies of This Paper

Having defined assumptions as regards the load generated by a single pedestrian, it is possible to generate the adjoining load-time history and to compute the maximum vertical bridge acceleration response, a, that occurs at bridge midspan, while a pedestrian crosses the bridge. This was accomplished using Newmark time integration, and Monte Carlo simulations were employed for establishing a statistical representation of bridge vibration response. For each of the studies of this paper, 100,000 bridge crossings by a single pedestrian were simulated.

From the statistical basis hereby obtained, the bridge acceleration quantile a_{95} was extracted. This quantile is believed to be a reasonable parameter to describe the vibrational performance of a footbridge.

The footbridges considered in the studies of this paper are artificial SDOF pin-supported bridges all having a fundamental frequency (in vertical bending) in the immediate vicinity of the mean value of the step frequency assumed for the pedestrians passing the bridge.

The modal properties of the bridges will be outlined for each of the studies presented below. The studies will have focus on the fact that the engineer in charge of computations of bridge response will have different options available for his calculations (decisions to be made). Hence, the general idea is to compare values of a_{95} computed on different assumptions in terms of modelling walking loads.

16.3.1 Impact of Decisions Related to the Choice of Load Model

Assumed for this study is a SDOF-bridge with the modal characteristics defined in Table 16.3.

There are other proposals in literature as to how to model $F(t)$ than the model defined by Eqs. (16.5 and 16.6).

An alternative, for example, would be to assume the walking load model proposed in [9].

Table 16.4 Computed values of a_{95}

Model	No leakage	Leakage
a_{95}	0.3382	0.3281
Unit	m/s^2	m/s^2

Table 16.5 Modal properties of bridge and bridge length (L)

Property	f_1	ζ_1	m_1	L
Value	1.9	0.5	44.0	45.0
Unit	Hz	%	10^3 kg	m

In that model, Eqs. (16.8 and 16.9) are to substitute Eqs. (16.5 and 16.6).

$$F_i(t) = W\alpha_i \sum_{\overline{f}_j = i-0.25}^{i+0.25} \overline{\alpha}_i\left(\overline{f}_j\right) \cos\left(2\pi \overline{f}_j f_s t + \theta\left(\overline{f}_j\right)\right) \tag{16.8}$$

$$F_i^S(t) = W\alpha_i^S \sum_{\overline{f}_j^S = i-0.75}^{i-0.25} \overline{\alpha}_i^S\left(\overline{f}_j^S\right) \cos\left(2\pi \overline{f}_j^S f_s t + \theta\left(\overline{f}_j^S\right)\right) \tag{16.9}$$

For a full description of the parameters in Eqs. (16.8 and 16.9), reference is made to [9].

This model also (as the model introduced in Sect. 16.2) consists of main load harmonics (Eq. (16.8)) and subharmonics (Eq. (16.9)). The difference is that this model accounts for a leakage of energy in the sense that a full periodic excitation is not assumed.

For both load model assumptions values of a_{95} were computed, and results are shown in Table 16.4.

It appears that the model that does not account for leakage of energy results in the higher value of a_{95}. This is as expected as when leakage is assumed to occur, it will be accompanied with less energy exciting at the fundamental frequency of the bridge.

The difference between the two results is only 3%. So for this particular scenario, it may not be worthwhile employing the quite advanced load model that accounts for leakage.

16.3.2 Impact of Decisions Related to Modelling the Load Amplification Factor

Assumed for this study is a SDOF-bridge with the modal characteristics defined in Table 16.5.

Again, it is a bridge with a fundamental frequency in the immediate vicinity of the mean value assumed for the step frequency.

For this study, the load model outlined in Sect. 16.2 was employed. For simplicity only the first main harmonic was considered.

Basically, there are different ways in which the dynamic load factor associated with first load harmonic can be derived.

In the more advanced approach, it is considered that for every pedestrian that crosses the bridge, different values of α_1 will come up for the calculation of bridge vibration, as this parameter (α_1) is a function of step frequency (see Eq. (16.7)), and as the step frequency is modelled as a random variable, the value of α_1 cannot be the same for every pedestrian.

However, a study was made in which the value of α_1 was picked from Eq. (16.7) by entering the mean value for the step frequency assumed for the entire population of pedestrians crossing the bridge for every pedestrian.

It turned out that the difference in the computed value of a_{95} differed by less than 2%.

16.4 Conclusion and Discussion

The paper has had focus on a subset of the decisions that the engineer in charge of calculations of the bridge acceleration quantile a_{95} (the acceleration level exceeded in 5% of the pedestrian crossings) need to make.

The decisions related to how to model the walking loads of the pedestrians assumed to cross the bridge one by one.

Two different load models were examined, and a simplified approach for determining dynamic load factors versus a more advanced approach was also studied.

In both cases (in both studies), it turned out that value of a_{95} was only slightly sensitive to the approach chosen for modelling the action of walking.

This suggests that it might not always be necessary to employ the most advanced load models (although they replicate the load mechanism better), which is useful to know.

This conclusion is drawn from studying only SDOF pin-supported footbridges with fundamental frequencies in the immediate vicinity of the mean value for the step frequency of the population of pedestrians. It would be interesting to study whether this is also valid for bridges with other bridge frequencies.

References

1. Dallard, P., Fitzpatrick, A.J., Flint, A., Le Bourva, S., Low, A., Ridsdill-Smith, R.M., Wilford, M.: The London Millennium Bridge. Struct. Eng. **79**, 17–33 (2001)
2. Ellis, B.R.: On the response of long-span floors to walking loads generated by individuals and crowds. Struct. Eng. **78**, 1–25 (2000)
3. Bachmann, H., Ammann, W.: Vibrations in Structures – Induced by Man and Machines, IABSE Structural Engineering Documents 3e, Zürich, Switzerland (1987)
4. Rainer, J.H., Pernica, G., Allen, D.E.: Dynamic loading and response of footbridges. Can. J. Civ. Eng. **15**, 66–78 (1998)
5. Matsumoto, Y., Nishioka, T., Shiojiri, H., Matsuzaki, K.: Dynamic design of footbridges, In: IABSE proceedings, No. P-17/78, pp. 1–15 (1978)
6. Živanovic, S.: Probability-based estimation of vibration for pedestrian structures due to walking, PhD thesis, Department of Civil and Structural Engineering, University of Sheffield, UK (2006)
7. Kerr, S.C., Bishop, N.W.M.: Human induced loading on flexible staircases. Eng. Struct. **23**, 37–45 (2001)
8. Pedersen, L., Frier, C.: Sensitivity of footbridge vibrations to stochastic walking parameters. J. Sound Vib. **329**, 2683–2701 (2009). https://doi.org/10.1016/j.jsv.2009.12.022
9. Živanovic, S., Pavic, A., Reynolds, P.: Probability-based prediction of multi-mode vibration response to walking excitation. Eng. Struct. **29**, 942–954 (2007). https://doi.org/10.1016/j.engstruct.2006.07.004
10. Pedersen, L., Frier, C.: Predictions of footbridge vibrations and influencing load model decisions. IMACXXXVIII, Houston (2020)

Chapter 17
Combining Simulation and Experiment for Acoustic-Load Identification

Garrett K. Lopp and Ryan Schultz

Abstract Bayesian inference is a technique that researchers have recently employed to solve inverse problems in structural dynamics and acoustics. More specifically, this technique can identify the spatial correlation of a distributed set of pressure loads generated during vibroacoustic testing. In this context, Bayesian inference augments the experimenter's prior knowledge of the acoustic field prior to testing with vibration measurements at several locations on the test article to update these pressure correlations. One method to incorporate prior knowledge is to use a theoretical form of the correlations; however, theoretical forms only exist for a few special cases, e.g., a diffuse field or uncorrelated pressures. For more complex loading scenarios, such as those arising in a direct-field acoustic test, utilizing one of these theoretical priors may not be able to accurately reproduce the acoustic loading generated during the experiment. As such, this work leverages the pressure correlations generated from an acoustic simulation as the Bayesian prior to increase the accuracy of the inference for complex loading scenarios.

Keywords Vibroacoustic testing · Structural dynamics · Load identification · Bayesian inference · Uncertainty quantification

17.1 Introduction

Correlating a model with an experiment requires an accurate measurement of the loads imparted into the test article. In many cases, these forces are readily available through measurements with a force sensor, e.g., when exciting the test article using electrodynamic shakers. Other cases may include distributed loads, resulting in the inability to obtain pressure measurements at every location on the test article, e.g., when exciting the test article with acoustic loads. As such, a distributed set of loads requires a method to infer the loads based on readily available measurements. One way to infer these distributed loads is through Bayesian inference, which researchers have used to solve inverse problems in structural dynamics and acoustics [1–10]. Bayesian inference is based on Bayes' Theorem, which states that the posterior probability of a set of unknown variables is proportional to the product of the prior probability and the likelihood of the unknowns given a set of observations.

In the application considered here, the variables that require identification are a distributed set of pressures acting on the test article's wetted surface, and the observations are the measured vibration responses on the test article. For the prior, we can include knowledge about the pressure field prior to performing any experiments and collecting any data. In some special cases, analytical expressions for the pressure field do exist, resulting in building the prior covariance matrix directly using closed-form expressions that are functions of the spatial distance between inputs, e.g., acoustic testing in a reverberation chamber leads to an approximate diffuse field that has a spatial correlation modeled by a sinc function [11], and pressure loads induced by a turbulent boundary layer have a spatial correlation approximately modeled by exponential functions [12].

Sandia National Laboratories is a multi-mission laboratory managed and operated by National Technology & Engineering Solutions of Sandia, LLC, a wholly owned subsidiary of Honeywell International Inc., for the U.S. Department of Energy's National Nuclear Security Administration under contract DE-NA0003525. This paper describes objective technical results and analysis. Any subjective views or opinions that might be expressed in the paper do not necessarily represent the views of the U.S. Department of Energy or the United States Government.

G. K. Lopp (✉) · R. Schultz
Sandia National Laboratories, Albuquerque, NM, USA
e-mail: glopp@sandia.gov; rschult@sandia.gov

Z. Mao (eds.), *Model Validation and Uncertainty Quantification, Volume 3*, Conference Proceedings of the Society for Experimental Mechanics Series, https://doi.org/10.1007/978-3-031-04090-0_17

In other cases, such as a direct-field acoustic test, the spatial correlation of the pressure loading does not have an analytical approximation.

This chapter specifically targets cases where the spatial correlations of the input loads do not have a closed-form expression; instead, this chapter details the use of a pressure field obtained through simulation as the Bayesian prior. Through Bayesian inference, the vibration measurements collected during the acoustic test can augment this simulated pressure field to better match the test environment.

17.2 Bayesian Load Estimation

When considering stationary random loads, the cross-power spectral density (CPSD) matrix of inputs, $\hat{\mathbf{S}}_{ff}$, can be estimated through Bayesian inference using the measured CPSD matrix of vibration responses, $\mathbf{S}_{xx,m}$ [8, 10]:

$$\hat{\mathbf{S}}_{ff} = \left[\frac{1}{\sigma_n^2}\hat{\mathbf{C}}_{ff}\mathbf{H}_{xf,m}^H\boldsymbol{\Sigma}_{nn}^{-1}\right]\mathbf{S}_{xx,m}\left[\frac{1}{\sigma_n^2}\hat{\mathbf{C}}_{ff}\mathbf{H}_{xf,m}^H\boldsymbol{\Sigma}_{nn}^{-1}\right]^H + \hat{\mathbf{C}}_{ff}, \tag{17.1}$$

where

$$\hat{\mathbf{C}}_{ff} = \sigma_n^2\left(\mathbf{H}_{xf,m}^H\boldsymbol{\Sigma}_{nn}^{-1}\mathbf{H}_{xf,m} + \tau^2\boldsymbol{\Sigma}_{ff}^{-1}\right)^{-1}. \tag{17.2}$$

In the above expressions, $\mathbf{H}_{xf,m}$ is the matrix of transfer functions relating the inputs to the outputs; $\mathbf{S}_{nn} = \sigma_n^2\Sigma_{nn}$ and $\mathbf{S}_{ff} = \sigma_f^2\Sigma_{ff}$ are the prior covariance matrices for the measurement/model errors and the inputs, respectively; and τ^2 serves as the regularization parameter, which is a ratio of the measurement noise/model error variance, σ_n^2, to the input variance, σ_f^2. The variables τ^2, σ_n^2, and σ_f^2 are known as hyperparameters and can be estimated using a number of strategies; here, we only consider the estimates obtained through maximizing the marginal likelihood [3, 10]. Reference [10] provides a full derivation of these equations and a more-detailed discussion.

If the characteristics of the measurement/model error are unknown a priori, setting Σ_{nn} as an identity matrix reflects the assumption of uncorrelated errors and allows the inference to proceed. Furthermore, setting Σ_{ff} as the spatial correlation of the simulated acoustic loads enables the inclusion of a simulated loads model in the inference procedure. Also note that Σ_{nn} and Σ_{ff} should be normalized such the trace of Σ_{nn} is equal to the number of response measurements and the trace of Σ_{ff} is equal to the number of unknown inputs.

Finally, the CPSD matrix for any of the system responses $\hat{\mathbf{S}}_{xx,*}$ can be recovered through

$$\hat{\mathbf{S}}_{xx,*} = \mathbf{H}_{xf,*}\hat{\mathbf{S}}_{ff}\mathbf{H}_{xf,*}^H, \tag{17.3}$$

where $\mathbf{H}_{xf,*}$ is the matrix of transfer functions relating the inputs to the outputs at the estimated locations.

17.3 Application to a Direct-Field Acoustic Test

To assess the performance of the inference, we utilized data collected from a direct-field acoustic test performed on a cylindrical test article. Figure 17.1a shows the test article, which consists of a hollow cylindrical shell with an internal beam, and Fig. 17.1b shows the test article suspended by bungee cords to approximate a free–free boundary condition. Four speakers received uncorrelated random voltage signals to generate the acoustic loads that excited the test article. Twelve triaxial accelerometers and six uniaxial accelerometers measured the vibration response at various locations on the test article. The responses from the triaxial accelerometers served as the target measurements in the inference procedure. The responses from the uniaxial accelerometers were not used in the inference procedure; instead, they served as a validation set to assess the responses generated by the estimated loads. An array of microphones measured the pressures at various locations in the field, including a roving line array of microphones that collected pressure measurements to provide a full 360° coverage around the test article.

The simulations utilized a calibrated finite-element model of the test article. Grouping neighboring nodes on the wetted surface into "patches" of constant pressure enabled the calculation of transfer functions relating the patch pressures to the

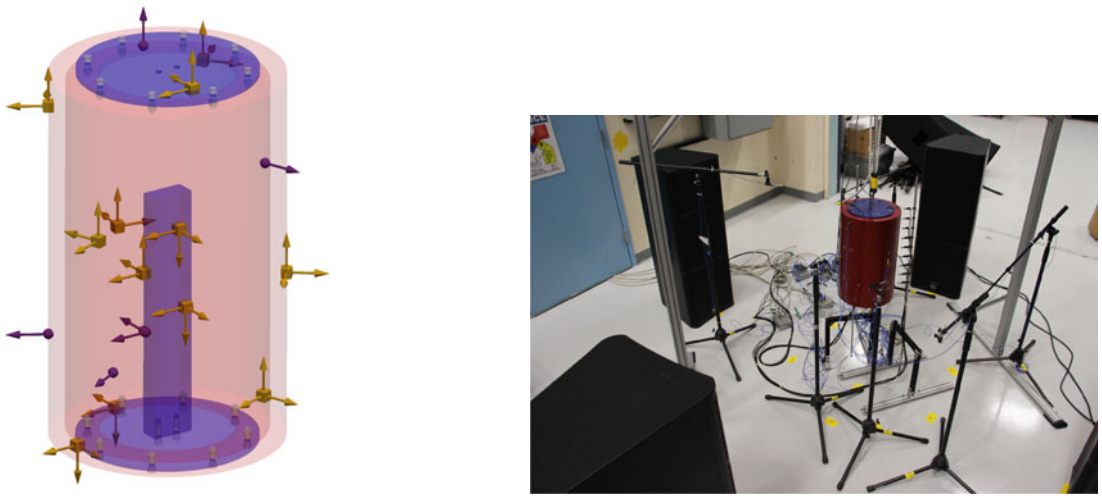

(a) (b)

Fig. 17.1 Experimental test setup. (**a**) Model of the test article composed of a cylinder with an internal beam. (**b**) The test setup with the test article surrounded by four speakers in a direct-field configuration

acceleration responses. Obtaining the Bayesian prior for the input covariance matrix required simulating the acoustic field test with an acoustic model, which utilized monopole sources to represent the speakers. This model also used mirror images of the monopole sources to simulate the reflective surface beneath the test article; however, it assumed that the test article and other objects in the domain were acoustically transparent and neglected any scattering effects. This acoustic modeling strategy enabled the calculation of a set of transfer functions relating the monopole sources to the pressures at the center of each patch of nodes on the cylinder's wetted surface. To simulate the uncorrelated signals sent to each speaker, the model treated the image–source pairs representing each speaker as uncorrelated with respect to the image–source pairs representing the other speakers to build the CPSD matrix of monopole sources. Finally, using the transfer functions relating the monopole sources to the patch pressures enabled the calculation of the CPSD matrix of patch pressures using the CPSD matrix of monopole sources. This CPSD matrix of patch pressures served as the Bayesian prior for the input covariance matrix.

To assess the inference strategy, we considered the cases of using the prior input covariance matrix obtained through the simulations directly and the one estimated using Bayesian inference in Eq. 17.1. During the hyperparameter-optimization step that maximized the marginal likelihood, the inference procedure placed a large weight on the field-microphone pressure measurements when calculating σ_f^2 using an additional prior [3, 8, 10]. That is, σ_f^2 closely matched the mean square of the measured field pressures. The metrics used to compare the estimates with the measured data consist of the sum of the auto-power spectral densities (APSDs), or the diagonal terms of the CPSD matrix, and magnitude and shape correlations, which comprise a normalized squared error summed over all real and imaginary elements of the CPSD matrix [10]. The magnitude and shape correlations compare the dominant eigenvalues and the corresponding eigenvectors of the CPSD matrix, respectively, and range between zero and unity with unity indicating a perfect match; the normalized error also ranges between zero and unity, but with zero indicating a perfect match with no error.

Figure 17.2 shows the sum of the APSDs and the comparison metrics for the input pressures at various locations on the wetted surface of the cylinder. At nearly all frequencies, the Bayesian update to the simulated covariance matrix resulted in higher correlations for both shape and magnitude and a reduced error, indicating better match, although slight, to the truth data. The estimated pressures did deteriorate at higher frequencies, indicating that there was significant error in the model that the Bayesian update step could not overcome. A possible source of this error is the absence of the scattering of the test article in the pressure field. Figure 17.3 shows a similar set of plots but compares the vibration responses at the target locations. The Bayesian update results in a significant increase in the quality of the vibration-response estimates, particularly for the response magnitudes, indicating that the inference procedure is able to augment the prior input covariance matrix in such a way that reproduces these measurements. Furthermore, although the inference procedure was unable to adequately estimate the input pressures at higher frequencies, it was still able to identify a solution that provided a better match to the vibration measurements. Although not shown here, the responses for the validation sensors followed a similar trend.

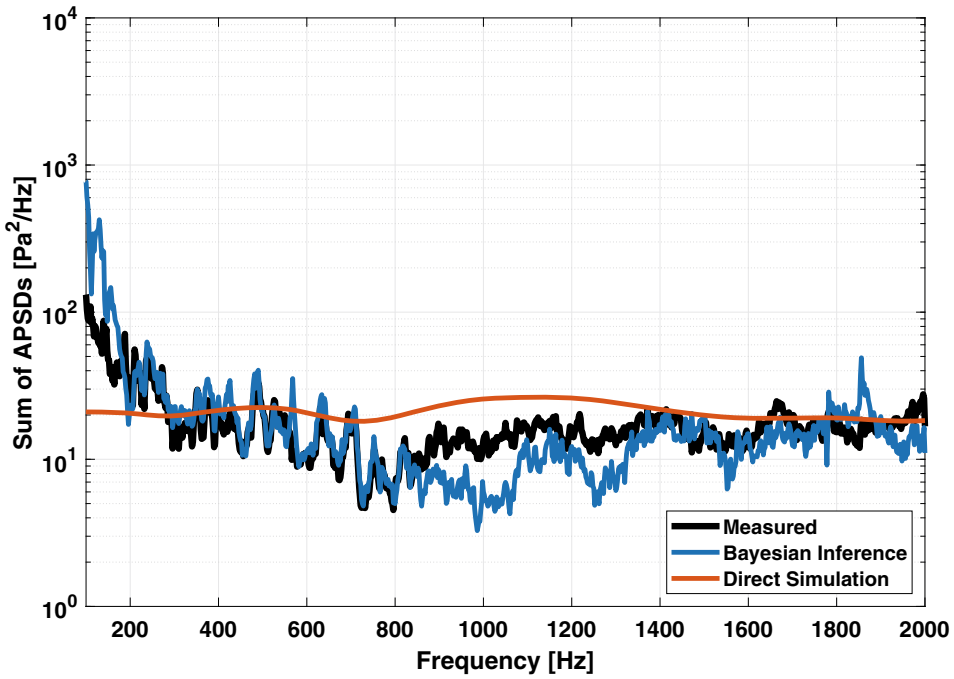

(a)

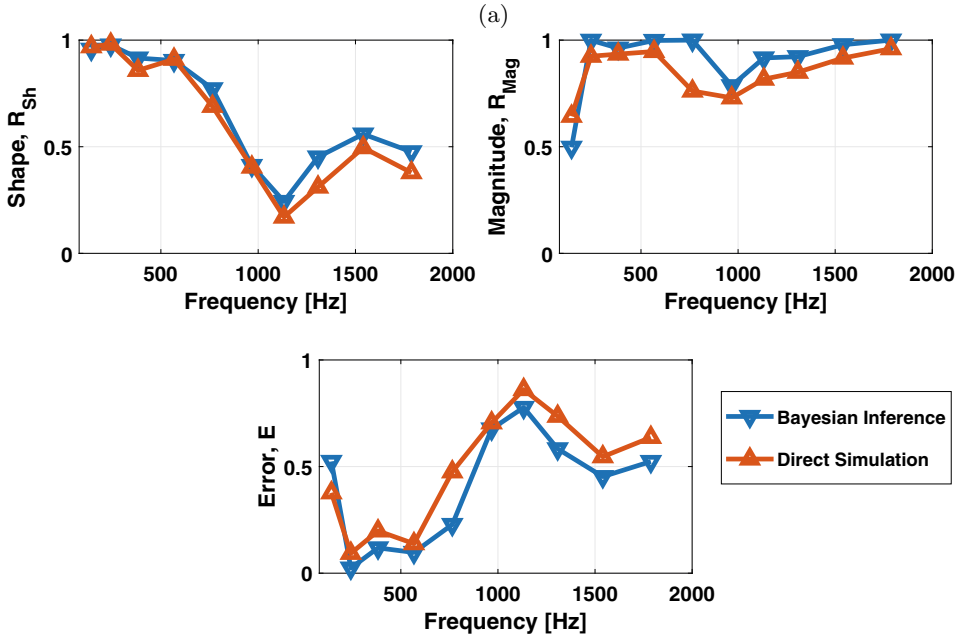

(b)

Fig. 17.2 Comparisons between the measured and estimated input pressures. (**a**) Sum of the APSDs. (**b**) Comparison metrics

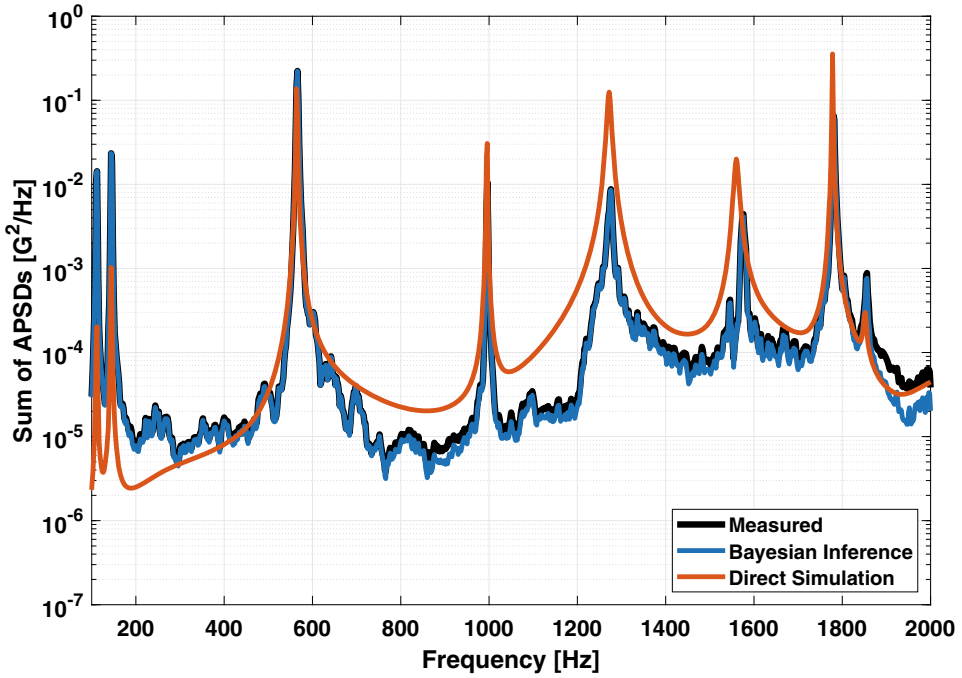

(a)

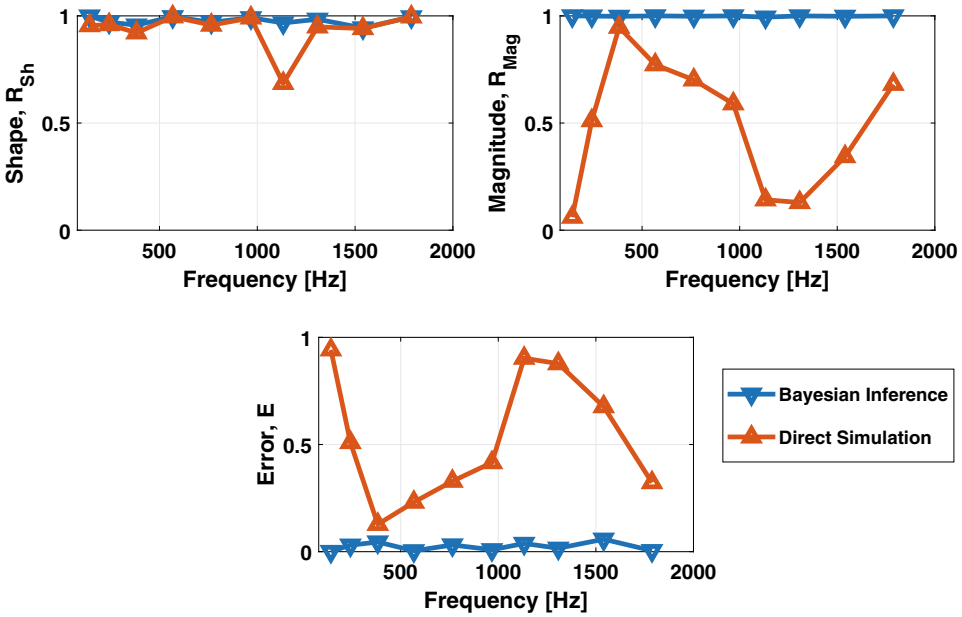

(b)

Fig. 17.3 Comparisons between the measured and estimated target responses. (**a**) Sum of the APSDs. (**b**) Comparison metrics

17.4 Conclusions

This chapter detailed the use of Bayesian inference to infer a distributed set of pressure loads during a direct-field acoustic test. The inference procedure used the distributed pressure field obtained from simulation for the prior and the vibration measurements at various locations of the test article for the likelihood function. The result was an updated pressure field that more-accurately matched the vibration on the test article compared to a simulation using the loads directly obtained from the simulation. For the application considered here, the inference procedure only produced an accurate pressure field at lower frequencies and was unable to overcome the pressure-field modeling errors at higher frequencies; however, it did produce an accurate representation of the vibration measurements at all frequencies. As such, a topic of future research is to investigate more-accurate loads models for use in the prior. The inference approach also relies heavily on an accurate set of transfer functions derived from a system model, which may be difficult to obtain for complex systems. To address this potential obstacle, future work should investigate the use of experimentally obtained transfer functions.

References

1. Zhang, E., Antoni, J., Feissel, P.: Bayesian force reconstruction with an uncertain model. J. Sound Vibration **331**(4), 798–814 (2012)
2. Antoni, J.: A Bayesian approach to sound source reconstruction: Optimal basis, regularization, and focusing. J. Acoust. Soc. Am. **131**(2873), 2873–2890 (2012)
3. Pereira, A., Antoni, J., Leclère, Q.: Empirical Bayesian regularization of the inverse acoustic problem. Appl. Acoust. **97**, 11–29 (2015)
4. Aucejo, M., Smet, O.D.: Bayesian source identification using local priors. Mech. Syst. Signal Process. **66–67**, 120–136 (2016)
5. Faure, C., Ablitzer, F., Antoni, J., Pézerat, C.: Empirical and fully Bayesian approaches for the identification of vibration sources from transverse displacement measurements. Mech. Syst. Signal Process. **94**, 180–201 (2017)
6. Aucejo, M., Smet, O.D.: On a full Bayesian inference for force reconstruction problems. Mech. Syst. Signal Process. **104**, 36–59 (2018)
7. Aucejo, M., Smet, O.D.: An optimal Bayesian regularization for force reconstruction problems. Mech. Syst. Signal Process. **126**, 98–115 (2019)
8. Lopp, G.K., Schultz, R.: A Bayesian approach for identifying the spatial correlation of acoustic loads during vibroacoustic testing. In: Paper Presented at the 38th International Modal Analysis Conference, February (2020)
9. Lopp, G.K., Schultz, R., Beale, D.: An experimental study of a Bayesian-based approach to identify full-field acoustic loads during vibroacoustic testing. In: Paper Presented at the 39th International Modal Analysis Conference, February (2021)
10. Lopp, G.K., Schultz, R.: Bayesian-based response estimation and uncertainty quantification using sparse measurement sets. Mech. Syst. Signal Process. **169**, 107566 (2022)
11. Cook, R.K., Waterhouse, R.V., Berendt, R.D., Edelman, S., Thompson Jr, M.C.: Measurement of correlation coefficients in reverberant sound fields. J. Acoust. Soc. Am. **27**(6), 1072–1077 (1955)
12. Corcos, G.M.: Resolution of pressure in turbulence. J. Acoust. Soc. Am. **35**, 192 (1963)